

Isospin breaking effects in hadronic matrix elements on the lattice

Dissertation
zur Erlangung des Grades
„Doktor der Naturwissenschaften“
am Fachbereich Physik, Mathematik und Informatik
der Johannes Gutenberg-Universität
in Mainz

Andreas Risch
geb. in Mannheim

Mainz, den 29.01.2021

Andreas Risch: Isospin breaking effects in hadronic matrix elements on the lattice

Tag der Promotionsprüfung: 10.05.2021

Abstract

In this thesis, we investigate the consequences of isospin symmetry breaking on hadronic matrix elements based on combined calculations in Quantum Chromodynamics (QCD) and Quantum Electrodynamics (QED). We employ the lattice regularisation for quantum field theories, which enables the access of both the perturbative and the non-perturbative regime of a coupling constant. The inclusion of isospin-breaking corrections in lattice QCD calculations is required to improve the theoretical prediction of hadronic contributions to high-precision observables, such as the muon anomalous magnetic moment a_μ and the running of the fine-structure constant α , which are determined from correlation functions of electromagnetic currents. We relate QCD+QED to isosymmetric QCD via Monte Carlo reweighting and formulate a perturbative expansion of correlation functions around isosymmetric QCD. Expansion parameters are the differences of the bare quark masses and their isosymmetric counterparts, a shift of the inverse strong coupling and the electromagnetic coupling. Expectation values with respect to isosymmetric QCD are evaluated by means of Monte Carlo simulations based on gauge ensembles generated with a $N_f = 2 + 1$ $O(a)$ -improved Wilson fermion action and tree-level improved Lüscher-Weisz gauge action. The handling of the manifest infrared divergence of non-compact lattice QED is addressed in this thesis. We regularise the divergence using the QED_L prescription. We derive the lattice photon propagator for open and periodic temporal boundary conditions in Feynman and Coulomb gauge. The perturbative expansion is truncated at leading order, so that the electromagnetic coupling does not renormalise. Further expansion parameters are fixed via a hadronic renormalisation scheme based on masses of pseudo-scalar mesons. In our calculation, we only consider isospin breaking effects in the valence quark sector and focus on quark-connected contributions. We derive the axial and vector Ward identity for continuum QCD+QED. A conserved vector current is deduced from the vector Ward identity for the particular lattice regularisation of QCD+QED considered in this thesis. We determine the masses of pseudo-scalar octet mesons including leading isospin breaking corrections and describe the application of the procedure to baryon masses. We provide a detailed discussion of the renormalisation of the local vector current in QCD+QED taking operator mixing into account. We further determine the leading isospin breaking correction for the renormalised HVP function, which is related to the hadronic contribution of the running of the fine-structure constant α and the anomalous magnetic moment of leptons. The presented formalism is finally used to compute the hadronic vacuum polarisation contribution to the anomalous magnetic moment of the muon a_μ including leading isospin breaking corrections. The knowledge of a precise Standard Model prediction for the latter is of particular interest, as it offers a probe for new physics. The calculations are performed on three Monte Carlo ensembles with pion masses of 354, 216 and 282 MeV and lattice spacings of 0.086, 0.076 and 0.064 fm.

Publications

Partial and intermediate results of this thesis have been published in the following articles:

- [1] A. Risch and H. Wittig, *Towards leading isospin breaking effects in mesonic masses with $O(a)$ improved Wilson fermions*, *EPJ Web Conf.* **175** (2018) 14019 [1710.06801].
- [2] A. Risch and H. Wittig, *Towards leading isospin breaking effects in mesonic masses with open boundaries*, *PoS LATTICE2018* (2018) 059 [1811.00895].
- [3] A. Risch and H. Wittig, *Leading isospin breaking effects in the hadronic vacuum polarisation with open boundaries*, *PoS LATTICE2019* (2019) 296 [1911.04230].

Contents

1. Introduction	1
1. Continuum QCD+QED	5
2. Euclidean field theories	7
2.1. Analytic continuation and Wick rotation of Minkowskian field theories . . .	7
2.2. Euclidean path integral formalism	8
2.2.1. Partition functions and expectation values for fixed temporal bound- ary conditions	8
2.2.2. Partition functions and expectation values for periodic temporal boundary conditions	9
2.3. Field transformations and symmetries	9
2.3.1. Field transformations	9
2.3.2. Quantum symmetries and quantum anomalies	11
2.3.3. Ward-Takahashi identities	12
2.4. Wick's theorem for path integrals	13
2.4.1. Wick's theorem for bosons	13
2.4.2. Wick's theorem for fermions	14
3. Euclidean QCD+QED	17
3.1. Gauge groups	17
3.1.1. U(1) gauge group	17
3.1.2. SU(3) gauge group	17
3.2. QCD+QED	18
3.2.1. QCD+QED Action	19
3.2.2. Gauge symmetries	20
3.2.3. Euclidean Dirac matrices	20
3.2.4. Colour confinement and the QCD phase diagram	22
3.3. QCD+QED β -functions	22
3.3.1. QCD β -function	22
3.3.2. QED β -function	24
3.3.3. QCD+QED β -functions	25
3.4. Flavour symmetries and conserved charges	26
3.4.1. QCD+QED	28
3.4.2. Isosymmetric QCD	28
3.4.3. Chiral QCD	29

3.4.4.	Chiral QCD with massive strange quark	30
3.4.5.	Chiral QCD+QED	30
3.4.6.	Chiral QCD+QED with massive strange quark	31
3.5.	Ward-Takahashi identities in Euclidean QCD+QED	31
3.5.1.	Vector Ward identity	32
3.5.2.	Axial Ward identity	33

II. Lattice QCD+QED 35

4. Lattice field theories 37

4.1.	Lattice regularisation	37
4.1.1.	Lattice actions and lattice operators	38
4.1.2.	Symanzik improvement programme	38
4.2.	Lattice gauge theories	39
4.2.1.	Local gauge transformations	39
4.2.2.	Gauge invariant objects	40
4.2.3.	The path integral measure for compact gauge groups	41
4.3.	Lattice gauge actions	41
4.3.1.	Wilson gauge action	41
4.3.2.	Lüscher-Weisz gauge action	42
4.4.	Lattice fermion actions	42
4.4.1.	Lattice derivatives	43
4.4.2.	Gauge covariant lattice derivatives	43
4.4.3.	Naive fermion action and doubling of fermion species	44
4.4.4.	Nielsen-Ninomiya-Theorem	44
4.4.5.	Wilson fermion action	45
4.4.6.	$O(a)$ -improved Wilson fermion action	46
4.4.7.	Alternative lattice fermion actions	47
4.5.	Non-compact lattice QED	48
4.5.1.	Inconsistency of electrodynamics on periodic volumes and IR problem of lattice QED	49
4.5.2.	QED _{TL}	50
4.5.3.	QED _L	51
4.5.4.	QED _M	52
4.5.5.	QED _C	52
4.6.	Monte Carlo simulations for gauge theories	52
4.6.1.	Importance sampling	53
4.6.2.	Markov chains	53
4.6.3.	Effective gauge action	54
4.6.4.	Monte Carlo simulations for fermion fields	55
4.6.5.	Hybrid Monte Carlo algorithm	56
4.6.6.	Thermalisation	57
4.6.7.	Monte Carlo reweighting	57

4.7. Systematic errors of lattice Monte Carlo simulations	58
5. CLS Monte Carlo simulations for lattice QCD_{iso}	61
5.1. Action and boundary conditions	61
5.2. Algorithmic setup	62
5.2.1. Even-odd preconditioning for light quarks	62
5.2.2. Twisted mass reweighting for light quarks	62
5.2.3. Factorisation of the light quark determinant	63
5.2.4. Rational approximation of strange quark determinant	63
5.2.5. Integration of molecular dynamics	64
5.2.6. Solver	64
5.3. Renormalisation scheme, chiral trajectory and scale setting	65
5.3.1. Renormalisation scheme	65
5.3.2. Chiral trajectory	66
5.3.3. Scale setting	66
5.4. CLS $N_f = 2 + 1$ gauge ensembles	67
6. Lattice QCD+QED	71
6.1. Lattice QCD+QED action	71
6.2. Boundary conditions	73
6.2.1. Spatial boundary conditions	74
6.2.2. (Anti-)periodic temporal boundary conditions	74
6.2.3. Open temporal boundary conditions	74
6.3. Symmetries of lattice QCD+QED	76
6.3.1. Charge conjugation	76
6.3.2. Euclidean reflections, spatial parity and time reflection	76
6.3.3. Translation invariance	77
6.3.4. Flavour symmetries and conserved charges	77
6.4. Ward-Takahashi identities in lattice QCD+QED	77
6.4.1. Vector Ward identity	77
6.5. Relating QCD+QED and QCD _{iso} via reweighting	80
6.5.1. QCD+QED and QCD _{iso}	80
6.5.2. Reweighting	81
6.5.3. Determination of the reweighting factor and the inner expectation value	83
6.6. Feynman rules for QCD+QED as a perturbation of QCD _{iso}	84
6.6.1. Isosymmetric quark and photon propagators	84
6.6.2. Expansion of the Wilson-Dirac operator	84
6.6.3. Expansion of the reweighting factor	86
6.6.4. Expansion of a correlation function	87
6.7. The free photon propagator on temporal periodic boundary conditions	88
6.7.1. Discrete Fourier transform	89
6.7.2. Transformation of first-order difference operators	89
6.7.3. Basis change of the photon field	90

6.7.4.	Basis change of the photon difference operator	90
6.8.	The free photon propagator on temporal open boundary conditions	92
6.8.1.	Discrete sine and cosine transformations	92
6.8.2.	Transformation of first-order difference operators	93
6.8.3.	Basis change of the photon field	94
6.8.4.	Basis change of the photon difference operator	94
7.	Computation strategies for correlation functions	97
7.1.	Infeasibility of computing the full quark propagator	97
7.2.	Stochastic treatment of all-to-all photon propagators	98
7.2.1.	Standard stochastic estimation	98
7.2.2.	Improved stochastic estimation	99
7.2.3.	The free photon half-propagator on temporal periodic boundary conditions	100
7.2.4.	The free photon half-propagator on temporal open boundary conditions	101
7.3.	Sequential quark sources and sequentially propagated sources	102
7.3.1.	No vertex	103
7.3.2.	One mass detuning vertex	103
7.3.3.	One 1-photon vertex	104
7.3.4.	Two 1-photon vertices	105
7.3.5.	Combined calculation of one 2-photon vertex and two 1-photon vertices with photon propagator	105
8.	Data analysis for Monte Carlo simulations	107
8.1.	Software for data analysis	107
8.2.	Error estimation via resampling methods	107
8.2.1.	Bootstrap for primary quantities	108
8.2.2.	Jackknife for primary quantities	109
8.2.3.	Resampling for derived quantities	109
8.2.4.	Pseudo-resampling of input parameters with associated errors	110
8.2.5.	Partial errors	110
8.3.	Autocorrelation analysis	111
8.4.	Regression analysis	111
8.4.1.	The χ^2 -function	112
8.4.2.	Inversion of the covariance matrix	113
8.4.3.	Multilinear regression models	113
8.4.4.	Linearisation of non-linear fit models by variable substitution	114
III.	Hadronic renormalisation scheme, scale setting and hadron masses	117
9.	Hadronic renormalisation scheme and scale setting	119
9.1.	Hadronic renormalisation scheme and scale setting	119

9.2. Discussion and Outlook	121
10. Hadron spectroscopy	123
10.1. Interpolation operators	123
10.2. Euclidean two-point correlation functions in the continuum	124
10.2.1. Fixed boundary conditions	124
10.2.2. Periodic boundary conditions	125
10.3. Mass determination by fitting the correlation function	125
10.3.1. Asymptotic behaviour for large time extents	125
10.3.2. Periodic temporal boundary conditions and symmetric correlation functions	126
10.4. Mass determination by fitting the effective mass	126
11. Meson masses	129
11.1. Mesonic interpolation operators	129
11.1.1. Point-like mesonic interpolation operators	129
11.1.2. Classification of interpolation operators	130
11.2. Mesonic two-point functions	131
11.2.1. Operator combinations	133
11.2.2. Diagrammatic expansion	134
11.3. Computation of quark-connected Feynman diagrams	137
11.3.1. Point sources	137
11.3.2. Stochastic sources	139
11.3.3. Computation of quark-connected Feynman diagrams with stochastic sources	140
11.4. Pseudo-scalar singlet and octet mesons	142
11.4.1. π^+ , π^- , π^0	143
11.4.2. K^+ , K^- , K^0 , \bar{K}^0	148
11.4.3. π^0 , η , η'	154
11.5. Discussion and Outlook	155
12. Baryon masses	159
12.1. Baryonic interpolation operators	159
12.2. Baryon two-point functions	159
12.2.1. Diagrammatic expansion	160
12.3. Discussion and Outlook	162
IV. The hadronic vacuum polarisation function and hadronic contributions to the anomalous magnetic moment of the muon	165
13. Vector current renormalisation	167
13.1. Lattice discretisations of the electromagnetic and flavour diagonal vector currents	167

13.2. The bare vector-vector correlation function	169
13.2.1. Diagrammatic expansion of the bare vector-vector correlation function	169
13.3. Computation of quark-connected Feynman diagrams	171
13.3.1. Local vector current	172
13.3.2. Conserved vector current	172
13.4. Renormalisation of the local electromagnetic current	174
13.4.1. Renormalisation condition	175
13.5. Discussion and Outlook	189
14. The hadronic vacuum polarisation function	193
14.1. The hadronic vacuum polarisation function	193
14.2. Time-momentum representation of the hadronic vacuum polarisation func- tion in the continuum	194
14.3. The renormalised hadronic vacuum polarisation function in lattice QCD+QED	195
14.3.1. $\hat{\Pi}_{\nu_R^\gamma \nu_R^\gamma}$ from $C_{\nu_{c,R}^\gamma \nu_{l,R}^\gamma}$	196
14.3.2. $\hat{\Pi}_{\nu_R^\gamma \nu_R^\gamma}$ from $C_{\nu_{l,R}^\gamma \nu_{l,R}^\gamma}$	197
14.4. Discussion and Outlook	202
15. The HVP contribution to the muon anomalous magnetic moment	207
15.1. The anomalous magnetic moment of the muon	207
15.1.1. Experimental determination	207
15.1.2. Theoretical prediction	209
15.2. The time-momentum representation of the hadronic vacuum polarisation contribution	211
15.3. The hadronic vacuum polarisation contribution from lattice QCD+QED . .	211
15.3.1. $a_{\mu,\text{HVP}}$ from $C_{\nu_{c,R}^\gamma \nu_{l,R}^\gamma}$	212
15.3.2. $a_{\mu,\text{HVP}}$ from $C_{\nu_{l,R}^\gamma \nu_{l,R}^\gamma}$	215
15.4. Discussion and Outlook	215
16. Conclusion and Outlook	219
V. Appendix	225

1. Introduction

The Standard Model of particle physics (SM) is a unified quantum field theory incorporating three fundamental interactions: the strong, the electromagnetic and the weak interaction. It was developed and established in several steps during the second half of the 20th century, based on the formulation of the strong interaction [1] as a *Yang-Mills theory* [2], the electroweak unification, known as the *Glashow-Weinberg-Salam theory* [3–5], and the *Englert-Brout-Higgs mechanism* [6–8], which is a method to achieve spontaneous symmetry breaking in gauge theories. The existence of several elementary particles predicted by the SM was confirmed experimentally. The existence of the charm quark, which is essential for the *Glashow-Iliopoulos-Maiani mechanism* [9], was inferred from the discovery of the J/Ψ meson [10, 11] at SLAC and BNL in 1974. The massive gauge bosons W^\pm [12, 13] and Z [14, 15], responsible for mediation of the weak interaction, were found at the SPS at CERN in 1983. This series of discoveries finally culminated with the Higgs boson, which was found at the ATLAS and CMS experiments at CERN [16, 17] in 2012.

Despite its success, the SM leaves several experimental and theoretical issues unanswered: Firstly, the SM does not include gravity, which is the remaining of the four known fundamental interactions. The formulation of general relativity as a quantum field theory is a highly non-trivial task, as it is a perturbatively non-renormalisable theory [18, 19]. Secondly, the SM treats neutrinos as massless, chiral Weyl fermions [20], although it is already known by neutrino oscillation experiments that neutrinos are massive, being either Dirac or Majorana particles. Thirdly, in today’s universe matter dominates anti-matter. The CP- and baryon number violating processes predicted by the SM are not capable of explaining the strength of baryogenesis. Furthermore, the SM describes the properties of only a small fraction of the matter in the universe, as evidenced by cosmological observations. Lastly, the SM depends on 18 fundamental parameters [20], which have to be determined by experiments. If the SM is understood as a low-energy effective description of a theory valid at higher scales, these parameters are not necessarily independent.

There are two main categories of experiments to probe the SM. Direct searches aim at the detection of unknown particles produced in particle colliders or in cosmic events, whereas indirect search experiments try to measure quantities with high accuracy to find deviations from the model predictions. One promising quantity for the investigation of physics beyond the SM is the anomalous magnetic moment of the muon [21, 22]. For the leptons $l = e, \mu, \tau$ the *Dirac* theory [23, 24] predicts a Landé-factor, which relates the magnetic moment of a particle with its spin, of $g_l = 2$. Quantum field theoretical corrections, first predicted by *Schwinger* [25] and parametrised by the anomalous contribution $a_l = \frac{1}{2}(g_l - 2)$, alter this value. The anomalous magnetic moment of the muon is one of the most precisely measured quantities in physics. The currently most accurate experimental determination,

1. Introduction

obtained at BNL [26], is

$$a_\mu = 11659209.1(5.4)(3.3) \cdot 10^{-10} \quad (1.1)$$

with a precision of 0.5 ppm. A reduction of the overall uncertainty by a factor of four is planned by experiments at Fermilab [27] and JPARC [28]. Comparing the experimental determination with the SM prediction, one finds a deviation of about 3-4 σ [29]. The largest source of uncertainty of the theory prediction stems from hadronic effects, in particular the contributions from the hadronic vacuum polarisation and hadronic light-by-light scattering [29]. The former can be determined with a phenomenological approach from the cross section of positron-electron collisions forming hadrons, from Dyson-Schwinger equations [30] or as a first principles calculation from lattice QCD [31–33]. A determination of the hadronic vacuum polarisation contribution with a relative precision of 0.2% is required to achieve the target accuracy of the upcoming experiments. This can only be attained in lattice simulations based on non-isosymmetric QCD including the effects of non-degenerate light quark masses and electromagnetism [34].

	p	n
m [MeV]	938.272081(6)	939.565413(5)
I	$1/2$	$1/2$
I_3	$1/2$	$-1/2$
q [e]	1	-1

Table 1.1.: Masses and electromagnetic charges of the proton and neutron forming an isospin doublet [35].

The concept of *isospin* predates the development of the SM and was originally introduced in 1932 by *Heisenberg* [36] under the name *isotopic spin*. Experiments showed that the excitation spectra of mirror nuclei, for which the number of protons and neutrons are interchanged, resemble each other. Heisenberg suggested that both the proton and the neutron form manifestations of the same state, the nucleon. Mathematically, this concept is described by a $SU(2)_I$ symmetry acting on a two dimensional space, in which the proton was interpreted as a state with $I_3 = +1/2$ and the neutron with $I_3 = -1/2$, depicted in table 1.1. In 1954, the attempt by *Yang* and *Mills* to interpret isospin symmetry as a local gauge symmetry [2] lead to the construction of non-Abelian gauge theories. At the time, this theory was not confirmed experimentally. Nevertheless, it laid the theoretical and mathematical foundations for the formulation of the strong and electro-weak interactions.

Although the concept of isospin was an early ancestor of the SM, the former is not strictly compatible with the latter. Neglecting the effects of the weak interaction, induced by the *Cabibbo-Kobayashi-Maskawa matrix* [37], the SM obeys isospin symmetry only in the limit in which the masses and the electric charges of the up and the down quarks are equal. Empirically, it is known that isospin symmetry is broken only on small scales relative to energies determined by the strong interaction, such as the hadron spectrum, as can be seen in tables 1.1 and 1.2 for the nucleons and the light pseudo-scalar mesons.

	π^\pm	π^0	K^\pm	K^0
m [MeV]	139.57039(18)	134.9768(5)	493.677(16)	497.611(13)
I	1	1	$1/2$	$1/2$
I_3	± 1	0	$\pm 1/2$	$\mp 1/2$
q [e]	± 1	0	± 1	0

Table 1.2.: Masses and electromagnetic charges of the light pseudo-scalar mesons forming isospin multiplets [35].

	u	d
m [MeV]	$2.16^{+0.49}_{-0.26}$	$4.67^{+0.48}_{-0.17}$
I	$\frac{1}{2}$	$1/2$
I_3	$1/2$	$-1/2$
q [e]	$2/3$	$-1/3$

Table 1.3.: Masses and electromagnetic charges of up and down quarks determined in the mass-independent subtraction scheme $\overline{\text{MS}}$ at a renormalisation scale of $\mu = 2 \text{ GeV}$ [35].

On the level of elementary particles, the situation is different. The difference of light quark masses is of the same order of magnitude as the masses themselves, c.f. table 1.3. Nevertheless, the quark mass splitting is of $O(1\%)$ compared to a typical energy scale of QCD [38]. Similarly, the typical relative size of electromagnetic corrections is given by the fine-structure constant $\alpha_{\text{em}} = 7.2973525693(11) \cdot 10^{-3}$ [35], which is also $O(1\%)$ [38]. Consequently, the general assumption is, that observables which are not invariant under isospin rotations are approximated by the isosymmetric theory with an $O(1\%)$ relative systematic error [38, 39].

The breaking of isospin symmetry is of great importance in nature. The magnitude of this symmetry violation influences the composition of nuclear and atomic matter in the universe [40]. In particular, the sign and magnitude of the mass splitting of the proton and the neutron ensure, that the proton and the hydrogen atom become physically stable [40, 41]. If the relative neutron-proton mass difference was smaller than one third of the observed value $m_n - m_p = 1.2933321(5) \text{ MeV}$ [35], the hydrogen atom would decay via an inverse beta decay into neutrons [41]. However, if the mass difference was considerably larger than the observed value, neutrons would decay faster and therefore, the formation of heavy elements in stars would have become more difficult [41].

Lattice QCD Monte Carlo simulations serve as a tool to compute hadronic observables from first principles, such as the hadronic spectrum, hadron form factors and charges as well as the hadronic contributions to the anomalous magnetic moment of leptons. These simulations are commonly performed in an isosymmetric setup, mainly for technical reasons. It is computationally less demanding to evaluate the quark determinant of two quarks with degenerate masses compared to a setup with non-degenerate masses [42]. The systematic error due to the assumption of isospin symmetry and the absence of the

1. Introduction

electromagnetic interaction was, for decades, negligible in comparison to the stochastic error associated with Monte Carlo simulations. During recent years, the development of more efficient simulation algorithms and the substantial progress in the provision of high-performance computing facilities enabled the community to reduce the stochastic errors to the percent level in several standard observables [39]. As a result, the assumption of isospin symmetry became a dominant and non-negligible source of systematic uncertainty in many hadronic observables [39]. Due to their partly compensating nature and the equal order of magnitude, both the quark mass splitting and the electromagnetic interaction have to be included into up-to-date lattice simulations [39, 43, 44].

This thesis lays the foundations for the inclusion of isospin breaking effects in calculations using the gauge ensembles generated by the CLS effort [45] based on a perturbative expansion around the isosymmetric limit [46]. It does not aim for a complete prediction of an observable including isospin breaking effects at the physical point, i.e. with performed extrapolations to the continuum and physical quark masses. It rather focusses on the formulation and implementation of the required theoretical and computational setup. Nevertheless, we will give first results on pseudo-scalar meson masses, which are used to fix the free parameters of the theory, on the renormalisation factors of the local discretisation of flavour neutral vector currents, on the hadronic vacuum polarisation function and on the hadronic vacuum contribution to the anomalous magnetic moment of the muon including leading isospin breaking effects at non-physical quark masses and finite lattice spacings. As a computational simplification, we only focus on quark-connected contributions. The concepts introduced and discussed in this thesis can be used in various future projects, such as the determination of isospin splittings in the baryon octet and decuplet [41, 47], the determination of isospin corrections in the hadronic contributions to the running of the fine-structure constant α and the weak mixing angle θ_W , as well as the determination of the masses of the up and down quark [48], which is relevant in the context of the strong CP problem [40, 49, 50].

We organise this work as follows: In Part I, we introduce relevant aspects of Euclidean field theories focussing on field transformations and symmetries. We further discuss properties of combined Euclidean QCD and QED under the aspect of symmetries, Ward identities and β -functions. Part II deals with the construction of lattice field theories as a regularisation of continuum field theories and with Monte Carlo simulations as a method to stochastically evaluate the path integral. We summarise the simulation setup for CLS gauge ensembles and introduce the setup for combined lattice QCD and QED, used for the determination of isospin corrections. We also discuss computational strategies for the evaluation of correlation functions and aspects of data analysis, applied to the results of Monte Carlo simulations. In Part III, we introduce the hadronic renormalisation scheme for combined QCD and QED utilised to fix the bare parameters and discuss hadron spectroscopy for mesons and baryons. Part IV covers the vector current renormalisation, the hadronic vacuum polarisation function and a discussion of hadronic contributions to the anomalous magnetic moment of the muon. We end this part with the final conclusion and outlook.

Part I.

Continuum QCD+QED

2. Euclidean field theories

In this chapter, we give a brief introduction into Euclidean field theories, which are essential for the application of Monte Carlo techniques. We discuss the Euclidean path integral formalism with a focus on boundary conditions, field transformations, symmetries, anomalies and Ward-Takahashi identities. This introduction is based on the standard text books by *Peskin and Schroeder* [51], *Srednicki* [52], *Mandl and Shaw* [53], *Weinberg* [54, 55] and *Pokorski* [56], which deal with field theories in Minkowski spacetime. Path integrals and quantum anomalies are discussed in *Fujikawa and Suzuki* [57], renormalisation in *Collins* [58]. The text books by *Zinn-Justin* [59] and *Wipf* [60] put a particular emphasis on Euclidean field theories. This chapter is partly inspired by the PhD theses [61–65].

2.1. Analytic continuation and Wick rotation of Minkowskian field theories

Euclidean field theories [66, 67] are derived from Minkowskian field theories by an analytic continuation of the fields and a Wick rotation of the time variable [68]. Starting with a Minkowski metric with tensor $g_M = \text{diag}(1, -1, -1, -1)$ the partition function of a quantum field theory in Minkowski spacetime reads

$$Z_M = \int D\Upsilon_M \exp \left(i \int d^4x_M \mathcal{L}_M[\Upsilon_M] \right). \quad (2.1)$$

The coordinate transformation from Minkowski to Euclidean spacetime is given by $x_E^{\mu_2} = \Lambda_{\text{Wick}}^{\mu_2 \mu_1} x_M^{\mu_1}$ with the transformation matrix $\Lambda_{\text{Wick}} = \text{diag}(-i, 1, 1, 1)$. The integration measure of the spacetime integral transforms as $d^4x_M = -i d^4x_E$. Absorbing an additional overall minus sign into the definition of the Euclidean Lagrange density \mathcal{L}_E , which originates from the transformation of the metric tensor, one defines the Euclidean partition function

$$Z_E = \int D\Upsilon_E \exp \left(- \int d^4x_E \mathcal{L}_E[\Upsilon_E] \right). \quad (2.2)$$

In comparison to the partition function in Minkowski spacetime, the integrand is now real and positive for a real action. This fact is of central relevance when Monte Carlo techniques are utilised for the evaluation of the path integral as the Boltzmann factor $\exp(-S_E[\Upsilon_E])$ is used as a probability weight.

In principle, correlation functions evaluated in the Euclidean formalism can also be analytically continued back to Minkowski spacetime. This is, however, highly non-trivial, as a unique analytic continuation demands the knowledge of the value of a function evaluated

2. Euclidean field theories

for an infinite set of points, which possesses a limit point. Consequently, if correlation functions are calculated by numeric methods, one has only direct access to the spacelike region. Nevertheless, an analytic continuation can be performed in this case, e.g. under model assumptions.

2.2. Euclidean path integral formalism

This work is based on the Euclidean path integral formalism for the evaluation of correlation functions of Euclidean quantum field theories. For simplicity, we only consider a field theory with a bosonic field Φ in this section, as a discussion for fermionic fields is more involved. Performing a Wick rotation to imaginary time requires also a modification of the quantum mechanical interpretation of a quantum field theory. The time evolution operator for quantum mechanics with imaginary time propagating a state from time t_1 to time t_2 becomes $\exp(-H(t_2 - t_1))$, where H is a time independent Hamilton operator. For the subsequent discussion, we consider a complete set of normalised eigenstates of the field operator Φ . We denote these states in the Schrödinger picture with $|\Phi, t\rangle$ and in Heisenberg picture with $|\Phi\rangle$. We match the Heisenberg and the Schrödinger picture at $t = 0$, i.e. $|\Phi, 0\rangle = |\Phi\rangle$. We consider two different types of temporal boundary conditions: fixed boundary conditions, where the fields take a fixed predetermined value and (anti-)periodic boundary conditions, where bosonic fields are continued periodically and fermionic fields antiperiodically. We usually omit the explicit reference to the boundary condition, i.e. leave the domain of integration in field space unspecified and denote the partition function Z and the expectation value of an operator $\langle \mathcal{O}[\Phi] \rangle$.

2.2.1. Partition functions and expectation values for fixed temporal boundary conditions

In the following, we consider a field theory of a bosonic field Φ that is defined on a spacetime with a time extent $[0, T]$. The field fulfils the boundary conditions $\Phi(0) = \Phi_1$ and $\Phi(T) = \Phi_2$, i.e. the field is in the eigenstate of the field operator $|\Phi_1\rangle$ at time $t = 0$ and in $|\Phi_2\rangle$ at time $t = T$. We define the partition function

$$\begin{aligned} Z &= \langle \Phi_2, T | \Phi_1, 0 \rangle = \langle \Phi_2 | \exp(-HT) | \Phi_1 \rangle \\ &= \int_{\Phi(0)=\Phi_1}^{\Phi(T)=\Phi_2} D\Phi \exp(-S[\Phi]). \end{aligned} \quad (2.3)$$

The measure $D\Phi$ is of formal character at this stage. Correlation functions of time-ordered operators are evaluated according to

$$\begin{aligned} \langle \mathcal{O}[\Phi] \rangle &= \frac{\langle \Phi_2, T | \mathcal{O}[\Phi] | \Phi_1, 0 \rangle}{\langle \Phi_2, T | \Phi_1, 0 \rangle} = \frac{\langle \Phi_2 | \exp(-HT) \mathcal{O}[\Phi] | \Phi_1 \rangle}{\langle \Phi_2 | \exp(-HT) | \Phi_1 \rangle} \\ &= \frac{1}{Z} \int_{\Phi(0)=\Phi_1}^{\Phi(T)=\Phi_2} D\Phi \exp(-S[\Phi]) \mathcal{O}[\Phi], \end{aligned} \quad (2.4)$$

where the expectation value is normalised such that $\langle 1 \rangle = 1$.

2.2.2. Partition functions and expectation values for periodic temporal boundary conditions

We now consider periodic boundary conditions, which can be related to the results of fixed boundary conditions by choosing the same boundary field at $t = 0$ and $t = T$ and a subsequent integration over all boundary fields with measure $D'\Phi$. We define the partition function [42]

$$\begin{aligned} Z &= \int D'\Phi_1 \langle \Phi_1, T | \Phi_1, 0 \rangle = \text{tr}(\exp(-HT)) \\ &= \int D'\Phi_1 \int_{\Phi(0)=\Phi_1}^{\Phi(T)=\Phi_1} D\Phi \exp(-S[\Phi]) = \int_{\Phi(0)=\Phi(T)} D\Phi \exp(-S[\Phi]) \end{aligned} \quad (2.5)$$

and the expectation value of time-ordered operators [42]

$$\begin{aligned} \langle \mathcal{O}[\Phi] \rangle &= \frac{\int D'\Phi_1 \langle \Phi_1, T | \mathcal{O}[\Phi] | \Phi_1, 0 \rangle}{\int D'\Phi_1 \langle \Phi_1, T | \Phi_1, 0 \rangle} = \frac{\text{tr}(\exp(-HT) \mathcal{O}[\Phi])}{\text{tr}(\exp(-HT))} \\ &= \frac{1}{Z} \int_{\Phi(0)=\Phi(T)} D\Phi \exp(-S[\Phi]) \mathcal{O}[\Phi], \end{aligned} \quad (2.6)$$

where the expectation value is again normalised such that $\langle 1 \rangle = 1$.

2.3. Field transformations and symmetries

In this section, we summarise how partition functions and expectation values transform under field transformations. We also briefly recapitulate the notion of quantum symmetries and quantum anomalies as special cases of field transformations. Eventually, we derive a general formula giving *Ward-Takahashi identities* for arbitrary field transformations. Ward-Takahashi identities are the quantum analogon of Noether's theorem in classical theories. The consideration of field transformations is particularly relevant for the determination of the mixing behaviour of operators under renormalisation. Operators are grouped into classes with the same transformational behaviour under a specific symmetry transformation. Operators from distinct classes are assumed not to mix under renormalisation as the renormalisation procedure should not spoil the symmetries of the theory [58].

2.3.1. Field transformations

In the following, we consider a general bijective differentiable field transformation \mathfrak{T}

$$\mathfrak{T} : \Upsilon \mapsto \mathfrak{T}[\Upsilon]. \quad (2.7)$$

Examples for such field transformations are global and local gauge transformations, flavour rotations, spacetime coordinate transformations, translations and rotations. A key ingredient of the following discussion is the theorem of multivariate coordinate transformations

2. Euclidean field theories

for integrals over superfields $\Upsilon = (\Upsilon_\Phi, \Upsilon_\Psi)$. The latter combine bosonic degrees of freedom Υ_Φ and fermionic degrees of freedom Υ_Ψ . We consider an invertible linear map of superfields represented by a supermatrix A [59, 69, 70]. For the further discussion, we decompose the map into bosonic and fermionic degrees of freedom

$$\begin{pmatrix} \Upsilon'_\Phi \\ \Upsilon'_\Psi \end{pmatrix} = \begin{pmatrix} A_{\Phi\Phi} & A_{\Phi\Psi} \\ A_{\Psi\Phi} & A_{\Psi\Psi} \end{pmatrix} \begin{pmatrix} \Upsilon_\Phi \\ \Upsilon_\Psi \end{pmatrix}. \quad (2.8)$$

Similar to matrices over real or complex numbers, it is possible to define a determinant for supermatrices, the so called *superdeterminant*, which is also known as the *Berezinian* [59, 69, 70]. It is defined as

$$\text{sdet}(A) = \det(A_{\Phi\Phi} - A_{\Phi\Psi}(A_{\Psi\Psi})^{-1}A_{\Psi\Phi}) \det(A_{\Psi\Psi})^{-1}. \quad (2.9)$$

The latter expression consists only of determinants of matrices with values in the commuting numbers and is therefore well defined. For linear maps that do not mix bosonic and fermionic degrees of freedom, i.e. $A_{\Phi\Psi} = 0$ and $A_{\Psi\Phi} = 0$, we obtain $\text{sdet}(A) = \det(A_{\Phi\Phi}) \det(A_{\Psi\Psi})^{-1}$. The theorem of multivariate coordinate transformations for integrals [59, 70] is given by

$$\int D\Upsilon f[\Upsilon] = \int D\Upsilon \text{sdet} \left(\frac{\delta \mathfrak{T}[\Upsilon]}{\delta \Upsilon} \right) f[\mathfrak{T}[\Upsilon]], \quad (2.10)$$

where we assume that the set of field configurations which the functional integral integrates over is invariant under the transformation. Otherwise, one would have to explicitly state the respective sets. For the special case, in which the transformation \mathfrak{T} does not mix bosonic and fermionic degrees of freedom, i.e. $\frac{\delta(\mathfrak{T}[\Upsilon])_\Psi}{\delta \Upsilon_\Phi} = 0$ and $\frac{\delta(\mathfrak{T}[\Upsilon])_\Phi}{\delta \Upsilon_\Psi} = 0$, we obtain the well known transformation behaviour of ordinary integrals and Grassmann integrals [42, 59].

As the choice of coordinates of the field space is to some degree arbitrary, it is interesting to investigate the behaviour of an expectation value of a general operator $\mathcal{O}[\Upsilon]$ under a field transformation. Making use of the theorem eq. (2.10), we find:

$$\begin{aligned} \langle \mathcal{O}[\mathfrak{T}[\Upsilon]] \rangle &= \frac{1}{Z} \int D\Upsilon \exp(-S[\Upsilon]) \mathcal{O}[\mathfrak{T}[\Upsilon]] \\ &= \frac{1}{Z} \int D\Upsilon \text{sdet} \left(\frac{\delta \mathfrak{T}^{-1}[\Upsilon]}{\delta \Upsilon} \right) \exp(-S[\mathfrak{T}^{-1}[\Upsilon]]) \mathcal{O}[\Upsilon] \\ &= \left\langle \text{sdet} \left(\frac{\delta \mathfrak{T}^{-1}[\Upsilon]}{\delta \Upsilon} \right) \exp(-(S[\mathfrak{T}^{-1}[\Upsilon]] - S[\Upsilon])) \mathcal{O}[\Upsilon] \right\rangle, \end{aligned} \quad (2.11)$$

i.e. not only the transformational behaviour of the operator is relevant, but also the change of the action, as well as the change of the path integral integration measure, that is encoded in the functional determinant of the field transformation. In addition, the set of field configurations which the functional integral integrates over must be invariant under the transformation, i.e. the boundary conditions are compatible with the transformation. It is essential to remark that the application of this theorem is only meaningful if the path

integral measure has been regulated appropriately. Naive calculations, that only have formal character, can lead to incorrect results. The most prominent example is the chiral transformation and the related derivation of the chiral anomaly [57]. Of particular interest are field transformations that leave the expectation value of general operators invariant. We will consider this class of transformations in the next section.

2.3.2. Quantum symmetries and quantum anomalies

In classical field theories, symmetries of the action, also known as off-shell symmetries, are defined as field transformations that leave the action invariant [51], i.e. a bijective field transformation \mathfrak{T} is a symmetry of the action if and only if

$$S[\mathfrak{T}[\Upsilon]] = S[\Upsilon] \quad \forall \Upsilon, \quad (2.12)$$

where the symmetry transformation might have to be compatible with given boundary conditions. Since $\frac{\delta S[\mathfrak{T}[\Upsilon]]}{\delta \Upsilon} = \frac{\delta S[\Upsilon]}{\delta \Upsilon} \quad \forall \Upsilon$, it immediately follows that all off-shell symmetries are in fact also symmetries of the classical equations of motion $\frac{\delta S[\Upsilon]}{\delta \Upsilon} = 0$, i.e. on-shell symmetries as solutions of the equation of motion are mapped to other solutions. Having discussed symmetries of the action, we are lead to the question, when a field transformation is a symmetry not only of the classical theory, but also of the related quantum field theory. Making use of eq. (2.11), we see that the expectation value of any operator $\mathcal{O}[\Upsilon]$ is invariant under the transformation \mathfrak{T} , if

$$\text{sdet} \left(\frac{\delta \mathfrak{T}^{-1}[\Upsilon]}{\delta \Upsilon} \right) \exp(-(S[\mathfrak{T}^{-1}[\Upsilon]] - S[\Upsilon])) = 1. \quad (2.13)$$

For this class of transformations, we find

$$\langle \mathcal{O}[\mathfrak{T}[\Upsilon]] \rangle = \langle \mathcal{O}[\Upsilon] \rangle, \quad (2.14)$$

which characterises a quantum symmetry. A sufficient condition, that is usually considered, is

$$S[\mathfrak{T}^{-1}[\Upsilon]] = S[\Upsilon] \quad \text{and} \quad \text{sdet} \left(\frac{\delta \mathfrak{T}^{-1}[\Upsilon]}{\delta \Upsilon} \right) = 1, \quad (2.15)$$

i.e. \mathfrak{T} is a symmetry of the action and the path integral measure is invariant under this transformation. Symmetries of the action that do not leave the path integral measure invariant are called *anomalous symmetry transformations* or *quantum anomalies*, as the classical symmetry is broken by quantum effects. In order to tell whether a symmetry is anomalous, a regularisation of the path integral measure compatible with that symmetry has to be chosen, i.e. the resulting action of the regulated theory still has to be invariant under the transformation.

An important application of symmetry transformations is to prove that particular correlation functions vanish. We discuss a simple example, which we use later to rule out

2. Euclidean field theories

combinations of operators with vanishing expectation values to save computer time. Nevertheless, a vanishing operator combination might serve as a consistency check. Assuming that we have found a quantum symmetry transformation \mathfrak{T} obeying

$$\mathfrak{T}[\mathcal{O}[\Upsilon]] = -\mathcal{O}[\Upsilon] \quad (2.16)$$

for a particular operator $\mathcal{O}[\Upsilon]$, it is easy to show, with the help of eq. (2.14), that the expectation value of this operator vanishes:

$$\langle \mathcal{O}[\Upsilon] \rangle = \langle \mathfrak{T}[\mathcal{O}[\Upsilon]] \rangle = -\langle \mathcal{O}[\Upsilon] \rangle. \quad (2.17)$$

2.3.3. Ward-Takahashi identities

In the following, we derive a general formula describing *Ward-Takahashi identities* for general field transformations. In standard textbooks [51, 52], one usually finds derivations only for specific transformations. We consider a class of bijective field transformations $(\mathfrak{T}[\varepsilon])_\varepsilon$, parametrised by a real scalar field ε

$$\mathfrak{T}[\varepsilon] : \Upsilon \mapsto \mathfrak{T}[\varepsilon][\Upsilon]. \quad (2.18)$$

We demand that ε parametrises distance of $\mathfrak{T}[\varepsilon]$ to the identity transformation, i.e.

$$\mathfrak{T}[\varepsilon][\Upsilon] \big|_{\varepsilon=0} = \Upsilon, \quad (2.19)$$

and that \mathfrak{T} is differentiable at $\varepsilon = 0$. Applying the transformation theorem for multivariate integrals eq. (2.10), we find

$$\int D\Upsilon \exp(-S[\Upsilon]) \mathcal{O}[\Upsilon] = \int D\Upsilon \text{sdet} \left(\frac{\delta \mathfrak{T}[\varepsilon][\Upsilon]}{\delta \Upsilon} \right) \exp(-S[\mathfrak{T}[\varepsilon][\Upsilon]]) \mathcal{O}[\mathfrak{T}[\varepsilon][\Upsilon]]. \quad (2.20)$$

We now differentiate this equation with respect to ε^x and evaluate the derivative at $\varepsilon = 0$:

$$\begin{aligned} 0 &= \frac{\delta}{\delta \varepsilon^x} \int D\Upsilon \text{sdet} \left(\frac{\delta \mathfrak{T}[\varepsilon][\Upsilon]}{\delta \Upsilon} \right) \exp(-S[\mathfrak{T}[\varepsilon][\Upsilon]]) \mathcal{O}[\mathfrak{T}[\varepsilon][\Upsilon]] \bigg|_{\varepsilon=0} \\ &= \int D\Upsilon \frac{\delta}{\delta \varepsilon^x} \text{sdet} \left(\frac{\delta \mathfrak{T}[\varepsilon][\Upsilon]}{\delta \Upsilon} \right) \bigg|_{\varepsilon=0} \exp(-S[\mathfrak{T}[\varepsilon][\Upsilon]]) \mathcal{O}[\mathfrak{T}[\varepsilon][\Upsilon]] \\ &\quad + \exp(-S[\mathfrak{T}[\varepsilon][\Upsilon]]) \frac{\delta}{\delta \varepsilon^x} S[\mathfrak{T}[\varepsilon][\Upsilon]] \bigg|_{\varepsilon=0} \mathcal{O}[\mathfrak{T}[\varepsilon][\Upsilon]] \\ &\quad + \text{sdet} \left(\frac{\delta \mathfrak{T}[\varepsilon][\Upsilon]}{\delta \Upsilon} \right) \exp(-S[\mathfrak{T}[\varepsilon][\Upsilon]]) \frac{\delta}{\delta \varepsilon^x} \mathcal{O}[\mathfrak{T}[\varepsilon][\Upsilon]] \bigg|_{\varepsilon=0} \\ &= \int D\Upsilon \exp(-S[\Upsilon]) \left(\frac{\delta}{\delta \varepsilon^x} \left(\text{sdet} \left(\frac{\delta \mathfrak{T}[\varepsilon][\Upsilon]}{\delta \Upsilon} \right) - S[\mathfrak{T}[\varepsilon][\Upsilon]] \right) \bigg|_{\varepsilon=0} \mathcal{O}[\Upsilon] \right. \\ &\quad \left. + \frac{\delta \mathcal{O}[\mathfrak{T}[\varepsilon][\Upsilon]]}{\delta \varepsilon^x} \bigg|_{\varepsilon=0} \right). \end{aligned} \quad (2.21)$$

Dividing the latter equation by the partition function Z leads to the *Ward-Takahashi identity* with respect to the class of field transformations \mathfrak{T} expressed in terms of a correlation function:

$$0 = \left\langle \left(\frac{\delta}{\delta \varepsilon^x} \text{sdet} \left(\frac{\delta \mathfrak{T}[\varepsilon][\Upsilon]}{\delta \Upsilon} \right) \bigg|_{\varepsilon=0} - \frac{\delta S[\mathfrak{T}[\varepsilon][\Upsilon]]}{\delta \varepsilon^x} \bigg|_{\varepsilon=0} \right) \mathcal{O}[\Upsilon] + \frac{\delta \mathcal{O}[\mathfrak{T}[\varepsilon][\Upsilon]]}{\delta \varepsilon^x} \bigg|_{\varepsilon=0} \right\rangle. \quad (2.22)$$

We will apply this theorem later in the context of continuum QCD+QED in section 3.5 and in the context of lattice QCD+QED in section 6.4.

2.4. Wick's theorem for path integrals

An important method for the evaluation of path integrals is the application of *Wick's theorem*. Considering a free field theory, i.e. a theory in which the action is either quadratic in the field or bilinear in the field and its conjugate, Wick's theorem allows us to express expectation values of field operators in terms of propagators, which are Green's functions of the operator appearing in the action. We revise Wick's theorem for bosons and fermions, which we will apply to the photon and quark fields in chapter 6.

2.4.1. Wick's theorem for bosons

We consider a real non-interacting bosonic theory, i.e. the action is bilinear in the bosonic field Φ and its dynamics is described by the operator Δ . The field Φ may have spatial and internal degrees of freedom denoted by the multi-index \mathbf{c} . We introduce a metric tensor $g_{\mathbf{c}_2 \mathbf{c}_1}$, which allows us to raise and lower indices. In the defining representation of the field, the metric tensor is unity. In this setup, the free action of a bosonic field is given by

$$S[\Phi] = \frac{1}{2} \Phi_{\mathbf{c}_2} \Delta^{\mathbf{c}_2}_{\mathbf{c}_1} \Phi^{\mathbf{c}_1}. \quad (2.23)$$

The tensor $\Delta^{\mathbf{c}_2}_{\mathbf{c}_1}$ is contracted with the symmetric tensor $\Phi_{\mathbf{c}_2} \Phi^{\mathbf{c}_1}$, such that its antisymmetric part is projected to zero. We therefore assume that Δ is a symmetric tensor, i.e. $\Delta^{\mathbf{c}_2}_{\mathbf{c}_1} = \Delta_{\mathbf{c}_1}^{\mathbf{c}_2}$. We define the generating functional Z by [59]

$$Z[J] = \int D\Phi \exp(-S[\Phi] + J_{\mathbf{c}} \Phi^{\mathbf{c}}), \quad (2.24)$$

where J is a source for the field Φ and $D\Phi$ denotes the path integral measure with respect to the defining representation of the field Φ

$$D\Phi = \prod_{\mathbf{c}} d\Phi^{\mathbf{c}}. \quad (2.25)$$

Correlation functions of the field Φ can then be expressed up to normalisation in terms of derivatives of the generating functional at vanishing source [59]:

$$\langle \Phi^{\mathbf{c}_n} \dots \Phi^{\mathbf{c}_1} \rangle = \frac{1}{Z[0]} \frac{\delta^n Z[J]}{\delta J_{\mathbf{c}_n} \dots \delta J_{\mathbf{c}_1}} \Big|_{J=0}. \quad (2.26)$$

Our aim is now to derive a simple and closed expression for correlation functions in terms of the operator Δ . For the following calculation, it is, however, convenient to introduce the propagator Σ as its inverse:

$$\Sigma^{\mathbf{c}_3}_{\mathbf{c}_2} \Delta^{\mathbf{c}_2}_{\mathbf{c}_1} = \delta^{\mathbf{c}_3}_{\mathbf{c}_1}. \quad (2.27)$$

2. Euclidean field theories

The symmetry property $\Sigma^{\mathbf{c}_2}_{\mathbf{c}_1} = \Sigma_{\mathbf{c}_1}^{\mathbf{c}_2}$ is inherited from Δ . It is important to note that, if Φ is a gauge field, the operator Δ is only invertible for a completely gauge fixed theory. Otherwise, the propagator is not well defined as Δ is a singular operator. We define a field transformation

$$\mathfrak{T}[\Phi^{\mathbf{c}_2}] = \Phi^{\mathbf{c}_2} - \Sigma^{\mathbf{c}_2}_{\mathbf{c}_1} J^{\mathbf{c}_1}, \quad (2.28)$$

which shifts the field variables linearly and therefore fulfils $\text{sdet}\left(\frac{\delta \mathfrak{T}[\Phi]}{\delta \Phi}\right) = 1$, i.e. the path integral measure is invariant. Completing the square and making use of the latter field transformation in combination with eq. (2.10) and the symmetry property of Σ , the generating functional can be rewritten as

$$\begin{aligned} Z[J] &= \int D\Phi \exp\left(-\frac{1}{2}(\Phi_{\mathbf{c}_3} - J_{\mathbf{c}_4} \Sigma^{\mathbf{c}_4}_{\mathbf{c}_3}) \Delta^{\mathbf{c}_3}_{\mathbf{c}_2} (\Phi^{\mathbf{c}_2} - \Sigma^{\mathbf{c}_2}_{\mathbf{c}_1} J^{\mathbf{c}_1}) + \frac{1}{2} J_{\mathbf{c}_2} \Sigma^{\mathbf{c}_2}_{\mathbf{c}_1} J^{\mathbf{c}_1}\right) \\ &= \int D\Phi \exp\left(-\frac{1}{2} \Phi_{\mathbf{c}_3} \Delta^{\mathbf{c}_3}_{\mathbf{c}_2} \Phi^{\mathbf{c}_2} + \frac{1}{2} J_{\mathbf{c}_2} \Sigma^{\mathbf{c}_2}_{\mathbf{c}_1} J^{\mathbf{c}_1}\right) \\ &= Z[0] \exp\left(\frac{1}{2} J_{\mathbf{c}_2} \Sigma^{\mathbf{c}_2}_{\mathbf{c}_1} J^{\mathbf{c}_1}\right). \end{aligned} \quad (2.29)$$

The derivatives in eq. (2.26) can now be easily applied to the partition function. The general expression for an arbitrary but even number n of fields is known as *Wick's theorem* [59]

$$\langle \Phi^{\mathbf{c}_n} \dots \Phi^{\mathbf{c}_1} \rangle = \sum_{\sigma \in P_n} \Sigma^{\mathbf{c}_{\sigma(n)}}_{\mathbf{c}_{\sigma(n-1)}} \dots \Sigma^{\mathbf{c}_{\sigma(2)}}_{\mathbf{c}_{\sigma(1)}}, \quad (2.30)$$

where the sum runs over the set of pairings P_n .

2.4.2. Wick's theorem for fermions

We consider a non-interacting fermionic theory of a pair of conjugated Grassmann fields Ψ and $\bar{\Psi}$ with an action that is bilinear in the fields. The dynamics are described by the operator D . Again, the fields Ψ and $\bar{\Psi}$ may have spatial and internal degrees of freedom denoted by the multi-indices \mathbf{a} and \mathbf{b} . The action is given by

$$S[\Psi, \bar{\Psi}] = \bar{\Psi}_{\mathbf{b}} D^{\mathbf{b}}_{\mathbf{a}} \Psi^{\mathbf{a}}. \quad (2.31)$$

We define the generating functional Z by [59]

$$Z[\bar{\eta}, \eta] = \int D\Psi D\bar{\Psi} \exp(-S[\Psi, \bar{\Psi}] + \bar{\eta}_{\mathbf{a}} \Psi^{\mathbf{a}} + \bar{\Psi}_{\mathbf{b}} \eta^{\mathbf{b}}), \quad (2.32)$$

where $\bar{\eta}$ and η are sources for the fields Ψ and $\bar{\Psi}$, respectively. $D\Psi D\bar{\Psi}$ denotes the combined path integral measure with respect to the defining representation of the fields Ψ and $\bar{\Psi}$

$$D\Psi D\bar{\Psi} = \prod_{\mathbf{a}} d\Psi^{\mathbf{a}} d\bar{\Psi}^{\mathbf{a}}, \quad (2.33)$$

2.4. Wick's theorem for path integrals

where the order is relevant due to the anti-commutating nature of Grassmann numbers. Expectation values can be related to the generating functional via [59]

$$\langle \bar{\Psi}_{\mathbf{b}_n} \Psi^{\mathbf{a}_n} \dots \bar{\Psi}_{\mathbf{b}_1} \Psi^{\mathbf{a}_1} \rangle = (-1)^n \frac{1}{Z[0,0]} \frac{\delta^{2n} Z[\bar{\eta}, \eta]}{\delta \bar{\eta}_{\mathbf{a}_n} \delta \eta^{\mathbf{b}_n} \dots \delta \bar{\eta}_{\mathbf{a}_1} \delta \eta^{\mathbf{b}_1}} \bigg|_{\eta=\bar{\eta}=0}. \quad (2.34)$$

We define a field transformation

$$\mathfrak{T}[(\Psi^{\mathbf{a}_2}, \bar{\Psi}_{\mathbf{b}_2})] = (\Psi^{\mathbf{a}_2} - S^{\mathbf{a}_2}_{\mathbf{b}_1} \eta^{\mathbf{b}_1}, \bar{\Psi}_{\mathbf{b}_2} - \bar{\eta}_{\mathbf{a}_1} S^{\mathbf{a}_1}_{\mathbf{b}_2}), \quad (2.35)$$

which shifts the field variables linearly and therefore fulfils $\text{sdet} \left(\frac{\delta \mathfrak{T}[(\Psi, \bar{\Psi})]}{\delta (\Psi, \bar{\Psi})} \right) = 1$. Completing the squares and making use of the field transformation in combination with eq. (2.10), the generating function can be rewritten as

$$\begin{aligned} Z[\bar{\eta}, \eta] &= \int D\Psi D\bar{\Psi} \exp(-(\bar{\Psi}_{\mathbf{b}_2} - \bar{\eta}_{\mathbf{a}_3} S^{\mathbf{a}_3}_{\mathbf{b}_2}) D^{\mathbf{b}_2}_{\mathbf{a}_2} (\Psi^{\mathbf{a}_2} - S^{\mathbf{a}_2}_{\mathbf{b}_1} \eta^{\mathbf{b}_1}) + \bar{\eta}_{\mathbf{a}} S^{\mathbf{a}}_{\mathbf{b}} \eta^{\mathbf{b}}) \\ &= \int D\Psi D\bar{\Psi} \exp(-\bar{\Psi}_{\mathbf{b}_2} D^{\mathbf{b}_2}_{\mathbf{a}_2} \Psi^{\mathbf{a}_2} + \bar{\eta}_{\mathbf{a}} S^{\mathbf{a}}_{\mathbf{b}} \eta^{\mathbf{b}}) \\ &= Z[0,0] \exp(\bar{\eta}_{\mathbf{a}} S^{\mathbf{a}}_{\mathbf{b}} \eta^{\mathbf{b}}). \end{aligned} \quad (2.36)$$

As in the bosonic case, the derivatives in eq. (2.34) can be applied to the latter representation of the partition function. The general expression for an arbitrary number n of pairs of conjugated fields is known as *Wick's theorem* [59]

$$\langle \bar{\Psi}_{\mathbf{b}_n} \Psi^{\mathbf{a}_n} \dots \bar{\Psi}_{\mathbf{b}_1} \Psi^{\mathbf{a}_1} \rangle = (-1)^n \sum_{\sigma \in S_n} \text{sgn}(\sigma) S^{\mathbf{a}_{\sigma(n)}}_{\mathbf{b}_n} \dots S^{\mathbf{a}_{\sigma(1)}}_{\mathbf{b}_1}, \quad (2.37)$$

where the sum runs over the set of permutations S_n .

3. Euclidean QCD+QED

In this chapter, we discuss properties of QCD+QED on Euclidean spacetime that are relevant for lattice Monte Carlo simulations, later covered in this thesis. We will briefly introduce the relevant gauge groups, specify the field content of the theory, give the full QCD+QED action and discuss the gauge invariance. We further discuss properties of β -functions for QCD+QED and their consequences for the existence of the continuum limit of a theory regulated by means of a spacetime lattice. We consider flavour symmetries and conserved charges and finally derive the vector and axial Ward identity for the theory. This chapter is partly inspired by the PhD theses [61–65].

3.1. Gauge groups

In this thesis, we consider two different gauge groups. The Abelian gauge group $U(1)$ of QED represents the electromagnetic interaction between electrically charged particles, mediated by the photon field, whereas the non-Abelian gauge group $SU(3)$ of QCD represents the strong interaction between colour charged particles, mediated by the gluon field.

3.1.1. $U(1)$ gauge group

The defining representation of the Abelian gauge group $U(1)$ is the set of complex numbers with unit norm, or equivalent the set of complex unitary numbers, which form a group under ordinary multiplication:

$$U(1) = \{\Omega \in \mathbb{C}^{1 \times 1} | \Omega^\dagger = \Omega^{-1}\}. \quad (3.1)$$

The associated Lie algebra $u(1)$ is given by the real numbers \mathbb{R} . Each element Ω of the compact Lie group $U(1)$ can be represented as an exponentiated element $\omega \in \mathbb{R}$

$$\Omega = \exp(i\omega). \quad (3.2)$$

3.1.2. $SU(3)$ gauge group

The defining representation of the non-Abelian gauge group $SU(3)$ is the set of complex unitary 3×3 matrices with unit determinant, which also form a group under matrix multiplication:

$$SU(3) = \{\Omega \in \mathbb{C}^{3 \times 3} | \Omega^\dagger = \Omega^{-1}, \det(\Omega) = 1\}. \quad (3.3)$$

3. Euclidean QCD+QED

The associated Lie algebra $su(3)$ is given by the set of complex, hermitian and traceless 3×3 matrices:

$$su(3) = \{T \in \mathbb{C}^{3 \times 3} | T^\dagger = T, \text{tr}(T) = 0\}. \quad (3.4)$$

As Lie algebras form vector spaces, one may choose a set of basis vectors, called generators T^a with $a \in \{1, \dots, 8\}$ in the case of $su(3)$. The generators T^a obey the defining commutation relation

$$[T^{a_1}, T^{a_2}] = if^{a_1 a_2 a_3} T^{a_3}, \quad (3.5)$$

where $f^{a_1 a_2 a_3}$ are the completely anti-symmetric structure constants of $SU(3)$, as well as the orthogonality condition

$$\text{tr}(T^{a_1} T^{a_2}) = \frac{1}{2} \delta^{a_1 a_2}. \quad (3.6)$$

Each element Ω of the compact Lie group $SU(3)$ can be represented as an exponentiated element $T = \omega^a T^a$ of the Lie algebra $su(3)$ with real numbers ω^a :

$$\Omega = \exp(i\omega^a T^a). \quad (3.7)$$

A standard choice of generators is $T^a = \frac{1}{2} \lambda^a$, where λ^a are the set of Gell-Mann matrices, defined as [20]

$$\begin{aligned} \lambda^1 &= \begin{pmatrix} 0 & 1 & 0 \\ 1 & 0 & 0 \\ 0 & 0 & 0 \end{pmatrix}, & \lambda^2 &= \begin{pmatrix} 0 & -i & 0 \\ i & 0 & 0 \\ 0 & 0 & 0 \end{pmatrix}, & \lambda^3 &= \begin{pmatrix} 1 & 0 & 0 \\ 0 & -1 & 0 \\ 0 & 0 & 0 \end{pmatrix}, \\ \lambda^4 &= \begin{pmatrix} 0 & 0 & 1 \\ 0 & 0 & 0 \\ 1 & 0 & 0 \end{pmatrix}, & \lambda^5 &= \begin{pmatrix} 0 & 0 & -i \\ 0 & 0 & 0 \\ i & 0 & 0 \end{pmatrix}, & \lambda^6 &= \begin{pmatrix} 0 & 0 & 0 \\ 0 & 0 & 1 \\ 0 & 1 & 0 \end{pmatrix}, \\ \lambda^7 &= \begin{pmatrix} 0 & 0 & 0 \\ 0 & 0 & -i \\ 0 & i & 0 \end{pmatrix}, & \lambda^8 &= \frac{1}{\sqrt{3}} \begin{pmatrix} 1 & 0 & 0 \\ 0 & 1 & 0 \\ 0 & 0 & -2 \end{pmatrix}. \end{aligned} \quad (3.8)$$

3.2. QCD+QED

The field content of QCD+QED, considered in this thesis, is given by the bosonic spin-1 $su(3)$ -valued gluon field A_g , the bosonic spin-1 \mathbb{R} -valued photon field A_e and the fermionic spin-1/2 quark fields Ψ and $\bar{\Psi}$, which combine quark fields of different flavours. As we focus on low-energy physics, we only consider the three lightest quark flavours u, d and s. We ignore all other electromagnetically charged particles, i.e. the heavy quarks, the charged leptons and the W^\pm bosons. The theory is characterised by the couplings g for the strong and e for the electromagnetic interaction. The matrix of fractional quark charges

$$Q = \text{diag}(q_u, q_d, q_s) \quad (3.9)$$

encodes the transformational behaviour of the quark fields under $U(1)$ gauge transformations. The mass matrix for the quark fields reads

$$M = \text{diag}(m_u, m_d, m_s). \quad (3.10)$$

Q and M are simultaneously diagonal. We conveniently group all relevant parameters in the quantity

$$\varepsilon = (m_u, m_d, m_s, g^2, e^2) \quad (3.11)$$

and understand the action as a function of this tuple of parameters.

3.2.1. QCD+QED Action

We decompose the action of Euclidean QCD+QED, called $S[\Psi, \bar{\Psi}, A_g, A_e]$, into three parts:

$$S[\Psi, \bar{\Psi}, A_g, A_e] = S_g[A_g] + S_e[A_e] + S_q[\bar{\Psi}, \Psi, A_g, A_e]. \quad (3.12)$$

$S_g[A_g]$ describes the gauge action of the strong interaction, $S_e[A_e]$ the gauge action of the electromagnetic interaction and $S_q[\bar{\Psi}, \Psi, A_g, A_e]$ the quark action, which includes the coupling to the strong and electromagnetic gauge fields. The Yang-Mills gauge action [2] for an $SU(3)$ gauge theory reads

$$S_g[A_g] = \frac{1}{2} \int d^4x \sum_{\mu_2, \mu_1} \text{tr}(F_g^{x\mu_2\mu_1} F_g^{x\mu_2\mu_1}) \quad (3.13)$$

with the field strength tensor

$$F_g^{x\mu_2\mu_1} = \vec{\partial}^{\mu_2} A_g^{\mu_1} - \vec{\partial}^{\mu_1} A_g^{\mu_2} - ig[A_g^{\mu_2}, A_g^{\mu_1}]. \quad (3.14)$$

The photon action is given by

$$S_e[A_e] = \frac{1}{4} \int d^4x F_e^{x\mu_2\mu_1} F_e^{x\mu_2\mu_1} \quad (3.15)$$

with the electromagnetic field strength tensor

$$F_e^{x\mu_2\mu_1} = \vec{\partial}^{\mu_2} A_e^{\mu_1} - \vec{\partial}^{\mu_1} A_e^{\mu_2}. \quad (3.16)$$

The quark action, describing the interaction of the quarks with the gauge fields, the kinetic term as well as the quark mass, reads

$$S_q[A_g, A_e, \bar{\Psi}, \Psi] = \int d^4x \left(\bar{\Psi} \left(\frac{1}{2} \gamma^\mu \left(\vec{D}^\mu - \overleftarrow{D}^\mu \right) + M \right) \Psi \right)^x, \quad (3.17)$$

where we use the right-acting and left-acting covariant derivatives

$$\vec{D}^\mu = \vec{\partial}^\mu + igA_g^\mu + ieQA_e^\mu, \quad (3.18)$$

$$\overleftarrow{D}^\mu = \overleftarrow{\partial}^\mu - igA_g^\mu - ieQA_e^\mu, \quad (3.19)$$

3. Euclidean QCD+QED

respectively. The covariant derivatives are related to the field strength tensors in eqs. (3.14) and (3.16) by

$$[\vec{D}^{\mu_2}, \vec{D}^{\mu_1}] = [\overleftarrow{D}^{\mu_2}, \overleftarrow{D}^{\mu_1}] = igF_g^{x\mu_2\mu_1} + ieQF_e^{x\mu_2\mu_1}. \quad (3.20)$$

We make use of a symmetric definition of the quark action with respect to the covariant derivatives such that Ψ and $\bar{\Psi}$ are treated in a similar way in algebraic calculations. The standard form, based on \vec{D}^μ only, is retrieved by partial integration. The definition of left-acting covariant derivatives becomes also relevant, when lattice gauge theories with a higher rate of convergence towards the continuum limit are systematically constructed. We will cover this topic later in chapter 4. We further utilise Euclidean Dirac matrices γ^μ in a chiral representation given in eq. (3.28), which will be discussed further in section 3.2.3.

3.2.2. Gauge symmetries

The QCD+QED action eq. (3.12) obeys a combined gauge symmetry $SU(3)_c \otimes U(1)$. We parametrise the QCD gauge transformations $\mathfrak{G}_{g,\Omega}$ by the $SU(3)$ matrix field Ω^x , belonging to the gauge group. The gauge transformations act on the fields according to

$$\mathfrak{G}_{g,\Omega}[(A_g^{\mu x}, A_e^{\mu x}, \Psi^x, \bar{\Psi}^x)] = \left(\Omega^x A_g^{\mu x} (\Omega^x)^\dagger + \frac{1}{g} i(\partial^\mu \Omega)^x (\Omega^x)^\dagger, A_e^{\mu x}, \Omega^x \Psi^x, \bar{\Psi}^x (\Omega^x)^\dagger \right). \quad (3.21)$$

In contrast, we parametrise the QED gauge transformations $\mathfrak{G}_{e,\alpha}$ by the scalar field α^x , belonging to the Lie algebra of the gauge group. This parametrisation is more convenient to account for the different electromagnetic charges of the quarks. The action of the gauge transformations on the fields reads

$$\mathfrak{G}_{e,\alpha}[(A_g^{x\mu}, A_e^{x\mu}, \Psi^x, \bar{\Psi}^x)] = (A_g^{x\mu}, A_e^{x\mu} - (\partial^\mu \alpha)^x, \exp(ieQ\alpha^x)\Psi^x, \bar{\Psi}^x \exp(-ieQ\alpha^x)). \quad (3.22)$$

To check the invariance of the action under both types of gauge transformations one investigates the transformational behaviour of the covariant derivatives from eqs. (3.18) and (3.19)

$$\mathfrak{G}_{g,\Omega}[\vec{D}^\mu] = \Omega \vec{D}^\mu \Omega^\dagger, \quad \mathfrak{G}_{e,\Omega}[\vec{D}^\mu] = \exp(ieQ\alpha) \vec{D}^\mu \exp(-ieQ\alpha), \quad (3.23)$$

$$\mathfrak{G}_{g,\Omega}[\overleftarrow{D}^\mu] = \Omega \overleftarrow{D}^\mu \Omega^\dagger, \quad \mathfrak{G}_{e,\Omega}[\overleftarrow{D}^\mu] = \exp(ieQ\alpha) \overleftarrow{D}^\mu \exp(-ieQ\alpha). \quad (3.24)$$

and of the field strength tensors from eqs. (3.14) and (3.16)

$$\mathfrak{G}_{g,\Omega}[F_g^{\mu_2\mu_1}] = \Omega F_g^{\mu_2\mu_1} \Omega^\dagger, \quad \mathfrak{G}_{e,\alpha}[F_g^{\mu_2\mu_1}] = F_g^{\mu_2\mu_1}, \quad (3.25)$$

$$\mathfrak{G}_{g,\Omega}[F_e^{\mu_2\mu_1}] = F_e^{\mu_2\mu_1}, \quad \mathfrak{G}_{e,\alpha}[F_e^{\mu_2\mu_1}] = F_e^{\mu_2\mu_1}. \quad (3.26)$$

3.2.3. Euclidean Dirac matrices

The Euclidean Dirac matrices are a set of 4×4 matrices γ^μ for $\mu = 0, 1, 2, 3$, which obey the anti-commutation relation

$$\{\gamma^{\mu_1}, \gamma^{\mu_2}\} = 2\delta^{\mu_1\mu_2} \mathbb{1}. \quad (3.27)$$

From this definition it is possible to construct a uniquely determined minimal group that encloses the Dirac matrices. In fact, the anti-commutation relation can be rewritten as multiplication laws for group elements. From these laws one can successively construct a finite matrix group with 32 elements. All linear representations of a finite group are equivalent through basis change to a unitary representation. In addition, one can show that all four-dimensional representations are equivalent to each other [71], i.e. there is only one four-dimensional representation up to basis change.

Chiral representation

A unitary representation commonly used is the chiral representation. This name does not uniquely define a set of Dirac matrices, but refers to a specific property. In this thesis, we use the convention from [72], which is also applied in the software package openQCD [73] utilised to numerically solve the Dirac equation for quarks. We define the Euclidean Dirac matrices in the chiral representation as [72]

$$\gamma^\mu = \begin{pmatrix} 0 & -i\sigma^\mu \\ (-i\sigma^\mu)^\dagger & 0 \end{pmatrix} \quad \mu = 0, 1, 2, 3 \quad (3.28)$$

with the anti-hermitian matrix σ^0 and the hermitian Pauli matrices σ^1, σ^2 and σ^3 reading

$$\sigma^0 = \begin{pmatrix} -i & 0 \\ 0 & -i \end{pmatrix}, \quad \sigma^1 = \begin{pmatrix} 0 & 1 \\ 1 & 0 \end{pmatrix}, \quad \sigma^2 = \begin{pmatrix} 0 & -i \\ i & 0 \end{pmatrix}, \quad \sigma^3 = \begin{pmatrix} 1 & 0 \\ 0 & -1 \end{pmatrix}. \quad (3.29)$$

As made obvious in the definition, all Dirac matrices are hermitian, unitary and self-inverse in this representation:

$$\gamma^\mu = (\gamma^\mu)^\dagger = (\gamma^\mu)^{-1} \quad \mu = 0, 1, 2, 3. \quad (3.30)$$

We further define a fifth Dirac matrix [72]

$$\gamma^5 = \gamma^0 \gamma^1 \gamma^2 \gamma^3 = \begin{pmatrix} \mathbb{1} & 0 \\ 0 & -\mathbb{1} \end{pmatrix}, \quad (3.31)$$

which is also hermitian, unitary and self-inverse in this particular representation,

$$\gamma^5 = (\gamma^5)^\dagger = (\gamma^5)^{-1}, \quad (3.32)$$

and fulfils the anti-commutation relation

$$\{\gamma^\mu, \gamma^5\} = 0 \quad \mu = 0, 1, 2, 3. \quad (3.33)$$

We also define the matrices

$$\sigma^{\mu_2 \mu_1} = \frac{i}{2} [\gamma^{\mu_2}, \gamma^{\mu_1}]. \quad (3.34)$$

The charge conjugation matrix in this representation reads [72]

$$C = i\gamma^0 \gamma^2. \quad (3.35)$$

It is also hermitian, self-inverse and unitary:

$$C = C^\dagger = C^{-1} = (C^\dagger)^{-1}. \quad (3.36)$$

3. Euclidean QCD+QED

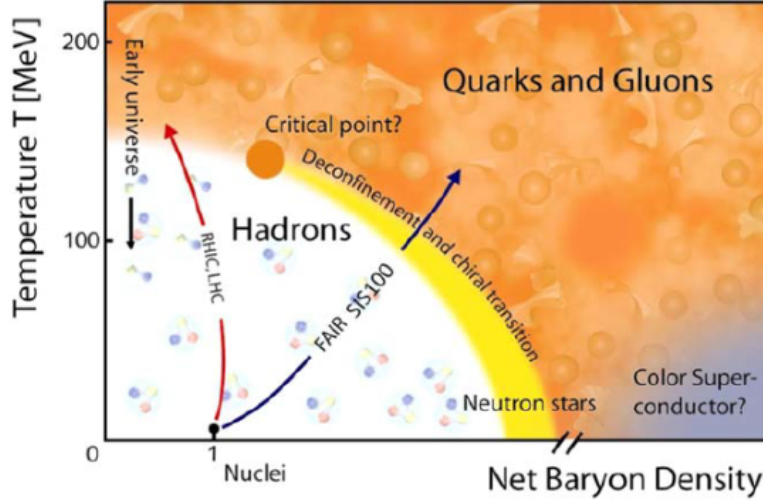


Figure 3.1.: Conjectured phase diagram of QCD. Figure extracted from [74].

3.2.4. Colour confinement and the QCD phase diagram

An important property of QCD, which should be mentioned for completeness, is colour confinement. Although quarks and gluons carry colour charge, only colour neutral states have been observed in experiments. In the hadronic phase, depicted in fig. 3.1, quarks and gluons form bound states. The situation changes, when the temperature and the baryon number density are increased. The deconfinement phase transition is crossed, and quarks and gluons exist as quasi-free particles in the quark-gluon plasma [75].

3.3. QCD+QED β -functions

β -functions encode the dependence of renormalised couplings on the renormalisation scale μ . Studying the β -functions of a theory is relevant to decide whether it is possible to remove the regularisation cutoff by sending it to infinity, i.e. whether a theory is asymptotically safe. A theory is called asymptotically safe if the corresponding renormalisation group possesses an ultra-violet fixed point. A special case of this scenario is the Gaussian fixed point, in which the coupling vanishes, when the cutoff is sent to infinity. This class of theories is called asymptotically free. *Gross* and *Wilczek* proved that QCD is asymptotically free [76]. For QED as a theory with an uncharged gauge boson, the situation is completely different.

3.3.1. QCD β -function

The β -function of QCD β_s is obtained from the scale derivative of the running coupling

$$\mu^2 \frac{\partial}{\partial \mu^2} \frac{\alpha_s(\mu^2)}{4\pi} = \beta_s\left(\frac{\alpha_s(\mu^2)}{4\pi}\right). \quad (3.37)$$

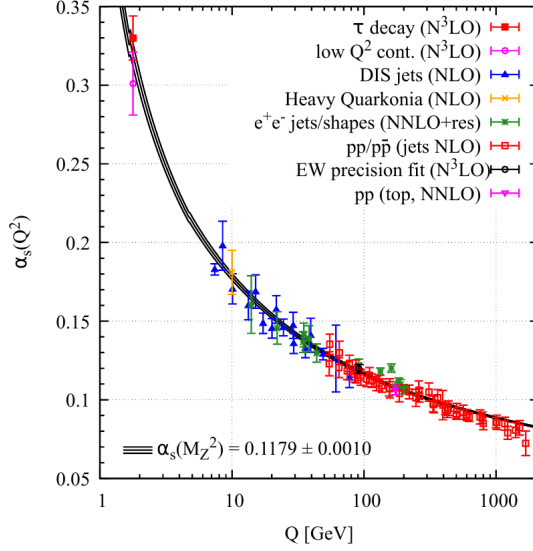


Figure 3.2.: Summary of measurements of α_s as a function of the energy scale Q . The respective degree of QCD perturbation theory used in the extraction of α_s is indicated in brackets. Figure extracted from [35].

In perturbation theory, it is expressed as a power series in the coupling, reading in the conventions of [77]

$$\beta_s\left(\frac{\alpha_s}{4\pi}\right) = \left(\frac{\alpha_s}{4\pi}\right)^2 \sum_{i=0}^{\infty} \beta_{s,i} \left(\frac{\alpha_s}{4\pi}\right)^i. \quad (3.38)$$

So far, the coefficients $\beta_{s,i}$ for $i = 0, \dots, 4$ have been determined [77]. We only give the first two coefficients $\beta_{s,0}$ [76] and $\beta_{s,1}$ [78] in the $\overline{\text{MS}}$ renormalisation scheme [79], depending on the number of Dirac fermion species n_f present in the theory. They read in the conventions of [77]

$$\beta_{s,0} = -11 + \frac{2}{3}n_f, \quad \beta_{s,1} = -102 + \frac{38}{3}n_f. \quad (3.39)$$

β_s is negative for all values of α_s , also when all known higher order contributions are included. As a consequence, α_s goes to zero for larger renormalisation scales μ^2 , i.e. QCD is asymptotically free [76]. In this high energy regime, perturbative calculations are self-consistent, as the running coupling is much smaller than 1. At the other hand, the coupling becomes large at small energy scales. A first-order solution of eq. (3.37), which relates $\alpha_s(\mu^2)$ to the value of the coupling $\alpha_s(\mu_0^2)$ at a scale μ_0^2 , is given in the conventions of [77] by [51]

$$\alpha_s(\mu^2) = \frac{\alpha_s(\mu_0^2)}{1 + \frac{\alpha_s(\mu_0^2)}{4\pi} \left(11 - \frac{2}{3}n_f\right) \log\left(\frac{\mu^2}{\mu_0^2}\right)}. \quad (3.40)$$

3. Euclidean QCD+QED

From the latter solution we deduce that the coupling diverges at the scale

$$\mu_{\text{Landau}}^2 = \mu_0^2 \exp \left(- \frac{1}{\frac{\alpha_s(\mu_0^2)}{4\pi} (11 - \frac{2}{3}n_f)} \right) \quad (3.41)$$

and is not defined for $\mu^2 < \mu_{\text{Landau}}^2$. The exact value depends on the order of the calculation and the applied renormalisation scheme. In non-perturbative calculations, e.g. lattice QCD, it is possible to determine α_s also at small energy scales [80]. Hence, the low-energy Landau-pole of QCD is a pure artefact of perturbation theory. In the latter, the power series expansion becomes inconsistent for couplings with size of $O(1)$ and larger. An overview over experimental determinations of the running strong coupling α_s is shown in fig. 3.2.

3.3.2. QED β -function

Similar to QCD, the QED β -function is implicitly defined by

$$\mu^2 \frac{\partial}{\partial \mu^2} \frac{\alpha_{\text{em}}(\mu^2)}{4\pi} = \beta_{\text{em}} \left(\frac{\alpha_{\text{em}}(\mu^2)}{4\pi} \right). \quad (3.42)$$

Again, we express the β -function as a power series reading:

$$\beta_{\text{em}} \left(\frac{\alpha_{\text{em}}}{4\pi} \right) = \left(\frac{\alpha_{\text{em}}}{4\pi} \right)^2 \sum_{i=0}^{\infty} \beta_{\text{em},i} \left(\frac{\alpha_{\text{em}}}{4\pi} \right)^i. \quad (3.43)$$

Currently, the coefficients $\beta_{\text{em},i}$ for $i = 0, \dots, 5$ are known [81]. Again, we only give the first two coefficients $\beta_{\text{em},0}$ and $\beta_{\text{em},1}$ in the $\overline{\text{MS}}$ renormalisation scheme [79], depending on the number n_f of Dirac fermion species with charges q_i for $i = 1, \dots, n_f$. They read in the conventions of [77]

$$\beta_{\text{em},0} = \frac{4}{3} \sum_{i=1}^{n_f} q_i^2, \quad \beta_{\text{em},1} = 4 \sum_{i=1}^{n_f} q_i^4. \quad (3.44)$$

β_{em} is positive for all values of α_{em} , also when all known higher order contributions are included. As a result, α_{em} grows arbitrarily for larger energy scales. A first-order solution of eq. (3.42), which relates $\alpha_{\text{em}}(\mu^2)$ to the value of the coupling $\alpha_{\text{em}}(\mu_0^2)$ at a scale μ_0^2 , is given by

$$\alpha_{\text{em}}(\mu^2) = \frac{\alpha_{\text{em}}(\mu_0^2)}{1 - \frac{\alpha_{\text{em}}(\mu_0^2)}{4\pi} \frac{4}{3} \sum_{i=1}^{n_f} q_i^2 \log \left(\frac{\mu^2}{\mu_0^2} \right)}. \quad (3.45)$$

From the latter solution, we deduce that the coupling diverges at the scale

$$\mu_{\text{Landau}}^2 = \mu_0^2 \exp \left(\frac{1}{\frac{\alpha_{\text{em}}(\mu_0^2)}{4\pi} \frac{4}{3} \sum_{i=1}^{n_f} q_i^2} \right) \quad (3.46)$$

and is not defined for $\mu^2 > \mu_{\text{Landau}}^2$. However, non-perturbative studies of QED, based on the lattice regularisation, indicate that the Landau pole in QED is not a perturbative artefact [82–84]. The setup was based on non-compact lattice QED, which we will discuss in chapter 4, with staggered fermions. The simulations showed that by altering the bare dimensionless mass am , where a denotes the lattice spacing, it is not possible to generate an arbitrarily small value of the renormalised dimensionless mass am_R . Hence, it is also not possible to perform calculations at arbitrarily small a . The theory provides itself a minimal cutoff by chiral symmetry breaking [82–84].

3.3.3. QCD+QED β -functions

Having discussed QCD and QED as separate theories, we now investigate QCD+QED as a combined theory. In this case, the running of the strong and the electromagnetic coupling is described by the system of ordinary differential equations with respect to the renormalisation scale μ in the conventions of [77]:

$$\mu^2 \frac{\partial}{\partial \mu^2} \left(\frac{\alpha_s(\mu^2)}{4\pi} \right) = \beta_s \left(\frac{\alpha_s(\mu^2)}{4\pi}, \frac{\alpha_{\text{em}}(\mu^2)}{4\pi} \right), \quad (3.47)$$

$$\mu^2 \frac{\partial}{\partial \mu^2} \left(\frac{\alpha_{\text{em}}(\mu^2)}{4\pi} \right) = \beta_{\text{em}} \left(\frac{\alpha_s(\mu^2)}{4\pi}, \frac{\alpha_{\text{em}}(\mu^2)}{4\pi} \right). \quad (3.48)$$

A combined power series expansion of β_s and β_{em} in terms of the couplings α_s and α_{em} reads

$$\beta_s \left(\frac{\alpha_s}{4\pi}, \frac{\alpha_{\text{em}}}{4\pi} \right) = \left(\frac{\alpha_s}{4\pi} \right)^2 \sum_{i,j=0}^{\infty} \beta_{s,ij} \left(\frac{\alpha_s}{4\pi} \right)^i \left(\frac{\alpha_{\text{em}}}{4\pi} \right)^j, \quad (3.49)$$

$$\beta_{\text{em}} \left(\frac{\alpha_s}{4\pi}, \frac{\alpha_{\text{em}}}{4\pi} \right) = \left(\frac{\alpha_{\text{em}}}{4\pi} \right)^2 \sum_{i,j=0}^{\infty} \beta_{\text{em},ij} \left(\frac{\alpha_s}{4\pi} \right)^i \left(\frac{\alpha_{\text{em}}}{4\pi} \right)^j. \quad (3.50)$$

The coefficients $\beta_{s,i0}$ describe the strong contributions to the running of α_s , whereas $\beta_{\text{em},0i}$ describe the electromagnetic contributions to the running of α_{em} . The coefficients $\beta_{s,ij}$ for $j \neq 0$ and $\beta_{\text{em},ij}$ for $i \neq 0$ describe the reciprocal influence of the interactions. The leading coefficients were determined in [85, 86] in the $\overline{\text{MS}}$ -scheme [79]. In the conventions of [77], the coefficients for β_s are given by

$$\beta_{s,00} = -11 + \frac{2}{3}n_q, \quad \beta_{s,10} = -102 + \frac{38}{3}n_f, \quad \beta_{s,01} = 2 \sum_{i=1}^{n_q} q_{q,i}^2 \quad (3.51)$$

and for β_{em} they read

$$\begin{aligned} \beta_{\text{em},00} &= \frac{4}{3} \left(3 \sum_{i=1}^{n_q} q_{q,i}^2 + \sum_{i=1}^{n_l} q_{l,i}^2 \right), & \beta_{\text{em},01} &= 4 \left(3 \sum_{i=1}^{n_q} q_{q,i}^4 + \sum_{i=1}^{n_l} q_{l,i}^4 \right), \\ \beta_{\text{em},10} &= 64 \sum_{i=1}^{n_q} q_{q,i}^2. \end{aligned} \quad (3.52)$$

3. Euclidean QCD+QED

n_q denotes the number of quark flavours and n_l the number of charged lepton species. The fractional charges are labelled with $q_{q,i}$ and $q_{l,i}$, respectively. For $n_q = 6$ and $n_l = 3$, we find the β -functions

$$\beta_s\left(\frac{\alpha_s}{4\pi}, \frac{\alpha_{em}}{4\pi}\right) = -7\left(\frac{\alpha_s}{4\pi}\right)^2 - 26\left(\frac{\alpha_s}{4\pi}\right)^3 + \frac{10}{3}\left(\frac{\alpha_s}{4\pi}\right)^2\left(\frac{\alpha_{em}}{4\pi}\right) + O((\alpha_s, \alpha_{em})^4), \quad (3.53)$$

$$\beta_{em}\left(\frac{\alpha_s}{4\pi}, \frac{\alpha_{em}}{4\pi}\right) = \frac{32}{3}\left(\frac{\alpha_{em}}{4\pi}\right)^2 + \frac{176}{9}\left(\frac{\alpha_{em}}{4\pi}\right)^3 + \frac{320}{3}\left(\frac{\alpha_s}{4\pi}\right)\left(\frac{\alpha_{em}}{4\pi}\right)^2 + O((\alpha_s, \alpha_{em})^4). \quad (3.54)$$

As all coefficients of β_{em} are positive, we find a positive β_{em} for all values of α_s and α_{em} . Hence, α_{em} also possesses a high-energy Landau pole similar to pure QED. As the two interactions are coupled, α_s diverges at the same energy scale. The strong interaction induces an even stronger growth of α_{em} , such that the Landau pole is shifted to smaller energy scales. For small energies, β_s is negative due to the weakness of the electromagnetic interaction. Consequently, α_s increases for smaller energies, such that the perturbative expansion breaks down. As a consequence of the high-energy Landau pole, QCD+QED is a trivial theory, i.e. all renormalised and bare couplings have to be set to zero in order to have a well-defined theory. In this case, only a non-interacting theory of free quarks and leptons remains. Nevertheless, it is possible to interpret QCD+QED as an effective theory, which is valid for energy scales much smaller than the high-energy Landau pole.

In this thesis, we will truncate the perturbative expansion in α_{em} at first-order, i.e. at tree-level such that the system of β -functions simplifies to

$$\beta_s\left(\frac{\alpha_s}{4\pi}, \frac{\alpha_{em}}{4\pi}\right) = \left(\frac{\alpha_s}{4\pi}\right)^2 \left(-7 - 26\left(\frac{\alpha_s}{4\pi}\right) + \frac{10}{3}\left(\frac{\alpha_{em}}{4\pi}\right)\right) + O((\alpha_s, \alpha_{em})^4), \quad (3.55)$$

$$\beta_{em}\left(\frac{\alpha_s}{4\pi}, \frac{\alpha_{em}}{4\pi}\right) = 0. \quad (3.56)$$

At this order, no Landau pole associated to α_{em} is formed. In addition, the electromagnetic correction of β_s is independent of the value of α_s too small to spoil its negativity assuming a value of $\alpha_{em} = \frac{1}{137.035\dots}$. Consequently, in this setup the cutoff μ^2 can be sent to infinity and therefore completely removed. In terms of the lattice regularisation, for which one could perform a similar calculation, this means that the continuum limit of combined QCD and tree-level QED exists. The arguments of this section also apply when only the three light quarks are considered, as the qualitative behaviour of the β -functions does not change.

3.4. Flavour symmetries and conserved charges

In order to obtain a deeper insight into QCD+QED, we discuss symmetries of the theory depending on particular choices of the parameters of the action in eq. (3.11). We remind, that a sufficient condition for a quantum symmetry is the invariance of the regulated action and of the regulated path integral measure, c.f. eq. (2.13). We investigate the vector and the axial transformation. We consider a group of vector transformations G_V , which is defined as a product of the groups $U(n)$ and $SU(n)$. The vector transformations act on

the fields according to

$$\begin{aligned} \mathfrak{T}_{G_V}(\alpha)[(\Psi^x, \bar{\Psi}^x, A_s^x, A_e^x)] = & \left(\exp \left(i \sum_i T_{G_V}^i \alpha^i \right) \Psi^x, \right. \\ & \left. \bar{\Psi}^x \exp \left(-i \sum_i T_{G_V}^i \alpha^i \right), A_s^x, A_e^x \right), \end{aligned} \quad (3.57)$$

where $T_{G_V}^i$ are the generators of the particular symmetry group, spanning its Lie algebra, and α^i are real parameters, parametrising the transformation group. The generators $T_{G_V}^i$ only act on the flavour indices of the quark fields. To evaluate the transformational behaviour of the path integral measure, one in principle has to regulate the theory first, e.g. with a covariant regularisation based on a heat-kernel as discussed by *Fujikawa* in [57, 87, 88]. We omit this step, as it is known that the vector transformations are non-anomalous. It can be shown that the action of QCD+QED is invariant under the group G_V , if

$$[M, T_{G_V}^i] = 0, \quad e[Q, T_{G_V}^i] = 0 \quad (3.58)$$

for all generators $T_{G_V}^i$. Similarly, we consider a group of axial transformations G_A , which act on the fields as

$$\begin{aligned} \mathfrak{T}_{G_A}(\alpha)[(\Psi^x, \bar{\Psi}^x, A_s^x, A_e^x)] = & \left(\exp \left(i \gamma^5 \sum_i T_{G_A}^i \alpha^i \right) \Psi^x, \right. \\ & \left. \bar{\Psi}^x \exp \left(i \gamma^5 \sum_i T_{G_A}^i \alpha^i \right), A_s^x, A_e^x \right). \end{aligned} \quad (3.59)$$

An additional γ^5 matrix was introduced compared to eq. (3.83). Consequently, the field transformation does not only mix quark field components in flavour space but also in spin space. To determine the transformational behaviour of the path integral measure we follow the steps of *Fujikawa* in [57, 87, 88] and modify the calculation such that it is valid for QCD+QED. As the latter is lengthy, we only give the result. The axial transformation is non-anomalous if all generators of the group are traceless

$$\text{tr}(T_{G_A}^i) = 0. \quad (3.60)$$

The action of QCD+QED is invariant under G_A if

$$\{M, T_{G_A}^i\} = 0, \quad e\{Q, T_{G_A}^i\} = 0 \quad (3.61)$$

for all generators $T_{G_A}^i$.

We will label the generators and the corresponding transformations with an index, which tells the flavours manipulated by the generator. In addition, we denote a generator with the index 1 if it belongs to the singlet representation, i.e. the generator T is proportional to unity, and with an index 8 if the transformation belongs to the octet representation, i.e. the generator T is traceless.

3. Euclidean QCD+QED

3.4.1. QCD+QED

For the most general choice of action parameters

$$\varepsilon = (m_u, m_d, m_s, g^2, e^2), \quad (3.11)$$

the theory is invariant under the combined symmetry group

$$U(1)_{V,u} \otimes U(1)_{V,d} \otimes U(1)_{V,s}. \quad (3.62)$$

The generators for the vector transformations $\mathfrak{T}_{U(1)_{V,f}}$ with quark flavours $f = u, d, s$ read

$$T_{U(1)_{V,u}} = \begin{pmatrix} 1 & 0 & 0 \\ 0 & 0 & 0 \\ 0 & 0 & 0 \end{pmatrix}, \quad T_{U(1)_{V,d}} = \begin{pmatrix} 0 & 0 & 0 \\ 0 & -1 & 0 \\ 0 & 0 & 0 \end{pmatrix}, \quad T_{U(1)_{V,s}} = \begin{pmatrix} 0 & 0 & 0 \\ 0 & 0 & 0 \\ 0 & 0 & -1 \end{pmatrix}. \quad (3.63)$$

The related conserved charges are upness U , downness D and strangeness S , describing the flavour-wise quark number conservation. The minus signs in the definition of the generators appear due to different conventions for up- and down-like quark flavours with respect to the sign of the quark numbers. Consequently, the total quark number $N = U - D - S$, the baryon number $B = \frac{1}{3}(U - D - S)$ and the electric charge $Q = \frac{2}{3}U + \frac{1}{3}D + \frac{1}{3}S$ are also conserved. For parameter choices with larger symmetry groups, the latter transformations are always present as a subgroup.

3.4.2. Isosymmetric QCD

Isosymmetric QCD, which we denote QCD_{iso} in this work, is characterised by the parameter tuple eq. (3.11)

$$\varepsilon = (m_{ud}, m_{ud}, m_s, g^2, 0), \quad (3.64)$$

i.e. the up and down quark masses are degenerate $m_{ud} = m_u = m_d$ and the electromagnetic coupling vanishes, such that the photon field decouples from the theory. Due to the absence of the electromagnetic interaction not only the bare but also the renormalised up and down quark masses are equal. In this limit, the theory is invariant under the combined symmetry group

$$U(1)_{V,ud} \otimes SU(2)_{V,ud8} \otimes U(1)_{V,s}. \quad (3.65)$$

The generator of $\mathfrak{T}_{U(1)_{V,ud}}$ reads

$$T_{U(1)_{V,ud}} = \frac{1}{2} \begin{pmatrix} 1 & 0 & 0 \\ 0 & 1 & 0 \\ 0 & 0 & 0 \end{pmatrix} \quad (3.66)$$

and the related conserved charge is $U - D$. The generators for the isospin transformations $SU(2)_{V,ud8}$ are given by

$$T_{SU(2)_{V,ud8}}^i = \frac{1}{2} \lambda^i \quad i = 1, 2, 3 \quad (3.67)$$

3.4. Flavour symmetries and conserved charges

with conserved charges I and $I_3 = U + D$. Although isospin symmetry is not realised in nature it is an approximate symmetry commonly assumed in lattice QCD simulations. In the isosymmetric limit all members of hadronic isospin multiplets possess the same mass such as the triplet of π^\pm and π^0 , the doublet p and n as well as the doublet K^+ and K^0 as well as K^- and \bar{K}^0 .

3.4.3. Chiral QCD

Restricting the set of parameters even further, one investigates chiral QCD, which is characterised by vanishing bare quark masses with the parameter tuple eq. (3.11)

$$\varepsilon = (0, 0, 0, g^2, 0). \quad (3.68)$$

In fact, not only the bare quark masses but also the renormalised quark masses vanish. This parameter set maximises the symmetry group to

$$U(1)_{V,1} \otimes SU(3)_{V,\text{uds}8} \otimes SU(3)_{A,\text{uds}8}, \quad (3.69)$$

with the vector generators

$$T_{U(1)_{V,1}} = \frac{1}{\sqrt{6}}\mathbb{1}, \quad T_{SU(3)_{V/A,\text{uds}8}}^i = \frac{1}{2}\lambda^i \quad i = 1, \dots, 8. \quad (3.70)$$

The appearance of the axial symmetry group $SU(3)_{A,\text{uds}8}$ is directly related to the vanishing quark masses. Although the axial singlet transformation $U(1)_{V,1}$ with generator

$$T_{U(1)_{A,1}} = \frac{1}{\sqrt{6}}\mathbb{1} \quad (3.71)$$

is a symmetry of the action, it is not a symmetry of the path integral measure and therefore a quantum anomaly.

Chiral symmetry and its spontaneous breaking in QCD is an important concept to understand the lightness of π^\pm , π^0 , K^\pm and η , which form the pseudo-scalar meson octet, compared to other hadronic states. Although the chiral symmetry is a quantum symmetry of the theory considered, it can be shown that the ground state of the Hamiltonian at vanishing temperature is not invariant under chiral transformations by investigating the chiral condensate [42, 89]

$$\langle \bar{\Psi}^x T_A^i \Psi^x \rangle \quad (3.72)$$

as an order parameter of the chiral phase transition. In this situation, the Goldstone theorem [90, 91] predicts a number of pseudo-scalar massless states appearing in the QCD spectrum, the so-called Goldstone bosons, equal to the number of generators of the broken symmetry. In the three flavour theory we have eight generators corresponding to the eight pseudo-scalar octet mesons. Hence, the chiral point can be characterised by vanishing quark masses or by vanishing masses of pseudo-scalar octet mesons. In fact, chiral QCD is not realised in nature. The light quarks possess a mass compared to hadronic scales.

3. Euclidean QCD+QED

This leads to an explicit breaking of chiral symmetry. The Goldstone bosons, now called pseudo-Goldstone bosons, consequently also become massive but their masses are still noticeably smaller compared to other hadronic state.

Chiral symmetry breaking is fundamental for the construction of chiral perturbation theory [92], which is an effective field theory for the description of the interaction of hadronic states. In addition, the notion of chiral symmetry is of particular relevance for the construction of lattice discretised quark actions as we will see later and it is common to impose renormalisation conditions for composite operators in lattice QCD simulations in the chiral limit.

3.4.4. Chiral QCD with massive strange quark

In lattice QCD simulations, it is not always possible to choose the masses of the light and strange quarks independently [45]. It is therefore not possible to obtain massless light and strange quarks simultaneously. Hence, the chiral point is defined via vanishing up and down quark masses in the presence of a massive strange quark with the parameter tuple eq. (3.11)

$$\varepsilon = (0, 0, m_s, g^2, 0). \quad (3.73)$$

The mass of the strange quark has to be fixed by an additional condition. The symmetry group is reduced compared to chiral QCD and enlarged compared to massive isosymmetric QCD:

$$U(1)_{V,ud} \otimes SU(2)_{V,ud8} \otimes U(1)_{V,s} \otimes SU(2)_{A,ud8}. \quad (3.74)$$

Again, assuming chiral symmetry breaking, the Goldstone theorem [90, 91] predicts three massless pseudo-scalar mesons linked to the three generators of the broken $SU(2)_{A,ud8}$ symmetry, the π^+ , π^0 and π^- . Consequently, the chiral point in the presence of a massive strange quark can be characterised by vanishing masses of the pion triplet.

3.4.5. Chiral QCD+QED

Introducing the QED interaction with eq. (3.11)

$$\varepsilon = (0, 0, 0, g^2, e^2) \quad (3.75)$$

reduces the symmetry group compared to chiral QCD due to the individual electromagnetic charges of the quarks. The remaining symmetry group is given by

$$U(1)_{V,u} \otimes U(1)_{V,ds} \otimes SU(2)_{V,ds} \otimes U(1)_{A,uds8} \otimes SU(2)_{A,ds8}, \quad (3.76)$$

with generators

$$T_{U(1)_{V,ds}} = \frac{1}{2} \begin{pmatrix} 0 & 0 & 0 \\ 0 & 1 & 0 \\ 0 & 0 & 1 \end{pmatrix}, \quad T_{U(1)_{A,ds}} = \frac{1}{2} \begin{pmatrix} -2 & 0 & 0 \\ 0 & 1 & 0 \\ 0 & 0 & 1 \end{pmatrix} \quad (3.77)$$

3.5. Ward-Takahashi identities in Euclidean QCD+QED

and

$$T_{SU(2)_{V/A,ds}}^1 = \frac{1}{2}\lambda^6, \quad T_{SU(2)_{V/A,ds}}^2 = \frac{1}{2}\lambda^7, \quad T_{SU(2)_{V/A,ds}}^3 = \frac{1}{2} \begin{pmatrix} 0 & 0 & 0 \\ 0 & 1 & 0 \\ 0 & 0 & -1 \end{pmatrix}. \quad (3.78)$$

Assuming that $U(1)_{A,uds} \otimes SU(2)_{A,ds}$ is spontaneously broken, the Goldstone theorem [90, 91] predicts four massless pseudo-scalar mesons K^0 , \bar{K}^0 , π^0 and η . The $SU(2)_{V,ds}$ symmetry predicts $m_{\pi^+} = m_{K^+}$ and $m_{\pi^-} = m_{K^-}$. Together with charge conjugation symmetry we see that only four particles of the pseudo-scalar meson octet are massive and they all possess the same mass. These findings are known as Dashen's theorem [93]. Nowadays, this theorem is proved by means of the chiral effective theory [94]. Corrections to Dashen's theorem due to explicit breaking of the chiral symmetry by massive quarks are parametrised by the parameter ε [39]

$$\varepsilon = \frac{(m_{K^+}^2 - m_{K^0}^2)^{\text{QED}} - (m_{\pi^+}^2 - m_{\pi^0}^2)^{\text{QED}}}{m_{\pi^+}^2 - m_{\pi^0}^2}, \quad (3.79)$$

where the superscript QED denotes corrections caused by the electromagnetic interaction only. Predictions of the breaking parameter ε are available based on the chiral effective theory [94] as well as lattice QCD+QED [46, 48, 95].

3.4.6. Chiral QCD+QED with massive strange quark

We again consider the situation of the last section in the presence of a massive strange quark with parameters eq. (3.11)

$$\varepsilon = (0, 0, m_s, g^2, e^2). \quad (3.80)$$

Compared to chiral QCD+QED the symmetry group is broken to

$$U(1)_{V,u} \otimes U(1)_{V,d} \otimes U(1)_{V,s} \otimes U(1)_{A,uds}. \quad (3.81)$$

A spontaneous breaking of the remaining chiral symmetry $U(1)_{A,uds}$ with generator

$$T_{U(1)_{A,uds}} = \frac{1}{2}\lambda^3 \quad (3.82)$$

results in a vanishing π^0 mass via the Goldstone theorem [90, 91].

3.5. Ward-Takahashi identities in Euclidean QCD+QED

Ward-Takahashi identities are commonly discussed in the literature for multi-flavour QCD and single-flavour QED separately. As we consider combined QCD and QED, we discuss the two Ward-Takahashi identities most relevant for this work, namely the *vector Ward identity* and the *axial Ward identity*, also known as the *chiral Ward identity*. Continuum Ward-Takahashi identities play an important role for the improvement of the convergences to the continuum limit of a lattice field theory. We will discuss the concept of improvement later in section 4.1.2 when we have introduced the lattice regularisation.

3. Euclidean QCD+QED

3.5.1. Vector Ward identity

The vector Ward identity is derived from the set of field transformations of the form

$$\mathfrak{T}[\alpha^x][(\Psi^x, \bar{\Psi}^x, A_s^x, A_e^x)] = (\exp(iT\alpha^x)\Psi^x, \bar{\Psi}^x \exp(-iT\alpha^x), A_s^x, A_e^x), \quad (3.83)$$

where T is a Hermitian matrix acting only on flavour indices of the quark fields and α is a scalar field, such that the $U(n_f)$ phases $\exp(iT\alpha^x)$ and $\exp(-iT\alpha^x)$ become space dependent. Naively, the path integral measure is invariant under the transformations considered, as

$$\text{sdet} \left(\frac{\delta \mathfrak{T}[\alpha][\Upsilon]}{\delta \Upsilon} \right) = \text{sdet} \left(\begin{pmatrix} \exp(iT\alpha) & & & \\ & \exp(-iT\alpha) & & \\ & & 1 & \\ & & & 1 \end{pmatrix} \right) = 1, \quad (3.84)$$

From the discussion in section 3.4 we know, that the vector transformations are non-anomalous, i.e. the invariance of path integral measure also holds in an appropriately regularised theory. Accordingly, there is no contribution from the Jacobian to the Ward identity:

$$\frac{\delta}{\delta \alpha^x} \text{sdet} \left(\frac{\delta \mathfrak{T}[\alpha][\Upsilon]}{\delta \Upsilon} \right) \Big|_{\alpha=0} = 0. \quad (3.85)$$

The derivative of the transformed action with respect to α^x reads

$$\begin{aligned} \frac{\delta S[\mathfrak{T}[\alpha][\Upsilon]]}{\delta \alpha^x} \Big|_{\alpha=0} &= -i \left((\partial^\mu (\bar{\Psi} \gamma^\mu T \Psi))^x + \left(\bar{\Psi} \left[T, \frac{1}{2} \gamma^\mu (\vec{D}^\mu - \overleftarrow{D}^\mu) + M \right] \Psi \right)^x \right) \\ &= -i \left((\partial^\mu (\bar{\Psi} \gamma^\mu T \Psi))^x - \bar{\Psi}^x [M, T] \Psi^x - ie A_e^{x\mu} \bar{\Psi}^x \gamma^\mu [Q, T] \Psi^x \right). \end{aligned} \quad (3.86)$$

Combining the last two equations with eq. (2.22) we obtain the vector Ward identity:

$$\begin{aligned} \left\langle (\partial^\mu (\bar{\Psi} \gamma^\mu T \Psi))^x \mathcal{O}[\Upsilon] \right\rangle &= \left\langle (\bar{\Psi}^x [M, T] \Psi^x + ie A_e^{x\mu} \bar{\Psi}^x \gamma^\mu [Q, T] \Psi^x) \mathcal{O}[\Upsilon] \right. \\ &\quad \left. + i \frac{\delta \mathcal{O}[\mathfrak{T}[\alpha][\Upsilon]]}{\delta \alpha^x} \Big|_{\alpha=0} \right\rangle. \end{aligned} \quad (3.87)$$

Associated to the partially conserved current $(\bar{\Psi} \gamma^\mu T \Psi)^x$, one defines a partially conserved charge

$$\mathcal{Q}_T^{x0} = \int d^3x (\bar{\Psi} \gamma^\mu T \Psi)^x. \quad (3.88)$$

For vanishing electromagnetic quark charges $Q = 0$, we reobtain the standard QCD vector Ward identity [42]. For flavour-diagonal T , in particular for $T = Q$, we find that the expectation values of flavour-neutral vector currents are also conserved up to contact terms in combined QCD and QED as all commutators vanish:

$$\left\langle (\partial^\mu (\bar{\Psi} \gamma^\mu T \Psi))^x \mathcal{O}[\Upsilon] \right\rangle = \left\langle i \frac{\delta \mathcal{O}[\mathfrak{T}[\alpha][\Upsilon]]}{\delta \alpha^x} \Big|_{\alpha=0} \right\rangle. \quad (3.89)$$

This is a conceptually important result, especially for the electromagnetic current. The vector Ward identity in pure QCD ensures that the renormalisation of the electromagnetic coupling only depends on the field strength renormalisation of the photon field, i.e. on the vacuum polarisation. Contributions from the vertex and mass renormalisation cancel to all orders, which can be shown using the vector Ward identity and its renormalised analogue. The latter argument can also be applied in the situation of the combined QCD and QED as the electromagnetic vector current fulfils the same Ward identity. The renormalisation of the electromagnetic coupling comes only from the vacuum polarisation. In a tree-level QED calculation, the vacuum polarisation is absent and hence, the electromagnetic coupling does not renormalise even in the presence of full QCD. In fact, not only the electromagnetic current is conserved but also any flavour-neutral vector current, for which T is a diagonal matrix.

3.5.2. Axial Ward identity

The axial Ward identity is derived from the set of field transformations of the form

$$\mathfrak{T}[\alpha][(\Psi^x, \bar{\Psi}^x, A_s^x, A_e^x)] = (\exp(iT\gamma^5\alpha^x)\Psi^x, \bar{\Psi}^x \exp(iT\gamma^5\alpha^x), A_s, A_e), \quad (3.90)$$

where T is a Hermitian matrix acting on flavour indices and α is a scalar field, such that we again have local $U(n_f)$ transformations. An additional γ^5 matrix was introduced compared to eq. (3.83). We do not demand that T is traceless. To determine the Jacobian of the axial transformation, we follow the steps of *Fujikawa* in [57, 87, 88] and modify the calculation for QCD+QED. As this calculation is very lengthy, we only give the result. The contribution from the Jacobian to the Ward identity is given by

$$\begin{aligned} \frac{\delta}{\delta\alpha^x} \det \left(\frac{\delta\mathfrak{T}[\alpha][\Upsilon]}{\delta\Upsilon} \right) \Big|_{\alpha=0} = & i \frac{1}{16} \varepsilon^{\mu_4\mu_3\mu_2\mu_1} (g^2 \text{tr}(T) \text{tr}(F_s^{\mu_4\mu_3} F_s^{\mu_2\mu_1}) \\ & + 3e^2 \text{tr}(TQ^2) F_e^{\mu_4\mu_3} F_e^{\mu_2\mu_1}). \end{aligned} \quad (3.91)$$

The derivative of the transformed action with respect to α^x reads

$$\begin{aligned} \frac{\delta S[\mathfrak{T}[\alpha][\Upsilon]]}{\delta\alpha^x} \Big|_{\alpha=0} = & -i \left((\partial^\mu (\bar{\Psi} \gamma^\mu \gamma^5 T \Psi))^x + \left(\bar{\Psi} \left\{ \gamma^5 T, \frac{1}{2} \gamma^\mu (\vec{D}^\mu - \overleftarrow{D}^\mu) + M \right\} \Psi \right)^x \right) \\ = & -i \left((\partial^\mu (\bar{\Psi} \gamma^\mu \gamma^5 T \Psi))^x - \bar{\Psi}^x \gamma^5 \{M, T\} \Psi^x \right. \\ & \left. - ie A_e^{x\mu} \bar{\Psi}^x \gamma^\mu \gamma^5 [Q, T] \Psi^x \right). \end{aligned} \quad (3.92)$$

Combining the last two equations with eq. (2.22) we obtain the axial-vector Ward identity, which is also known as the partially conserved axial vector (PCAC) relation:

$$\begin{aligned} \left\langle (\partial^\mu (\bar{\Psi} \gamma^\mu \gamma^5 T \Psi))^x O[\Upsilon] \right\rangle = & \left\langle (\bar{\Psi}^x \{M, T\} \gamma^5 \Psi^x + ie A_e^{x\mu} \bar{\Psi}^x \gamma^\mu \gamma^5 [Q, T] \Psi^x \right. \\ & + \frac{1}{16} \varepsilon^{\mu_4\mu_3\mu_2\mu_1} (g^2 \text{tr}(T) \text{tr}(F_s^{\mu_4\mu_3} F_s^{\mu_2\mu_1}) \\ & \left. + 3e^2 \text{tr}(TQ^2) F_e^{\mu_4\mu_3} F_e^{\mu_2\mu_1})) O[\Upsilon] \right. \\ & \left. + i \frac{\delta O[\mathfrak{T}[\alpha][\Upsilon]]}{\delta\alpha^x} \Big|_{\alpha=0} \right\rangle. \end{aligned} \quad (3.93)$$

3. Euclidean QCD+QED

For vanishing electromagnetic quark charges $Q = 0$, we reobtain the standard QCD axial Ward identity [42]. The PCAC relation takes an important role for the definition of quark masses, which renormalise multiplicatively in lattice calculations [42]. Measuring both sides of the PCAC relation gives access to the quark mass matrix. Probing the PCAC relation for different T , linear combinations of entries of M can be extracted.

Part II.

Lattice QCD+QED

4. Lattice field theories

In this chapter, we summarise the formulation of field theories on spacetime lattices. We discuss the lattice regularisation of continuum field theories, introduce the notion of gauge symmetries on the lattice and present gauge and fermion actions with a focus on the Wilson fermion discretisation in the context of lattice QCD. We further discuss subtleties of non-compact lattice QED related to the manifest infrared divergence. We describe Monte Carlo simulations as a stochastic tool to compute the path integral. We finally comment on systematic errors of lattice Monte Carlo simulations. In this chapter, we follow the standard text books of *Montvay* and *Münster* [96], *Gattringer* and *Lang* [42], *Rothe* [97], *DeGrand* and *DeTar* [98], *Smit* [99], *Wipf* [60] and *Creutz* [100]. Further helpful introductory texts were published by *Gupta* [101], *Wiese* [102] and *Lüscher* [103, 104]. Text books with focus on the application of lattice QCD in combination with advanced computational techniques are [105, 106]. This chapter is partly inspired by the PhD theses [61–65].

4.1. Lattice regularisation

For the quantisation of an interacting Euclidean quantum field theory, a regularisation procedure has to be applied. Wilson suggested to restrict a continuum field theory to a discretised version of Euclidean spacetime, a spacetime lattice [107]. In this thesis, we deal with lattices with a finite number of sites. Infinite lattices are not suited for Monte Carlo simulations as computers can only deal with a finite number of degrees of freedom. We consider a hypercubic lattice [42]

$$\Lambda = \{x \in \mathbb{R}^4 | x^\mu = an^\mu, n^\mu \in \{0, 1, \dots, N^\mu - 1\}, \mu \in \{0, 1, 2, 3\}\} \quad (4.1)$$

with equal lattice spacings in all directions. The extent is commonly chosen equal for all spatial dimension, $N^1 = N^2 = N^3$, such that the lattice is compatible with the octahedral symmetry group. The restriction to a finite volume requires the definition of boundary conditions. To understand the implication of a finite spacetime lattice, we consider a generic lattice field Φ and decompose it into its Fourier modes, assuming periodic boundary conditions for simplicity:

$$\Phi^x = \sum_p \sqrt{\frac{a}{X^\mu}} \exp\left(i \sum_\mu p^\mu x^\mu\right) \Phi^p, \quad \Phi^p = \sum_x \sqrt{\frac{a}{X^\mu}} \exp\left(-i \sum_\mu p^\mu x^\mu\right) \Phi^x. \quad (4.2)$$

The definition of the momenta is invariant under shifts by multiples of $\frac{2\pi}{a}$, i.e. the momentum lattice is also periodic. It is common to shift the momenta to the first Brillouin

4. Lattice field theories

zone [42]:

$$\tilde{\Lambda} = \left\{ p \in \mathbb{R}^4 \left| p^\mu = \frac{2\pi}{a} \frac{n^\mu}{N^\mu}, n^\mu \in \left\{ -\frac{N^\mu}{2} + 1, \dots, 0, \dots, \frac{N^\mu}{2} \right\}, \mu \in \{0, 1, 2, 3\} \right. \right\}. \quad (4.3)$$

The minimum distance between two lattice sites a induces a sharp cutoff in momentum space at $\frac{\pi}{a}$ in each direction. Loop integrals known from continuum perturbation theory are replaced by a finite sum over the lattice momenta, i.e. the spacetime lattice serves as a UV regulator of a quantum field theory. Lattice perturbation theory calculations can also be performed on infinite lattices. In this case, the momenta form a continuous set but are also bound to the first Brillouin zone. Anisotropic lattices with a smaller lattice spacing in the temporal direction are relevant for finite-temperature calculations.

4.1.1. Lattice actions and lattice operators

If a spacetime lattice is used to regularise a continuum quantum field theory, lattice counterparts have to be constructed for all ingredients of the continuum theory. In detail, a lattice action S^{lat} and lattice operators O^{lat} have to be constructed that converge to their continuum counterparts S^{cont} and O^{cont} , when the lattice cutoff is removed:

$$\lim_{a \rightarrow 0} S^{\text{lat}} = S^{\text{cont}}, \quad \lim_{a \rightarrow 0} O^{\text{lat}} = O^{\text{cont}}. \quad (4.4)$$

It is clear, that these requirements do not uniquely define S^{lat} and O^{lat} . This fact can be used to influence the rate of convergence towards the continuum limit.

4.1.2. Symanzik improvement programme

The formulation of lattice quantum field theories as discretised versions of continuum quantum field theories can be altered in such a way that the rate of the convergence towards continuum, which is measured in powers of the lattice spacing a , is increased. A systematic approach was formulated by *Symanzik* [108, 109]. Close to the continuum, the lattice theory can be understood as an effective theory and be expanded in terms of a [42, 110]:

$$S = \int d^4x \mathcal{L}_0^x + \sum_{i=1}^{n-1} a^i \mathcal{L}_i^x + O(a^n). \quad (4.5)$$

$\mathcal{L}^{(0)}$ denotes the Lagrange density of the corresponding continuum theory. The densities \mathcal{L}_i^x consist of linear combinations of local operators with mass dimension $4 + i$, which are compatible with the symmetries of the lattice action:

$$\mathcal{L}_i^x = \sum_{k=1}^{l_i} c_{ik} \mathcal{L}_{ik}^x. \quad (4.6)$$

The lattice action is now modified in such a way that these contributions vanish to the desired order. This is achieved by adding discretised versions of $\int d^4x \mathcal{L}_{ik}^x$ to the lattice

action. The corresponding improvement coefficients c_{ik} have to be tuned appropriately. In order to obtain improved correlation functions, the improvement also has to be applied to operators. The procedure is completely analogous. Improvement coefficients can be determined by means of perturbation theory. Nevertheless, a non-perturbative determination is preferred. This can be achieved by imposing Ward-Takahashi identities of the continuum theory on lattice correlation functions [110, 111]. The improvement coefficients are tuned such that lattice artefacts in the identity vanish to the desired order.

4.2. Lattice gauge theories

Lattice gauge theories are defined on a spacetime lattice and possess a gauge symmetry. In particular, they provide gauge-invariant non-perturbative regularisations of continuum gauge theories. A typical application is the investigation of low-energy QCD, where perturbation theory breaks down. In addition, lattice gauge theories also offer the possibility to perform a strong and a weak coupling expansion [96, 97].

4.2.1. Local gauge transformations

Local gauge transformations \mathfrak{G}_Ω , where $\Omega^x \in G$ and G denotes the gauge group, act on lattice fermion fields Ψ and $\bar{\Psi}$ similar to the continuum [42]

$$\mathfrak{G}_\Omega[(\Psi^x, \bar{\Psi}^x)] = (\Omega^x \Psi^x, \bar{\Psi}^x (\Omega^x)^\dagger). \quad (4.7)$$

A local combination of the conjugated pair of fermion fields is gauge invariant [42],

$$\mathfrak{G}_\Omega[\bar{\Psi}^x \Psi^x] = \bar{\Psi}^x (\Omega^x)^\dagger \Omega^x \Psi^x = \bar{\Psi}^x \Psi^x, \quad (4.8)$$

i.e. a gauge invariant mass term can directly be constructed. This situation is different for the kinetic term of a lattice field theory. Lattice derivatives require the combination of fields at different lattice sites such that gauge invariance is spoiled. An object from continuum field theory which can be used to define gauge-invariant combinations of displaced lattice fields is the *parallel transporter* $U_P^{x_2 x_1}$ along a path P connecting the points x_1 and x_2 . It is defined as [42]

$$U_P^{x_2 x_1} = \text{P} \left[\exp \left(ig \int_P dx^\mu A^{x\mu} \right) \right], \quad (4.9)$$

where P denotes the path ordering operator and g is the coupling of the gauge field to the fermions. Under a local gauge transformation, the parallel transporter transforms as [42]

$$\mathfrak{G}_\Omega[U_P^{x_2 x_1}] = \Omega^{x_2} U_P^{x_2 x_1} (\Omega^{x_1})^\dagger, \quad (4.10)$$

i.e. a term of the form [42]

$$\mathfrak{G}_\Omega[\bar{\Psi}^{x_2} U_P^{x_2 x_1} \Psi^{x_1}] = \bar{\Psi}^{x_2} (\Omega^{x_2})^\dagger \Omega^{x_2} U_P^{x_2 x_1} (\Omega^{x_1})^\dagger \Omega^{x_1} \Psi^{x_1} = \bar{\Psi}^{x_2} U_P^{x_2 x_1} \Psi^{x_1} \quad (4.11)$$

4. Lattice field theories

is gauge invariant. So far, the gauge transporter is defined on the basis of a gauge field in continuous spacetime. For the lattice discretisation, we define *gauge links* $U^{x\mu} \in G$, which connect neighbouring lattice sites x and $x + a\hat{\mu}$ and transform in the same way as the parallel transporter [42, 98]:

$$\mathfrak{G}_\Omega[U^{x\mu}] = \Omega^x U^{x\mu} (\Omega^{x+a\hat{\mu}})^\dagger. \quad (4.12)$$

They can be understood as discretised versions of the parallel transporter between two neighbouring lattice sites:

$$U_P^{x, x+a\hat{\mu}} = \text{P} \left[\exp \left(ig \int_P dx^\mu A^{x\mu} \right) \right] = \exp(igaA^{x\mu}) + O(a). \quad (4.13)$$

In lattice gauge theories, the gauge links U , which are elements of the gauge group, form the fundamental fields. The path integral quantisation is performed with respect to an integration over the gauge links U , which we will introduce in section 4.2.3. Nevertheless, it is possible to implicitly define a lattice gauge field A , which is an element of the Lie algebra of the gauge group, by the exponential map [42, 98]

$$U^{x\mu} = \exp(igaA^{x\mu}). \quad (4.14)$$

4.2.2. Gauge invariant objects

As we aim for the construction of gauge invariant actions, we discuss elementary gauge invariant building blocks composed from gauge links and fermion fields. We consider an ordered product of gauge links, which are defined along a path $(x_0, x_1 = x_0 + a\hat{\mu}_0, \dots, x_n = x_{n-1} + a\hat{\mu}_{n-1})$:

$$P[U] = U^{x_0\mu_0} U^{x_1\mu_1} \dots U^{x_{n-1}\mu_{n-1}} = \prod_{i=0}^{n-1} U^{x_i\mu_i}. \quad (4.15)$$

It is convenient to define $U^{x, -\mu} = (U^{x-a\hat{\mu}, \mu})^\dagger$ to allow for paths in the $-\hat{\mu}$ direction. The product of gauge links along a path transforms under gauge transformations as [42]

$$\mathfrak{G}_\Omega[P[U]] = \Omega^{x_0} P[U] (\Omega^{x_n})^\dagger. \quad (4.16)$$

We can build gauge invariant objects if we attach fermion and conjugated fermion fields at both ends of an arbitrary path [42]:

$$\mathfrak{G}_\Omega[\bar{\Psi}^{x_0} P[U] \Psi^{x_n}] = \bar{\Psi}^{x_0} (\Omega^{x_0})^\dagger \Omega^{x_0} P[U] (\Omega^{x_n})^\dagger \Omega^{x_n} \Psi^{x_n} = \bar{\Psi}^{x_0} P[U] \Psi^{x_n}. \quad (4.17)$$

For a closed path, i.e. $x_0 = x_n$, we obtain a gauge invariant object when taking the trace [42]:

$$\mathfrak{G}_\Omega[\text{tr}(P[U])] = \text{tr}(\Omega^{x_0} P[U] (\Omega^{x_0})^\dagger) = \text{tr}((\Omega^{x_0})^\dagger \Omega^{x_0} P[U]) = \text{tr}(P[U]). \quad (4.18)$$

4.2.3. The path integral measure for compact gauge groups

In order to construct the path integral over link variables, a path integral measure DU has to be introduced. It is defined as the product of Lie group measures dU for each site x and direction μ [42]:

$$DU = \prod_x \prod_{\mu=0}^3 dU^{x\mu}. \quad (4.19)$$

An essential requirement for this measure is its invariance under gauge transformations. For compact Lie groups G , there exists a unique measure, the so called *Haar measure*, with the properties [42]

$$dU_1 = d(U_1 U_2) = d(U_2 U_1) \quad \forall U_2 \in G, \quad \int_G dU = 1, \quad (4.20)$$

i.e. the measure is invariant under right- and left-translations and normalised. The translational invariance ensures the demanded gauge invariance of the path integral measure [42]:

$$d(\mathfrak{G}[U^{x\mu}]) = d(\Omega^x U^{x\mu} (\Omega^{x+a\hat{\mu}})^\dagger) = dU^{x\mu}. \quad (4.21)$$

Group elements U of the Lie groups $SU(n)$ and $U(n)$ can be represented as $U = \exp(i\omega^a T^a)$, where the ω^a are real numbers and the T^a denote the Lie group generators. On the Lie group, a metric tensor $g = g(\omega)_{a_2 a_1} d\omega^{a_2} d\omega^{a_1}$ can be constructed with entries [42]

$$g(\omega)_{a_2 a_1} = \text{tr} \left(\frac{\partial U(\omega)}{\partial \omega^{a_2}} \frac{\partial U(\omega)^\dagger}{\partial \omega^{a_1}} \right). \quad (4.22)$$

The Haar measure of the group is then defined by [42]

$$dU = c \sqrt{\det(g(\omega))} \prod_a d\omega^a, \quad (4.23)$$

where the constant c is determined by the normalisation condition. A proof that this measure fulfils the properties in eq. (4.20) can be found in [42].

4.3. Lattice gauge actions

In general, lattice gauge actions can be constructed from closed paths of gauge links. In this section, we describe the construction of two lattice gauge actions that reproduce the Yang-Mills action in the continuum limit $a \rightarrow 0$.

4.3.1. Wilson gauge action

The shortest non-trivial closed path on the lattice is a square in the μ_1 - μ_2 -plane. It is defined by the corner points x , $x + a\hat{\mu}_1$, $x + a\hat{\mu}_1 + a\hat{\mu}_2$ and $x + a\hat{\mu}_2$. The corresponding ordered product of gauge links is the so-called *plaquette* $P^{x\mu_2\mu_1}$, which reads [42, 98]

$$P^{x\mu_1\mu_2} = U^{x\mu_1} U^{x+a\hat{\mu}_1,\mu_2} (U^{x+a\hat{\mu}_2,\mu_1})^\dagger (U^{x,\mu_2})^\dagger. \quad (4.24)$$

4. Lattice field theories

Using the identification between gauge links and gauge fields in eq. (4.14), one finds [42, 98]

$$P^{x\mu_2\mu_1} = \exp(\mathrm{i}a^2 F^{x\mu_2\mu_1} + O(a^3)) = \mathbb{1} + \mathrm{i}a^2 F^{x\mu_2\mu_1} - \frac{1}{2}a^4 (F^{x\mu_2\mu_1})^2 + O(a^3), \quad (4.25)$$

i.e. the plaquette is directly related to the field strength tensor of the continuum theory. This observation allows to construct the *Wilson gauge action*. Assuming a $SU(3)$ gauge theory, it is defined as [42, 98, 107]

$$S[U] = \frac{\beta}{3} \sum_x \sum_{\mu_2 < \mu_1} \mathrm{Re} \, \mathrm{tr} \left(\mathbb{1} - P^{x\mu_2\mu_1} \right) \quad (4.26)$$

with the inverse coupling $\beta = \frac{6}{g^2}$. The definition ensures that in the limit $a \rightarrow 0$ the continuum action is obtained [42]:

$$S[U] = \frac{2a^4}{g^2} \sum_x \sum_{\mu_2, \mu_1} \mathrm{tr}((F^{x\mu_2\mu_1})^2) + O(a^2). \quad (4.27)$$

4.3.2. Lüscher-Weisz gauge action

The Symanzik improvement programme, as discussed in section 4.1.2, can be applied to the Wilson gauge action to eliminate lattice artefacts to the desired order. *Lüscher* and *Weisz* derived a gauge action that is tree-level $O(a^2)$ -improved [112, 113], i.e. the improvement coefficients are determined at the classical level neglecting corrections from quantum loops. In this setting, the improvement coefficients do not depend on the inverse coupling β . We will apply this gauge action for the simulation of QCD in this thesis. In addition to the plaquette, the rectangle in the μ_1 - μ_2 -plane has to be added to the action [65]:

$$R^{\mu_2\mu_1} = U^{x\mu_1} U^{x+a\hat{\mu}_1, \mu_2} U^{x+a\hat{\mu}_1+a\hat{\mu}_2, \mu_2} (U^{x+2a\hat{\mu}_2, \mu_1})^\dagger (U^{x+a\hat{\mu}_2, \mu_2})^\dagger (U^{x, \mu_2})^\dagger. \quad (4.28)$$

The tree-level on-shell improved Lüscher-Weisz gauge action is defined as [73, 112, 113]

$$S_g[U] = \frac{\beta}{6} \sum_x \sum_{\mu_2 > \mu_1} (c_0 \mathrm{Re} \, \mathrm{tr}(\mathbb{1} - P^{\mu_1\mu_2}) + c_1 \mathrm{tr}(\mathbb{1} - R^{\mu_1\mu_2} + \mathbb{1} - R^{\mu_2\mu_1})) \quad (4.29)$$

with the coefficients $c_0 = \frac{5}{3}$ and $c_1 = -\frac{1}{12}$. For the choice $c_0 = 3.648$ and $c_1 = -0.331$ the renormalisation group-inspired [98] Iwasaki gauge action is obtained [114].

4.4. Lattice fermion actions

In addition to the gauge action, the formulation of a lattice gauge theory also requires a discretised fermion action. In this section, we discuss the fermion doubling problem, present $O(a)$ -improved Wilson fermions, which are used in this theses, and summarise alternative lattice fermion formulations. A helpful review on the topic of chiral symmetry on the lattice and lattice fermion formulations is [115].

4.4.1. Lattice derivatives

Kinetic terms for lattice field theory actions can be constructed by means of the lattice counterpart of derivative operators. These discrete derivative operators are commonly denoted as *lattice derivatives* or *finite differences*. We define the right-acting forward and backward derivatives acting on a generic field Φ as [72, 97]

$$\begin{aligned} (\vec{\partial}_F^\mu \Phi)^x &= \frac{1}{a}(\Phi^{x+a\hat{\mu}} - \Phi^x), & \vec{\partial}_F^{\mu x_2}{}_{x_1} &= \frac{1}{a}(\delta_{x_1}^{x_2+a\hat{\mu}} - \delta_{x_1}^{x_2}), \\ (\vec{\partial}_B^\mu \Phi)^x &= \frac{1}{a}(\Phi^x - \Phi^{x-a\hat{\mu}}), & \vec{\partial}_B^{\mu x_2}{}_{x_1} &= \frac{1}{a}(\delta_{x_1}^{x_2} - \delta_{x_1-a\hat{\mu}}^{x_2}), \end{aligned} \quad (4.30)$$

and the left-acting forward and backward derivatives as [72]

$$\begin{aligned} (\overleftarrow{\partial}_F^\mu)^x &= \frac{1}{a}(\Phi^{x+a\hat{\mu}} - \Phi^x), & \overleftarrow{\partial}_F^{\mu x_2}{}_{x_1} &= \frac{1}{a}(\delta_{x_1+a\hat{\mu}}^{x_2} - \delta_{x_1}^{x_2}), \\ (\overleftarrow{\partial}_B^\mu)^x &= \frac{1}{a}(\Phi^x - \Phi^{x-a\hat{\mu}}), & \overleftarrow{\partial}_B^{\mu x_2}{}_{x_1} &= \frac{1}{a}(\delta_{x_1}^{x_2} - \delta_{x_1-a\hat{\mu}}^{x_2}), \end{aligned} \quad (4.31)$$

respectively. Making use of the Taylor expansion, we find $O(a)$ lattice artefacts for the forward and backward derivatives. Considering a lattice of finite extent, $\vec{\partial}_F^\mu$ and $\overleftarrow{\partial}_B^\mu$ as well as $\vec{\partial}_B^\mu$ and $\overleftarrow{\partial}_F^\mu$ are related to each other via partial integration including boundary terms [97].

4.4.2. Gauge covariant lattice derivatives

The construction of lattice gauge theories requires a discretised version of the continuum gauge covariant derivative. Introducing parallel transporters, i.e. the gauge links U , the discrete derivatives in eqs. (4.30) and (4.31) can be modified so that they transform covariantly under gauge transformations. We define the right-acting forward and backward covariant lattice derivatives as [72]

$$\begin{aligned} (\vec{D}_F^\mu \Psi)^x &= \frac{1}{a}(U^{x\mu} \Psi^{x+a\hat{\mu}} - \Psi^x), & \vec{D}_F^{\mu x_2}{}_{x_1} &= \frac{1}{a}(U^{x_2\mu} \delta_{x_1}^{x_2+a\hat{\mu}} - \delta_{x_1}^{x_2}), \\ (\vec{D}_B^\mu \Psi)^x &= \frac{1}{a}(\Psi^x - (U^{x-a\hat{\mu},\mu})^\dagger \Psi^{x-a\hat{\mu}}), & \vec{D}_B^{\mu x_2}{}_{x_1} &= \frac{1}{a}(\delta_{x_1}^{x_2} - (U^{x_2-a\hat{\mu},\mu})^\dagger \delta_{x_1-a\hat{\mu}}^{x_2}), \end{aligned} \quad (4.32)$$

and the left-acting covariant lattice derivatives as [72]

$$\begin{aligned} (\overleftarrow{\Psi} \overleftarrow{D}_F^\mu)^x &= \frac{1}{a}(\overleftarrow{\Psi}^{x+a\hat{\mu}} (U^{x\mu})^\dagger - \overleftarrow{\Psi}^x), & \overleftarrow{D}_F^{\mu x_2}{}_{x_1} &= \frac{1}{a}(\delta_{x_1+a\hat{\mu}}^{x_2} (U^{x_1\mu})^\dagger - \delta_{x_1}^{x_2}), \\ (\overleftarrow{\Psi} \overleftarrow{D}_B^\mu)^x &= \frac{1}{a}(\overleftarrow{\Psi}^x - \overleftarrow{\Psi}^{x-a\hat{\mu}} U^{x-a\hat{\mu},\mu}), & \overleftarrow{D}_B^{\mu x_2}{}_{x_1} &= \frac{1}{a}(\delta_{x_1}^{x_2} - \delta_{x_1-a\hat{\mu}}^{x_2} U^{x_1-a\hat{\mu},\mu}), \end{aligned} \quad (4.33)$$

respectively. Making use of the Taylor expansion and the relation between the gauge links and gauge fields in eq. (4.14), it is straightforward to show, that the covariant lattice derivatives fulfil the correct continuum limit up to $O(a)$. Similar as in the previous section, the derivatives \vec{D}_F^μ and \overleftarrow{D}_B^μ as well as \vec{D}_B^μ and \overleftarrow{D}_F^μ are related to each other via partial integration including boundary terms.

4. Lattice field theories

4.4.3. Naive fermion action and doubling of fermion species

A straightforward discretisation of the continuum fermion action is obtained by replacing the continuum covariant derivatives by lattice covariant derivatives [42, 116], defined in eq. (4.32), ensuring that the continuum action is restored in the limit $a \rightarrow 0$. It is clear that this choice is not unique, as additional terms which vanish in the continuum limit can always be added. We write the fermion action as a bilinear form in the pair of conjugated fermion fields:

$$S[U, \Psi, \bar{\Psi}] = \bar{\Psi}_{\mathbf{b}} D[U] \Psi_{\mathbf{a}}. \quad (4.34)$$

$D[U]$ denotes the Dirac operator, which depends on the gauge links U . For quark fields in the defining representation, we have $\mathbf{a}, \mathbf{b} \equiv x f c s$, where x denotes the spacetime, f the flavour, c the colour and s the spin index. Using a symmetric combination of forward and backward covariant derivatives, the naive Dirac operator is given by [42, 116]

$$D_{\text{naive}}[U] = \frac{1}{2} \left(\sum_{\mu} \gamma^{\mu} (\vec{D}_{\text{F}}^{\mu} + \vec{D}_{\text{B}}^{\mu}) \right) + M \quad (4.35)$$

with the mass matrix M . A straightforward calculation shows that the Dirac operator possesses the correct continuum limit and lattice artefacts are of $O(a^2)$ [42]. Applying a Fourier transformation and assuming a unit gauge background $U^{x\mu} = \mathbb{1}$, the naive Dirac operator can be written as [42, 116]

$$D_{\text{naive}}^{p_2}_{p_1} = \left(\frac{i}{a} \sum_{\mu} \gamma^{\mu} \sin(ap_1^{\mu}) + M \right) \delta_{p_1}^{p_2}. \quad (4.36)$$

The quark propagator, which is the inverse of the Dirac operator, possesses a pole whenever $p^{\mu} \in \{0, \frac{\pi}{a}\}$ for all $\mu = 0, \dots, 3$ [42, 116]. Consequently, there are in total 16 poles in the first Brillouin zone, i.e. 16 fermion flavours are present in the theory instead of one with a pole at $p = 0$. The additional 15 fermion flavours are referred to as *fermion doublers*. The presence of fermion doublers is a fundamental issue in the formulation of discretised fermion actions, which is directly related to the preservation of chiral symmetry on the lattice. A fundamental theorem which summarises these issues was formulated by *Nielsen* and *Ninomiya*.

4.4.4. Nielsen-Ninomiya-Theorem

We phrase the Nielsen-Ninomiya theorem [117–120] in the version of [121]. No lattice Dirac operator D can be constructed which simultaneously fulfils the following four properties:

1. $D(p)$ is an analytic function in the momenta p with periodicity $\frac{2\pi}{a}$.
2. $D(p) = i\gamma^{\mu} p^{\mu} + O(ap^2)$ for $|p| \ll \frac{\pi}{a}$, i.e. D shows the correct behaviour in the continuum limit.
3. $D(p)$ is invertible for $p \neq 0 \pmod{\frac{2\pi}{a}}$.

4. D anti-commutes with γ^5 , i.e. $\{D, \gamma^5\} = 0$, which is required such that the fermion action is invariant under continuous chiral transformations.

All existing lattice fermion discretisations have to violate at least one of the four properties. Common formulations rely on an explicit breaking of chiral symmetry, on the introduction of a lattice version of chiral symmetry or on a partial reduction of fermion doublers. In the following, we will present several lattice fermion formulations.

4.4.5. Wilson fermion action

Wilson removed the fermion degeneracy by adding an irrelevant, dimension-5 operator which vanishes in the continuum limit [107]. This modification gives the fermion doublers an additive mass, which diverges in the continuum limit, such that they eventually decouple from the theory. In order to distinguish the doubler modes with poles at $p \neq 0$ from the physical mode with a pole at $p = 0$, it is useful to introduce a mass term which depends on the momentum. The mass term has to vanish at $p = 0$ and diverge in the continuum limit for the unphysical poles. A suitable choice for this purpose is the gauge covariant Laplace operator $\sum_\mu \vec{D}_B^\mu \vec{D}_F^\mu$. The Wilson-Dirac operator D_W is defined as the sum of the naive Dirac operator in eq. (4.35) and the *Wilson term*:

$$D_W[U] = \frac{1}{2} \sum_\mu \gamma^\mu (\vec{D}_F^\mu + \vec{D}_B^\mu) - \frac{1}{2} \sum_\mu \vec{D}_B^\mu \vec{D}_F^\mu + M. \quad (4.37)$$

Making use of the definitions of the lattice covariant derivatives in terms of gauge links and of partial integration, the Wilson-Dirac operator can also be written in a symmetric fashion, which we will use in this thesis:

$$D_W[U] = \frac{1}{4} \sum_\mu \left((\vec{D}_F^\mu - \overleftarrow{D}_B^\mu)(\gamma^\mu + \mathbb{1}) + (\vec{D}_B^\mu - \overleftarrow{D}_F^\mu)(\gamma^\mu - \mathbb{1}) \right) + M. \quad (4.38)$$

Applying a Fourier transformation and assuming a unit gauge background $U^{x\mu} = \mathbb{1}$, the Wilson-Dirac operator becomes [42, 116]

$$D_W^{p_2}_{p_1} = \left(\frac{i}{a} \sum_\mu \gamma^\mu \sin(ap_1^\mu) + \frac{1}{a} \mathbb{1} \sum_\mu (1 - \cos(ap_1^\mu)) + M \right) \delta_{p_1}^{p_2}. \quad (4.39)$$

The Wilson term vanishes only at $p = 0$. The remaining 15 fermion doublers acquire an additional mass contribution, which is proportional to $1/a$. The major drawback of this construction is the fact that the Wilson term explicitly breaks chiral symmetry even for massless fermions. In addition, a vanishing bare mass $m = 0$ does not lead to a vanishing renormalised fermion mass due to the additive mass renormalisation caused by the Wilson term. The Wilson fermion action also only approaches the continuum limit with a rate of $O(a)$ instead of $O(a^2)$ as for the naive fermion formulation. *Lüscher* was able to prove the existence of a self-adjoint, strictly positive transfer matrix for the Wilson plaquette gauge

4. Lattice field theories

action in combination with the Wilson fermion action [122]. An important property of the Wilson-Dirac operator $D[U, A]$ is its γ^5 -hermiticity [42]:

$$D_W[U] = \gamma^5 (D_W[U])^\dagger \gamma^5, \quad (4.40)$$

γ^5 -hermiticity implies that the eigenvalues of $D[U]$ are either real or appear as complex conjugated pairs [42].

4.4.6. $O(a)$ -improved Wilson fermion action

The Symanzik improvement program, introduced in section 4.1.2, can also be applied to the Wilson fermion action, leading to an $O(a)$ -improved Wilson fermion action. This fermion discretisation will be used for the quark fields later in this thesis. We summarise the improvement procedure for the isosymmetric 2-flavour case. In total, there are five dimension-5 operators, which are compatible with the symmetries of continuum QCD [42, 72]:

$$\mathcal{L}_1^x = \sum_{\mu_2, \mu_1} \bar{\Psi}^x \sigma^{\mu_2 \mu_1} F^{\mu_2 \mu_1} \Psi^x, \quad (4.41)$$

$$\mathcal{L}_2^x = \sum_{\mu} \bar{\Psi}^x (\vec{D}^\mu \vec{D}^\mu \Psi)^x + \sum_{\mu} (\bar{\Psi} \overleftarrow{D}^\mu \overleftarrow{D}^\mu)^x \Psi^x, \quad (4.42)$$

$$\mathcal{L}_3^x = m \sum_{\mu_2, \mu_1} \text{tr}(F^{\mu_2 \mu_1} F^{\mu_2 \mu_1}), \quad (4.43)$$

$$\mathcal{L}_4^x = \sum_{\mu} \bar{\Psi}^x \gamma^\mu (\vec{D}^\mu \Psi)^x + \sum_{\mu} (\bar{\Psi} \overleftarrow{D}^\mu)^x \gamma^\mu \Psi^x, \quad (4.44)$$

$$\mathcal{L}_5^x = m^2 \bar{\Psi}^x \Psi^x. \quad (4.45)$$

Making use of the on-shell improvement condition in form of the continuum field equation $(\gamma^\mu \vec{D}^\mu + m)\Psi = 0$, one finds that the operators are not independent [42, 72]:

$$\mathcal{L}_1 - \mathcal{L}_2 + 2\mathcal{L}_5 = 0, \quad \mathcal{L}_4 + 2\mathcal{L}_5 = 0. \quad (4.46)$$

These relations can be used to eliminate the operators \mathcal{L}_2 and \mathcal{L}_4 , such that only \mathcal{L}_1 , \mathcal{L}_3 and \mathcal{L}_5 are left [42, 72]. However, \mathcal{L}_1 is proportional to the gauge action term and \mathcal{L}_5 is proportional to the quark mass term. The bare parameters m and β are just rescaled, $g^2 \rightarrow g^2(1 + c_3 am)$ and $m \rightarrow m(1 + c_5 am)$, such that one can omit these operators as well. The only operator which has to be added to the action is \mathcal{L}_1 [42, 72], the so called Pauli, Clover or Sheikholeslami-Wohlert term. The Wilson-Dirac operator in eq. (4.38) is altered to

$$\begin{aligned} D_{\text{IW}}[U] = & \frac{1}{4} \sum_{\mu} \left((\vec{D}_{\text{F}}^\mu - \overleftarrow{D}_{\text{B}}^\mu)(\gamma^\mu + \mathbb{1}) + (\vec{D}_{\text{B}}^\mu - \overleftarrow{D}_{\text{F}}^\mu)(\gamma^\mu - \mathbb{1}) \right) \\ & + M + c_{\text{SW}} a \sum_{\mu_1 < \mu_2} \frac{1}{2} \sigma^{\mu_1 \mu_2} \hat{F}_{\text{S}}^{\mu_1 \mu_2}. \end{aligned} \quad (4.47)$$

\hat{F} denotes a lattice discretisation of the continuum field strength tensor. A common choice is [42, 72]

$$\hat{F}^{x\mu_1\mu_2} = -\frac{i}{8a^2}(Q^{x\mu_1\mu_2} - Q^{x\mu_2\mu_1}). \quad (4.48)$$

$Q^{x\mu_1\mu_2}$ is the sum of the plaquettes in the μ_1 - μ_2 plane of which x is a corner point:

$$Q^{x\mu_1\mu_2} = U^{x\mu_1\mu_2} + U^{x\mu_2,-\mu_1} + U^{x,-\mu_1,-\mu_2} + U^{x,-\mu_2\mu_1}. \quad (4.49)$$

c_{SW} is the Sheikholeslami-Wohlert coefficient [123]. As c_{SW} is a function of β , it has to be determined for each lattice spacing separately. This computation can either be performed perturbatively or non-perturbatively. To lowest order in perturbation theory, $c_{\text{SW}} = 1$. The non-perturbative determination commonly relies on the imposition of the continuum PCAC relation [72, 110], which required also the improvement of the axial current and the pseudo-scalar density operators [72, 110]. For multi-flavour QCD with non-degenerate quark masses, the improvement program turns out to be more sophisticated, as a larger number of irrelevant operators has to be considered and the corresponding improvement coefficients have to be determined [111].

4.4.7. Alternative lattice fermion actions

Ginsparg and *Wilson* formulated a relaxed version of the anti-commutation condition of D and γ^5 , responsible for the preservation of chiral symmetry of the lattice fermion action [124]. The Ginsparg-Wilson relation allows a massless Dirac operator $D_{\text{GW},0}$ to break chiral symmetry in the form of a lattice artefact:

$$D_{\text{GW},0}\gamma^5 + \gamma^5 D_{\text{GW},0} = aD_{\text{GW},0}\gamma^5 D_{\text{GW},0}. \quad (4.50)$$

The right-hand side vanishes in the continuum limit, i.e. the chiral symmetry is restored. *Lüscher* constructed a $U(1)$ group of transformations \mathfrak{T}_α [121], reading

$$\mathfrak{T}_\alpha[(\Psi, \bar{\Psi})] = \left(\exp\left(i\alpha\gamma^5\left(1 - \frac{a}{2}D\right)\right)\Psi, \bar{\Psi} \exp\left(i\alpha\left(1 - \frac{a}{2}D\right)\gamma^5\right) \right), \quad (4.51)$$

which reduces to the standard chiral transformation in the continuum limit $a \rightarrow 0$. Fermion actions with Dirac operators satisfying the Ginsparg-Wilson relation are invariant under these transformations [121]. Thus, it is possible to construct a doubler free lattice fermion theory that still obeys a lattice version of the continuum chiral symmetry. In contrast, the path integral measure is not invariant and an anomalous term in the axial Ward identity appears, which is a discretised version of the Adler-Bell-Jackiw anomaly [42]. It is further possible to construct massive fermions from a massless Ginsparg-Wilson Dirac operator $D_{\text{GW},0}$ [125]:

$$D_{\text{GW},m} = D_{\text{GW},0} + m\left(1 - \frac{a}{2}D\right) = \left(1 - \frac{am}{2}\right)D_{\text{GW},0} + m\mathbb{1}. \quad (4.52)$$

4. Lattice field theories

Two established realisations of Ginsparg-Wilson fermions are domain wall fermions [126–129] and overlap fermions [130, 131]. However, both fermion discretisations are computationally expensive such that other fermion formulations are commonly preferred.

Another discretisation that is based on a doublet of Wilson fermions and also breaks chiral symmetry is the twisted-mass fermion formulation, in which a chirally twisted mass term $i\mu\gamma^5\tau^3$ is added to the Wilson action [132, 133]. The corresponding Dirac operator is protected from zero modes, such that numerical simulations are stabilised, and the fermion determinant is strictly positive. In addition, the theory is $O(a)$ -improved at maximal twist, i.e. the twisting angle $\alpha = \arctan(\mu/m)$ is set to $\pi/2$ and the bare fermion mass m to its critical value [134, 135]. A significant drawback of the formulation is the explicit breaking of isospin symmetry, which is, however, restored in the continuum limit [42, 135].

A lattice fermion formulation that preserves a remnant chiral symmetry is staggered fermions [136]. A transformation that mixes spinor and spacetime indices is used to distribute the four components of a Dirac spinor over the spacetime lattice. This reduces the number of fermion doublers from 16 to 4. A further reduction of the number of species is achieved by computing roots of the fermion determinant [42]. A major advantage of staggered fermions are the reduced computational costs. However, a discussion about the conceptual issues related to the rooting of the determinant is on-going [137, 138].

4.5. Non-compact lattice QED

In the case of an Abelian gauge theory, a different type of lattice gauge action can be defined, which depends on the gauge fields and not on gauge links. Derivatives in the continuum gauge action are replaced by their discrete counterparts. On the lattice, the photon action is given by

$$S_\gamma[A] = \frac{1}{4} \sum_x \sum_{\mu_1, \mu_2} F^{x\mu_1\mu_2} F^{x\mu_1\mu_2} \quad (4.53)$$

with the discretised field strength tensor [97]

$$F^{\mu_1\mu_2} = \vec{\partial}_F^{\mu_1} A^{\mu_2} - \vec{\partial}_F^{\mu_2} A^{\mu_1}, \quad (4.54)$$

where we used the lattice derivatives defined in eq. (4.30). Using the relations between the right-acting and left-acting derivatives, we can rewrite the action as a bilinear form in the photon field, reading

$$S_\gamma[A] = \frac{1}{2} A_{\mathbf{c}_2} \Delta^{\mathbf{c}_2}{}_{\mathbf{c}_1} A^{\mathbf{c}_1} \quad (4.55)$$

with the photon difference operator

$$\Delta^{\mu_2}{}_{\mu_1} = \left(\sum_\mu \overleftarrow{\partial}_F^\mu \overrightarrow{\partial}_F^\mu \right) \delta_{\mu_1}^{\mu_2} - \overleftarrow{\partial}_F^{\mu_1} \overrightarrow{\partial}_F^{\mu_2}. \quad (4.56)$$

$\mathbf{c} \equiv x_\mu$ in position space representation and the metric tensor, which is used to raise and lower indices of the photon field and of the photon difference operator, is $g_{(x_\mu)_2(x_\mu)_1} = \delta_{x_1}^{x_2} \delta_{\mu_1}^{\mu_2}$, i.e. $A_{(x_\mu)_2} = g_{(x_\mu)_2(x_\mu)_1} A^{(x_\mu)_1} = A_{(x_\mu)_2}$. We have not included a specific gauge fixing term yet, which will become relevant for two reasons: Without gauge fixing the path integral is divergent as one integrates over an infinite set of equivalent photon field configurations. In addition, the perturbative photon propagator is ill-defined. The existence of gauge symmetries is related to a non-trivial kernel of the photon difference operator, such that the inverse does not exist. Non-compact lattice QED suffers from several conceptual problems which we will discuss in the following. In general, one is interested in a lattice discretisation of a continuum theory which possesses a transfer matrix for a rigorous quantum mechanical interpretation of the lattice field theory as well as the possibility of applying the Symanzik improvement program to remove lattice artefacts successively order by order. Helpful review articles for this topic are [38, 43, 44, 139].

4.5.1. Inconsistency of electrodynamics on periodic volumes and IR problem of lattice QED

In lattice Monte Carlo simulations it is necessary to define boundary conditions as only a finite number of lattice sites, i.e. a finite volume, can be simulated on the computer. A straight forward choice is the application of periodic boundary conditions in the spatial directions. In order to understand the effect of this choice, we consider classical electrodynamics in the continuum on a periodic volume, e.g. a three-dimensional torus \mathbb{T}^3 [44, 140]. It is easy to show that this setup leads to unwanted problems. The total electric charge enclosed in the periodic volume can be related to the divergence of the electric field via Gauss's law [44, 140]:

$$Q = \int_{\mathbb{T}^3} d^3x \rho = \int_{\mathbb{T}^3} d^3x \partial^i E^i = \int_{\partial\mathbb{T}^3} dS^i E^i = 0. \quad (4.57)$$

Due to the periodic boundary conditions the electric flux over the toroidal surface vanishes, i.e. the periodic volume is incompatible with a total non-vanishing charge. This contradicts the aim of studying unbounded charged particles.

In order to further investigate the problem related to the periodic boundary conditions, we consider the action of Euclidean QED on a four-dimensional torus with periodic boundary conditions and investigate its gauge symmetries. The QED action reads

$$S[A, \Psi, \bar{\Psi}] = \int d^4x \frac{1}{4} \sum_{\mu_2, \mu_1} F^{x\mu_2\mu_1} F^{x\mu_2\mu_1} + \bar{\Psi}^x ((\gamma^\mu D^\mu + m)\Psi)^x, \quad (4.58)$$

where $D^\mu = \partial^\mu + ieA^\mu$ is the covariant derivative and $F^{\mu_2\mu_1} = \partial^{\mu_2} A^{\mu_1} - \partial^{\mu_1} A^{\mu_2}$ the field strength tensor. The periodic boundary conditions are implemented as

$$A^x|_{x^\mu=0} = A^x|_{x^\mu=X^\mu}, \quad \Psi^x|_{x^\mu=0} = \Psi^x|_{x^\mu=X^\mu}, \quad \bar{\Psi}^x|_{x^\mu=0} = \bar{\Psi}^x|_{x^\mu=X^\mu} \quad (4.59)$$

for $\mu = 0, 1, 2, 3$. Similar as in infinite volume, we find that the action is invariant under the gauge transformation \mathfrak{G} of the form

$$\mathfrak{G}[(A^{x\mu}, \Psi^x, \bar{\Psi}^x)] = (A^{x\mu} - (\partial^\mu \alpha)^x, \exp(ie\alpha^x)\Psi^x, \bar{\Psi}^x \exp(-ie\alpha^x)), \quad (4.60)$$

4. Lattice field theories

if α is a periodic function. In fact, demanding α to be a periodic function is far to restrictive. Inserting the gauge transformed fields into eq. (4.59) we find the two conditions

$$(\partial^\mu \alpha)^x|_{x^\mu=0} = (\partial^\mu \alpha)^x|_{x^\mu=X^\mu}, \quad \exp(i e \alpha^x)|_{x^\mu=0} = \exp(i e \alpha^x)|_{x^\mu=X^\mu}. \quad (4.61)$$

Due to the $2\pi i$ -periodicity of the exponential function, the conditions are equivalent to

$$(\partial^\mu \alpha)^x|_{x^\mu=0} = (\partial^\mu \alpha)^x|_{x^\mu=X^\mu}, \quad \alpha^x|_{x^\mu=0} = \alpha^x|_{x^\mu=X^\mu} - \frac{2\pi}{e} n^\mu, \quad (4.62)$$

where $n \in \mathbb{Z}^4$. A simple solution to eq. (4.62) is given by the choice $\alpha^x = \frac{2\pi n^\mu}{e X^\mu} x^\mu$, i.e. the respective gauge transformation reads

$$\mathfrak{G}[(A^{x\mu}, \Psi^x, \bar{\Psi}^x)] = \left(A^{x\mu} - \frac{2\pi n^\mu}{e X^\mu}, \exp\left(i e \frac{2\pi n^\mu}{e X^\mu} x^\mu\right) \Psi^x, \bar{\Psi}^x \exp\left(-i e \frac{2\pi n^\mu}{e X^\mu} x^\mu\right) \right). \quad (4.63)$$

For the photon field, this type of gauge transformation is a *shift symmetry* as the value of the entire field is shifted homogeneously [41]. From the previous discussion, it is clear that a gauge transformation, which satisfies eq. (4.62), can always be decomposed into a gauge transformation with periodic α and a non-periodic remainder for some $n \in \mathbb{Z}^4$:

$$\alpha^x = \alpha_{\text{per}}^x + \frac{2\pi n^\mu}{e X^\mu} x^\mu. \quad (4.64)$$

Gauge transformations which are characterised by a non-periodic α are referred to as *large gauge transformations*.

In general, gauge symmetries cause a non-trivial kernel of the photon differential operator. The large gauge transformations, defined in eq. (4.63), shift the value of the photon field by a constant. Hence, the photon propagator possesses a divergence at $p = 0$. In order to invert the photon differential operator, the gauge freedom has to be fixed. Commonly, one uses local gauge-fixing conditions that do not relate different sites of the gauge field. However, according to [44], large gauge transformations survive local gauge-fixing procedures as they are not continuously connected to the identity transformation. Therefore, a global gauge constraint has to be imposed in addition. There are several proposals to remove or avoid the problematic zero mode. In principle, there are two distinct solutions: Either one alters the action by excluding field modes manually or one chooses boundary conditions that avoid the zero mode [44].

4.5.2. QED_{TL}

QED_{TL} [141] is a particular infrared regularisation of non-compact lattice QED on a periodic lattice based on the action eq. (4.55). The photon field is restricted to field configurations satisfying

$$\sum_x A^{x\mu} = 0 \quad \forall \mu \in \{0, 1, 2, 3\} \quad (4.65)$$

on all Euclidean components of the photon field. The name convention describes the fact that the summation in the constraint is both over the temporal and spatial directions. The latter condition is equivalent to demanding a vanishing zero-mode in Fourier space

$$A^{p\mu}|_{p=0} = 0 \quad \forall \mu \in \{0, 1, 2, 3\}, \quad (4.66)$$

i.e. the mode is removed as a dynamical degree of freedom from the theory, such that the photon difference operator can be inverted and the infrared singularity in the photon propagator is avoided. It is commonly argued that removing a set of modes with measure zero in the infinite-volume limit does not alter the theory in this limit [44]. QED_{TL} was used in early QCD+QED simulations [141, 142], but also in the original setup of the BMW collaboration for the investigation of isospin breaking [47] and of the Rome approach [46, 143], which will be relevant later in this work. Despite its simplicity, QED_{TL} suffers from several conceptual problems [44, 47, 140], such that the application of this type of lattice QED discretisation is nowadays avoided. The constraint connects fields at arbitrary times and spoils reflection positivity. As a consequence, this prevents the construction of a transfer matrix [41]. In addition, charged particle propagators are ill-behaved if the time extent of the box is sent to infinity while keeping its spatial size fixed: The effective mass for charged states at fixed order in e^2 diverges in the infinite time limit [41].

4.5.3. QED_L

A significant improvement with regard to the conceptual problems of QED_{TL} is offered by QED_L, which was introduced by *Hayakawa* and *Uno* [140], featuring a more restrictive constraint on the field variables

$$\sum_{\vec{x}} A^{x\mu} = 0 \quad \forall \mu \in \{0, 1, 2, 3\} \quad \forall x^0 \in \{0, \dots, X^0 - a\}, \quad (4.67)$$

i.e. the spatial zero mode is removed from the theory on each timeslice

$$A^{p\mu}|_{\vec{p}=0} = 0 \quad \forall \mu \in \{0, 1, 2, 3\} \quad \forall p^0. \quad (4.68)$$

The constraint is local in time and respects reflection positivity. Hence, the existence of a transfer matrix is guaranteed [41]. In [44] the QED_L constraint is applied to a ϕ^4 scalar field theory in order to investigate its consequences with respect to the renormalisability of higher-dimensional operators. It was observed that the required counterterms possess non-local contributions, such that the operator product expansion, the Symanzik effective-theory description of the lattice theory close to the continuum and the related improvement program break down. This leads to the assumption that an $O(a)$ -improved version of QED_L, which removes leading lattice artefacts, cannot be constructed. According to [44], it is possible to avoid these conceptual problems if one restricts the calculations to leading order considerations. In [139], it is further suggested to also modify modes beyond the spatial zero modes in order to eliminate the leading finite-volume corrections to hadron masses.

4. Lattice field theories

4.5.4. QED_M

Another approach is to regulate the divergence of the photon propagator by introducing a finite photon mass m_γ after fixing the gauge to R_ξ -gauge, similar to the procedure in continuum QED [144, 145]. In this setup, the photon difference operator reads

$$\Delta_{\text{QED}_M}^{\mu_2 \mu_1} = \left(\sum_\mu \overleftarrow{\partial}_F^\mu \overrightarrow{\partial}_F^\mu + m_\gamma^2 \right) \delta_{\mu_1}^{\mu_2} + \left(\frac{1}{\xi} - 1 \right) \overleftarrow{\partial}_F^{\mu_1} \overrightarrow{\partial}_F^{\mu_2}. \quad (4.69)$$

As QED_M employs two IR regulators, the photon mass and the finite volume, it is important to realise that the limits do not commute, which makes the extrapolation challenging. In order to recover infinite-volume QED, first one has to perform the infinite volume extrapolation of the observable and then extrapolate to vanishing photon mass. According to [44], if m_γ is too small in comparison with the lattice volume, the effective mass of charged particles will show the same problems as for QED_{TL}. In [144, 145], it is argued that hadron masses can, however, be reliably estimated in the regime $m_\gamma/m_\pi \leq 1$ and $m_\gamma L \geq 1$.

4.5.5. QED_C

So far, we have discussed solutions to the IR problem of non-compact lattice QED based on an alteration of the theory. A different approach is to modify the boundary conditions, such that large gauge transformations are spoiled. We briefly discuss QED_C [146–148], which was introduced to the lattice community after this project had been started. QED_C is defined by applying spatial C-parity boundary conditions instead of periodic boundary conditions in the spatial directions $\mu = 1, 2, 3$, i.e.

$$A^x|_{x^\mu=0} = -A^x|_{x^\mu=X^\mu}, \quad \Psi^x|_{x^\mu=0} = C^{-1}(\overline{\Psi}^x)^T|_{x^\mu=X^\mu}, \quad (4.70)$$

where $C = i\gamma^0\gamma^2$ is the charge conjugation matrix for Dirac spinors. For this choice, an argument similar to eq. (4.57) cannot be constructed, as the electric and flavour charge can flow in and out at the boundaries. However, charge and flavour symmetries are partially broken by the boundary conditions, such that charge and flavour quantum numbers are not conserved. In fact, only the quantum numbers $(-1)^Q$ and $(-1)^F$ are conserved, such that states with charges differing by multiples of 2 have non-vanishing overlap [146–148]. E.g. a Ξ^- baryon can decay into a proton [44]. The major disadvantage of QED_C is the requirement of the generation of completely new gauge ensembles, which is very costly. A code for lattice simulations of (QCD+QED)_C based on the openQCD library is available [149, 150], where isospin breaking is treated non-perturbatively.

4.6. Monte Carlo simulations for gauge theories

The large number of degrees of freedom, which have to be integrated over in order to evaluate the path integral, makes standard numerical integration methods inapplicable [42, 60]. A straightforward numerical computation using quadrature formulas is too expensive

in terms of computing time. A solution to this problem is the application of Monte Carlo integration, i.e. the integral is stochastically estimated by the average of the integrand, evaluated at randomly chosen values of the integration variable.

4.6.1. Importance sampling

The expectation value of an observable, which depends on the gauge field U , can be estimated by

$$\langle \mathcal{O}[U] \rangle \approx \frac{1}{n} \sum_{i=1}^n \exp(-S[U_i]) \mathcal{O}[U_i], \quad (4.71)$$

where the U_i are drawn from a flat distribution. This method is rather inefficient, as a gauge configuration U_i only contributes very little to the path integral if the corresponding Boltzmann weight $\exp(-S[U_i])/Z$ is small. A more efficient approach is *importance sampling*, in which the U_i are sampled according to the probability density distribution

$$dP(U) = \frac{\exp(-S[U])}{Z} DU. \quad (4.72)$$

The path integral over the gauge field U can then be approximated by a summation over the set of gauge configurations $(U_i)_{i=1,\dots,n}$:

$$\langle \mathcal{O}[U] \rangle \approx \frac{1}{n} \sum_{i=1}^n \mathcal{O}[U_i]. \quad (4.73)$$

According to the central limit theorem, the statistical error of the result scales with $1/\sqrt{n}$ [42].

4.6.2. Markov chains

The generation of gauge configurations $(U_i)_{i=1,\dots,n}$ can be performed by means of a Markov chain. Starting from a given U_1 , U_{i+1} is obtained from U_i in a Monte Carlo update step. The Markov chain is characterised by the transition probability $T(U'|U)$, which describes the probability to obtain a configuration U' from U within an update step. The Markov chain is in equilibrium if the probability distribution of the gauge configurations $P(U)$ fulfils the balance equation [42, 60]

$$\sum_U T(U'|U)P(U) = \sum_U T(U|U')P(U'). \quad (4.74)$$

A more restrictive solution to the latter equation is the detailed balance condition [42, 60]

$$T(U'|U)P(U) = T(U|U')P(U'). \quad (4.75)$$

In section 4.6.5 we present the Hybrid Monte Carlo algorithm, which is used to generate gauge configurations based on Markov chains and the detailed balance condition.

4. Lattice field theories

4.6.3. Effective gauge action

So far, we have only considered an action that depends on the gauge field U . In practice, one is interested to simulate theories with additional fields, which we described by the field Υ . We consider an action

$$S_{\Upsilon}[U, \Upsilon] = S_g[U] + S_{\Upsilon}[U, \Upsilon], \quad (4.76)$$

where $S_g[U]$ describes the self-interaction of U and $S_{\Upsilon}[U, \Upsilon]$ the remaining interactions. The theory is described by the partition function and expectation value

$$Z = \int DU D\Upsilon \exp(-S_g[U] - S_{\Upsilon}[U, \Upsilon]), \quad (4.77)$$

$$\langle \mathcal{O}[U, \Upsilon] \rangle = \frac{1}{Z} \int DU D\Upsilon \exp(-S_g[U] - S_{\Upsilon}[U, \Upsilon]) \mathcal{O}[U, \Upsilon]. \quad (4.78)$$

In the following, we assume that are able to integrate over the field Υ , i.e. we can evaluate the partition function and expectation value

$$Z_{\Upsilon}[U] = \int D\Upsilon \exp(-S_{\Upsilon}[U, \Upsilon]), \quad (4.79)$$

$$\langle \mathcal{O}[U, \Upsilon] \rangle_{\Upsilon} = \frac{1}{Z_{\Upsilon}} \int D\Upsilon \exp(-S_{\Upsilon}[U, \Upsilon]) \mathcal{O}[U, \Upsilon], \quad (4.80)$$

which both depend on the background gauge field U . Assuming that the partition function Z_{Υ} is positive, we may define the effective gauge action [151, 152]

$$S_{\text{eff}}[U] = S_g[U] - \log(Z_{\Upsilon}[U]). \quad (4.81)$$

We also define the corresponding objects of the Υ , which are defined on a background gauge field U :

$$\langle \mathcal{O}_{\text{eff}}[U] \rangle_{\text{eff}} = \frac{1}{Z_{\text{eff}}} \int DU \exp(-S_{\text{eff}}[U]) \mathcal{O}_{\text{eff}}[U], \quad (4.82)$$

$$Z_{\text{eff}} = \int DU \exp(-S_{\text{eff}}[U]). \quad (4.83)$$

By construction, the two partition functions Z and Z_{eff} are identical:

$$Z = \int DU D\Upsilon \exp(-S_g[U] - S_{\Upsilon}[U, \Upsilon]) = \int DU \exp(-S_g[U]) Z_{\Upsilon}[U] = Z_{\text{eff}}. \quad (4.84)$$

The expectation value of the full and the effective action are related through

$$\begin{aligned} \langle \mathcal{O}[U, \Upsilon] \rangle &= \frac{1}{Z} \int DU D\Upsilon \exp(-S_g[U] - S_{\Upsilon}[U, \Upsilon]) \mathcal{O}[U, \Upsilon] \\ &= \frac{1}{Z} \int DU \exp(-S_{\text{eff}}[U]) \frac{1}{Z_{\Upsilon}[U]} \int D\Upsilon \exp(-S_{\Upsilon}[U, \Upsilon]) \mathcal{O}[U, \Upsilon] \\ &= \frac{1}{Z_{\text{eff}}} \int DU \exp(-S_{\text{eff}}[U]) \langle \mathcal{O}[U, \Upsilon] \rangle_{\Upsilon} = \langle \langle \mathcal{O}[U, \Upsilon] \rangle_{\Upsilon} \rangle_{\text{eff}}, \end{aligned} \quad (4.85)$$

i.e. as a first step $\mathcal{O}_{\text{eff}}[U] = \langle \mathcal{O}[U, \Upsilon] \rangle_{\Upsilon}$ is evaluated for each value of the gauge field U and then the expectation value with respect to the effective action $\langle \mathcal{O}_{\text{eff}}[U] \rangle_{\text{eff}}$ is taken. $\mathcal{O}_{\text{eff}}[U]$ is an effective operator, which only depends on the gauge field U . The Monte Carlo estimation is now performed with respect to the effective gauge action S_{eff} . Equation (4.73) is altered to

$$\langle \mathcal{O}[U, \Upsilon] \rangle \approx \frac{1}{n} \sum_{i=1}^n \langle \mathcal{O}[U_i, \Upsilon] \rangle_{\Upsilon} \quad (4.86)$$

and the gauge configurations are generated with respect to the distribution

$$dP(U) = \frac{\exp(-S_{\text{eff}}[U])}{Z} DU = \frac{\exp(-S_g[U]) Z_{\Upsilon}[U]}{Z} DU, \quad (4.87)$$

i.e. the partition function $Z_{\Upsilon}[U]$ becomes part of the Boltzmann weight.

4.6.4. Monte Carlo simulations for fermion fields

We consider a fermion action which is bilinear in the conjugated fermionic fields Ψ and $\bar{\Psi}$, reading

$$S[\Psi, \bar{\Psi}] = \bar{\Psi}_{\mathbf{a}} D^{\mathbf{a}}_{\mathbf{b}} \Psi^{\mathbf{b}}. \quad (4.88)$$

The Dirac operator D depends on a background gauge field U , which we suppress for better readability. For this action, it is possible to formally compute the partition function Z , as the integral over the Grassmann variables can be performed algebraically [59, 151–153]:

$$Z = \int D\Psi D\bar{\Psi} \exp(-S[\Psi, \bar{\Psi}]) = \det(-D). \quad (4.89)$$

For a γ^5 -hermitian Dirac operator, e.g. the Wilson Dirac operator in eq. (4.40), the partition function is real [42]:

$$Z = \det(-D) = \det(-\gamma^5 D \gamma^5) = \det(-D^{\dagger}) = \det(-D)^* = (Z)^*. \quad (4.90)$$

To include the fermion partition function into the weight factor, as discussed in section 4.6.3, Z has to be positive. If we consider a doublet of mass-degenerate fermions with flavours 1 and 2, the Dirac operator is block-diagonal $D = \text{diag}(D_1, D_2)$ and $D_1 = D_2$. Hence, the partition function is not only real but positive semi-definite [42]:

$$\begin{aligned} Z &= \det(-D) = \det(-D_1) \det(-D_2) = (\det(-D_1))^2 \\ &= \det(-D_1) \det(-D_1^{\dagger}) = \det(D_1 D_1^{\dagger}) \geq 0. \end{aligned} \quad (4.91)$$

Assuming D has no zero eigenvalues, $\det(D_1 D_1^{\dagger})$ can be evaluated by an integration over complex bosonic fields Φ and Φ^{\dagger} , which are commonly referred to as *pseudo-fermions* [42]:

$$\det(D_1 D_1^{\dagger}) = \frac{1}{\pi^{\Lambda}} \int D\Phi D\Phi^{\dagger} \exp(-\Phi^{\dagger} (D_1 D_1^{\dagger})^{-1} \Phi). \quad (4.92)$$

4. Lattice field theories

Λ denotes the total number of lattice sites. For single fermion species with a Dirac operator D_1 , a rooting trick can be applied, assuming that the quark determinant is positive. In this case, it can be represented by an integral over pseudofermion fields, reading

$$\begin{aligned}\det(D_1) &= \det(\sqrt{D_1^2}) = \det\left(\sqrt{D_1}\sqrt{D_1^\dagger}\right) \\ &= \frac{1}{\pi^\Lambda} \int D\Phi D\Phi^\dagger \exp(-\Phi^\dagger(\sqrt{D_1}\sqrt{D_1^\dagger})^{-1}\Phi).\end{aligned}\quad (4.93)$$

Technically, $\sqrt{D_1}$ is approximated by a polynomial [154] or rational [155, 156] function in D_1 . We will discuss this in more detail in section 5.2.4. Another possibility to compute the single fermion determinant assuming a spectrum with positive real parts, which does not apply to the Wilson-Dirac operator, is discussed in [157, 158].

4.6.5. Hybrid Monte Carlo algorithm

The Hybrid Monte Carlo (HMC) algorithm [159] is a tool to generate gauge configurations $(U_i)_{i=1,\dots,n}$ for a lattice gauge theory including fermion fields. For simplicity, we assume to have a doublet of mass-degenerate Wilson fermions with a single flavour Dirac operator $D[U]$, for which the partition function $Z_\Upsilon[U]$ is positive. We understand the gauge links U as a function of the Markov time τ , which parametrises the Markov chain, and identify U_i with $U(i\Delta\tau)$. The gauge links

$$U^{x\mu} = \exp(i \sum_i Q^{x\mu i} T^i) \quad (4.94)$$

are parametrised by the real coefficients $Q^{x\mu i}$, where T^i are the generators of the gauge group. For each coordinate $Q^{x\mu i}$ a conjugate momentum $P^{x\mu i}$ is introduced. The Hamilton function of the molecular dynamics, which describes the time evolution of the coordinates Q and momenta P with respect to τ , is defined as [42]

$$H[Q, P] = \frac{1}{2} \sum_{x,\mu,i} (P^{x\mu i})^2 + S_g[U[Q]] - \phi^\dagger (D[U[Q]] (D[U[Q]])^\dagger)^{-1} \phi. \quad (4.95)$$

From the corresponding Hamilton equations one derives the equations of motion [42]

$$\frac{d}{d\tau} P^{x\mu i} = -\frac{\partial H[Q, P]}{\partial Q^{x\mu i}} = -F[U[Q], \phi]^{x\mu i}, \quad (4.96)$$

$$\frac{d}{d\tau} Q^{x\mu i} = \frac{\partial H[Q, P]}{\partial P^{x\mu i}} = P^{x\mu i} \quad (4.97)$$

with the force term [42]

$$F[U[Q], \phi]^{x\mu i} = \frac{\partial}{\partial Q^{x\mu i}} (S_g[U[Q]] + \phi^\dagger (D[U[Q]] (D[U[Q]])^\dagger)^{-1} \phi). \quad (4.98)$$

The HMC algorithm generates a new gauge configuration U_{i+1} from a gauge configuration U_i in the following way [42]: The gauge configuration $U(i\Delta\tau)$ is translated into coordinates

$Q(i\Delta\tau)$. A pseudofermion field $\phi = D\xi$ is generated, where ξ is distributed according to $\exp(-\xi^\dagger \xi)$. The initial random conjugated fields $P(i\Delta\tau)$ are drawn from a Gaussian distribution $\exp(-\text{tr } P^2)$. $Q(i\Delta\tau)$ and $P(i\Delta\tau)$ are used as initial values for the integration of the molecular dynamics equations of motion. The latter are integrated numerically over a distance $\Delta\tau$, leading to coordinates $Q((i+1)\Delta\tau)$ and momenta $P((i+1)\Delta\tau)$. From $Q((i+1)\Delta\tau)$ a new gauge configuration U_{i+1} is constructed. The numerical integrator requires the computation of the force term for each step. This is the most expensive part of the HMC algorithm, as the Dirac equation has to be solved [42]. The HMC algorithm only fulfils the detailed balance equation in eq. (4.75) if the numerical integration scheme satisfies two requirements [42]: The integration measure is area preserving and the integration scheme is reversible. A class of integration schemes, which satisfy these conditions, are leapfrog integration schemes [42]. Due to translation invariance with respect to Markov time, the value of the Hamilton function is, in principle, conserved along a solution of the equation of motion. However, the numerical integration will lead to deviations from the exact solution. To correct for this violation, a Monte Carlo accept-reject step is added to the algorithm [42]. The suggested gauge configuration U_{i+1} is only accepted if a random number r , which is drawn from the interval $[0, 1)$, satisfies

$$r < \exp(H[P_{i+1}, Q_{i+1}] - H[P_i, Q_i]). \quad (4.99)$$

The new configuration U_{i+1} is rejected otherwise. Instead, the initial gauge configuration is reused a second time, $U_{i+1} = U_i$. In order to obtain a high acceptance rate, the step size of the numerical integration scheme has to be chosen small. However, this leads to a smaller number of generated gauge configuration at equal computational cost. To find the optimal choice of parameters is non-trivial and depends on the lattice spacing, the bare masses and the lattice volume.

4.6.6. Thermalisation

The HMC algorithm has to be started from an initial gauge configuration U_0 . This can be a random gauge configuration or a gauge field, which is generated from a different HMC run with similar parameters [42]. The generated gauge configurations will not immediately fulfil the desired equilibrium probability distribution. This is only the case after a thermalisation time, which depends on the bare parameters, the lattice size and the investigated observable.

4.6.7. Monte Carlo reweighting

Depending on the specific theory, the generation of gauge configurations can be extremely computationally demanding. In particular, the consideration of dynamical fermions is computationally expensive. The reweighting method [160, 161], which we discuss in the following, was introduced by *Ferrenberg* and *Swendsen*. It allows to reuse existing gauge configurations of a gauge field U , generated with respect to an effective action $S_{\text{eff},1}$, for a similar theory with an effective action $S_{\text{eff},2}$ correcting the Boltzmann weights of the gauge configurations. In the following discussion, we only consider effective actions,

4. Lattice field theories

assuming that all degrees of freedom but the gauge field, which is sampled by the Monte Carlo simulation, have already been integrated out by the path integral. We consider two effective actions $S_{\text{eff},i}$ for $i = 1, 2$. The corresponding partition functions $Z_{\text{eff},i}$ and expectation values $\langle \mathcal{O}[U] \rangle_{\text{eff},i}$ read

$$Z_{\text{eff},i} = \int DU \exp(-S_{\text{eff},i}[U]), \quad (4.100)$$

$$\langle \mathcal{O}[U] \rangle_{\text{eff},i} = \frac{1}{Z_{\text{eff},i}} \int DU \exp(-S_{\text{eff},i}[U]) \mathcal{O}[U]. \quad (4.101)$$

The expectation value of the second action can be related to the expectation value of the first action by

$$\begin{aligned} \langle \mathcal{O}[U] \rangle_{\text{eff},2} &= \frac{\int DU \exp(-S_{\text{eff},2}[U]) \mathcal{O}[U]}{\int DU \exp(-S_{\text{eff},2}[U])} \\ &= \frac{\int DU \exp(-S_{\text{eff},1}[U]) \frac{\exp(-S_{\text{eff},2}[U])}{\exp(-S_{\text{eff},1}[U])} \mathcal{O}[U]}{\int DU \exp(-S_{\text{eff},1}[U]) \frac{\exp(-S_{\text{eff},2}[U])}{\exp(-S_{\text{eff},1}[U])}} = \frac{\langle R[U] \mathcal{O}[U] \rangle_{\text{eff},1}}{\langle R[U] \rangle_{\text{eff},1}}. \end{aligned} \quad (4.102)$$

We have introduced the reweighting factor $R[U]$, given by

$$R[U] = \frac{\exp(-S_{\text{eff},2}[U])}{\exp(-S_{\text{eff},1}[U])}, \quad (4.103)$$

which corrects for the wrong statistical weight of each gauge configuration with respect to the new action. The estimation of the reweighting factor introduces additional statistical noise. It can also be very expensive to evaluate the reweighting factor, depending on the physical content of the two theories and their difference. One typical application is the modification of bare parameters after the gauge configurations have been generated. In finite-temperature simulations, the observables have to be computed for various values of the temperature to explore the phase diagram. The temperature is related to the temporal lattice extent and therefore to the lattice spacing, which depends on the inverse coupling β . It is usually too expensive to generate gauge ensembles for each desired value of the temperature and its corresponding β , such that the inverse coupling β is altered by reweighting [162]. A chemical potential can be treated in the same way [162]. The quark masses can also be fine-tuned by means of the reweighting method [157, 163, 164]. Another example is the alteration of the entire physical theory. Non-degenerate quark masses can be introduced on isosymmetric ensembles by means of reweighting [158] or even an additional interaction such as QED [165]. This will become important in this thesis.

4.7. Systematic errors of lattice Monte Carlo simulations

In this section, we briefly discuss various potential systematic errors which accompany lattice gauge theory calculations.

Finite lattice spacing

Lattice field theory calculations compute physical observables at finite lattice spacing. A prediction at the physical point is only possible when the results from different lattice spacings are extrapolated to the continuum by means of a fit. The Symanzik improvement programme [108, 109] allows to systematically remove lattice artefacts order by order. Nevertheless, smaller lattice spacings require a larger number of lattice sites to keep the physical volume constant, which significantly increases the computational cost [42]. The rotational symmetry of the continuum theory is clearly broken by the lattice discretisation. Nevertheless, it is possible to relate irreducible representations of the octahedral group, which is the rotational symmetry group of a spatial cubic lattice, to irreducible representations of the continuum rotation group $SO(3)$ [166].

Unphysical quark masses

The relation between the bare parameters and the quantities defining the renormalisation scheme is non-trivial and can only be determined via the lattice simulation. Therefore, it is not possible to know the correct bare parameters at the physical point in advance. Simulations are commonly performed at various values of the bare parameters. To obtain results at the physical point, fits in terms of the quantities belonging to the renormalisation scheme, so-called chiral extrapolations, are performed. The required fit models can be motivated by chiral perturbation theory. In addition, lattice simulations are often performed preferably at unphysically large quark masses as the computational cost is significantly reduced [42].

Finite volume effects

Numerical results which are obtained from lattice Monte Carlo simulations suffer from finite volume effects as computer simulations can only deal with a finite number of lattice points. In principle, it is possible to simulate the same theory on systems with different box sizes to investigate the dependence on the physical volume. The extrapolation can then be performed as a fit in powers of $\frac{1}{L}$, where L describes the spatial extent of the lattice [42]. For a systematic expansion, chiral perturbation theory on finite volumes can be used [98]. Hadronic masses are altered by an interaction around the spatial torus, which leads to exponential corrections $O(\exp(-mL))$ [42] for pure QCD. This is most relevant for the smallest accessible mass of the theory, i.e. m_π . One usually chooses $m_\pi L > 4$ [45] such that finite volume corrections are negligible at the level of current statistical precisions. For simulations involving QED the situation is different. QED does not possess a spectral gap and the interaction is long-ranged. One therefore expects relevant finite size corrections depending on the simulated volume [139].

Excited state effects

Spectroscopy calculations rely on fitting procedures to correlation functions. In interacting theories, interpolation operators usually do not create a pure eigenstate of the Hamilton

4. Lattice field theories

operator when applied to the vacuum state, but a superposition of eigenstates. It is not always possible to reliably isolate the desired state, such that the value of the corresponding mass or matrix element is biased. Nevertheless, it is possible to optimise interpolation operators in a variational analysis, reducing excited state effects [42].

(Partial) Quenching of the fermion determinant and disregard of Feynman diagrams

The computation of the fermion determinant $Z_q[U]$ in the process of the gauge ensemble generation is computationally expensive. It was common to neglect the sea quark contribution in lattice Monte Carlo simulations completely, i.e. the quark determinant was set to unity, which is equivalent of having infinitely heavy sea quarks. This procedure is referred to as the *quenched approximation* [42] and leads to various unphysical results. In particular, the η' becomes a pseudo-Goldstone boson [42] as the contribution to the mass caused by the anomaly, which is related to sea quark loops [98, 105], is missing. In addition, exceptional configurations characterised by small or negative eigenvalues of the Dirac operator appear more often [42]. A further simplification in lattice simulations is to focus on Feynman diagrams, which are computationally easy to handle. The evaluation of quark-disconnected diagrams demands a much higher computational effort compared to quark-connected diagrams [42], which usually form the dominant contribution. Nevertheless, quark-disconnected diagrams are relevant to correctly predict various physical phenomena, such as the mass of the η meson and the value of the $\eta - \eta'$ mixing angle [167].

5. CLS Monte Carlo simulations for lattice QCD_{iso}

The gauge configurations used in this thesis for Monte Carlo simulations are provided by the CLS effort. They are generated with respect to a lattice gauge theory describing QCD with $N_f = 2 + 1$ dynamical quark flavours, i.e. the quark masses of the two lightest quarks are degenerate. The setup and the production strategy are discussed in [45], based on the simulation concepts introduced in [168]. In this chapter, we will briefly discuss the lattice action, give details on the treatment of fermions and the fermion determinants, describe the determination of required reweighting factors, present the renormalisation scheme and the scale setting and finally give an overview over generated gauge ensembles. This chapter mainly summarises the most important aspects of the publications [45, 168–172] and is partly inspired by the PhD thesis [65].

5.1. Action and boundary conditions

Gauge ensembles generated within the CLS effort are characterised by the following action: For the $SU(3)$ gauge fields the Lüscher-Weisz gauge action is employed, given in eq. (4.29). The fermion discretisation is based on $O(a)$ -improved Wilson fermions including the Sheikholeslami-Wohlert term, c.f. eq. (4.47). The required improvement coefficient c_{SW} is determined non-perturbatively in [172], based on the evaluation of the PCAC relation. Simulations are performed with the three quark flavours up, down and strange and degenerate up and down quark masses, i.e. the isosymmetric limit is considered.

Periodic boundary conditions are the most common choice in lattice QCD, as they preserve translational invariance. In simulations performed at smaller lattice spacings a freezing of the topological charge was observed [173], which is an integer number on periodic lattices. As a consequence, autocorrelation times grow, as the HMC algorithm is not able to sweep through many topological sectors and the representativeness of the generated gauge configurations has to be questioned. In particular, the ergodicity of the simulation algorithm cannot be assured when approaching the continuum limit [169]. A way to alleviate the topology freezing is to alter the temporal boundary conditions. In [173] the introduction of open temporal boundary conditions is suggested, imposing Dirichlet boundary conditions on components of the quark fields and demanding the colour-electric field to vanish. On this geometry, the topological charge is not an integer, but a real number, and it can flow into and out of the lattice during the HMC process, i.e. the topological barriers are removed. In the CLS effort, ensembles with both types of boundary conditions, i.e. periodic temporal and open temporal are generated. We will discuss the

5. CLS Monte Carlo simulations for lattice QCD_{iso}

two types of boundary conditions and their actual implementation in more detail in the context of combined QCD and QED in section 6.2.

5.2. Algorithmic setup

Several advanced computational techniques are applied to speed up the HMC algorithm, in particular to compute the fermion determinant, which is the most expensive part.

5.2.1. Even-odd preconditioning for light quarks

The calculation of the light quark determinant is not performed by considering the single flavour γ^5 -hermitian Dirac-Wilson operator D , but the hermitian operator [45]

$$Q = \gamma^5 D. \quad (5.1)$$

A simplification of the calculation called *even-odd preconditioning* [174] is achieved by decomposing the lattice into even and odd lattice sites

$$Q = \begin{pmatrix} Q_{ee} & Q_{eo} \\ Q_{oe} & Q_{oo} \end{pmatrix}. \quad (5.2)$$

As the operator Q involves only self-interactions and nearest neighbour interactions Q_{ee} and Q_{oo} are diagonal matrices for which both the inverse and the diagonal can directly be calculated. In order to calculate the determinant of Q it is convenient to decomposed Q further into

$$Q = \begin{pmatrix} 1 & Q_{eo}(Q_{oo})^{-1} \\ 0 & 1 \end{pmatrix} \begin{pmatrix} \hat{Q} & 0 \\ 0 & Q_{oo} \end{pmatrix} \begin{pmatrix} 1 & 0 \\ (Q_{oo})^{-1}Q_{oe} & 1 \end{pmatrix}, \quad (5.3)$$

where we have introduced the asymmetric even-odd preconditioned Schur complement

$$\hat{Q} = Q_{ee} - Q_{eo}(Q_{oo})^{-1}Q_{oe}. \quad (5.4)$$

Making use of the fact that the determinants of the leftmost and rightmost matrices in the above decomposition are unity, the squared quark determinant can be written as a product of squared determinants of Q_{oo} and of the Schur complement \hat{Q} [45]:

$$\det(Q^2) = \det((Q_{oo})^2) \det(\hat{Q}^2). \quad (5.5)$$

The determination of $\det(\hat{Q}^2)$ is computationally simplified compared to $\det(Q^2)$ as \hat{Q}^2 is an operator on a lattice with only half the number of sites.

5.2.2. Twisted mass reweighting for light quarks

The Wilson Dirac operator does not only possess eigenvalues equal or larger than the bare quark mass. Consequently, field space is divided by surfaces of zero eigenvalue, which

cannot be crossed by the HMC algorithm due to the infinite action [45]. The introduction of a small twisted mass term makes the spectrum of the Wilson Dirac operator strictly positive. In addition, it reduces the fluctuations of the forces to be integrated, such that a larger step widths in the HMC integrator can be applied and therefore makes the simulations cheaper and more reliable. The squared light quark determinant is written as [45]

$$\det(Q^2) = \det((Q_{\text{oo}})^2) \det(\hat{Q}^2) = W_0 \det((Q_{\text{oo}})^2) \det\left(\frac{\hat{Q}^2 + \mu_0^2}{\hat{Q}^2 + 2\mu_0^2}\right) \det(\hat{Q}^2 + \mu_0^2), \quad (5.6)$$

where we have introduced the twisted-mass reweighting factor

$$W_0 = \det\left(\frac{(\hat{Q}^2 + 2\mu_0^2)\hat{Q}^2}{(\hat{Q}^2 + \mu_0^2)^2}\right) \quad (5.7)$$

that compensates for the twisted mass term. A larger choice of the twisted-mass parameter μ_0 leads to a more stable performance of the HMC algorithm as force fluctuations are removed but reintroduces larger fluctuations in the reweighting factor. W_0 is removed from the quark action used to generate the gauge configurations. To correct for the wrong statistical weight of the generated gauge configurations due to the altered quark action a reweighting according to section 4.6.7 is performed, where W_0 appears as the reweighting factor. W_0 is later stochastically estimated by means of pseudofermion fields [45].

5.2.3. Factorisation of the light quark determinant

A further reduction of the fluctuation of the forces in the HMC algorithm can be achieved by a determinant factorisation [175] with different values for the twisted masses [176]. The twisted mass quark determinant is decomposed as [45]

$$\det(\hat{Q}^2 + \mu_0^2) = \det(\hat{Q}^2 + \mu_n^2) \prod_{i=1}^n \det\left(\frac{\hat{Q}^2 + \mu_{i-1}^2}{\hat{Q}^2 + \mu_i^2}\right) \quad (5.8)$$

with $\mu_0 < \dots < \mu_n$. Each determinant is estimated by its own pseudofermion field. Hence, the integrator step width in the HMC algorithm can be optimised for each pseudofermion force and larger step widths become feasible. The values were chosen with equal distance on the logarithmic scale and can be found in [45].

5.2.4. Rational approximation of strange quark determinant

The quark determinant for the strange quark has to be treated differently compared to the doublet of light quarks, for which the combined light quark determinant is considered. The strange quark determinant is evaluated by approximating the square root of \hat{Q}^2 by a rational function [155, 156] with n_p poles [45]

$$\det(Q) = \det(Q_{\text{oo}}) \det(\sqrt{\hat{Q}^2}) = \det(Q_{\text{oo}}) \det\left(A^{-1} \prod_{i=1}^{n_p} \frac{\hat{Q}^2 + \bar{\mu}_i^2}{\hat{Q}^2 + \bar{\nu}_i^2}\right) W_1 \quad (5.9)$$

5. CLS Monte Carlo simulations for lattice QCD_{iso}

with an optimal choice of the parameters $\bar{\nu}_i$ and $\bar{\mu}_i$ and $\bar{\mu}_1 < \dots < \bar{\mu}_{n_p}$. In addition, a reweighting factor W_1 has to be introduced, which absorbs the inaccuracy of the rational approximation. Similar to the twisted-mass reweighting factor W_0 for the light quark determinant, W_1 is removed from the simulated action and later reintroduced by reweighting. It is also estimated by means of pseudofermion fields. The determinant of the rational function is further split into several factors [45]:

$$\det \left(\prod_{i=1}^{n_p} \frac{\hat{Q}^2 + \bar{\mu}_i^2}{\hat{Q}^2 + \bar{\nu}_i^2} \right) = \prod_{i=1}^{n'_p} \det \left(\frac{\hat{Q}^2 + \bar{\mu}_i^2}{\hat{Q}^2 + \bar{\nu}_i^2} \right) \det \left(\prod_{i=n'_p+1}^{n_p} \frac{\hat{Q}^2 + \bar{\mu}_i^2}{\hat{Q}^2 + \bar{\nu}_i^2} \right). \quad (5.10)$$

The first n'_p terms with smallest $\bar{\mu}_i$, $i = 1, \dots, n'_p$ are evaluated by individual pseudofermion fields, whereas the determinant of the remaining factors is evaluated by a single pseudofermion field. Again, this determinant factorisation allows for an optimisation of the HMC algorithm with respect to the step width applied, when integrating individual pseudofermion forces. As mentioned above, the Wilson Dirac operator can possess negative eigenvalues. Consequently, the determinant can have a negative sign on particular gauge configurations. It is possible to correct for this sign, investigating the spectrum of the Dirac operator on each gauge configuration [177] and including the missing sign in the reweighting factor W_1 . This issue is absent for the light quark determinant, as a pair of degenerate quarks is considered.

5.2.5. Integration of molecular dynamics

Gauge and fermion forces vary over several orders of magnitude and their evaluation is of different computational effort. To achieve a high acceptance rate of the gauge configuration it is computationally more efficient to treat individual forces in the HMC, which we have discussed in section 4.6.5, by suitable integration schemes [178]. For the generation of CLS gauge ensembles, a three-level integration scheme is applied [45, 169]. They are integrated by the first-level integrator, which is based in a forth-order integration scheme by Omelyan, Mryglod and Folk (OMF) [179]. Due to the large magnitude of the gauge forces, the step width has to be chosen small and hence, a high number of evaluations of the forces has to be performed. This is computationally feasible, as the gauge forces are cheap to compute. The majority of the fermion forces is treated by the second-level integrator, which is also based on a forth-order OMF integration scheme. Due to the costly evaluation of the fermion forces, the step is chosen larger compared to the first-level integrator. Small components of the fermion forces are treated by the third-level integrator, which integrates with the largest step width and is based on a second-order OMF integration scheme.

5.2.6. Solver

In order to compute the fermionic forces in the HMC algorithm, the Dirac equation $D\Psi = \eta$ has to be solved for Ψ for a given source η . The computation of a solution by means of a direct method is computationally too demanding due to the large system size. Hence,

iterative solvers have to be applied. Aiming for smaller quark masses am , one observes that the condition number of the Dirac operator increases, which is reflected by a rise in the iteration count [169]. Several methods were developed to speed up the numerical determination of the solution. For the generation of CLS gauge ensembles, a locally deflated solver [180] is applied. Deflation techniques remove the lowest eigenmodes of the Dirac operator from the Dirac equation. On the deflation subspace spanned by the lowest eigenmodes, the system can be solved exactly. The iterative solver is only used to determine the solution on the complementary subspace. It was observed that when the lattice volume is increased, the number of considered lowest eigenmodes has to be increased to keep the condition number of the Dirac operator fixed [169, 180]. However, the exact determination of a larger number of eigenmodes is computationally too expensive for large lattices. The computational cost can be reduced when a domain-decomposed deflation subspace is used, i.e. the eigenmodes are computed on local sublattices, approximating the global eigenmodes [180]. A further improvement is obtained from the application of the Schwarz alternating procedure as a preconditioner of the Dirac equation [181]. The deflated, Schwarz preconditioned Dirac equation is then solved by means of the generalized conjugate residual (GCR) algorithm [181], which belongs to the class of Krylov subspace solvers and is mathematically equivalent to the generalized minimal residual methods (GMRES) [182].

5.3. Renormalisation scheme, chiral trajectory and scale setting

In order to relate the bare parameters of the lattice action with observables determined in experiments, a hadronic renormalisation scheme is utilised. For a given strong inverse coupling β , the bare quark masses are tuned such that the observables included in the hadronic renormalisation scheme take their physical values. Commonly, gauge ensembles with different sets of bare parameters are generated and the theory predictions, determined on each ensemble, are then extrapolated to the physical point. The lattice spacing corresponding to the value of β is determined by relating an additional dimensionful observable to its experimental value. In the following, we present the strategy applied for the generation of CLS gauge ensembles [45].

5.3.1. Renormalisation scheme

The isosymmetric pion and kaon masses are used as a hadronic renormalisation scheme in order to determine the bare quark masses. Lattices with different lattice spacings are matched via the dimensionless quantities [45]

$$\phi_2 = 8t_0 m_\pi^2, \quad \phi_4 = 8t_0 \left(m_K^2 + \frac{1}{2} m_\pi^2 \right), \quad (5.11)$$

where the scale t_0 is the Wilson flow parameter [183, 184], discussed later in this chapter. In leading chiral perturbation theory, these two quantities can be related to the quark masses and are proportional to sums of those, $\phi_2 \propto (m_u + m_d)$ and $\phi_4 \propto (m_u + m_d + m_s)$ [45].

5. CLS Monte Carlo simulations for lattice QCD_{iso}

The physical point is characterised by the masses of the pion and kaon in the isosymmetric limit without electromagnetic contributions [45], reading

$$m_\pi^{\text{phys}} = 134.8(3) \text{ MeV}, \quad m_K^{\text{phys}} = 494.2(4) \text{ MeV}. \quad (5.12)$$

These values can be translated into

$$\phi_2^{\text{phys}} = 0.0801(27), \quad \phi_4^{\text{phys}} = 1.117(38). \quad (5.13)$$

5.3.2. Chiral trajectory

As the CLS setup is based on an $O(a)$ -improved action, the bare strong coupling g also has to be improved. The bare improved coupling g_I in terms of the bare coupling g reads [45]

$$g_I^2 = g^2 \left(1 + \frac{1}{3} b_g a \sum_f (m_f - m_{\text{cr}}) \right). \quad (5.14)$$

In order to keep the lattice spacing constant, when varying the bare quark masses, the improved coupling constant has to be kept fixed. However, the improvement coefficient b_g is not known non-perturbatively [45]. The improved coupling stays constant, if the bare quark masses are varied on a trajectory, implicitly defined by the equation [45]

$$\sum_{f=u,d,s} m_f = 3 m_{\text{sym}} \quad (5.15)$$

with $m_u = m_d$, i.e. the kaon mass becomes a function of the pion mass and vice versa. This trajectory can be uniquely characterised by the bare quark mass at the $SU(3)$ symmetric point m_{sym} .

5.3.3. Scale setting

As computer calculations are always performed in dimensionless units, only dimensionless quantities such as am , where m is a mass and a denotes the lattice spacing, are accessible. In order to give to a a physical meaning, and consequently to be able to extract a dimensionful mass m from the simulation, a has to be related to an experimentally determined observable. A common possibility is based on an additional hadron mass, m_H , such that $a = (am_H)(m_H^{\text{phys}})^{-1}$ and am_H is determined in a lattice simulation. Alternatively, other dimensionful quantities, e.g. decay constants, can be used.

The scale setting of the CLS ensembles relies on a more elaborated procedure described in [171]. This procedure is performed in two steps. In a first step, a physical observable, namely a combination of decay constants of the pion f_π and the kaon f_K

$$f_{\pi K} = \frac{2}{3} \left(f_K + \frac{1}{2} f_\pi \right) \quad (5.16)$$

based on the decay constants [45]

$$f_\pi^{\text{phys}} = 130.4(2) \text{ MeV}, \quad f_K^{\text{phys}} = 156.2(7) \text{ MeV} \quad (5.17)$$

5.4. CLS $N_f = 2 + 1$ gauge ensembles

is related to a theory scale, the Wilson flow parameter t_0 [183, 184]. Theory scales such as t_0 , w_0 or the Sommer parameter r_0 [185], which have no physical counterpart, usually have the advantage that they can be easily determined in simulations with high statistical precision [186]. The dimensionless quantities $\sqrt{t_0}/a$ and $af_{\pi K}$ are determined on each ensemble. The product $\sqrt{t_0}f_{\pi K}$ is dimensionless and independent of a . Combining the results from different ensembles, a chiral extrapolation to physical pion and kaon masses is performed, resulting in $(\sqrt{t_0}f_{\pi K})^{\text{phys}}$. In order to obtain $\sqrt{t_0^{\text{phys}}}$, $f_{\pi K}^{\text{phys}}$ is used as experimental input:

$$\sqrt{t_0^{\text{phys}}} = \frac{(\sqrt{t_0}f_{\pi K})^{\text{phys}}}{f_{\pi K}^{\text{phys}}}. \quad (5.18)$$

The result is given by [171]

$$\sqrt{8t_0^{\text{phys}}} = 0.415(4)(2) \text{ fm}. \quad (5.19)$$

Alternatively, one may use the Wilson flow parameter determined at the symmetric point [171],

$$\sqrt{8t_0^{\text{sym}}} = 0.413(5)(1) \text{ fm}, \quad (5.20)$$

which is compatible with $\sqrt{8t_0^{\text{phys}}}$ within errors, i.e. t_0 changes very mildly along the chiral trajectory. Therefore, one may in practice omit the determination of t_0/a^2 for each ensemble and just use the value computed at the symmetric point t_0^{sym}/a^2 for a given value of β . The lattice spacing a in physical units is finally obtained from

$$a = \sqrt{\frac{t_0^{\text{sym}}}{t_0^{\text{sym}}/a^2}}. \quad (5.21)$$

We give the results for t_0^{sym}/a^2 and a as a function of β in the next section.

5.4. CLS $N_f = 2 + 1$ gauge ensembles

During the years, a large set of CLS $N_f = 2 + 1$ gauge ensembles has been generated [45]. The parameters used for these ensembles are listed in table 5.1. The dimensionless Wilson flow time t_0^{sym}/a^2 and the lattice spacings a as a function of the inverse strong coupling β are listed in table 5.2. An overview over the gauge ensembles with respect to the pion mass and the lattice spacing is displayed in fig. 5.1. The generation of additional gauge ensembles with physical light- and strange-quark masses is in progress [188]. In addition to the gauge ensembles with $\text{tr } M = \text{const}$, ensembles with fixed strange quark mass and $N_f = 3$ ensembles with completely degenerated quark masses have been produced [189, 190], which we, however, do not use in this thesis. Nevertheless, a second chiral trajectory is beneficial to cross-check extrapolation strategies.

5. CLS Monte Carlo simulations for lattice QCD_{iso}

id	β	$L^3 \times T$	a [fm]	κ_l	κ_s	m_π [MeV]	m_K [MeV]	$m_\pi L$	L [fm]
H101	3.40	$32^3 \times 96$	0.08636	0.136760	0.136760	416(5)	416(5)	5.8	2.8
H102		$32^3 \times 96$		0.136865	0.13654934	354(5)	438(4)	5.0	2.8
H105		$32^3 \times 96$		0.136970	0.13634079	284(4)	460(4)	3.9	2.8
N101		$48^3 \times 128$		0.136970	0.13634079	282(4)	460(4)	5.9	4.1
C101		$48^3 \times 96$		0.137030	0.13622204	221(2)	472(8)	4.7	4.1
B450	3.46	$32^3 \times 64$	0.07634	0.136890	0.136890	416(4)	416(4)	5.2	2.4
S400		$32^3 \times 128$		0.136984	0.13670239	351(4)	438(5)	4.3	2.4
N401		$48^3 \times 128$		0.137062	0.13654808	287(4)	462(5)	5.3	3.7
D450		$64^3 \times 128$		0.137126	0.13642042	217(3)	476(6)	5.4	4.9
H200	3.55	$32^3 \times 96$	0.06426	0.137000	0.137000	419(5)	419(5)	4.4	2.1
N202		$48^3 \times 128$		0.137000	0.137000	410(5)	410(5)	6.4	3.1
N203		$48^3 \times 128$		0.137080	0.13684028	345(4)	441(5)	5.4	3.1
N200		$48^3 \times 128$		0.137140	0.13672086	282(3)	463(5)	4.4	3.1
D200		$64^3 \times 128$		0.137200	0.13660175	200(2)	480(5)	4.2	4.1
E250		$96^3 \times 192$		0.137233	0.13653663	130(1)	488(5)	4.1	6.2
N300	3.70	$48^3 \times 128$	0.04981	0.137000	0.137000	421(4)	421(4)	5.1	2.4
N302		$48^3 \times 128$		0.137064	0.13687218	346(4)	458(5)	4.2	2.4
J303		$64^3 \times 192$		0.137123	0.13675466	257(3)	476(5)	4.2	3.2

Table 5.1.: β , lattice layout $L^3 \times T$, lattice spacing a , hopping parameters κ_l and κ_s for light and strange quarks, pion and kaon masses m_π and m_K , $m_\pi L$ as a measure for QCD finite volume effects and physical extent L of the simulated volume of various CLS 2+1 flavour ensembles. Table taken from [187] and extended by the entry D450.

β	t_0^{sym}/a^2	a [fm]
3.4	2.860(11)(03)	$0.08636(98)_{\text{st}}(40)_{\text{sys}}[106]_{\text{tot}}$
3.46	3.659(16)(03)	$0.07634(92)_{\text{st}}(31)_{\text{sys}}[97]_{\text{tot}}$
3.55	5.164(18)(03)	$0.06426(74)_{\text{st}}(17)_{\text{sys}}[76]_{\text{tot}}$
3.7	8.595(29)(02)	$0.04981(56)_{\text{st}}(10)_{\text{sys}}[57]_{\text{tot}}$

Table 5.2.: Dimensionless Wilson flow time t_0^{sym}/a^2 at the symmetric point and lattice spacing a as a function of the inverse strong coupling β from [171]. The total error is determined by adding the statistical and the systematic errors in quadrature. Only the total error is considered in this work.

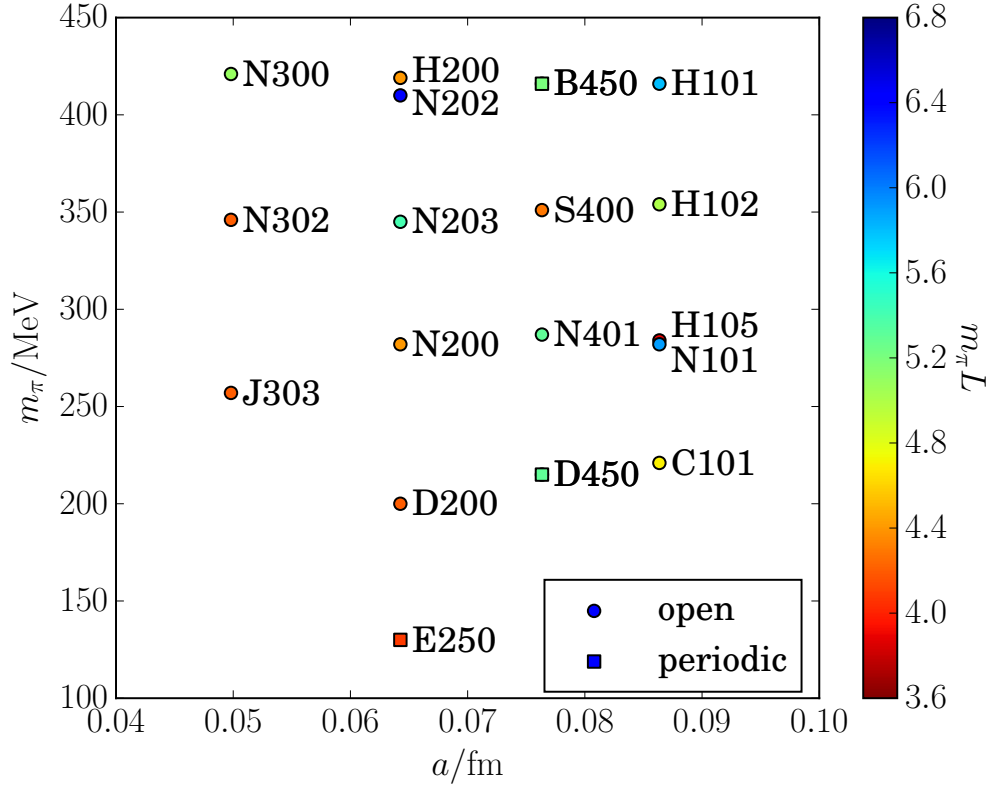


Figure 5.1.: Pion mass m_π , lattice spacing a and $m_\pi L$ as a measure for QCD finite volume effects of various CLS 2+1 flavour ensemble.

6. Lattice QCD+QED

In this chapter, we introduce the setup for QCD+QED lattice Monte Carlo simulations performed in this thesis, which is based on the discussions in chapters 4 and 5. We specify the QCD+QED action and describe the boundary conditions. We introduce the relevant symmetries of lattice QCD+QED and discuss Ward-Takahashi identities. We relate QCD+QED to QCD_{iso} by reweighting and further expand QCD+QED perturbatively around QCD_{iso} [46, 143]. We derive a set of corresponding Feynman rules to investigate leading isospin breaking effects. We formulate QED_L [41, 44, 140] on a lattice with open temporal boundary conditions [173] and derive the Fourier representation of the free photon propagator for Feynman and Coulomb gauge on periodic temporal and open temporal boundary conditions. Similar computations of QCD+QED, which are based on twisted mass, domain wall and staggered fermions, are performed by the *RM123* collaboration [46, 143, 191, 192], the *RBC-UKQCD* collaboration [193–199] and the *BMW* collaboration [200], respectively.

6.1. Lattice QCD+QED action

The lattice action for QCD+QED, which is employed in this thesis, is oriented at the QCD_{iso} action used to generate the CLS gauge ensembles. It is constructed so that in the isosymmetric limit the QCD_{iso} action is restored. We split the action S into components

$$S[U, A, \Psi, \bar{\Psi}] = S_g[U] + S_\gamma[A] + S_q[U, A, \Psi, \bar{\Psi}], \quad (6.1)$$

where S_g describes the QCD gauge action with the QCD gauge links U , S_γ the QED_L gauge action with the photon field A and S_q the quark action with the quark and antiquark fields Ψ and $\bar{\Psi}$. Considering only the lightest three quark flavours, the theory is characterised by the five bare parameters

$$\varepsilon = (m_u, m_d, m_s, \beta, e^2). \quad (6.2)$$

Later, we want to apply weak coupling perturbation theory for isospin breaking effects. Hence, we use e^2 as a parameter instead of the corresponding inverse squared coupling. For the QCD gauge action S_g we use the Lüscher-Weisz gauge action, described in eq. (4.29), which is predetermined by the setup of the gauge ensembles generated within the CLS effort. We utilise a non-compact lattice photon action and use the QED_L prescription to regularise the manifest IR divergence, as discussed in section 4.5.3. The QED_L action including a gauge fixing term is given by the bilinear form

$$S_\gamma[A] = \frac{1}{2} A_{\mathbf{c}_2} \Delta^{\mathbf{c}_2}{}_{\mathbf{c}_1} A^{\mathbf{c}_1}. \quad (4.55)$$

6. Lattice QCD+QED

The QED_L constraint to the photon field reads

$$\sum_{\vec{x}} A^{x\mu} = 0 \quad \mu \in \{0, 1, 2, 3\} \quad \forall x^0. \quad (4.67)$$

We consider two different types of gauges: Feynman gauge, which is easy to implement due to its simple structure, and Coulomb gauge, for which a transfer matrix can be constructed [41]. We add a gauge fixing term $S_{\gamma\text{gf}}$ to the photon action:

$$\begin{aligned} S_\gamma[A] &= \frac{1}{4} \sum_x \sum_{\mu_1, \mu_2} F^{x\mu_1\mu_2} F^{x\mu_1\mu_2} + S_{\gamma\text{gf}}[A] \\ &= \frac{1}{2} \sum_x \sum_{\mu_1, \mu_2} \left((A^{\mu_1} \overleftarrow{\partial}_F^{\mu_2})^x (\overrightarrow{\partial}_F^{\mu_2} A^{\mu_1})^x - (A^{\mu_1} \overleftarrow{\partial}_F^{\mu_2})^x (\overrightarrow{\partial}_F^{\mu_1} A^{\mu_2})^x \right) + S_{\gamma\text{gf}}[A]. \end{aligned} \quad (6.3)$$

We have used the discretised photon field strength tensor

$$F^{\mu_1\mu_2} = \overrightarrow{\partial}_F^{\mu_1} A^{\mu_2} - \overrightarrow{\partial}_F^{\mu_2} A^{\mu_1}. \quad (4.54)$$

To obtain Feynman gauge, the gauge fixing term is chosen as [97]

$$S_{\gamma\text{gf}}[A] = \frac{1}{2} \sum_x \left(\sum_\mu (\overrightarrow{\partial}_B^\mu A^\mu)^x \right)^2 = \frac{1}{2} \sum_x \sum_{\mu_1, \mu_2} (A^{\mu_1} \overleftarrow{\partial}_F^{\mu_2})^x (\overrightarrow{\partial}_F^{\mu_1} A^{\mu_2})^x. \quad (6.4)$$

We used partial integrations to transform $\overrightarrow{\partial}_B^\mu$ into $\overrightarrow{\partial}_F^\mu$. Combining eqs. (6.3) and (6.4), we can read off the photon difference operator Δ in Feynman gauge:

$$\Delta^{\mu_2}_{\mu_1} = \left(\sum_\mu \overleftarrow{\partial}_F^\mu \overrightarrow{\partial}_F^\mu \right) \delta_{\mu_1}^{\mu_2}. \quad (6.5)$$

The Coulomb gauge condition is a constraint to the photon field: $\overrightarrow{\partial}_B^\mu A^\mu = 0$. To enforce strict Coulomb gauge, we use the gauge fixing term for generalised Coulomb gauge:

$$S_{\gamma\text{gf}}[A] = \frac{1}{2\xi} \sum_x \left(\sum_{\mu \neq 0} (\overrightarrow{\partial}_B^\mu A^\mu)^x \right)^2 = \frac{1}{2\xi} \sum_x \sum_{\mu_1, \mu_2 \neq 0} (A^{\mu_1} \overleftarrow{\partial}_F^{\mu_2})^x (\overrightarrow{\partial}_F^{\mu_1} A^{\mu_2})^x. \quad (6.6)$$

ξ denotes the gauge fixing parameter. In the limit $\xi \rightarrow 0$, the exponential of the gauge fixing term creates a delta distribution in the path integral such that the photon field obeys $\overrightarrow{\partial}_B^\mu A^\mu = 0$. Combining eqs. (6.3) and (6.6), the photon difference operator Δ in generalised Coulomb gauge becomes

$$\begin{aligned} \Delta^{\mu_2}_{\mu_1} &= \left(\begin{array}{cccc} \sum_{\mu \neq 0} \overleftarrow{\partial}_F^\mu \overrightarrow{\partial}_F^\mu & -\overleftarrow{\partial}_F^1 \overrightarrow{\partial}_F^0 & -\overleftarrow{\partial}_F^2 \overrightarrow{\partial}_F^0 & -\overleftarrow{\partial}_F^3 \overrightarrow{\partial}_F^0 \\ -\overleftarrow{\partial}_F^0 \overrightarrow{\partial}_F^1 & \sum_\mu \overleftarrow{\partial}_F^\mu \overrightarrow{\partial}_F^\mu & & \\ -\overleftarrow{\partial}_F^0 \overrightarrow{\partial}_F^2 & & \sum_\mu \overleftarrow{\partial}_F^\mu \overrightarrow{\partial}_F^\mu & \\ -\overleftarrow{\partial}_F^0 \overrightarrow{\partial}_F^3 & & & \sum_\mu \overleftarrow{\partial}_F^\mu \overrightarrow{\partial}_F^\mu \end{array} \right)^{\mu_2}_{\mu_1} \\ &\quad + \left(\frac{1}{\xi} - 1 \right) \left(\begin{array}{ccc} 0 & \overleftarrow{\partial}_F^1 \overrightarrow{\partial}_F^1 & \overleftarrow{\partial}_F^2 \overrightarrow{\partial}_F^1 & \overleftarrow{\partial}_F^3 \overrightarrow{\partial}_F^1 \\ \overleftarrow{\partial}_F^1 \overrightarrow{\partial}_F^2 & \overleftarrow{\partial}_F^2 \overrightarrow{\partial}_F^2 & \overleftarrow{\partial}_F^3 \overrightarrow{\partial}_F^2 & \\ \overleftarrow{\partial}_F^1 \overrightarrow{\partial}_F^3 & \overleftarrow{\partial}_F^2 \overrightarrow{\partial}_F^3 & \overleftarrow{\partial}_F^3 \overrightarrow{\partial}_F^3 & \end{array} \right)^{\mu_2}_{\mu_1}. \end{aligned} \quad (6.7)$$

6.2. Boundary conditions

The lattice discretisation for the quark fields is also predetermined by the CLS setup, i.e. in the isosymmetric limit an $O(a)$ -improvement Wilson fermion action has to be reobtained. In order to introduce the electromagnetic interaction, we replace the QCD gauge links $U^{x\mu}$ in the Dirac operator by the combined gauge links [41]

$$W^{x\mu} = U^{x\mu} \exp(i a e Q A^{x\mu}). \quad (6.8)$$

The quark action is given in bilinear form as

$$S_q[U, A, \Psi, \bar{\Psi}] = \bar{\Psi}_{\mathbf{a}} D[U, A]_{\mathbf{a}\mathbf{b}} \Psi_{\mathbf{b}} \quad (6.9)$$

with the Wilson-Dirac operator

$$\begin{aligned} D[U, A] = & \frac{1}{4} \sum_{\mu} \left((\vec{D}_{\mathbf{F}}^{\mu} - \overleftarrow{D}_{\mathbf{B}}^{\mu})(\gamma^{\mu} + \mathbb{1}) + (\vec{D}_{\mathbf{B}}^{\mu} - \overleftarrow{D}_{\mathbf{F}}^{\mu})(\gamma^{\mu} - \mathbb{1}) \right) \\ & + M + c_{\text{SW}} a \sum_{\mu_1 < \mu_2} \frac{1}{2} \sigma^{\mu_1 \mu_2} \hat{F}_{\mathbf{s}}^{\mu_1 \mu_2}. \end{aligned} \quad (6.10)$$

The lattice covariant derivatives, defined in eqs. (4.32) and (4.33) depend on the combined gauge links W . The discretisation of the QCD field strength tensor $\hat{F}_{\mathbf{s}}$ only depends on the QCD gauge links U . The matrix of fractional quark charges and the mass matrix are given by $Q = \text{diag}(q_u, q_d, q_s)$ and $M = \text{diag}(m_u, m_d, m_s)$. The value of the Sheikholeslami-Wohlert coefficient c_{SW} is adopted from QCD_{iso}. Hence, this action is only $O(a)$ -improved for QCD_{iso}, i.e. a deviation from QCD_{iso} leads to a violation of the $O(a^2)$ -convergence to the continuum. To obtain a fully $O(a)$ -improved action, one in principle has to add an additional QED Sheikholeslami-Wohlert term, which depends on the electromagnetic field strength tensor. A corresponding Sheikholeslami-Wohlert coefficient has to be introduced and the improvement coefficients recomputed.

6.2. Boundary conditions

We will perform Monte Carlo simulations on lattices with two different types of boundary conditions, which we will discuss in the following. The spacetime manifold $[0, T] \times \mathbb{T}_L^3$ describes a continuous spacetime with fixed temporal boundary conditions, whereas $S_T^1 \times \mathbb{T}_L^3$ possesses (anti-)periodic boundary conditions depending on the field type. In both cases the boundary conditions in spatial directions are periodic. We consider a lattice discretisation of $[0, T] \times \mathbb{T}_L^3$ and of $S_T^1 \times \mathbb{T}_L^3$ of the form

$$\Lambda = \{x \in \mathbb{R}^4 | x^{\mu} = a n^{\mu}, n^{\mu} \in \{0, 1, \dots, N^{\mu} - 1\}, \mu \in \{0, 1, 2, 3\}\}. \quad (6.11)$$

The lattice layout is determined by the software package openQCD [73], which is used to generate CLS gauge configuration [45]. We will now further specify both types of boundary conditions. In particular, the boundary conditions will become relevant when we derive the free lattice photon propagator in sections 6.7 and 6.8.

6. Lattice QCD+QED

6.2.1. Spatial boundary conditions

For the spatial directions $\mu \in \{1, 2, 3\}$, we make use of periodic boundary conditions. The extent in spatial directions reads [73]

$$L = X^\mu = aN^\mu \quad \mu = 1, 2, 3. \quad (6.12)$$

i.e. we have to specify the values of the fields at $x^\mu = -a$ and $x^\mu = X^\mu$. All fields are continued periodically [73], i.e.

$$U^x|_{x^\mu=-a} = U^x|_{x^\mu=X^\mu-a}, \quad U^x|_{x^\mu=X^\mu} = U^x|_{x^\mu=0}, \quad (6.13)$$

$$A^x|_{x^\mu=-a} = A^x|_{x^\mu=X^\mu-a}, \quad A^x|_{x^\mu=X^\mu} = A^x|_{x^\mu=0}, \quad (6.14)$$

$$\Psi^x|_{x^\mu=-a} = \Psi^x|_{x^\mu=X^\mu-a}, \quad \Psi^x|_{x^\mu=X^\mu} = \Psi^x|_{x^\mu=0}, \quad (6.15)$$

$$\bar{\Psi}^x|_{x^\mu=-a} = \bar{\Psi}^x|_{x^\mu=X^\mu-a}, \quad \bar{\Psi}^x|_{x^\mu=X^\mu} = \bar{\Psi}^x|_{x^\mu=0}. \quad (6.16)$$

6.2.2. (Anti-)periodic temporal boundary conditions

One possible choice for the temporal direction $\mu = 0$, which we consider in this thesis, are periodic boundary conditions for bosonic fields and anti-periodic boundary conditions for fermionic fields. The extent of the lattice in the temporal direction is given by [73]

$$T = X^0 = aN^0, \quad (6.17)$$

i.e. we have to specify the values of the fields at $x^0 = -a$ and $x^0 = X^0$. We continue bosonic fields periodically [73],

$$U^x|_{x^0=-a} = U^x|_{x^0=X^0-a}, \quad U^x|_{x^0=X^0} = U^x|_{x^0=0}, \quad (6.18)$$

$$A^x|_{x^0=-a} = A^x|_{x^0=X^0-a}, \quad A^x|_{x^0=X^0} = A^x|_{x^0=0}, \quad (6.19)$$

and fermionic fields anti-periodically [73],

$$\Psi^x|_{x^0=-a} = -\Psi^x|_{x^0=X^0-a}, \quad \Psi^x|_{x^0=X^0} = -\Psi^x|_{x^0=0}, \quad (6.20)$$

$$\bar{\Psi}^x|_{x^0=-a} = -\bar{\Psi}^x|_{x^0=X^0-a}, \quad \bar{\Psi}^x|_{x^0=X^0} = -\bar{\Psi}^x|_{x^0=0}. \quad (6.21)$$

6.2.3. Open temporal boundary conditions

The second option are open temporal boundary conditions, for which the temporal extent is reduced by one unit [73], reading

$$T = X^0 - a = a(N^0 - 1), \quad (6.22)$$

i.e. we have to specify the values of the fields at $x^0 = -a$ and $x^0 = X^0 - a$. Open boundary conditions are imposed by demanding that the colour electrical field, which itself is not an observable, vanishes at the temporal boundaries [173], i.e.

$$F_s^{x0\mu}|_{x^0=-a} = 0, \quad F_s^{x0\mu}|_{x^0=X^0-a} = 0 \quad (6.23)$$

6.2. Boundary conditions

for $\mu = 1, 2, 3$. As the continuum QCD field strength tensor F_s transforms under a gauge transformation according to $\mathfrak{G}_\Omega[F^{x\mu_2\mu_1}] = \Omega^x F^{x\mu_2\mu_1}(\Omega^x)^\dagger$, this boundary condition is QCD gauge invariant [173]. In terms of gauge links, open temporal boundary conditions are imposed by vanishing gauge links at the temporal boundaries [73]:

$$U^{x0\mu}|_{x^0=-a} = 0, \quad U^{x0\mu}|_{x^0=X^0-a} = 0. \quad (6.24)$$

In analogy to the boundary condition for the QCD gauge fields, we demand that the components of the electromagnetic field strength tensor $F^{\mu_2\mu_1} = \vec{\partial}_F^{\mu_2} A^{\mu_1} - \vec{\partial}_F^{\mu_1} A^{\mu_2}$, which represent the electric field, vanish at the temporal boundaries, i.e.

$$F^{x0\mu}|_{x^0=-a} = 0, \quad F^{x0\mu}|_{X^0-a} = 0 \quad (6.25)$$

for $\mu = 1, 2, 3$. This choice will lead to a consistent and rigorous extension of QCD defined on open boundary conditions [173]. The boundary conditions for the field strength tensor can be satisfied by imposing homogeneous Dirichlet boundary conditions on the temporal component A^0 and homogeneous Neumann boundary conditions on the spatial components A^μ for $\mu = 1, 2, 3$

$$A^{x0}|_{x^0=-a} = 0, \quad A^{x0}|_{x^0=X^0-a} = 0, \quad (6.26)$$

$$(\vec{\partial}_F^0 A^\mu)^x|_{x^0=-a} = 0, \quad (\vec{\partial}_F^0 A^\mu)^x|_{x^0=X^0-a} = 0. \quad (6.27)$$

We can easily check that the electric components of $F^{x0\mu}$ for $\mu = 1, 2, 3$ vanish at the temporal boundary:

$$\begin{aligned} F^{x0\mu}|_{x^0=-a, X^0-a} &= (\vec{\partial}_F^0 A^\mu)^x|_{x^0=-a, X^0-a} - (\vec{\partial}_F^\mu A^0)^x|_{x^0=-a, X^0-a} \\ &= (\vec{\partial}_F^0 0)|_{x^0=-a, X^0-a} - 0 = 0. \end{aligned} \quad (6.28)$$

The imposition of the boundary conditions on the vector potential is a partial gauge fixing. Hence, one should in principle prove, that a vector field, for which the boundary conditions of the field strength tensor are satisfied, can be gauge transformed such that the boundary conditions eqs. (6.26) and (6.27) hold. In order to introduce open temporal boundary conditions for quark and antiquark fields one defines the projectors [73, 173]

$$P_\pm^0 = \frac{1}{2}(\mathbb{1} \pm \gamma^0). \quad (6.29)$$

The boundary conditions read

$$P_+^0 \Psi^x|_{x^0=0} = 0, \quad P_-^0 \Psi^x|_{x^0=X^0-a} = 0, \quad (6.30)$$

$$\bar{\Psi}^x P_-^0|_{x^0=0} = 0, \quad \bar{\Psi}^x P_+^0|_{x^0=X^0-a} = 0. \quad (6.31)$$

One can show that the state represented by the fields $\Psi, \bar{\Psi}, U$ and A evaluated at the temporal boundary is invariant under QCD gauge transformations, spatial rotations, the parity transformation, time reflection and the vector flavour transformations [173, 201], which we will discuss in the next section 6.3, i.e. the boundary state has the same quantum numbers as the vacuum state [173]. Open boundary conditions spoil the $O(a)$ -improved QCD_{iso} action. Nevertheless, it is possible to alter the action at the temporal boundaries to restore $O(a)$ -improvement. We refer to [73, 173] for further details.

6.3. Symmetries of lattice QCD+QED

In this section, we discuss spacetime and internal symmetries of lattice QCD+QED, i.e. Euclidean reflections, spatial parity and time reflection, translational invariance, the charge conjugation symmetry and flavour symmetries.

6.3.1. Charge conjugation

The charge conjugation transformation is a field transformation which maps fields to their anti-fields including additional phases and vice versa. Uncharged fields are eigenfunctions of the charge conjugation transformation. The latter acts on the elementary fields according to [42, 72]

$$\mathfrak{C}[(U^{\mu x}, A^{x\mu}, \Psi^x, \bar{\Psi}^x)] = \left((U^{\mu x})^{\dagger T}, -A^{x\mu}, C^{-1}(\bar{\Psi}^x)^T, -(\Psi^x)^T C \right), \quad (6.32)$$

where we made use of the charge conjugation matrix

$$C = i\gamma^0\gamma^2. \quad (3.35)$$

This transformation is a symmetry of the QCD+QED action. It is compatible with both periodic and open temporal boundary conditions and leaves the path integral measure invariant. For a discussion for lattice QCD with Wilson fermions we refer to [42]. A proof for QCD+QED can be performed in an analogous manner.

6.3.2. Euclidean reflections, spatial parity and time reflection

For a more compact and convenient notation in the following discussion we define the symbol $(-1)^{\mu_2\mu_1}$

$$(-1)^{\mu_2\mu_1} = \begin{cases} 1 & \text{for } \mu_2 = \mu_1 \\ -1 & \text{for } \mu_2 \neq \mu_1 \end{cases}. \quad (6.33)$$

For periodic boundary ensembles, the Euclidean reflection \mathfrak{P}^μ transforms a coordinate tuple x according to

$$(\mathfrak{P}^\mu(x))^\nu = (-1)^{\mu\nu} x^\nu, \quad (6.34)$$

i.e. all components of the coordinates but the μ -th component are reflected. The definition holds modulo the lattice extent in periodic directions. For open temporal boundary conditions, $\mathfrak{P}^{\mu \neq 0}$ reflects with respect to the time slice located in the middle of the temporal direction. The Euclidean reflection is self-inverse $(\mathfrak{P}^\mu)^{-1} = \mathfrak{P}^\mu$. We demand that the elementary lattice fields transform under \mathfrak{P}^μ according to [42]

$$\begin{aligned} \mathfrak{P}^\mu[\Psi^x] &= \gamma^\mu \Psi^{\mathfrak{P}^\mu(x)}, & \mathfrak{P}^\mu[\bar{\Psi}^x] &= \bar{\Psi}^{\mathfrak{P}^\mu(x)} \gamma^\mu, \\ \mathfrak{P}^\mu[U^{x\nu}] &= (U^{\mathfrak{P}^\mu(x)-a\hat{\nu},\nu})^\dagger \quad \forall \nu \neq \mu, & \mathfrak{P}^\mu[A^{x\nu}] &= -A^{\mathfrak{P}^\mu(x)-a\hat{\nu},\nu} \quad \forall \nu \neq \mu, \\ \mathfrak{P}^\mu[U^{x\mu}] &= U^{\mathfrak{P}^\mu(x)\mu}, & \mathfrak{P}^\mu[A^{x\mu}] &= A^{\mathfrak{P}^\mu(x)\mu}. \end{aligned} \quad (6.35)$$

6.4. Ward-Takahashi identities in lattice QCD+QED

It can be shown that this transformation is in fact a symmetry of the action and that it leaves the path integral measure invariant. For a proof for pure QCD we again refer to [42]. The spatial parity transformation \mathfrak{P} and the time reversal transformation \mathfrak{T} can be expressed in terms of concatenations of Euclidean reflections:

$$\mathfrak{P} = \mathfrak{P}^0, \quad \mathfrak{T} = \mathfrak{P}^1 \mathfrak{P}^2 \mathfrak{P}^3. \quad (6.36)$$

According to [173], open boundary conditions were designed such that they are compatible with parity symmetry and time reflection symmetry.

6.3.3. Translation invariance

As periodic boundary conditions are applied in the spatial directions, the theory is invariant under spatial translations. Consequently, spatial momentum is a conserved quantity. The same holds for (anti-)periodic boundary conditions in the time direction. However, open temporal boundary conditions break the translational invariance in the time direction.

6.3.4. Flavour symmetries and conserved charges

We have discussed flavour symmetries in great detail for the continuum QCD+QED action in section 3.4. As the Wilson lattice discretisation of fermions breaks the axial symmetry explicitly, only the vector symmetries remain. For the latter class of symmetries the same results hold as derived in section 3.4.

6.4. Ward-Takahashi identities in lattice QCD+QED

We have derived two Ward-Takahashi identities for continuum QCD+QED in section 3.5. The question, whether the Ward identities are altered, naturally arises when we introduce a lattice regularisation for a quantum field theory. In fact, both the vector and the axial Ward identity will change significantly. The naive point-like vector-current, known from continuum field theory, does not satisfy the lattice identity. It is, however, possible to define a lattice discretisation of the continuum vector current, which fulfils a Ward identity. For lattice QCD with Wilson fermions it is known that no partially conserved axial current can be defined [202]. Therefore, we only focus on the vector Ward identity.

6.4.1. Vector Ward identity

In order to derive the vector Ward identity for lattice QCD+QED we consider the same class of field transformations as in the continuum

$$\mathfrak{T}[\varepsilon][(U, A, \Psi, \bar{\Psi})]^x = (U, A, \exp(iT\varepsilon^x)\Psi^x, \bar{\Psi}^x \exp(-iT\varepsilon^x)) \quad (3.83)$$

with a Hermitian generator T acting on flavour indices of the quark fields and a scalar field ε . We can directly evaluate the transformation behaviour of the path integral measure as

6. Lattice QCD+QED

we work in the regularised theory, where the path integral measure is meaningful. As we have defined the theory on a finite spacetime lattice, the path integral measure is in fact the measure of an ordinary multi-dimensional integral. Hence, the Jacobian of the field transformation is a finite-dimensional matrix and its determinant is well defined. The path integral measure is invariant under this transformation as in the continuum eq. (3.84), i.e. there is no contribution from the Jacobian to the Ward identity:

$$\frac{\delta}{\delta \varepsilon^x} \det \left(\frac{\delta \mathfrak{T}[\varepsilon][\Upsilon]}{\delta \Upsilon} \right) \Big|_{\varepsilon=0} = 0. \quad (6.37)$$

The contribution from the derivative of the action, defined in eqs. (6.9) and (6.10), is given by

$$\begin{aligned} \frac{\delta S[\mathfrak{T}[\varepsilon][\Upsilon]]}{\delta \varepsilon^x} \Big|_{\varepsilon=0} = & -i \left(\frac{1}{4} \sum_{\mu=0}^3 \left((\bar{\Psi}(\overleftarrow{D}_F^\mu - \overrightarrow{D}_B^\mu) T (\mathbb{1} + \gamma^\mu) \Psi)^x \right. \right. \\ & + (\bar{\Psi} T (\overleftarrow{D}_B^\mu - \overrightarrow{D}_F^\mu) (\mathbb{1} - \gamma^\mu) \Psi)^x \\ & \left. \left. - \bar{\Psi}^x [M, T] \Psi^x \right) \right). \end{aligned} \quad (6.38)$$

In order to be able to define a conserved vector current we rewrite the former expression in terms of commutators and anticommutators of the covariant derivatives and T :

$$\begin{aligned} \frac{\delta S[\mathfrak{T}[\varepsilon][\Upsilon]]}{\delta \varepsilon^x} \Big|_{\varepsilon=0} = & -i \left(\frac{1}{4} \sum_{\mu=0}^3 \left((\bar{\Psi} \{ \overleftarrow{D}_F^\mu - \overrightarrow{D}_B^\mu, T \} (\gamma^\mu + \mathbb{1}) \Psi)^x \right. \right. \\ & + (\bar{\Psi} \{ \overrightarrow{D}_F^\mu - \overleftarrow{D}_B^\mu, T \} (\gamma^\mu - \mathbb{1}) \Psi)^x \\ & - \bar{\Psi}^x [M, T] \Psi^x \\ & - \frac{1}{4} \sum_{\mu=0}^3 \left((\bar{\Psi} [\overrightarrow{D}_B^\mu - \overleftarrow{D}_F^\mu, T] (\gamma^\mu + \mathbb{1}) \Psi)^x \right. \\ & \left. \left. + (\bar{\Psi} (\gamma^\mu - \mathbb{1}) [\overrightarrow{D}_F^\mu - \overleftarrow{D}_B^\mu, T] \Psi)^x \right) \right). \end{aligned} \quad (6.39)$$

The first part of eq. (6.39) can now be expressed as a derivative of a lattice discretisation of the vector current

$$\begin{aligned} & \frac{1}{4} \sum_{\mu=0}^3 \left((\bar{\Psi} \{ \overleftarrow{D}_F^\mu - \overrightarrow{D}_B^\mu, T \} (\gamma^\mu + \mathbb{1}) \Psi)^x + (\bar{\Psi} \{ \overrightarrow{D}_F^\mu - \overleftarrow{D}_B^\mu, T \} (\gamma^\mu - \mathbb{1}) \Psi)^x \right) \\ & = \sum_{\mu=0}^3 \left(\frac{1}{4} \left(\bar{\Psi}^{x+a\hat{\mu}} \{ (W^{x\mu})^\dagger, T \} (\gamma^\mu + \mathbb{1}) \Psi^x + \bar{\Psi}^x \{ W^{x\mu}, T \} (\gamma^\mu - \mathbb{1}) \Psi^{x+a\hat{\mu}} \right) \right. \\ & \quad \left. - \frac{1}{4} \left(\bar{\Psi}^x \{ (W^{x-a\hat{\mu},\mu})^\dagger, T \} (\gamma^\mu + \mathbb{1}) \Psi^{x-a\hat{\mu}} + \bar{\Psi}^{x-a\hat{\mu}} \{ W^{x-a\hat{\mu},\mu}, T \} (\gamma^\mu - \mathbb{1}) \Psi^x \right) \right) \\ & = \sum_{\mu=0}^3 (\overrightarrow{\partial}_B^\mu \mathcal{V}_F^\mu)^x = \sum_{\mu=0}^3 (\overrightarrow{\partial}_F^\mu \mathcal{V}_B^\mu)^x, \end{aligned} \quad (6.40)$$

6.4. Ward-Takahashi identities in lattice QCD+QED

where we have introduced the forward point-split vector current \mathcal{V}_F reading

$$\begin{aligned}\mathcal{V}_F^{x\mu} &= \frac{1}{4} \left(\bar{\Psi}^{x+a\hat{\mu}} \{ (W^{x\mu})^\dagger, T \} (\gamma^\mu + \mathbb{1}) \Psi^x + \bar{\Psi}^x \{ W^{x\mu}, T \} (\gamma^\mu - \mathbb{1}) \Psi^{x+\mu} \right) \\ &= \frac{1}{4} \left(\bar{\Psi}^{x+a\hat{\mu}} (U^{x\mu})^\dagger \{ \exp(-iaeQA^{x\mu}), T \} (\gamma^\mu + \mathbb{1}) \Psi^x \right. \\ &\quad \left. - \bar{\Psi}^x U^{x\mu} \{ \exp(iaeQA^{x\mu}), T \} (\gamma^\mu - \mathbb{1}) \Psi^{x+\mu} \right)\end{aligned}\quad (6.41)$$

and the backward point-split vector current \mathcal{V}_B which is just a displaced forward point-split vector current:

$$\mathcal{V}_B^{x\mu} = \mathcal{V}_F^{x-a\hat{\mu},\mu}. \quad (6.42)$$

These definitions fulfil the correct classical continuum limit for both flavour diagonal and flavour non-diagonal vector currents in the presence of QED. For vanishing electromagnetic quark charges $Q = 0$, the anticommutators in eq. (6.41) equal $2T$ and we reobtain the standard definition of the partially conserved vector current in QCD [42, 202]. In order to understand the meaning of the third part of eq. (6.39), we express it in terms of gauge links:

$$\begin{aligned}& \frac{1}{4} \sum_{\mu=0}^3 \left((\bar{\Psi} [\vec{D}_B^\mu - \overleftarrow{D}_F^\mu, T] (\gamma^\mu + \mathbb{1}) \Psi)^x + \bar{\Psi}^x (\gamma^\mu - \mathbb{1}) ([\vec{D}_F^\mu - \overleftarrow{D}_B^\mu, T] \Psi)^x \right) \\ &= \frac{1}{4} \sum_{\mu=0}^3 \left(\bar{\Psi}^{x+a\hat{\mu}} [T, (W^{x\mu})^\dagger] (\gamma^\mu + \mathbb{1}) \Psi^x + \bar{\Psi}^x [W^{x\mu}, T] (\gamma^\mu - \mathbb{1}) \Psi^{x+a\hat{\mu}} \right. \\ &\quad \left. + \bar{\Psi}^x [T, (W^{x-a\hat{\mu},\mu})^\dagger] (\gamma^\mu + \mathbb{1}) \Psi^{x-a\hat{\mu}} + \bar{\Psi}^{x-a\hat{\mu}} [W^{x-a\hat{\mu},\mu}, T] (\gamma^\mu - \mathbb{1}) \Psi^x \right) \\ &= \frac{1}{4} \sum_{\mu=0}^3 \left(\bar{\Psi}^{x+a\hat{\mu}} (U^{x\mu})^\dagger [T, \exp(-iaeQA^{x\mu})] (\gamma^\mu + \mathbb{1}) \Psi^x \right. \\ &\quad + \bar{\Psi}^x U^{x\mu} [\exp(iaeQA^{x\mu}), T] (\gamma^\mu - \mathbb{1}) \Psi^{x+a\hat{\mu}} \\ &\quad + \bar{\Psi}^x (U^{x-a\hat{\mu},\mu})^\dagger [T, \exp(-iaeQA^{x-a\hat{\mu},\mu})] (\gamma^\mu + \mathbb{1}) \Psi^{x-a\hat{\mu}} \\ &\quad \left. + \bar{\Psi}^{x-a\hat{\mu}} U^{x-a\hat{\mu},\mu} [\exp(iaeQA^{x-a\hat{\mu},\mu}), T] (\gamma^\mu - \mathbb{1}) \Psi^x \right) \\ &= i\mathcal{X}^x.\end{aligned}\quad (6.43)$$

The operator \mathcal{X}^x defined above is in fact a lattice discretisation of the continuum operator $eA_e^{x\mu} \bar{\Psi}^x \gamma^\mu [Q, T] \Psi^x$, which we find in eq. (3.86). We combine all intermediate results with eq. (2.22) and obtain the vector Ward identity for lattice QCD+QED, which reads

$$\left\langle \sum_{\mu=0}^3 (\vec{\partial}_B^\mu \mathcal{V}_F^\mu)^x \mathcal{O}[\Upsilon] \right\rangle = \left\langle (\bar{\Psi}^x [M, T] \Psi^x + iX^x) \mathcal{O}[\Upsilon] + i \frac{\delta \mathcal{O}[\mathfrak{T}[\varepsilon][\Upsilon]]}{\delta \varepsilon^x} \Big|_{\varepsilon=0} \right\rangle. \quad (6.44)$$

We observe that the vector Ward identity on the lattice has the same form as in the continuum eq. (3.87), however with replaced operators. For vanishing electromagnetic quark

6. Lattice QCD+QED

charges $Q = 0$, we have $\mathcal{X} = 0$, such that we reobtain the standard lattice QCD vector Ward identity [42, 202]. Considering transformations for which T is flavour diagonal, the expression for the vector current can be simplified to

$$\mathcal{V}_F^{x\mu} = \frac{1}{2} \left(\bar{\Psi}^{x+a\hat{\mu}} (W^{x\mu})^\dagger T (\gamma^\mu + \mathbb{1}) \Psi^x + \bar{\Psi}^x W^{x\mu} T (\gamma^\mu - \mathbb{1}) \Psi^{x+\mu} \right). \quad (6.45)$$

Comparing eq. (6.41) with eq. (6.45), we see that we have removed the anti-commutators, as the gauge links W and the matrices T commute. We find that the expectation value of flavour-neutral currents is also conserved in combined lattice QCD and QED up to contact terms:

$$\left\langle \sum_{\mu=0}^3 (\vec{\partial}_B^\mu \mathcal{V}_F^\mu)^x \mathcal{O}[\Upsilon] \right\rangle = \left\langle i \frac{\delta \mathcal{O}[\mathfrak{T}[\varepsilon][\Upsilon]]}{\delta \varepsilon^x} \Big|_{\varepsilon=0} \right\rangle. \quad (6.46)$$

Our annotations with regard to the renormalisation of the electromagnetic charge in continuum QCD+QED in section 3.5.1 do also apply for lattice QCD+QED. Consequently, in a tree-level lattice QED calculation, the vacuum polarisation is absent and the electromagnetic coupling does not renormalise even in the presence of full lattice QCD.

6.5. Relating QCD+QED and QCD_{iso} via reweighting

For our QCD+QED calculation we want to make use of existing QCD_{iso} gauge configurations generated by the CLS effort discussed in chapter 5. In order to relate QCD+QED to QCD_{iso}, we make use of Monte Carlo reweighting introduced in section 4.6.7 as first suggested in [46, 143] for the twisted-mass lattice fermion discretisation [132, 133]. Although we apply the concept developed in the latter publications, we formulate the following derivations and results in a different way that allows for an easier interpretation of the individual components of equations as well as for the straightforward definition of Feynman rules.

6.5.1. QCD+QED and QCD_{iso}

Starting from the lattice QCD+QED action

$$S[U, A, \Psi, \bar{\Psi}] = S_g[U] + S_\gamma[A] + S_q[U, A, \Psi, \bar{\Psi}], \quad (6.1)$$

we define the partition function and expectation value

$$Z = \int DU DAD\Psi D\bar{\Psi} \exp(-S[U, A, \Psi, \bar{\Psi}]), \quad (6.47)$$

$$\langle \mathcal{O}[U, A, \Psi, \bar{\Psi}] \rangle = \frac{1}{Z} \int DU DAD\Psi D\bar{\Psi} \exp(-S[U, A, \Psi, \bar{\Psi}]) \mathcal{O}[U, A, \Psi, \bar{\Psi}]. \quad (6.48)$$

6.5. Relating QCD+QED and QCD_{iso} via reweighting

The action eq. (6.1) representing QCD+QED like theories can be parametrised by the tuple ε [46, 143], which contains the bare quark masses, the squared inverse strong coupling and the squared electromagnetic coupling:

$$\varepsilon = (m_u, m_d, m_s, \beta, e^2). \quad (6.2)$$

A particular type of QCD+QED like theories is formed by QCD_{iso} theories, with an additional free, decoupled photon field. These theories are characterised by the choice of parameters

$$\varepsilon^{(0)} = (m_{ud}^{(0)}, m_{ud}^{(0)}, m_s^{(0)}, \beta^{(0)}, 0), \quad (6.49)$$

i.e. the light quarks have the same bare mass $m_u^{(0)} = m_d^{(0)} = m_{ud}^{(0)}$ and the electromagnetic coupling vanishes $(e^2)^{(0)} = 0$, such that the quarks lose their electromagnetic charge. As a consequence, the light quarks also have the same renormalised quark mass. As the relation between the bare and the renormalised strong coupling constant is different in QCD_{iso} compared to QCD+QED, it is reasonable to also allow for an altered value of the bare inverse strong coupling $\beta^{(0)}$.

6.5.2. Reweighting

In principle, it is possible to generate gauge ensembles of the combined QCD+QED introduced in this chapter. The *BMW* collaboration followed this approach with the staggered fermion discretisation to compute the proton-neutron mass difference from first principles [41]. However, this strategy is computationally demanding, as the generation of gauge ensembles accounts for a large amount of the total computer time. Hence, it is reasonable to use a computational strategy that allows for the reuse of existing QCD_{iso} gauge ensembles. The idea to introduce the electromagnetic interaction on existing unquenched QCD gauge ensembles by means of the reweighting technique [160, 161], as described in section 4.6.7, was already suggested in 2004 by [165]. The first lattice QCD+QED simulations were performed in the quenched approximation by *Duncan, Eichten and Thacker* [141, 142] in 1996, neglecting sea-quark effects. In this setup, QCD and QED gauge configurations can be generated independently. The gauge configurations are only combined at the stage when the valence-quark propagator is computed. Later efforts were based on unquenched QCD combined with quenched QED [203, 204], which still allows for an independent generation of gauge configurations. The CLS gauge configurations possess mass-degenerate up and down quarks. Consequently, the reweighting should not only introduce the electromagnetic interaction but also allow for an alteration of the quark masses, as suggested in [157, 163, 164]. The strong gauge action should also be reweighted to absorb the shift in the inverse strong coupling. This overall strategy was first used by the *RM123* collaboration [46, 143].

In the following, we derive the reweighting factor that relates QCD+QED to QCD_{iso} for the lattice action used in this thesis. The existing QCD_{iso} gauge configurations are generated with respect to the effective isosymmetric gauge action

$$S_{\text{eff}}^{(0)}[U] = S_g^{(0)}[U] - \log(Z_q^{(0)}[U]), \quad (6.50)$$

6. Lattice QCD+QED

which is used to evaluate the expectation value

$$\langle \mathcal{O}[U] \rangle_{\text{eff}}^{(0)} = \frac{1}{Z_{\text{eff}}^{(0)}} \int DU \exp(-S_{\text{eff}}^{(0)}[U]) \mathcal{O}[U]. \quad (6.51)$$

$Z_{\text{eff}}^{(0)}$ and $Z_{\text{q}}^{(0)}[U]$ denote the partition functions corresponding to the isosymmetric effective gauge action $S_{\text{eff}}^{(0)}$ and to a free isosymmetric fermion theory on a fixed gauge background U with action $S_{\text{q}}^{(0)}$, respectively:

$$Z_{\text{eff}}^{(0)} = \int DU \exp(-S_{\text{eff}}^{(0)}[U]), \quad (6.52)$$

$$Z_{\text{q}}^{(0)}[U] = \int D\Psi D\bar{\Psi} \exp(-S_{\text{q}}^{(0)}[U, \Psi, \bar{\Psi}]). \quad (6.53)$$

Our aim is to express the expectation of QCD+QED eq. (6.48) in terms of the expectation value of the effective isosymmetric gauge action eq. (6.51). In order to introduce the photon field into our calculation and allow for arbitrary quark masses, we define a partition function $Z_{\text{q}\gamma}[U]$ in analogy to eq. (6.53) and the corresponding expectation value, which now describes quarks and photons on a given gauge background U ,

$$Z_{\text{q}\gamma}[U] = \int DAD\Psi D\bar{\Psi} \exp(-S_{\gamma}[A] - S_{\text{q}}[U, A, \Psi, \bar{\Psi}]), \quad (6.54)$$

$$\langle \mathcal{O}[U, A, \Psi, \bar{\Psi}] \rangle_{\text{q}\gamma} = \frac{1}{Z_{\text{q}\gamma}[U]} \int DAD\Psi D\bar{\Psi} \exp(-S_{\gamma}[A] - S_{\text{q}}[U, A, \Psi, \bar{\Psi}]) \cdot \mathcal{O}[U, A, \Psi, \bar{\Psi}]. \quad (6.55)$$

Defining the effective gauge action with respect to the perturbed gauge action and the partition function $Z_{\text{q}\gamma}[U]$,

$$S_{\text{eff}}[U] = S_{\text{g}}[U] - \log(Z_{\text{q}\gamma}[U]), \quad (6.56)$$

we introduce the partition function and the corresponding expectation value

$$Z_{\text{eff}} = \int DU \exp(-S_{\text{eff}}[U]), \quad (6.57)$$

$$\langle \mathcal{O}[U] \rangle_{\text{eff}} = \frac{1}{Z_{\text{eff}}} \int DU \exp(-S_{\text{eff}}[U]) \mathcal{O}[U]. \quad (6.58)$$

From the last definitions we immediately see that we can reobtain the QCD+QED parti-

tion function and the corresponding expectation value given in eqs. (6.47) and (6.48):

$$\begin{aligned} Z_{\text{eff}} &= \int DU \exp(-S_g[U]) Z_{q\gamma}[U] \\ &= \int DUDAD\Psi D\bar{\Psi} \exp(-S[U, A, \Psi, \bar{\Psi}]) = Z, \end{aligned} \quad (6.59)$$

$$\begin{aligned} \langle \langle \mathcal{O}[U, A, \Psi, \bar{\Psi}] \rangle_{q\gamma} \rangle_{\text{eff}} &= \frac{1}{Z_{\text{eff}}} \int DU \exp(-S_g[U]) Z_{q\gamma}[U] \langle \mathcal{O}[U, A, \Psi, \bar{\Psi}] \rangle_{q\gamma} \\ &= \frac{1}{Z} \int DUDAD\Psi D\bar{\Psi} \exp(-S[U, A, \Psi, \bar{\Psi}]) \mathcal{O}[U, A, \Psi, \bar{\Psi}] \\ &= \langle \mathcal{O}[U, A, \Psi, \bar{\Psi}] \rangle. \end{aligned} \quad (6.60)$$

Having two effective actions $S_{\text{eff}}^{(0)}[U]$ in eq. (6.50) and $S_{\text{eff}}[U]$ in eq. (6.56), which belong to distinct physical theories with the same gauge field U , we are now just in the situation discussed in section 4.6.7, when we introduced the reweighting technique. Equation (4.102) allows us to relate these two theories via

$$\langle \mathcal{O}[U, A, \Psi, \bar{\Psi}] \rangle = \langle \langle \mathcal{O}[U, A, \Psi, \bar{\Psi}] \rangle_{q\gamma} \rangle_{\text{eff}} = \frac{\langle R[U] \langle \mathcal{O}[U, A, \Psi, \bar{\Psi}] \rangle_{q\gamma} \rangle_{\text{eff}}^{(0)}}{\langle R[U] \rangle_{\text{eff}}^{(0)}}. \quad (6.61)$$

According to eq. (4.103), the reweighting factor is given by the ratio of the Boltzmann weights of the two theories:

$$R[U] = \frac{\exp(-S_{\text{eff}}[U])}{\exp(-S_{\text{eff}}^{(0)}[U])} = \frac{\exp(-S_g[U]) Z_{q\gamma}[U]}{\exp(-S_g^{(0)}[U]) Z_q^{(0)}[U]}. \quad (6.62)$$

The latter factor replaces the Boltzmann weight of the unperturbed strong gauge action $\exp(-S_g^{(0)}[U])$ by the Boltzmann weight of the perturbed strong gauge action $\exp(-S_g[U])$ and the partition function $Z_q^{(0)}[U]$ of a free and isosymmetric fermionic theory on a background gauge field U by the partition function $Z_{q\gamma}[U]$ describing QED on a background gauge field U .

6.5.3. Determination of the reweighting factor and the inner expectation value

The ratio of Boltzmann weights $\frac{\exp(-S_g[U])}{\exp(-S_g^{(0)}[U])}$ in eq. (6.62) can be computed directly, as it is cheap to evaluate the two actions S_g and $S_g^{(0)}$ on a given gauge configuration U . In contrast, the determination of the expectation value $\langle \mathcal{O}[U, A, \Psi, \bar{\Psi}] \rangle_{q\gamma}$ and the ratio of partition functions $\frac{Z_{q\gamma}[U]}{Z_q^{(0)}[U]}$ is rather involved and computationally non-trivial. There are in principle two options: The two quantities can either be evaluated using stochastic estimators [157, 163–165] or by means of a perturbative expansion as suggested in [46, 143]. A common simplification is to neglect isospin breaking effects in the sea-quark sector, which is known as the electro-quenched setup [203, 204]. This is equivalent to assume

6. Lattice QCD+QED

$Z_{q\gamma}[U] = Z_q^{(0)}[U] Z_\gamma^{(0)}$, where $Z_\gamma^{(0)} = \int DA \exp(-S_\gamma^{(0)}[A])$ is the partition function of the free photon field. In this thesis, we treat isospin breaking effects perturbatively, as they are expected to be of small magnitude. A major advantage is, that we can work in leading order in e^2 , such that we can avoid having to deal with the renormalisation of the electromagnetic coupling.

6.6. Feynman rules for QCD+QED as a perturbation of QCD_{iso}

As discussed in the previous section, we treat isospin breaking effects in the framework of weak coupling perturbation theory [46, 143]. In order to evaluate $\langle \mathcal{O}[U, A, \Psi, \bar{\Psi}] \rangle_{q\gamma}$ in eq. (6.61) and $R[U]$ given in eq. (6.62), we expand the latter expressions in terms of $\Delta\varepsilon = \varepsilon - \varepsilon^{(0)}$ around $\varepsilon^{(0)}$. Our aim is to formulate Feynman rules that allow for a diagrammatic representation of the expansions of $\langle \mathcal{O}[U, A, \Psi, \bar{\Psi}] \rangle_{q\gamma}$ and $R[U]$. First, we define the quark and photon propagators in the isosymmetric theory. In order to derive expressions for the vertices, we expand the Wilson-Dirac operator around its isosymmetric counterpart. To be able to construct Feynman diagrams, we introduce corresponding graphical representations for propagators and vertices. As usual, for each closed fermion loop and for each crossing of fermion lines we have to multiply the amplitude by a factor of -1 . We also have to divide by the appropriate symmetry factor of the diagram. We finally determine the expansion of the reweighting factor $R[U]$ and discuss the expansion of a generic correlation function.

6.6.1. Isosymmetric quark and photon propagators

We use the standard graphical representations for the isosymmetric quark propagator on a fixed gauge background U

$$S^{(0)}[U]_{\mathbf{a}}^{\mathbf{b}} = (D^{(0)}[U]^{-1})_{\mathbf{a}}^{\mathbf{b}} = \begin{array}{c} \mathbf{b} \longrightarrow \longleftarrow \mathbf{a} \end{array} \quad (6.63)$$

and for the photon propagator

$$\Sigma_{\mathbf{c}_1}^{\mathbf{c}_2} = (\Delta^{-1})_{\mathbf{c}_1}^{\mathbf{c}_2} = \mathbf{c}_2 \text{---}\text{wavy line}\text{---}\mathbf{c}_1. \quad (6.64)$$

We will give more details on how we compute the isosymmetric quark propagator in section 7.1 and the photon propagator in sections 6.7 and 6.8.

6.6.2. Expansion of the Wilson-Dirac operator

For the definition of vertices involving quark fields, we expand the Wilson-Dirac operator $D[U, A]$ of QCD+QED defined in eq. (6.10) around the Wilson-Dirac operator $D^{(0)}[U]$ of QCD_{iso}. Formally, this expansion reads

$$\begin{aligned} D[U, A]_{\mathbf{b}}^{\mathbf{a}} &= D^{(0)}[U]_{\mathbf{b}}^{\mathbf{a}} - \sum_f \Delta m_f V_{\bar{q}qf}[U]_{\mathbf{b}}^{\mathbf{a}} \\ &\quad - e V_{\bar{q}q\gamma}[U]_{\mathbf{b}\mathbf{c}}^{\mathbf{a}} A^{\mathbf{c}} - \frac{1}{2} e^2 V_{\bar{q}q\gamma\gamma}[U]_{\mathbf{b}\mathbf{c}_2\mathbf{c}_1}^{\mathbf{a}} A^{\mathbf{c}_2} A^{\mathbf{c}_1} + O(e^3), \end{aligned} \quad (6.65)$$

6.6. Feynman rules for QCD+QED as a perturbation of QCD_{iso}

which implicitly defines the quark-antiquark vertex $V_{\bar{q}qf}$, photon-quark-antiquark vertex $V_{\bar{q}q\gamma}$ and the 2-photon-quark-antiquark vertex $V_{\bar{q}q\gamma\gamma}$. Due to the exponential form of the QED gauge links $\exp(iaeqA)$, we find contributions to the electromagnetic interaction to all orders in e . This is typical for lattice perturbation theory calculations. A truncation of this expansion has to be consistent with the order of the entire calculation [97]. We truncate the expansion at $O(e^3)$ as we are only interested in leading isospin breaking effects, i.e. in contributions up to order e^2 . The minus sign introduced in front of the vertices in eq. (6.65) is due to the minus sign in the Boltzmann weight factor $\exp(-S)$ in Euclidean spacetime. In Minkowskian spacetime factors of i and $-i$ would appear instead. The factor $\frac{1}{2}$ in front of $V_{\bar{q}q\gamma\gamma}$ ensures the correct determination of the symmetry factor in Feynman diagrams. We represent the vertices by the diagrams

$$V_{\bar{q}qf}[U]_{\mathbf{b}}^{\mathbf{a}} = \text{a} \leftarrow \overset{f}{\bullet} \leftarrow \text{b} , \quad (6.66)$$

$$V_{\bar{q}q\gamma}[U]^a{}_{bc} = \begin{array}{c} c \\ | \\ a \leftarrow \bullet \leftarrow b \end{array}, \quad (6.67)$$

$$V_{\bar{q}q\gamma\gamma}[U]^{\mathbf{a}}_{\mathbf{bc_2c_1}} = \text{Diagram} \quad (6.68)$$

For a better readability we omit colour and spinor indices and leave them implicit in the following discussion. Inserting the definition of the lattice covariant derivatives, defined in eqs. (4.32) and (4.33), into the definition of the Wilson-Dirac operator in eq. (6.10), the left-hand side of eq. (6.65) becomes

$$D[U]^{(xf)^2}_{(xf)_1} = \delta_{f_1}^{f_2} \left(\left(4a + m_{f_1}^{(0)} + \Delta m_{f_1} + c_{\text{SW}} a \sum_{\mu_1 < \mu_2} \frac{1}{2} \sigma^{\mu_1 \mu_2} \hat{F}_s^{x_2 \mu_1 \mu_2} \right) \delta_{x_1}^{x_2} \right. \\ \left. - \frac{1}{2} \sum_{\mu} \left((\mathbb{1} - \gamma^{\mu}) U^{x_2 \mu} \exp(i a e q_{f_1} A^{x \mu}) \delta_{x_1}^{x_2 + a \hat{\mu}} \right. \right. \\ \left. \left. + (\mathbb{1} + \gamma^{\mu}) (W^{x_1 \mu})^{\dagger} \exp(-i a e q_{f_1} A^{x \mu}) \delta_{x_1}^{x_2 - a \hat{\mu}} \right) \right). \quad (6.69)$$

In order to expand $D[U, A]$ around its isosymmetric counterpart $D^{(0)}[U]$, given by

$$D^{(0)}[U]^{(xf)^2}_{(xf)_1} = \delta_{f_1}^{f_2} \left(\left(4 + m_{f_1}^{(0)} + c_{\text{SW}} a \sum_{\mu_1 < \mu_2} \frac{1}{2} \sigma^{\mu_1 \mu_2} \hat{F}_{\text{S}}^{x_2 \mu_1 \mu_2} \right) \delta_{x_1}^{x_2} \right. \\ \left. - \frac{1}{2} \sum_{\mu} \left((\mathbb{1} - \gamma^{\mu}) U^{x_2 \mu} \delta_{x_1}^{x_2 + a \hat{\mu}} + (\mathbb{1} + \gamma^{\mu}) (U^{x_1 \mu})^{\dagger} \delta_{x_1}^{x_2 - a \hat{\mu}} \right) \right), \quad (6.70)$$

we expand the QED gauge links up to $O(e^2)$:

$$\exp(iaeQA^{x\mu}) = \mathbb{1} + iaeQA^{x\mu} - \frac{1}{2}a^2e^2Q^2(A^{x\mu})^2 + O(e^3), \quad (6.71)$$

$$\exp(-iaeQA^{x\mu}) = \mathbb{1} - iaeQA^{x\mu} - \frac{1}{2}a^2e^2Q^2(A^{x\mu})^2 + O(e^3). \quad (6.72)$$

6. Lattice QCD+QED

The definition of the vertices can now be read off from eq. (6.65) order by order in the expansion parameters $\Delta\epsilon$. The quark-antiquark vertex $V_{\bar{q}qf}$ used for the explicit detuning of the mass of the quark field with flavour f is given by

$$V_{\bar{q}qf}[U]^{(xf)^2}_{(xf)_1} = -\delta_{x_1}^{x_2} \delta_f^{f_2} \delta_{f_1}^{f_2}. \quad (6.73)$$

As the mass detuning vertex is a point-like vertex, it is in fact independent of the QCD gauge links U . The photon-quark-antiquark vertex $V_{\bar{q}q\gamma}$ reads

$$V_{\bar{q}q\gamma}[U]^{(xf)^2}_{(xf)_1(x\mu)_3} = \frac{i}{2} a q_{f_1} \delta_{f_1}^{f_2} \left(-(\mathbb{1} - \gamma^{\mu_3}) U^{x_2\mu_3} \delta_{x_1}^{x_2+a\hat{\mu}_3} \delta_{x_3}^{x_2} \right. \\ \left. + (\mathbb{1} + \gamma^{\mu_3}) (U^{x_1\mu_3})^\dagger \delta_{x_1}^{x_2-a\hat{\mu}_3} \delta_{x_3}^{x_1} \right). \quad (6.74)$$

Finally, the 2-photon-quark-antiquark vertex $V_{\bar{q}q\gamma\gamma}$ is given by

$$V_{\bar{q}q\gamma\gamma}[U]^{(xf)^2}_{(xf)_1(x\mu)_4(x\mu)_3} = \frac{1}{2} a^2 q_{f_1}^2 \delta_{f_1}^{f_2} \left((\mathbb{1} - \gamma^{\mu_3}) U^{x_2\mu_3} \delta_{x_1}^{x_2+a\hat{\mu}_3} \delta_{\mu_4}^{\mu_3} \delta_{x_4}^{x_2} \delta_{x_3}^{x_2} \right. \\ \left. + (\mathbb{1} + \gamma^{\mu_3}) (U^{x_1\mu_3})^\dagger \delta_{x_1}^{x_2-a\hat{\mu}_3} \delta_{\mu_4}^{\mu_3} \delta_{x_4}^{x_1} \delta_{x_3}^{x_1} \right). \quad (6.75)$$

The γ^5 -hermiticity of the Wilson-Dirac operator in eq. (4.40) is passed on to the vertices in the following way: Applying the γ^5 -hermiticity to eq. (6.65) and comparing order by order in the expansion parameters we can derive the γ^5 -hermiticity relations for the vertices contracted with photon fields:

$$V_{\bar{q}qf}^{(fx)^2}_{(fx)_1} = \gamma^5 (V_{\bar{q}qf}^{(fx)^1}_{(fx)_2})^\dagger \gamma^5, \quad (6.76)$$

$$V_{\bar{q}q\gamma}^{(fx)^2}_{(fx)_1\mathbf{c}} A^{\mathbf{c}} = \gamma^5 (V_{\bar{q}q\gamma}^{(fx)^1}_{(fx)_1\mathbf{c}} A^{\mathbf{c}})^\dagger \gamma^5, \quad (6.77)$$

$$V_{\bar{q}q\gamma\gamma}^{(fx)^2}_{(fx)_1\mathbf{c}_2\mathbf{c}_1} A^{\mathbf{c}} = \gamma^5 (V_{\bar{q}q\gamma}^{(fx)^1}_{(fx)_2\mathbf{c}_2\mathbf{c}_1} A^{\mathbf{c}_2} A^{\mathbf{c}_1})^\dagger \gamma^5. \quad (6.78)$$

As the photon field is a real field, i.e. $A^{x\mu} = (A^{x\mu})^*$ in position space representation, we can also deduce the γ^5 -hermiticity for the vertices themselves:

$$V_{\bar{q}q\gamma}^{(fx)^2}_{(fx)_1(x\mu)_3} = \gamma^5 (V_{\bar{q}q\gamma}^{(fx)^1}_{(fx)_2(x\mu)_3})^\dagger \gamma^5, \quad (6.79)$$

$$V_{\bar{q}q\gamma\gamma}^{(fx)^2}_{(fx)_1(x\mu)_4(x\mu)_3} = \gamma^5 (V_{\bar{q}q\gamma\gamma}^{(fx)^1}_{(fx)_2(x\mu)_4(x\mu)_3})^\dagger \gamma^5. \quad (6.80)$$

It is straight forward to proof the correctness of these relations by a direct computation.

6.6.3. Expansion of the reweighting factor

In order to expand the reweighting factor

$$R[U] = \frac{\exp(-S_g[U]) Z_{q\gamma}[U]}{\exp(-S_g^{(0)}[U]) Z_q^{(0)}[U]}, \quad (6.62)$$

6.6. Feynman rules for QCD+QED as a perturbation of QCD_{iso}

we treat the contributions from the QCD gauge action and the partition functions separately. For the first part, we introduce a vertex $V_g[U]$, which accounts for the expansion in $\Delta\beta = \beta - \beta^{(0)}$,

$$\frac{\exp(-S_g[U])}{\exp(-S_g^{(0)}[U])} = 1 + \Delta\beta V_g[U] + O(\Delta\beta^2), \quad (6.81)$$

and which we represent by

$$V_g[U] = \text{⦿} \Delta\beta. \quad (6.82)$$

Making use of the relation $S_g[U] = \frac{\beta}{\beta^{(0)}} S_g^{(0)}[U]$, i.e. $S_g[U]$ and $S_g^{(0)}[U]$ only differ by the value of the strong coupling, which enters linearly into the gauge action, we find the simple definition

$$V_g[U] = -\frac{1}{\beta^{(0)}} S_g^{(0)}[U]. \quad (6.83)$$

The second part in eq. (6.62) can be calculated using the standard perturbative expansions of the partition function $Z_{q\gamma}$ around the free partition functions $Z_\gamma^{(0)} = \int DA \exp(-S_\gamma^{(0)}[A])$ and $Z_q^{(0)}[U]$ [59]. Consequently, the graphical representation of the reweighting factor up to order $\Delta\epsilon$ reads

$$R[U] = Z_\gamma^{(0)} \left(1 + \sum_f \Delta m_f \text{⦿} + \Delta\beta \text{⦿} \Delta\beta + e^2 \left(\text{⦿} \text{⦿} + \text{⦿} \text{⦿} + \text{⦿} \text{⦿} \right) + O(\Delta\epsilon^2) \right). \quad (6.84)$$

6.6.4. Expansion of a correlation function

According to eq. (6.61), a generic correlation function $\langle \mathcal{O}[U, A, \Psi, \bar{\Psi}] \rangle$ is evaluated by

$$C = \langle \mathcal{O}[U, A, \Psi, \bar{\Psi}] \rangle = \frac{\langle R[U] \langle \mathcal{O}[U, A, \Psi, \bar{\Psi}] \rangle_{q\gamma}^{(0)} \rangle_{\text{eff}}^{(0)}}{\langle R[U] \rangle_{\text{eff}}^{(0)}}. \quad (6.61)$$

In this section, we formally expand the latter perturbatively up to first order in $\Delta\epsilon$:

$$C = C^{(0)} + \sum_l \Delta\epsilon_l C_l^{(1)} + O(\Delta\epsilon^2). \quad (6.85)$$

It is important to note that the operator $\mathcal{O}[U, A, \Psi, \bar{\Psi}]$ itself may depend on e via the QED gauge links $\exp(iaeQA)$. Therefore, it also has to be expanded:

$$\mathcal{O} = \mathcal{O}^{(0)} + e\mathcal{O}_{e^2}^{(\frac{1}{2})} + \frac{1}{2}e^2\mathcal{O}_{e^2}^{(1)} + O(e^3). \quad (6.86)$$

6. Lattice QCD+QED

The zeroth-order contribution to the correlation function is given by

$$C^{(0)} = (\langle \mathcal{O} \rangle)^{(0)} = \frac{\langle (R[U])^{(0)} (\langle \mathcal{O}^{(0)} \rangle_{q\gamma})^{(0)} \rangle_{\text{eff}}^{(0)}}{\langle (R[U])^{(0)} \rangle_{\text{eff}}^{(0)}}. \quad (6.87)$$

The first-order contributions for the expansion parameters $l = \Delta m_u, \Delta m_d, \Delta m_s$ read

$$\begin{aligned} (\langle \mathcal{O} \rangle)_l^{(1)} &= \frac{\langle (R[U])^{(0)} (\langle \mathcal{O}^{(0)} \rangle_{q\gamma})_l^{(1)} \rangle_{\text{eff}}^{(0)}}{\langle (R[U])^{(0)} \rangle_{\text{eff}}^{(0)}} + \frac{\langle (R[U])_l^{(1)} (\langle \mathcal{O}^{(0)} \rangle_{q\gamma})^{(0)} \rangle_{\text{eff}}^{(0)}}{\langle (R[U])^{(0)} \rangle_{\text{eff}}^{(0)}} \\ &\quad - \frac{\langle (R[U])_l^{(1)} \rangle_{\text{eff}}^{(0)}}{\langle (R[U])^{(0)} \rangle_{\text{eff}}^{(0)}} \frac{\langle (R[U])^{(0)} (\langle \mathcal{O}^{(0)} \rangle_{q\gamma})^{(0)} \rangle_{\text{eff}}^{(0)}}{\langle (R[U])^{(0)} \rangle_{\text{eff}}^{(0)}}. \end{aligned} \quad (6.88)$$

For the expansion parameter e^2 we find

$$\begin{aligned} (\langle \mathcal{O} \rangle)_{e^2}^{(1)} &= \frac{\langle (R[U])^{(0)} (\langle \mathcal{O}^{(0)} + e\mathcal{O}_{e^2}^{(\frac{1}{2})} + \frac{1}{2}e^2\mathcal{O}_{e^2}^{(1)})_{q\gamma} \rangle_{e^2}^{(1)} \rangle_{\text{eff}}^{(0)}}{\langle (R[U])^{(0)} \rangle_{\text{eff}}^{(0)}} + \frac{\langle (R[U])_{e^2}^{(1)} (\langle \mathcal{O}^{(0)} \rangle_{q\gamma})^{(0)} \rangle_{\text{eff}}^{(0)}}{\langle (R[U])^{(0)} \rangle_{\text{eff}}^{(0)}} \\ &\quad - \frac{\langle (R[U])_{e^2}^{(1)} \rangle_{\text{eff}}^{(0)}}{\langle (R[U])^{(0)} \rangle_{\text{eff}}^{(0)}} \frac{\langle (R[U])^{(0)} (\langle \mathcal{O}^{(0)} \rangle_{q\gamma})^{(0)} \rangle_{\text{eff}}^{(0)}}{\langle (R[U])^{(0)} \rangle_{\text{eff}}^{(0)}}. \end{aligned} \quad (6.89)$$

As the expansion parameter $\Delta\beta$ is only present in the reweighting factor $R[U]$, the first-order contribution from the correlation function $\langle \mathcal{O} \rangle_{q\gamma}$ is absent:

$$\begin{aligned} (\langle \mathcal{O} \rangle)_{\Delta\beta}^{(1)} &= \frac{\langle (R[U])_{\Delta\beta}^{(1)} (\langle \mathcal{O}^{(0)} \rangle_{q\gamma})^{(0)} \rangle_{\text{eff}}^{(0)}}{\langle (R[U])^{(0)} \rangle_{\text{eff}}^{(0)}} \\ &\quad - \frac{\langle (R[U])_{\Delta\beta}^{(1)} \rangle_{\text{eff}}^{(0)}}{\langle (R[U])^{(0)} \rangle_{\text{eff}}^{(0)}} \frac{\langle (R[U])^{(0)} (\langle \mathcal{O} \rangle_{q\gamma})^{(0)} \rangle_{\text{eff}}^{(0)}}{\langle (R[U])^{(0)} \rangle_{\text{eff}}^{(0)}}. \end{aligned} \quad (6.90)$$

We will give diagrammatic representations of these equations in chapters 11 to 13, when we discuss meson and baryon spectroscopy as well as the hadronic vacuum polarisation function.

6.7. The free photon propagator on temporal periodic boundary conditions

In the following section, we introduce a basis transformation that is compatible with periodic boundary conditions in spatial and temporal directions and block-diagonalises the photon difference operator Δ . In this new basis, the photon propagator can be obtained by a simple algebraic inversion. The key transformation for this purpose is the *discrete Fourier transform* (DFT), which we will introduce now.

6.7.1. Discrete Fourier transform

We define the one-dimensional discrete Fourier transform [205] \mathfrak{F}_μ and its inverse $(\mathfrak{F}_\mu)^{-1}$ in direction μ as

$$\mathfrak{F}_\mu^{p^\mu}_{x^\mu} = \sqrt{\frac{a}{X^\mu}} \exp(-ip^\mu x^\mu), \quad (\mathfrak{F}_\mu^{-1})^{x^\mu}_{p^\mu} = \sqrt{\frac{a}{X^\mu}} \exp(ip^\mu x^\mu) \quad (6.91)$$

with $x^\mu \in \{0, \dots, X^\mu - a\}$ and $p^\mu \in \frac{2\pi}{aX^\mu} \{0, \dots, X^\mu - a\}$. We make use of a normalisation which ensures the unitarity of the Fourier transform in integer coordinates $n^\mu = \frac{x^\mu}{a}$ and $m^\mu = \frac{p^\mu X^\mu}{2\pi}$. This is convenient for the implementation on the computer, where integer coordinates have to be applied. We define the negative value of a momentum as $-p^\mu \equiv \frac{2\pi}{aX^\mu} - p^\mu$, which is consistent with the fact that the Fourier transform and its inverse are $\frac{2\pi}{aX^\mu}$ -periodic with respect to p^μ . The simulation code is based on the implementation of the DFT in the *FFTW3* library [205]. The inverse discrete Fourier transform \mathfrak{F}^{-1} fulfils the periodic boundary condition for all components of the photon field A at the spatial boundaries, defined in eq. (6.14), and at the temporal boundaries, defined in eq. (6.19):

$$(\mathfrak{F}_\mu^{-1})^{-a}_{p^\mu} = \sqrt{\frac{a}{X^\mu}} \exp(-ip^\mu(-a)) = \frac{1}{\sqrt{X^\mu}} \exp(-ip^\mu(X^\mu - a)) = (\mathfrak{F}_\mu^{-1})^{X^\mu - a}_{p^\mu}, \quad (6.92)$$

$$(\mathfrak{F}_\mu^{-1})^{X^\mu}_{p^\mu} = \sqrt{\frac{a}{X^\mu}} \exp(-ip^\mu X^\mu) = \frac{1}{\sqrt{X^\mu}} \exp(-ip^\mu 0) = (\mathfrak{F}_\mu^{-1})^0_{p^\mu}, \quad (6.93)$$

where we made use of the key identity

$$\exp(-ip^\mu X^\mu) = 1 \quad \forall p^\mu \in \frac{2\pi}{aX^\mu} \{0, \dots, X^\mu - a\}. \quad (6.94)$$

6.7.2. Transformation of first-order difference operators

We now consider the transformation properties of first-order difference operators under the Fourier transform. For a more convenient notation, we introduce the lattice momenta p_F^μ and p_B^μ , which are up to a coefficient i eigenvalues of the first-order difference operators:

$$p_F^\mu = -\frac{i}{a}(\exp(iap^\mu) - 1), \quad p_B^\mu = -\frac{i}{a}(1 - \exp(-iap^\mu)). \quad (6.95)$$

In the limit $a \rightarrow 0$ the continuum momentum is restored as $p_F^\mu \rightarrow p^\mu$ and $p_B^\mu \rightarrow p^\mu$. The lattice momenta fulfil the following identities:

$$p_F^\mu = (p_B^\mu)^* = -(-p^\mu)_B, \quad p_B^\mu = (p_F^\mu)^* = -(-p^\mu)_F. \quad (6.96)$$

There are two combinations of lattice derivatives and Fourier transforms that will be relevant:

$$\vec{\partial}_F^{\mu x_2^\mu}_{x_1^\mu} (\mathfrak{F}_\mu^{-1})^{x_1^\mu}_{p^\mu} = ip_F^\mu (\mathfrak{F}_\mu^{-1})^{x_2^\mu}_{p^\mu}, \quad \mathfrak{F}_\mu^{p^\mu}_{x_2^\mu} \overleftarrow{\partial}_F^{\mu x_2^\mu}_{x_1^\mu} = -ip_B^\mu \mathfrak{F}_\mu^{p^\mu}_{x_2^\mu}. \quad (6.97)$$

6. Lattice QCD+QED

We illustrate the computation on the first example,

$$\begin{aligned}\vec{\partial}_{\text{F}}^{0x_2^0}_{x_1^0}(\mathfrak{F}^{-1})^{x_1^0}_{p^0} &= \frac{1}{a} \sqrt{\frac{a}{X^\mu}} (\exp(ip^\mu x_2^\mu) - \exp(ip^\mu(x_2^\mu + a))) \\ &= \frac{1}{a} \sqrt{\frac{a}{X^\mu}} \exp(ip^\mu x_2^\mu) (1 - \exp(ip^\mu a)) = ip^\mu_{\text{F}} (\mathfrak{F}_\mu^{-1})^{x_2^\mu}_{p^\mu}.\end{aligned}\quad (6.98)$$

6.7.3. Basis change of the photon field

We define a basis change for the photon field that relates the momentum space and the position space representation:

$$A^{(p\mu)_2} = \mathfrak{B}^{(p\mu)_2}_{(x\mu)_1} A^{(x\mu)_1}, \quad A^{(x\mu)_2} = (\mathfrak{B}^{-1})^{(x\mu)_2}_{(p\mu)_1} A^{(p\mu)_1}. \quad (6.99)$$

The basis change matrices \mathfrak{B} and \mathfrak{B}^{-1} read

$$\mathfrak{B}^{(p\mu)_2}_{(x\mu)_1} = \delta_{\mu_1}^{\mu_2} \prod_{\mu=0}^3 \mathfrak{F}_\mu^{p^\mu}_{x_1^\mu}, \quad (\mathfrak{B}^{-1})^{(x\mu)_2}_{(p\mu)_1} = \delta_{\mu_1}^{\mu_2} \prod_{\mu=0}^3 (\mathfrak{F}_\mu^{-1})^{x_2^\mu}_{p_1^\mu}. \quad (6.100)$$

The metric tensor for the photon field in the defining position space representation reads

$$g_{(x\mu)_2(x\mu)_1} = \delta_{x_1}^{x_2} \delta_{\mu_1}^{\mu_2}, \quad (6.101)$$

such that $A_{x\mu} = A^{x\mu}$. However, in momentum space representation it is not equal to unity as

$$g_{(p\mu)_3(p\mu)_1} = g_{(x\mu)_4(x\mu)_2} (\mathfrak{B}^{-1})^{(x\mu)_4}_{(p\mu)_3} (\mathfrak{B}^{-1})^{(x\mu)_2}_{(p\mu)_1} = \delta_{p_1}^{-p_3} \delta_{\mu_1}^{\mu_3}, \quad (6.102)$$

i.e. one has to distinguish photon fields with lowered and raised indices in momentum space representation and $A_{p\mu} = A^{-p\mu}$.

6.7.4. Basis change of the photon difference operator

The Fourier transform of second-order difference operators leads to products of the lattice momenta, given in eq. (6.95). The two relevant combinations can be simplified to

$$p_{\text{B}}^{\mu_2} p_{\text{F}}^{\mu_1} = \frac{4}{a^2} \exp\left(\frac{ia(p^{\mu_1} - p^{\mu_2})}{2}\right) \sin\left(\frac{ap^{\mu_1}}{2}\right) \sin\left(\frac{ap^{\mu_2}}{2}\right), \quad (6.103)$$

$$p_{\text{B}}^\mu p_{\text{F}}^\mu = \frac{4}{a^2} \left(\sin\left(\frac{ap^\mu}{2}\right) \right)^2. \quad (6.104)$$

We transform the photon difference operator, which maps photon fields on photon fields, according to

$$\Delta^{(p\mu)_4}_{(p\mu)_1} = \mathfrak{B}^{(p\mu)_4}_{(x\mu)_3} \Delta^{(x\mu)_3}_{(x\mu)_2} (\mathfrak{B}^{-1})^{(x\mu)_2}_{(p\mu)_1} \quad (6.105)$$

with the basis change matrices given in eq. (6.100).

6.7. The free photon propagator on temporal periodic boundary conditions

Feynman gauge

The photon difference operator Δ in Feynman gauge, defined in eq. (6.5), reads

$$\Delta^{(p\mu)_2}_{(p\mu)_1} = \sum_{\mu} p_{1B}^{\mu} p_{1F}^{\mu} \delta_{p_1}^{p_2} \delta_{\mu_1}^{\mu_2} \quad (6.106)$$

in momentum space representation. It is diagonal both in the momentum p and in the Euclidean index μ . Hence, its inverse, the photon propagator Σ , can directly be obtained:

$$\Sigma^{(p\mu)_2}_{(p\mu)_1} = \frac{1}{\sum_{\mu} p_{1B}^{\mu} p_{1F}^{\mu}} \delta_{p_1}^{p_2} \delta_{\mu_1}^{\mu_2}. \quad (6.107)$$

According to the QED_L prescription only momenta p with non-vanishing spatial momentum $\vec{p} \neq \vec{0}$ are considered such that the manifest divergence of the propagator at $p = 0$ is avoided.

Coulomb gauge

Making use of eq. (6.7), the momentum space representation of Δ in generalised Coulomb gauge reads

$$\begin{aligned} \Delta^{p\mu_2}_{p\mu_1} &= \begin{pmatrix} \sum_{\mu \neq 0} p_B^{\mu} p_F^{\mu} & -p_B^1 p_F^0 & -p_B^2 p_F^0 & -p_B^3 p_F^0 \\ -p_B^0 p_F^1 & \sum_{\mu} p_B^{\mu} p_F^{\mu} & & \\ -p_B^0 p_F^2 & & \sum_{\mu} p_B^{\mu} p_F^{\mu} & \\ -p_B^0 p_F^3 & & & \sum_{\mu} p_B^{\mu} p_F^{\mu} \end{pmatrix}^{\mu_2}_{\mu_1} \\ &\quad + \left(\frac{1}{\xi} - 1 \right) \begin{pmatrix} 0 & & & \\ p_B^1 p_F^1 & p_B^2 p_F^1 & p_B^3 p_F^1 & \\ p_B^1 p_F^2 & p_B^2 p_F^2 & p_B^3 p_F^2 & \\ p_B^1 p_F^3 & p_B^2 p_F^3 & p_B^3 p_F^3 & \end{pmatrix}^{\mu_2}_{\mu_1}, \\ \Delta^{(p\mu)_2}_{(p\mu)_1} &= 0 \quad p_2 \neq p_1. \end{aligned} \quad (6.108)$$

To obtain the photon propagator in generalised Coulomb gauge, we invert the photon difference operator in momentum space representation by means of a computer algebra program. As the expression is lengthy, we only give the result in Coulomb gauge, where the limit $\xi \rightarrow 0$ has been performed already:

$$\begin{aligned} \Sigma^{p\mu_2}_{p\mu_1} &= \frac{1}{(\sum_{\mu} p_B^{\mu} p_F^{\mu})(\sum_{\mu \neq 0} p_B^{\mu} p_F^{\mu})} \\ &\quad \cdot \begin{pmatrix} \sum_{\mu} p_B^{\mu} p_F^{\mu} & & & \\ p_B^2 p_F^2 + p_B^3 p_F^3 & -p_B^2 p_F^1 & -p_B^3 p_F^1 & \\ -p_B^1 p_F^2 & p_B^1 p_F^1 + p_B^3 p_F^3 & -p_B^3 p_F^2 & \\ -p_B^1 p_F^3 & -p_B^2 p_F^3 & p_B^1 p_F^1 + p_B^2 p_F^2 & \end{pmatrix}^{\mu_2}_{\mu_1}, \\ \Sigma^{(p\mu)_2}_{(p\mu)_1} &= 0 \quad p_2 \neq p_1. \end{aligned} \quad (6.109)$$

6. Lattice QCD+QED

A useful cross check for a computer implementation of the photon propagator in Fourier representation is the projection property

$$\Sigma^{p\mu_2}_{p\mu_1} p_F^{\mu_1} = \left(\sum_{\mu} p_B^{\mu} p_F^{\mu} \right) \begin{pmatrix} p_F^0 \\ 0 \\ 0 \\ 0 \end{pmatrix}^{\mu_2}, \quad (6.110)$$

i.e. the vector p_F is a zero-eigenvector of the photon propagator in Coulomb gauge for vanishing temporal momentum $p^0 = 0$.

6.8. The free photon propagator on temporal open boundary conditions

The calculation of the free photon propagator on temporal open boundary conditions and spatial periodic boundary conditions is more sophisticated compared to the purely periodic case, but in principle works in the same manner. The main task is to find a basis transformation which allows for the block diagonalisation of the photon difference operator and which is at the same time compatible with the open temporal boundary conditions. This can be achieved by the *discrete sine transformation* (DST) and the *discrete sine transformation* (DCT) combined with the discrete Fourier transform.

6.8.1. Discrete sine and cosine transformations

The discrete sine and cosine transformations are the real valued counterparts of the complex valued discrete Fourier transform. Depending on the boundary conditions, there exist different types of discrete sine and discrete cosine transformations [205]. We apply a modified version of the discrete sine transformation of type DST-I and the discrete cosine transformation of types DCT-II and DCT-III, which are suitable for open temporal boundary conditions, as we will see later. Consequently, we introduce for the temporal direction the one-dimensional discrete sine transformations \mathfrak{S}_0 and its inverse \mathfrak{S}_0^{-1}

$$\mathfrak{S}_0^{p^0}_{x^0} = (\mathfrak{S}_0^{-1})^{x^0}_{p^0} = \sqrt{\frac{2a}{X^0}} \sin(p^0(x^0 + a)) \quad (6.111)$$

with $x^0 \in \{0, \dots, X^0 - 2a\}$ and $p^0 \in \frac{\pi}{aX^0}\{a, \dots, X^0 - a\}$, and the discrete cosine transformation \mathfrak{C}_0 and its inverse \mathfrak{C}_0^{-1}

$$\mathfrak{C}_0^{p^0}_{x^0} = (\mathfrak{C}_0^{-1})^{x^0}_{p^0} = \begin{cases} \sqrt{\frac{a}{X^0}} & p^0 = 0 \\ \sqrt{\frac{2a}{X^0}} \cos(p^0(x^0 + \frac{a}{2})) & p^0 \neq 0 \end{cases} \quad (6.112)$$

with $x^0 \in \{0, \dots, X^0 - a\}$ and $p^0 \in \frac{\pi}{aX^0}\{0, \dots, X^0 - a\}$. It is important to point out, that the domain for x^0 and p^0 is different in comparison to the Fourier transforms. We use a particular normalisation that also includes the independent normalisation factor of

6.8. The free photon propagator on temporal open boundary conditions

\mathfrak{C}_0 for $p^0 = 0$ and that differs from the standard definition of the DST-I, the DCT-II and the DCT-III [205]. However, it ensures the orthogonality of the transformations in integer coordinates $n^0 = \frac{x^0}{a}$ and $m^0 = \frac{p^0 X^0}{\pi}$. This is again convenient for the implementation on the computer. The simulation code is based on the implementations of the DST and the DCT in the *FFTW3* library [205]. The inverse discrete sine transformation \mathfrak{S}_0^{-1} fulfils the open boundary condition for the temporal component of the photon field A^0 at the temporal boundaries, defined in eq. (6.26), i.e. Dirichlet boundary conditions:

$$(\mathfrak{S}_0^{-1})^{-a}_{p^0} = \sqrt{\frac{2a}{X^0}} \sin(0) = 0, \quad (6.113)$$

$$(\mathfrak{S}_0^{-1})^{X^0-a}_{p^0} = \sqrt{\frac{2a}{X^0}} \sin(p^0 X^0) = 0. \quad (6.114)$$

The discrete cosine transformation \mathfrak{C}_0^{-1} fulfils the open boundary condition for the spatial component of the photon field A^μ for $\mu = 1, 2, 3$ at the temporal boundaries, defined in eq. (6.27), i.e. Neumann boundary conditions:

$$\begin{aligned} (\vec{\partial}_F^0)^{-a}_{x^0} (\mathfrak{C}_0^{-1})^{x^0}_{p^0} &= \begin{cases} \sqrt{\frac{a}{X^0}} - \sqrt{\frac{a}{X^0}} & p^0 = 0 \\ \sqrt{\frac{2a}{X^0}} (\cos(p^0 \frac{a}{2}) - \cos(-p^0 \frac{a}{2})) & p^0 \neq 0 \end{cases} \\ &= 0, \end{aligned} \quad (6.115)$$

$$\begin{aligned} (\vec{\partial}_F^0)^{X^0-a}_{x^0} (\mathfrak{C}_0^{-1})^{x^0}_{p^0} &= \begin{cases} \sqrt{\frac{a}{X^0}} - \sqrt{\frac{a}{X^0}} & p^0 = 0 \\ \sqrt{\frac{2a}{X^0}} (\cos(p^0 (X^0 + \frac{a}{2})) - \cos(p^0 (X^0 - \frac{a}{2}))) & p^0 \neq 0 \end{cases} \\ &= 0. \end{aligned} \quad (6.116)$$

6.8.2. Transformation of first-order difference operators

We can express first-order lattice derivatives applied to cosine transforms in terms of sine transforms, which are multiplied by a factor, and vice versa. For this purpose, we define the generalised lattice momenta p_{FSC}^0 and p_{BCS}^0 :

$$p_{\text{FSC}}^0 = \frac{2i}{a} \sin\left(\frac{ap^0}{2}\right), \quad p_{\text{BCS}}^0 = -\frac{2i}{a} \sin\left(\frac{ap^0}{2}\right). \quad (6.117)$$

The generalised lattice momenta fulfil the following identities:

$$p_{\text{FSC}}^0 = (p_{\text{BCS}}^0)^* = -(-p^0)_{\text{FSC}}, \quad p_{\text{BCS}}^0 = (p_{\text{FSC}}^0)^* = -(-p^0)_{\text{BCS}}. \quad (6.118)$$

There are four combinations of lattice derivatives and sine and cosine transforms that will be relevant:

$$\vec{\partial}_F^{0x_2^0}_{x_1^0} (\mathfrak{C}^{-1})^{x_1^0}_{p^0} = ip_{\text{FSC}}^0 (\mathfrak{C}^{-1})^{x_2^0+a}_{p^0}, \quad \mathfrak{S}^{p^0}_{x_2^0} \overleftarrow{\partial}_F^{0x_2^0}_{x_1^0} = -ip_{\text{BCS}}^0 \mathfrak{C}^{p^0}_{x_1^0+a}, \quad (6.119)$$

$$\vec{\partial}_F^{0x_1^0}_{x_2^0} (\mathfrak{C}^{-1})^{x_2^0}_{p^0} = ip_{\text{BCS}}^0 (\mathfrak{C}^{-1})^{x_1^0}_{p^0}, \quad \mathfrak{C}^{p^0}_{x_2^0} \overleftarrow{\partial}_F^{0x_2^0}_{x_1^0} = -ip_{\text{FSC}}^0 \mathfrak{S}^{p^0}_{x_1^0}. \quad (6.120)$$

6. Lattice QCD+QED

We illustrate the computation on the third example,

$$\begin{aligned}
\vec{\partial}_F^0 x_2^0 x_1^0 (\mathfrak{E}^{-1})^{x_1^0}_{p^0} &= \frac{1}{a} \sqrt{\frac{2a}{X^0}} \left(\cos \left(p^0 \left(x_2^0 + \frac{3a}{2} \right) \right) - \cos \left(p^0 \left(x_2^0 + \frac{a}{2} \right) \right) \right) \\
&= -\frac{2}{a} \sqrt{\frac{2a}{X^0}} \sin(p^0(x_2^0 + a)) \sin\left(\frac{ap^0}{2}\right) \\
&= -(\mathfrak{E}^{-1})^{x_2^0}_{p^0} \frac{2}{a} \sin\left(\frac{ap^0}{2}\right) = ip_{\text{FSC}}^0 (\mathfrak{E}^{-1})^{x_2^0}_{p^0}, \tag{6.121}
\end{aligned}$$

where we made use of the identity $\cos(\alpha) - \cos(\beta) = -2 \sin(\frac{\alpha+\beta}{2}) \sin(\frac{\alpha-\beta}{2})$.

6.8.3. Basis change of the photon field

We again introduce a convenient basis change transformation for the photon field, relating the generalised momentum space representation with the position space representation:

$$A^{(p\mu)_2} = \mathfrak{B}^{(p\mu)_2}_{(x\mu)_1} A^{(x\mu)_1}, \quad A^{(x\mu)_2} = (\mathfrak{B}^{-1})^{(x\mu)_2}_{(p\mu)_1} A^{(p\mu)_1}. \tag{6.99}$$

We define the basis change matrices \mathfrak{B} and \mathfrak{B}^{-1} as

$$\begin{aligned}
\mathfrak{B}^{p\mu_2}_{x\mu_1} &= \begin{pmatrix} \mathfrak{E}_0^{p^0}_{x^0} & & & \\ & \mathfrak{E}_0^{p^0}_{x^0} & & \\ & & \mathfrak{E}_0^{p^0}_{x^0} & \\ & & & \mathfrak{E}_0^{p^0}_{x^0} \end{pmatrix}_{\mu_1}^{\mu_2} \cdot \prod_{\mu \neq 0} \mathfrak{F}_\mu^{p^\mu}_{x^\mu}, \\
(\mathfrak{B}^{-1})^{p\mu_2}_{x\mu_1} &= \begin{pmatrix} (\mathfrak{E}_0^{-1})^{p^0}_{x^0} & & & \\ & (\mathfrak{E}_0^{-1})^{p^0}_{x^0} & & \\ & & (\mathfrak{E}_0^{-1})^{p^0}_{x^0} & \\ & & & (\mathfrak{E}_0^{-1})^{p^0}_{x^0} \end{pmatrix}_{\mu_1}^{\mu_2} \cdot \prod_{\mu \neq 0} (\mathfrak{F}_\mu^{-1})^{p^\mu}_{x^\mu}. \tag{6.122}
\end{aligned}$$

The choice of transformations depends on the Euclidean index, as different components of the photon field satisfy different boundary conditions. The metric tensor for the photon field in this generalised momentum space representation reads

$$g_{(p\mu)_3(p\mu)_1} = g_{(x\mu)_4(x\mu)_2} (\mathfrak{B}^{-1})^{(x\mu)_4}_{(p\mu)_3} (\mathfrak{B}^{-1})^{(x\mu)_2}_{(p\mu)_1} = \delta_{\vec{p}_1}^{-\vec{p}_3} \delta_{p_1^0}^{p_3^0} \delta_{\mu_1}^{\mu_3}, \tag{6.123}$$

i.e. one has to distinguish photon fields with lowered and raised indices in generalised momentum space representation as $A_{p\mu} = A^{(p^0, -\vec{p})\mu}$.

6.8.4. Basis change of the photon difference operator

The sine and cosine transforms of second-order difference operators lead to products of the generalised lattice momenta, given in eq. (6.117). There is one relevant combination, which can be simplified to

$$p_{\text{BCS}}^0 p_{\text{FSC}}^0 = \frac{4}{a^2} \left(\sin\left(\frac{ap^\mu}{2}\right) \right)^2. \tag{6.124}$$

6.8. The free photon propagator on temporal open boundary conditions

We again transform the photon difference operator Δ according to

$$\Delta^{(p\mu)_4}_{(p\mu)_1} = \mathfrak{B}^{(p\mu)_4}_{(x\mu)_3} \Delta^{(x\mu)_3}_{(x\mu)_2} (\mathfrak{B}^{-1})^{(x\mu)_2}_{(p\mu)_1}, \quad (6.105)$$

but now make use of the basis change matrices defined in eq. (6.122).

Feynman gauge

The photon difference operator Δ in Feynman gauge, defined in eq. (6.5), reads

$$\Delta^{(p\mu)_2}_{(p\mu)_1} = \left(p_{1\text{BCS}}^0 p_{1\text{FSC}}^0 + \sum_{\mu \neq 0} p_{1\text{B}}^\mu p_{1\text{F}}^\mu \right) \delta_{p_1}^{p_2} \delta_{\mu_1}^{\mu_2} \quad (6.125)$$

in generalised momentum space representation. Thus, the photon propagator Σ is given by

$$\Delta^{p\mu_2}_{p\mu_1} = \frac{1}{p_{1\text{BCS}}^0 p_{1\text{FSC}}^0 + \sum_{\mu \neq 0} p_{1\text{B}}^\mu p_{1\text{F}}^\mu} \delta_{p_1}^{p_2} \delta_{\mu_1}^{\mu_2}. \quad (6.126)$$

Coulomb gauge

For Δ in generalised Coulomb gauge, given in eq. (6.7), we obtain

$$\begin{aligned} \Delta^{p\mu_2}_{p\mu_1} = & \left(\begin{array}{cccc} \sum_{\mu \neq 0} p_{\text{B}}^\mu p_{\text{F}}^\mu & -p_{\text{B}}^1 p_{\text{FSC}}^0 & -p_{\text{B}}^2 p_{\text{FSC}}^0 & -p_{\text{B}}^3 p_{\text{FSC}}^0 \\ -p_{\text{BCS}}^0 p_{\text{F}}^1 & p_{\text{BCS}}^0 p_{\text{FSC}}^0 + \sum_{\mu \neq 0} p_{\text{B}}^\mu p_{\text{F}}^\mu & & \\ -p_{\text{BCS}}^0 p_{\text{F}}^2 & & p_{\text{BCS}}^0 p_{\text{FSC}}^0 + \sum_{\mu \neq 0} p_{\text{B}}^\mu p_{\text{F}}^\mu & \\ -p_{\text{BCS}}^0 p_{\text{F}}^3 & & & p_{\text{BCS}}^0 p_{\text{FSC}}^0 + \sum_{\mu \neq 0} p_{\text{B}}^\mu p_{\text{F}}^\mu \end{array} \right)_{\mu_1}^{\mu_2} \\ & + \left(\frac{1}{\xi} - 1 \right) \left(\begin{array}{ccc} 0 & & \\ p_{\text{B}}^1 p_{\text{F}}^1 & p_{\text{B}}^2 p_{\text{F}}^1 & p_{\text{B}}^3 p_{\text{F}}^1 \\ p_{\text{B}}^1 p_{\text{F}}^2 & p_{\text{B}}^2 p_{\text{F}}^2 & p_{\text{B}}^3 p_{\text{F}}^2 \\ p_{\text{B}}^1 p_{\text{F}}^3 & p_{\text{B}}^2 p_{\text{F}}^3 & p_{\text{B}}^3 p_{\text{F}}^3 \end{array} \right)_{\mu_1}^{\mu_2}, \end{aligned} \quad (6.127)$$

$$\Delta^{(p\mu)_2}_{(p\mu)_1} = 0 \quad p_2 \neq p_1.$$

We proceed as in the case for temporal periodic boundary conditions. After taking the limit $\xi \rightarrow 0$, the photon propagator in Coulomb gauge reads

$$\begin{aligned} \Sigma^{p\mu_2}_{p\mu_1} = & \frac{1}{(p_{\text{BCS}}^0 p_{\text{FSC}}^0 + \sum_{\mu \neq 0} p_{\text{B}}^\mu p_{\text{F}}^\mu) (\sum_{\mu \neq 0} p_{\text{B}}^\mu p_{\text{F}}^\mu)} \\ & \cdot \left(\begin{array}{ccc} p_{\text{BCS}}^0 p_{\text{FSC}}^0 + \sum_{\mu \neq 0} p_{\text{F}}^\mu p_{\text{B}}^\mu & & \\ & p_{\text{B}}^2 p_{\text{F}}^2 + p_{\text{B}}^3 p_{\text{F}}^3 & -p_{\text{B}}^2 p_{\text{F}}^1 \\ & -p_{\text{B}}^1 p_{\text{F}}^2 & p_{\text{B}}^1 p_{\text{F}}^1 + p_{\text{B}}^3 p_{\text{F}}^3 \\ & -p_{\text{B}}^1 p_{\text{F}}^3 & -p_{\text{B}}^2 p_{\text{F}}^3 & p_{\text{B}}^1 p_{\text{F}}^1 + p_{\text{B}}^2 p_{\text{F}}^2 \end{array} \right)_{\mu_1}^{\mu_2}, \end{aligned} \quad (6.128)$$

$$\Sigma^{(p\mu)_2}_{(p\mu)_1} = 0 \quad p_2 \neq p_1.$$

7. Computation strategies for correlation functions

In this chapter, we introduce strategies to evaluate correlation functions which are relevant for this thesis. We briefly discuss the infeasibility to compute the full quark propagator and the need of quark sources. We describe the stochastic treatment of the all-to-all photon propagator, which is used in some Feynman diagrams. Finally, we introduce reusable building blocks to evaluate Feynman diagrams in QCD+QED.

7.1. Infeasibility of computing the full quark propagator

The quark propagator S is defined as the inverse of the Dirac operator D , i.e. S is obtained as a solution of the linear equation

$$D^{\mathbf{a}2}{}_{\mathbf{b}} S^{\mathbf{b}}{}_{\mathbf{a}1} = \delta^{\mathbf{a}2}{}_{\mathbf{a}1}. \quad (7.1)$$

S and D both have to be understood as functions of the gauge field U . The full determination of the all-to-all propagator S on a given gauge configuration U , which describes the propagation from any lattice site to another, is computationally unattainable [42], even if fast iterative solvers are used. For a single quark flavour, S is a full matrix of dimensions $(V \cdot 12) \times (V \cdot 12)$, where V denotes the number of lattice sites. The currently available CLS ensembles possess volumes of V of $O(10^7 - 10^9)$, c.f. table 5.1. To determine the full quark propagator, one would have to solve V systems of linear equations of system size V . In fact, it is only computationally feasible to solve the Dirac equation

$$D^{\mathbf{a}2}{}_{\mathbf{b}} \Psi[\eta]^{\mathbf{b}} = \eta^{\mathbf{a}}, \quad (7.2)$$

where $\Psi[\eta]$ denotes the propagator with respect to the source η , as $\Psi[\eta]^{\mathbf{b}} = S^{\mathbf{b}}{}_{\mathbf{a}} \eta^{\mathbf{a}}$, for a small number of quark sources η . To solve the Dirac equation for a given source, we apply the generalized conjugate residual (GCR) algorithm to the deflated, Schwarz preconditioned Dirac equation, as discussed in section 5.2.6 for the generation of gauge configurations. There are several types of sources used to evaluate correlation functions. The choice of the source type depends on the particular correlation function to be computed. In this thesis, we mainly apply two types of quark sources, which are used to evaluate quark-connected contributions to two-point functions: point sources, which have support on a single lattice site, and stochastic sources with support on one timeslice. We will give more details on the sources when we discuss the computation of mesonic and baryonic two-point functions in chapters 11 and 12, respectively.

7.2. Stochastic treatment of all-to-all photon propagators

The photon difference operator Δ is a sparse matrix of dimensions $(V \cdot 4) \times (V \cdot 4)$. In the considered Feynman diagrams, the photon propagator may connect two different vertices such that all entries of the photon propagator are required in the calculation. The computation of the full photon propagator matrix in position space representation is impractical for the same reasons as for the quark propagator. Therefore, we make use of a stochastic estimation of the photon propagator, which we will discuss below. The major difference between a quark and a photon propagator is that the photon propagator can be computed algebraically by a convenient basis transformation, such that the necessity to solve a linear system of equations by means of a fast iterative solver can be avoided. The case in which the photon propagator is attached to the same vertex with both ends can be treated without stochastic sources, as only the diagonal elements in position space representation are required. Due to periodic spatial boundary conditions, we can apply translational invariance and further reduce the number of entries which have to be determined. The implementation of the simulation code is based on data structures provided by the QDP++ library [206].

7.2.1. Standard stochastic estimation

We introduce general stochastic sources for the photon field J , which satisfy the relation

$$\langle J_{\mathbf{c}2} (J^{\mathbf{c}1})^* \rangle = \delta_{\mathbf{c}2}^{\mathbf{c}1}, \quad (7.3)$$

where the sources can be either real- or complex-valued. We further define a propagated source as an abbreviation by

$$A[J]^{\mathbf{c}2} = \Sigma^{\mathbf{c}2\mathbf{c}1} J_{\mathbf{c}1}. \quad (7.4)$$

The photon propagator can be estimated stochastically via the expectation value of a source and the corresponding propagated source:

$$\langle A[J]^{\mathbf{c}3} (J^{\mathbf{c}1})^* \rangle = \Sigma^{\mathbf{c}3\mathbf{c}2} \langle J_{\mathbf{c}2} J^{\mathbf{c}1*} \rangle = \Sigma^{\mathbf{c}3\mathbf{c}2} \delta_{\mathbf{c}2}^{\mathbf{c}1} = \Sigma^{\mathbf{c}3\mathbf{c}1}. \quad (7.5)$$

In order to determine the stochastic estimate of the photon propagator in position space representation, we calculate the propagated source by performing a basis change to momentum coordinates 6.99, in which we know the algebraic form of the photon propagator:

$$A[J]^{x_2\mu_2} = (\mathfrak{B}^{-1})^{(x\mu)_4}_{(p\mu)_3} \Sigma^{(p\mu)_3}_{(p\mu)_2} \mathfrak{B}^{(p\mu)_2}_{(x\mu)_1} J^{(x\mu)_1}. \quad (7.6)$$

For a given set of sources $(J_i)_{i=1\dots n}$ the propagator is then estimated via

$$\Sigma^{(x\mu)_2(x\mu)_1} \approx \frac{1}{n} \sum_{i=1}^n A[J_i]^{(x\mu)_2} (J_i^{(x\mu)_1})^*. \quad (7.7)$$

7.2.2. Improved stochastic estimation

A general disadvantage of the latter stochastic estimate is the fact that the symmetry property of the photon propagator $\Sigma^{\mathbf{c}_2\mathbf{c}_1} = \Sigma^{\mathbf{c}_1\mathbf{c}_2}$ is not preserved due to the introduction of stochastic noise. The most straight forward way to overcome this disadvantage is to project out the anti-symmetric part of the estimate, redefining $\Sigma^{\mathbf{c}_2\mathbf{c}_1}$ as only its symmetric part

$$\Sigma^{\mathbf{c}_2\mathbf{c}_1} = \frac{1}{2n} \sum_{i=1}^n (A[J_i]^{\mathbf{c}_2} (J_i^{\mathbf{c}_1})^* + J_i^{\mathbf{c}_2} (A[J_i]^{\mathbf{c}_1})^*). \quad (7.8)$$

However, with this improved estimator, the computational cost grows by a factor between one and two, as all sequential propagators over photon sources and photon fields have to be computed twice per photon source.

Let us assume we can construct the square root of the photon propagator $\sqrt{\Sigma}$, which we will refer to as a half-propagator,

$$\Sigma^{\mathbf{c}_3}_{\mathbf{c}_1} = \sqrt{\Sigma}^{\mathbf{c}_3}_{\mathbf{c}_2} \sqrt{\Sigma}^{\mathbf{c}_2}_{\mathbf{c}_1}, \quad (7.9)$$

and let us further assume that it is a symmetric tensor, i.e.

$$\sqrt{\Sigma}^{\mathbf{c}_2}_{\mathbf{c}_1} = \sqrt{\Sigma}^{\mathbf{c}_1}_{\mathbf{c}_2}. \quad (7.10)$$

We introduce stochastic sources satisfying the relation

$$\langle J^{\mathbf{c}_2} J^{\mathbf{c}_1} \rangle_J = g^{\mathbf{c}_2\mathbf{c}_1}, \quad (7.11)$$

where g is the metric tensor, which is used to raise and lower indices of the photon fields, and we define, similar to eq. (7.4), the half-propagated photon source $A[J]$ as

$$A[J]^{\mathbf{c}_2} = \sqrt{\Sigma}^{\mathbf{c}_2}_{\mathbf{c}_1} J^{\mathbf{c}_1}. \quad (7.12)$$

If we determine the expectation value of two half-propagated photon sources $A[J]$ with respect to the stochastic source J , we can reconstruct the photon propagator:

$$\begin{aligned} \langle A[J]^{\mathbf{c}_4} A[J]^{\mathbf{c}_2} \rangle_J &= \langle \sqrt{\Sigma}^{\mathbf{c}_4}_{\mathbf{c}_3} J^{\mathbf{c}_3} \sqrt{\Sigma}^{\mathbf{c}_2}_{\mathbf{c}_1} J^{\mathbf{c}_1} \rangle_J = \langle \sqrt{\Sigma}^{\mathbf{c}_4}_{\mathbf{c}_3} J^{\mathbf{c}_3} \sqrt{\Sigma}^{\mathbf{c}_1}_{\mathbf{c}_2} J^{\mathbf{c}_2} \rangle_J \\ &= \sqrt{\Sigma}^{\mathbf{c}_4}_{\mathbf{c}_3} \langle J^{\mathbf{c}_3} J^{\mathbf{c}_1} \rangle_J \sqrt{\Sigma}^{\mathbf{c}_1}_{\mathbf{c}_2} = \sqrt{\Sigma}^{\mathbf{c}_4}_{\mathbf{c}_3} g^{\mathbf{c}_3\mathbf{c}_1} \sqrt{\Sigma}^{\mathbf{c}_1}_{\mathbf{c}_2} \\ &= \Sigma^{\mathbf{c}_4\mathbf{c}_2}. \end{aligned} \quad (7.13)$$

Similar to eq. (7.6), we compute the half-propagated photon source in position space representation via a basis change:

$$A[J]^{x_2\mu_2} = (\mathfrak{B}^{-1})^{(x\mu)_4}_{(p\mu)_3} \sqrt{\Sigma}^{(p\mu)_3}_{(p\mu)_2} \mathfrak{B}^{(p\mu)_2}_{(x\mu)_1} J^{(x\mu)_1}. \quad (7.14)$$

The estimated photon propagator for a given set of sources $(J_i)_{i=1\dots n}$ is now manifestly symmetric, reading

$$\Sigma^{(x\mu)_2(x\mu)_1} \approx \frac{1}{n} \sum_{i=1}^n A[J_i]^{(x\mu)_2} A[J_i]^{(x\mu)_1}. \quad (7.15)$$

7. Computation strategies for correlation functions

A major advantage of this construction is the fact that the fields $A[J]^{x\mu}$ are real-valued for real-valued sources $J^{x\mu}$. This becomes relevant for the application of the generalised one-end trick, introduced in chapter 11, where the γ^5 -hermicity of the quark propagator S and the quark-photon vertices is used. In this construction, the photon field $A^{x\mu}$ has to be invariant under complex conjugation.

7.2.3. The free photon half-propagator on temporal periodic boundary conditions

In the following, we will explicitly construct the photon half-propagators for Feynman and Coulomb gauge on a lattice with periodic temporal boundary conditions.

Feynman gauge

As the photon propagator in Feynman gauge is diagonal, real-valued and positive,

$$\Sigma^{(p\mu)_2}_{(p\mu)_1} = \frac{1}{\sum_{\mu} p_{1F}^{\mu} p_{1B}^{\mu}} \delta_{p_1}^{p_2} \delta_{\mu_1}^{\mu_2}, \quad (6.107)$$

the construction of the photon half-propagator, i.e. the square root of the photon propagator, is simple,

$$\sqrt{\Sigma}^{(p\mu)_2}_{(p\mu)_1} = \frac{1}{\sqrt{\sum_{\mu} p_{1F}^{\mu} p_{1B}^{\mu}}} \delta_{p_1}^{p_2} \delta_{\mu_1}^{\mu_2}, \quad (7.16)$$

such that eq. (7.9) is obviously fulfilled.

Coulomb gauge

The construction of the photon half-propagator in Coulomb gauge is more sophisticated, as the propagator is not diagonal but only block-diagonal:

$$\begin{aligned} \Sigma^{p\mu_2}_{p\mu_1} &= \frac{1}{(\sum_{\mu} p_B^{\mu} p_F^{\mu})(\sum_{\mu \neq 0} p_B^{\mu} p_F^{\mu})} \\ &\cdot \begin{pmatrix} \sum_{\mu} p_B^{\mu} p_F^{\mu} & & \\ & p_B^2 p_F^2 + p_B^3 p_F^3 & -p_B^2 p_F^1 & -p_B^3 p_F^1 \\ & -p_B^1 p_F^2 & p_B^1 p_F^1 + p_B^3 p_F^3 & -p_B^3 p_F^2 \\ & -p_B^1 p_F^3 & -p_B^2 p_F^3 & p_B^1 p_F^1 + p_B^2 p_F^2 \end{pmatrix}^{\mu_2}_{\mu_1}, \\ \Sigma^{(p\mu)_2}_{(p\mu)_1} &= 0 \quad p_2 \neq p_1. \end{aligned} \quad (6.109)$$

As Σ_p^p is a hermitian matrix, we can construct a unitary basis change matrix $U(p) = (u_0(p), u_1(p), u_2(p), u_3(p))$ which diagonalises Σ_p^p . Assuming $p^1 \neq 0$ or $p^2 \neq 0$, an or-

7.2. Stochastic treatment of all-to-all photon propagators

thonormal basis of eigenvectors is given by

$$\begin{aligned} u_0(p) &= \begin{pmatrix} 1 \\ 0 \\ 0 \\ 0 \end{pmatrix}, & u_2(p) &= \frac{1}{\sqrt{(p_B^1 p_F^1 + p_B^2 p_F^2)(\sum_{\mu \neq 0} p_B^\mu p_F^\mu)}} \begin{pmatrix} 0 \\ -p_B^3 p_F^1 \\ -p_B^3 p_F^2 \\ p_B^1 p_F^1 + p_B^2 p_F^2 \end{pmatrix}, \\ u_1(p) &= \frac{1}{\sqrt{p_B^1 p_F^1 + p_B^2 p_F^2}} \begin{pmatrix} 0 \\ -p_B^2 \\ p_B^1 \\ 0 \end{pmatrix}, & u_3(p) &= \frac{1}{\sqrt{\sum_{\mu \neq 0} p_B^\mu p_F^\mu}} \begin{pmatrix} 0 \\ p_F^1 \\ p_F^2 \\ p_F^3 \end{pmatrix}. \end{aligned} \quad (7.17)$$

The diagonalised propagator in Coulomb gauge, which is positive semi-definite, reads

$$(U(p))^{-1} \Sigma_p U(p) = \text{diag} \left(\frac{1}{\sum_{\mu \neq 0} p_B^\mu p_F^\mu}, \frac{1}{\sum_{\mu} p_B^\mu p_F^\mu}, \frac{1}{\sum_{\mu} p_B^\mu p_F^\mu}, 0 \right). \quad (7.18)$$

Consequently, we define the half-propagator $\sqrt{\Sigma}_p$ as

$$\sqrt{\Sigma}_p = U(p) \text{diag} \left(\frac{1}{\sqrt{\sum_{\mu \neq 0} p_B^\mu p_F^\mu}}, \frac{1}{\sqrt{\sum_{\mu} p_B^\mu p_F^\mu}}, \frac{1}{\sqrt{\sum_{\mu} p_B^\mu p_F^\mu}}, 0 \right) (U(p))^{-1}. \quad (7.19)$$

In the remaining case $p^1 = 0$ and $p^2 = 0$, the photon propagator in eq. (6.109) is diagonal. Hence, we choose $U(p) = \mathbb{1}$, for which the half-propagator is also given by eq. (7.19).

7.2.4. The free photon half-propagator on temporal open boundary conditions

The construction for temporal open boundary conditions is analogue to temporal periodic boundary conditions.

Feynman gauge

The photon propagator in Feynman gauge reads

$$\Sigma^{p\mu_2}_{p\mu_1} = \frac{1}{p_{1\text{BCS}}^0 p_{1\text{FSC}}^0 + \sum_{\mu \neq 0} p_{1\text{B}}^\mu p_{1\text{F}}^\mu} \delta_{p_1}^{p_2} \delta_{\mu_1}^{\mu_2}. \quad (6.126)$$

Hence, the photon half-propagator is given by

$$\sqrt{\Sigma}^{(p\mu)_2}_{(p\mu)_1} = \frac{1}{\sqrt{p_{1\text{BCS}}^0 p_{1\text{FSC}}^0 + \sum_{\mu \neq 0} p_{1\text{B}}^\mu p_{1\text{F}}^\mu}} \delta_{p_1}^{p_2} \delta_{\mu_1}^{\mu_2}. \quad (7.20)$$

7. Computation strategies for correlation functions

Coulomb gauge

The photon propagator in Coulomb gauge is defined as

$$\Sigma^{p\mu_2}_{p\mu_1} = \frac{1}{(p_{\text{BCS}}^0 p_{\text{FSC}}^0 + \sum_{\mu \neq 0} p_{\text{B}}^\mu p_{\text{F}}^\mu) (\sum_{\mu \neq 0} p_{\text{B}}^\mu p_{\text{F}}^\mu)} \cdot \begin{pmatrix} p_{\text{BCS}}^0 p_{\text{FSC}}^0 + \sum_{\mu \neq 0} p_{\text{B}}^\mu p_{\text{F}}^\mu & & & \\ & p_{\text{B}}^2 p_{\text{F}}^2 + p_{\text{B}}^3 p_{\text{F}}^3 & -p_{\text{B}}^2 p_{\text{F}}^1 & -p_{\text{B}}^3 p_{\text{F}}^1 \\ & -p_{\text{B}}^1 p_{\text{F}}^2 & p_{\text{B}}^1 p_{\text{F}}^1 + p_{\text{B}}^3 p_{\text{F}}^3 & -p_{\text{B}}^3 p_{\text{F}}^2 \\ & -p_{\text{B}}^1 p_{\text{F}}^3 & -p_{\text{B}}^2 p_{\text{F}}^3 & p_{\text{B}}^1 p_{\text{F}}^1 + p_{\text{B}}^2 p_{\text{F}}^2 \end{pmatrix}^{\mu_2}_{\mu_1},$$

$$\Sigma^{(p\mu)_2}_{(p\mu)_1} = 0 \quad p_2 \neq p_1. \quad (6.128)$$

We may utilise the same unitary basis change matrices $U(p)$ to diagonalise $\Sigma^{p\mu_2}_{p\mu_1}$ as in the case of temporal periodic boundary conditions, i.e. for $p^1 \neq 0$ or $p^2 \neq 0$ we make use of the eigenvectors in eq. (7.17) and for $p^1 = 0$ and $p^2 = 0$ we define $U(p) = \mathbb{1}$. The half-propagator reads

$$\sqrt{\Sigma}_p = U(p) \text{diag} \left(\frac{1}{\sqrt{\sum_{\mu \neq 0} p_{\text{B}}^\mu p_{\text{F}}^\mu}}, \frac{1}{\sqrt{p_{\text{BCS}}^0 p_{\text{FSC}}^0 + \sum_{\mu \neq 0} p_{\text{B}}^\mu p_{\text{F}}^\mu}}, \right. \quad (7.21)$$

$$\left. \frac{1}{\sqrt{p_{\text{BCS}}^0 p_{\text{FSC}}^0 + \sum_{\mu \neq 0} p_{\text{B}}^\mu p_{\text{F}}^\mu}}, 0 \right) (U(p))^{-1}.$$

7.3. Sequential quark sources and sequentially propagated sources

The numerical evaluation of a Feynman diagram can be broken down to building blocks, which appear in the evaluation process of various diagrams. We distinguish two types of building blocks. Propagated sources, which are composed of a quark propagator and a quark source, and sequential sources, which themselves can be composed of a vertex attached to a propagated source. We introduce various sequential sources and sequential propagators with different vertices inserted. As we consider leading isospin breaking effects, we maximally find one mass detuning vertex $V_{\bar{q}qf}$, one 2-photon vertex $V_{\bar{q}q\gamma\gamma}$ or two 1-photon vertices $V_{\bar{q}q\gamma}$ in our diagrams. In general, all objects discussed in the following depend on the QCD gauge background U . For better readability, we suppress this dependence. Spin and colour indices are kept implicit. The implementation of the simulation code is based on data structures provided by the QDP++ library [206].

7.3. Sequential quark sources and sequentially propagated sources

7.3.1. No vertex

The most simple object, appearing in isosymmetric calculations, is the quark propagator $\Psi[\eta]$ of a source η , which is defined by

$$\Psi[\eta]^b = S^{(0)b}{}_a \eta^a = \begin{array}{c} b \longrightarrow \longleftarrow a \end{array} \eta^a. \quad (7.22)$$

With regard to a computer implementation, attaching a propagator to a source always means that a Dirac equation of the form

$$D^{(0)a}{}_b \Psi[\eta]^b = \eta^a \quad (7.23)$$

has to be solved for $\Psi[\eta]$.

7.3.2. One mass detuning vertex

In order to evaluate diagrams which exhibit a mass detuning vertex $V_{\bar{q}qf}$, we define the sequential source

$$\eta_{V_{\bar{q}qf}}[\eta]^{a_2} = V_{\bar{q}qf}{}^{a_2}{}_b \Psi[\eta]^b = \begin{array}{c} a_2 \bullet \longrightarrow \longleftarrow a_1 \end{array} \eta^{a_1}, \quad (7.24)$$

where the mass detuning vertex in eq. (6.73) is applied to Ψ^b according to

$$V_{\bar{q}qf}{}^{(xf)_1}{}_b \Psi^b = -\delta_f^{f_1} \Psi^{(xf)_1}. \quad (7.25)$$

We also define the corresponding propagated sequential source

$$\Psi_{V_{\bar{q}qf}}[\eta]^b = S^b{}_a \eta_{V_{\bar{q}qf}}[\eta]^a = \begin{array}{c} b \longrightarrow \bullet \longrightarrow \longleftarrow a \end{array} \eta^a, \quad (7.26)$$

which is calculated according to eq. (7.23).

One integrated 2-photon vertex

Diagrams with a 2-photon vertex $V_{\bar{q}q\gamma\gamma}$ combined with a photon propagator Σ , which is attached to both photon legs of the vertex, require the determination of

$$\eta_{V_{\bar{q}q\gamma\gamma}\Sigma}^{(0)}[\eta]^{a_2} = \frac{1}{2} V_{\bar{q}q\gamma\gamma}{}^{a_2}{}_{bc_2c_1} \Sigma^{c_2c_1} \Psi[\eta]^b = \begin{array}{c} \text{wavy line} \\ a_2 \bullet \longrightarrow \bullet \longrightarrow \longleftarrow a_1 \end{array} \eta^{a_1}, \quad (7.27)$$

where the integrated 2-photon vertex $V_{\bar{q}q\gamma\gamma}\Sigma$ in eq. (6.75) is applied to Ψ and according to

$$V_{\bar{q}q\gamma\gamma}{}^{xf}{}_{bc_2c_1} \Sigma^{c_2c_1} \Psi^b = \frac{1}{2} a^2 q_f^2 \sum_{\mu} \left((\mathbb{1} - \gamma^{\mu}) U^{x\mu} \Psi^{x+a\hat{\mu},f} \Sigma^{x\mu x\mu} + (\mathbb{1} + \gamma^{\mu}) (U^{x-a\hat{\mu},\mu})^{\dagger} \Psi^{x-a\hat{\mu},f} \Sigma^{x-a\hat{\mu},\mu, x-a\hat{\mu},\mu} \right). \quad (7.28)$$

7. Computation strategies for correlation functions

In order to evaluate the shifted fields in the latter expression, the chosen boundary conditions have to be considered as discussed in section 6.2. We also define the corresponding propagated sequential source

$$\Psi_{V_{\bar{q}q\gamma\gamma}\Sigma}[\eta]^{\mathbf{b}} = S^{\mathbf{b}}_{\mathbf{a}} \eta_{V_{\bar{q}q\gamma\gamma}\Sigma}^{(0)}[\eta]^{\mathbf{a}} = \text{b} \xleftarrow{\text{star}} \text{a} \eta^{\mathbf{a}}, \quad (7.29)$$

which is calculated according to eq. (7.23).

The definition of the integrated 2-photon vertex $V_{\bar{q}q\gamma\gamma}\Sigma$ requires the computation of the diagonal elements of the photon propagator in position space representation $\Sigma^{x\mu x\mu}$. Making use of translation invariance for periodic boundary conditions, we find $\Sigma^{x\mu x\mu} = \Sigma^{0\mu 0\mu}$, i.e. we only have to evaluate the photon propagator at a single lattice site. We compute the photon propagator by means of the diagonal representation:

$$\Sigma^{0\mu 4}_{0\mu_1} = (\mathfrak{B}^{-1})^{0\mu 2}_{(p\mu)_3} \Sigma^{(p\mu)_3}_{(p\mu)_2} \mathfrak{B}^{(p\mu)_2}_{0\mu_1}. \quad (7.30)$$

The basis change matrices \mathfrak{B} and \mathfrak{B}^{-1} for periodic boundary conditions are defined in eq. (6.100). $\Sigma^{(p\mu)_3}_{(p\mu)_2}$ is either given by eq. (6.107) for Feynman gauge or by eq. (6.109) for Coulomb gauge.

If open temporal boundary conditions are applied, the translational symmetry in the temporal direction is spoiled. Hence, we can only relate sites located on the same timeslice and find $\Sigma^{x\mu x\mu} = \Sigma^{(x^0, \vec{0})\mu (x^0, \vec{0})\mu}$. Consequently, the photon propagator has to be evaluated on each timeslice $x^0 = 0, \dots, X^0 - a$:

$$\Sigma^{(x^0, \vec{0})\mu 4}_{0\mu_1} = (\mathfrak{B}^{-1})^{0\mu 2}_{(p\mu)_3} \Sigma^{(p\mu)_3}_{(p\mu)_2} \mathfrak{B}^{(p\mu)_2}_{(x^0, \vec{0})\mu_1}. \quad (7.31)$$

The basis change matrices \mathfrak{B} and \mathfrak{B}^{-1} for temporal open boundary conditions are defined in eq. (6.122). $\Sigma^{(p\mu)_3}_{(p\mu)_2}$ is either given by eq. (6.126) for Feynman gauge or by eq. (6.128) for Coulomb gauge. The evaluation of the latter equation for each timeslice of the lattice is time consuming. To save computation time, we precompute the results and write them to disk such that they can be reused for every execution of the simulation program.

7.3.3. One 1-photon vertex

Sequential sources with one 1-photon vertex $V_{\bar{q}q\gamma}$ are defined as

$$\eta_{V_{\bar{q}q\gamma}\sqrt{\Sigma}}^{(0)}[J, \eta]^{\mathbf{a}2} = V_{\bar{q}q\gamma}^{\mathbf{a}2}_{\mathbf{b}c2} \Psi[\eta]^{\mathbf{b}} \sqrt{\Sigma}^{\mathbf{c}2}_{\mathbf{c}1} J^{\mathbf{c}1} = \text{a}_2 \xleftarrow{\text{c}} \text{a}_1 J^{\mathbf{c}1} \eta^{\mathbf{a}1}. \quad (7.32)$$

The vertex defined in eq. (6.74) is applied to $\Psi^{\mathbf{b}}$ and $A^{\mathbf{c}1} = \sqrt{\Sigma}^{\mathbf{c}2}_{\mathbf{c}1} J^{\mathbf{c}1}$ according to

$$\begin{aligned} V_{\bar{q}q\gamma}^{xf} \mathbf{b}c \Psi^{\mathbf{b}} A^{\mathbf{c}} &= \frac{i}{2} a q_f \sum_{\mu} \left(- (1 - \gamma^{\mu}) U^{x\mu} \Psi^{x+a\hat{\mu}, f} A^{x\mu} \right. \\ &\quad \left. + (1 + \gamma^{\mu}) (U^{x-a\hat{\mu}, \mu})^{\dagger} \Psi^{x-a\hat{\mu}, f} A^{x-a\hat{\mu}, \mu} \right). \end{aligned} \quad (7.33)$$

7.3. Sequential quark sources and sequentially propagated sources

Again, the boundary conditions discussed in section 6.2 have to be considered in order to evaluate this expression. We also define the corresponding propagated sequential source

$$\Psi_{V_{\bar{q}q\gamma}\sqrt{\Sigma}}^{(0)}[J, \eta]^b = S^b_a \eta_{V_{\bar{q}q\gamma}\sqrt{\Sigma}}^{(0)}[J, \eta]^a = \text{b} \xleftarrow{\text{c}} \text{a} J^c \eta^a, \quad (7.34)$$

which is calculated according to eq. (7.23).

7.3.4. Two 1-photon vertices

In some Feynman diagrams, the two 1-photon vertices $V_{\bar{q}q\gamma}$ appear on the same quark line next to each other. We define the corresponding sequential source as

$$\begin{aligned} \eta_{V_{\bar{q}q\gamma}\sqrt{\Sigma}V_{\bar{q}q\gamma}\sqrt{\Sigma}}^{(0)}[J_2, J_2, \eta]^{a_2} &= V_{\bar{q}q\gamma}^{a_2 b c_2} \Psi_{V_{\bar{q}q\gamma}\sqrt{\Sigma}}[\eta]^b \sqrt{\Sigma}^{c_2 c_1} J^{c_1} \\ &= \text{a}_2 \xleftarrow{\text{c}_2} \text{a}_1 J_2^{c_2} J_1^{c_1} \eta^{a_1}. \end{aligned} \quad (7.35)$$

We may directly contract the two photon half-propagators in the latter diagram, making use of eq. (7.11)

$$\langle J^{c_2} J^{c_1} \rangle_J = g^{c_2 c_1}, \quad (7.11)$$

i.e. we insert the same stochastic photon source $J = J_1 = J_2$ in eq. (7.35) and take the expectation value. Consequently, we define the sequential source

$$\eta_{V_{\bar{q}q\gamma}\Sigma V_{\bar{q}q\gamma}}^{(0)}[\eta]^{a_2} = \left\langle \eta_{V_{\bar{q}q\gamma}\sqrt{\Sigma}V_{\bar{q}q\gamma}\sqrt{\Sigma}}^{(0)}[\eta, J, J]^{a_2} \right\rangle_J = \text{a}_2 \xleftarrow{\text{a}_1} \eta^{a_1}. \quad (7.36)$$

In practice, the latter expectation value is estimated on each QCD_{iso} gauge configuration U only for a small number of stochastic sources J . In addition, we introduce the corresponding propagated sequential source

$$\Psi_{V_{\bar{q}q\gamma}\Sigma V_{\bar{q}q\gamma}}^{(0)}[J, \eta]^b = S^b_a \eta_{V_{\bar{q}q\gamma}\Sigma V_{\bar{q}q\gamma}}^{(0)}[J, \eta]^a = \text{b} \xleftarrow{\text{a}} \eta^a. \quad (7.37)$$

7.3.5. Combined calculation of one 2-photon vertex and two 1-photon vertices with photon propagator

Combining the calculation of sequential propagators with one 2-photon vertex $V_{\bar{q}q\gamma\gamma}$ and two 1-photon vertices $V_{\bar{q}q\gamma}$ contracted with a photon propagator Σ allows us to significantly reduce the number of inversions of the Dirac equation eq. (7.23), which is the most time consuming part of the calculation. The last quark propagator can be applied after the

7. Computation strategies for correlation functions

expectation value over the photon sources is taken and after the two sequential sources are added up:

$$\begin{aligned}
 (\Psi_{V_{\bar{q}q\gamma\gamma}\Sigma} + \Psi_{V_{\bar{q}q\gamma}\Sigma V_{\bar{q}q\gamma}})[\eta]^{\mathbf{b}} &= S^{\mathbf{b}}_{\mathbf{a}} \left(\eta_{V_{\bar{q}q\gamma\gamma}\Sigma}^{(0)}[\eta]^{\mathbf{a}} + \eta_{V_{\bar{q}q\gamma}\Sigma V_{\bar{q}q\gamma}}^{(0)}[\eta]^{\mathbf{a}} \right) \\
 &= \text{diagram 1} + \text{diagram 2} . \quad (7.38)
 \end{aligned}$$

8. Data analysis for Monte Carlo simulations

In this chapter we introduce and discuss methods required for the analysis of data generated within Monte Carlo simulations. We will apply these methods intensively in the following chapters. We also briefly discuss relevant software packages. The textbooks *Gattringer* and *Lang* [42] and *DeGrand* and *DeTar* [98] as well as [207] and [104] provide helpful introductory remarks. A textbook on resampling methods, which we use for the estimation of statistical errors, is *Efron* [208]. Helpful guides for regression analysis are [209, 210].

8.1. Software for data analysis

The data analysis is performed using *Python3* [211]. Hdf5 files containing the Monte Carlo simulation results are read by means of the *Python3* package *h5py* [212]. The data is processed using the *Python3* libraries *NumPy* [213] and *SciPy* [214] and displayed by *matplotlib* [215]. Input files are stored in the json format and read by the *Python3* package *json* [216]. Random numbers used within the analysis are generated with the Mersenne Twister random number generator package *random* [217] of *Python3*.

8.2. Error estimation via resampling methods

In the following, we consider an observable $O[U]$ that depends on the gauge field U . Its expectation value $\langle O[U] \rangle_{\text{eff}}$ with respect to the effective action S_{eff} is estimated via a Monte Carlo simulation, as discussed in section 4.6. In the latter, a finite set of gauge configurations $(U_{n_M})_{n_M=1, \dots, N_M}$ is generated. We define the n_M -th measurement O_{n_M} as the evaluation of the observable O on the n_M -th gauge configuration U_{n_M}

$$O_{n_M} = O[U_{n_M}]. \quad (8.1)$$

The average of the measurements is then an estimator for the expectation value $\langle O[U] \rangle_U$ [42], reading

$$\bar{O}_M = \frac{1}{N_M} \sum_{n_M=1}^{N_M} O_{n_M}. \quad (8.2)$$

As \bar{O}_M is a stochastic estimate, it is important to quantify the related estimation error. In principle, one could determine the error from N individual averages $(\bar{O}_{M,n})_{n=1, \dots, N}$ generated from N individual sets of N_M measurements [42]. This procedure is usually far

8. Data analysis for Monte Carlo simulations

too costly and therefore infeasible. A solution to this problem is offered by resampling methods. They allow an error estimation from the same set of measurements used to estimate the expectation value. In the following we will describe two resampling techniques, bootstrap and jackknife resampling [218]. A more detailed introduction can be found in the book of *Efron* [208].

8.2.1. Bootstrap for primary quantities

Given N_M measurement samples $(O_{M,n_M})_{n=1,\dots,N_M}$ of a quantity O one constructs N_B bootstrap samples $(O_{B,n_B})_{n=1,\dots,N_B}$ by drawing with replacement N_M times from the N_M measurements and averaging [42, 98, 207]. This procedure can be implemented according to [207]

$$O_{B,n_B} = \frac{1}{N_M} \sum_{n_M=1}^{N_M} \theta_{n_B n_M} O_{M,n_M}, \quad (8.3)$$

where we have introduced integer numbers $\theta_{n_B n_M} \in \mathbb{N}_0^+$ with the constraint

$$\sum_{n_M=1}^{N_M} \theta_{n_B n_M} = N_M. \quad (8.4)$$

$\frac{\theta_{n_B n_M}}{N_M}$ is the statistical weight of the n_M -th measurement in the n_B -th bootstrap sample. The numbers $\theta_{n_B n_M}$ are generated by a random generator once for an entire bootstrap analysis. The main advantage of bootstrap resampling is that the number of samples can be chosen independently of the number of measurements. It is therefore possible to combine results of gauge ensembles with differing numbers of measurements in the same analysis. In this thesis we work with $N_B = 500$ bootstrap samples. The bootstrap estimate of the expectation value reads [42, 98, 207]

$$\bar{O}_B = \frac{1}{N_B} \sum_{n_B=1}^{N_B} O_{B,n_B}. \quad (8.5)$$

However, one commonly uses the average of the measurements eq. (8.2) as an estimator. The bootstrap estimate of the error is given by [42, 207]

$$\sigma_{O,B} = \sqrt{\frac{1}{N_B} \sum_{n_B=1}^{N_B} (O_{B,n_B} - \bar{O}_B)^2}, \quad (8.6)$$

where we have used eq. (8.2). It is also possible to estimate the covariance between various quantities O^i like, e.g. correlation functions with operators evaluated at different times. The bootstrap estimate of the covariance matrix reads

$$Cov_B^{i_2 i_1} = \frac{1}{N_B} \sum_{n_B=1}^{N_B} (O_{B,n_B}^{i_2} - \bar{O}_B^{i_2})(O_{B,n_B}^{i_1} - \bar{O}_B^{i_1}). \quad (8.7)$$

For the diagonal elements of Cov_B we have $Cov_B^{ii} = (\sigma_{O_i,B})^2$.

8.2.2. Jackknife for primary quantities

In contrast to the bootstrap resampling, the jackknife method does not depend on random numbers. Here, we will focus on the delete-1 jackknife for which the sample number is equal to the number of measurements. We have implemented jackknife resampling as a cross check for our analysis software based on bootstrap resampling. The N_J jackknife samples $(O_{J,n_J})_{n=1,\dots,N_J}$ are computed according to [42, 98, 207]

$$O_{J,n_J} = \frac{1}{N_J - 1} \sum_{\substack{n_M=1 \\ n_M \neq n_J}}^{N_M} O_{M,n_M}. \quad (8.8)$$

By construction $N_J = N_M$. In contrast to bootstrap resampling, results of gauge ensembles with differing numbers of measurements cannot be combined, which is a major disadvantage. The jackknife estimate for the expectation value reads [42, 98, 207]

$$\overline{O}_J = \frac{1}{N_J} \sum_{n_J=1}^{N_J} O_{J,n_J}. \quad (8.9)$$

A simple calculation shows that for primary quantities this estimate is identical to the average of the measurements $\overline{O}_J = \overline{O}_M$ in eq. (8.2). The jackknife estimate of the error is given by [42, 98, 207]

$$\sigma_{O,J} = \sqrt{\frac{N_J - 1}{N_J} \sum_{n_J=1}^{N_J} (O_{J,n_J} - \overline{O}_M)^2} \quad (8.10)$$

and the estimate for the covariance matrix is

$$Cov_J^{i_2 i_1} = \frac{N_J - 1}{N_J} \sum_{n_J=1}^{N_J} (O_{J,n_J}^{i_2} - \overline{O}_M^{i_2})(O_{J,n_J}^{i_1} - \overline{O}_M^{i_1}). \quad (8.11)$$

Compared to the corresponding bootstrap estimators, an additional prefactor has to be introduced for a bias correction.

8.2.3. Resampling for derived quantities

Usually, we are not interested in primary quantities, i.e. correlation functions, but in derived quantities, such as hadron masses obtained from fits to a correlation function, evaluated at different times, or ratios and products of correlation functions. Let us assume that the derived quantity $O'(O_1, \dots, O_n)$ depends on the primary quantities O_1, \dots, O_n . The different O_i may be the same type of correlation function, where the operators have only changed their time position, or correlation functions of different types. It can be shown that the best estimate for the mean of the derived quantity is given by the plug-in result [208]

$$\overline{O'(O_1, \dots, O_n)} = O'(\overline{O}_1, \dots, \overline{O}_n) \quad (8.12)$$

8. Data analysis for Monte Carlo simulations

as it is free of any estimation bias. The error of O' can be estimated by resampling methods. From the samples for O_1, \dots, O_n , namely $(O_{1,R,n_R})_{n_R=1,\dots,N_R}, \dots, (O_{n,R,n_R})_{n_R=1,\dots,N_R}$, where R denotes the resampling method using B for bootstrap and J for jackknife, we construct samples $((O'(O_1, \dots, O_n))_{R,n_R})_{n_R=1,\dots,N_R}$ for the derived quantity O' by means of the plug-in result [208]:

$$(O'(O_1, \dots, O_n))_{R,n_R} = O'(O_{1,R,n_R}, \dots, O_{n,R,n_R}). \quad (8.13)$$

The error and the covariance matrix can now be determined from the derived samples in the same manner as for primary samples. However, non-linear functions O' will in general introduce a small bias in the error estimate. Additionally, it should be noted that the jackknife resampling method is only applicable for error propagation if the derived quantity is a smooth function with respect to the relevant primary quantities [208]. The statistical bootstrap is also able to cope with a functional dependence that is not smooth [208].

8.2.4. Pseudo-resampling of input parameters with associated errors

In order to introduce an input parameter equipped with an error into the analysis, it is convenient to create a pseudo-resampling distribution that mimics a resampling distribution and yields the value of the input parameter and its associated error. Assuming that the distribution of the quantity O is approximated by a Gaussian distribution with central value \bar{O} and width σ_O , one can construct pseudo-resampling distributions $f_R(O)$ from which the correct estimate for the mean \bar{O}_R and the error $\sigma_{O,R}$ can be derived. For bootstrap resampling the corresponding probability density reads

$$f_B(O) = \frac{1}{\sqrt{2\pi}\sigma_O} \exp\left(-\frac{1}{2}\left(\frac{O - \bar{O}}{\sigma_O}\right)^2\right). \quad (8.14)$$

For jackknife resampling a factor for bias correction has to be introduced:

$$f_J(O) = \frac{\sqrt{N_J - 1}}{\sqrt{2\pi}\sigma_O} \exp\left(-\frac{1}{N_J - 1} \frac{1}{2} \left(\frac{O - \bar{O}}{\sigma_O}\right)^2\right). \quad (8.15)$$

The correctness of these formula can easily be checked numerically.

8.2.5. Partial errors

Often, the analysis requires the input of quantities determined by experiments or by other Monte Carlo simulations. These input parameters are usually equipped with errors and it is natural to ask how this particular error influences the final result of the analysis in addition to further errors inherent to the analysis. We again consider a derived quantity $O'(O_1, \dots, O_n)$. The quantities O_i are represented by resampling or pseudo-resampling samples $(O_{i,R,n_R})_{n_R=1,\dots,N_R}$. The partial error σ_{O',O_i} of the derived quantity O' with respect to the input parameter O_i is then estimated from the resampling distribution

$$(O'(O_1, \dots, O_n))_{R,O_i,n_R} = O'(\bar{O}_1, \dots, O_{i,R,n_R}, \dots, \bar{O}_n), \quad (8.16)$$

ensemble	N_{cnfg}	$N_{\text{cnfg/blk}}$	N_{blk}
N200	1712	4	428
D450	500	2	250
H102	2004	4	501

Table 8.1.: Number of gauge configurations N_{cnfg} , the block size $N_{\text{cnfg/bin}}$ and the resulting number of blocks N_{blk} .

i.e. only the quantity O_i is represented by the resampling samples. The total error is not necessarily given by the square root of the sum of the squared partial errors due to correlations between the different input parameters. However, deviations should only appear if a complete resampling analysis was performed such that valid correlations can form. Quantities from different resampling distributions are uncorrelated and therefore the corresponding errors added in quadrature should equal the total error.

8.3. Autocorrelation analysis

As gauge configurations are derived from each other sequentially by a deterministic computer algorithm, we have to assume that the measurements of a quantity on these gauge configurations are not statistically independent. This type of intrinsic correlation of Monte Carlo simulations is called autocorrelation. The strength of the autocorrelations depends on the particular algorithm used for the generation of the gauge configurations and on the quantity investigated. Autocorrelations lead to an underestimation of the statistical error. A simple way to investigate the influence of autocorrelations is to vary the effective algorithmic distance between sequential gauge configurations [42, 219]. This can be achieved by binning/blocking sequential measurements on the Markov chain and investigating the behaviour of the error estimate as a function of the bin/block size. We list the block sizes for the considered gauge ensembles in table 8.1. A more sophisticated method to determine errors including effects due to autocorrelations is the Γ -method [219], which we do not apply in this thesis. A Python program for the implementation of the Γ -method for Monte Carlo simulations is also available [220].

8.4. Regression analysis

In order to extract physically meaningful results from Monte Carlo simulations, it is often useful to employ regression analysis. In many cases, an analytically derived model with free parameters is known predicting the outcome of Monte Carlo simulations. Regression analysis allows the prediction of these model parameters in the presence of the intrinsic statistical noise.

8. Data analysis for Monte Carlo simulations

8.4.1. The χ^2 -function

Let us assume that we have independent variables $X = (X_1, \dots, X_m)$ and a dependent variable Y that are related by an unknown functional dependence of the form

$$Y = f(X) + \varepsilon, \quad (8.17)$$

where ε is assumed to be a Gaussian random noise. This relation is probed by a statistical experiment, such as a Monte Carlo simulation, resulting in n individual measurements $(x_i, y_i) = ((x_{1,i}, \dots, x_{m,i}), y_i)$ for $i = 1, \dots, n$. In general, these n determinations are not statistically independent. In a typical situation, a correlation function determined by a Monte Carlo simulation is fitted to its asymptotic form for different time separations. In this example, the time separation is the independent variable X , and the value of the correlation function is the dependent variable Y . The latter is equipped with random noise caused by the Monte Carlo simulation. Considering a set of model functions f_a parametrised by $a = (a_1, \dots, a_l)$, the task of a regression analysis is now to determine the optimal choice a_{opt} of these parameters. The fit problem is characterised by the χ^2 -function [42, 98]

$$\chi_a^2 = \sum_{i,j=1}^n (y_i - f_a(x_i))(Cov^{-1})_{ij}(y_j - f_a(x_j)), \quad (8.18)$$

where Cov is the covariance matrix, encoding the correlations between different data points (x_i, y_i) . The solution of the fit problem is the given by the value a_{opt} , which minimises the function χ_a^2 :

$$a_{\text{opt}} = \arg \min_{a \in \mathbb{R}^l} \chi_a^2. \quad (8.19)$$

Only for specific types of regression models, it is possible to calculate the optimal parameter choice a_{opt} analytically. In general, the minimisation has to be performed numerically. We make use of suitable minimisation routines provided by *scipy.optimize.minimize* [221]. For a comparison of regression models with different numbers of fit parameters it is common to define the reduced χ^2 -function χ_{red}^2 [209]

$$\chi_{\text{red}}^2 = \chi^2 / \text{dof} = \frac{\chi^2}{N - M}, \quad (8.20)$$

where N is the number of measurements and M is the number of fit parameters. It should be noted that the number of degrees of freedom $N - M$ is not always a well defined quantity for non-linear regression models [209].

The value of χ_{red}^2 for a regression model can be used as a measure of the fit quality, assuming that we have access to a good stochastic estimate of the covariance matrix Cov . A $\chi_{\text{red}}^2 \approx 1$ is an indicator for a suitable regression model [209]. If $\chi_{\text{red}}^2 > 1$ the regression model does not represent the data and if $\chi_{\text{red}}^2 < 1$ the data is overfitted, i.e. the number of free model parameters in the regression model is too high. χ_{red}^2 can also be used to discriminate two distinct fit models. The more suitable regression model is characterised by χ_{red}^2 that is closer to one [209].

8.4.2. Inversion of the covariance matrix

The covariance matrix is by construction a real, symmetric, positive semi-definite matrix. Poor statistical estimates due to a limited amount of measurements can possess eigenvalues that are very close to zero or even negative due to numerical rounding errors, which makes the numerical inversion of the covariance matrix unstable [98, 222]. A method to numerically invert the covariance matrix in a controlled fashion is a singular value decomposition based on *numpy.linalg.svd*. For a real symmetric matrix Cov the decomposition ensures the existence of real, orthogonal matrices U and V , such that

$$Cov = U\Sigma V^T, \quad \Sigma = \text{diag}(\sigma_1, \dots, \sigma_n), \quad (8.21)$$

where $\sigma_1 \geq \dots \geq \sigma_n \geq 0$ are the singular values and $\sigma_i = |\lambda_i|$ for $i = 1, \dots, n$ with λ_i are the eigenvalues of Cov . For positive definite matrices we have $V = U$ and $\sigma_i = \lambda_i$ for $i = 1, \dots, n$. If singular values that are very close to zero exist, it can be reasonable to apply a truncation [98] or smoothing procedure [223]. In the first case singular values below a certain threshold λ_{\min} are set to zero in Σ and Σ^{-1} , which is to be understood as a pseudo-inverse [98]. In the second case, singular values below the threshold are fixed to a small value computed from the average of the modified singular values [223]. After this singular value modification the inverse covariance matrix is expressed as

$$Cov^{-1} = V\Sigma^{-1}U^T. \quad (8.22)$$

Modifying singular values one has to check that the choice of λ_{\min} does not severely influence the fit results. By choosing fit intervals that are not too wide, we avoid completely the use of these methods, but stress that a badly estimated covariance matrix may result in a fit that does not reproduce the data. Another common simplification for regression models is the truncation of the covariance matrix to its diagonal components if the latter cannot be estimated safely. This procedure corresponds to an uncorrelated fit, which only weights values with their respective errors but neglects cross correlations between different values. As the interpretation of uncorrelated fits is less obvious we avoid this practice.

8.4.3. Multilinear regression models

Multilinear regression models are characterised by a model function which is multilinear in the fit parameters a , i.e.

$$f_a(X) = \sum_{k=1}^l a_k g_k(X), \quad (8.23)$$

where $X = (X_1, \dots, X_m)$ denotes the set of random variables, and the functions $(g_k)_{k=1, \dots, l}$ determine the particular fit model. We will give more details on this at the end of the section. The advantage of this type of model is that the solution to the fit problem can be determined analytically. Having n individual measurements $(x_i, y_i) = ((x_{1,i}, \dots, x_{m,i}), y_i)$

8. Data analysis for Monte Carlo simulations

for $i = 1, \dots, n$, the χ^2 function reads:

$$\chi_a^2 = \sum_{i,j=1}^n \left(y_i - \sum_{k=1}^l a_k g_k(x_i) \right) (Cov^{-1})_{ij} \left(y_j - \sum_{k=1}^l a_k g_k(x_j) \right). \quad (8.24)$$

In order to solve the minimisation problem, we determine the first and second derivatives of χ_a^2 with respect to the model parameters a using the fact that the covariance matrix and its inverse are symmetric:

$$\frac{\partial \chi_a^2}{\partial a_p} = -2 \sum_{i,j=1}^n g_p(x_i) (Cov^{-1})_{ij} \left(y_j - \sum_{l=1}^m a_l g_l(x_j) \right), \quad (8.25)$$

$$\frac{\partial \chi_a^2}{\partial a_p \partial a_q} = 2 \sum_{i,j=1}^n g_p(x_i) (Cov^{-1})_{ij} g_q(x_j). \quad (8.26)$$

As the covariance matrix and so its inverse are positive definite matrices we can see from the form of $\frac{\partial \chi_a^2}{\partial a_p \partial a_q}$ that any critical point is a local minimum. The optimal choice for the fit parameters a_{opt} is found by solving the system of linear equations $\frac{\partial \chi_a^2}{\partial a_p} |_{a=a_{\text{opt}}} = 0$, i.e.

$$\sum_{l=1}^m \left(\sum_{i,j=1}^n x_{k,i} (Cov^{-1})_{ij} x_{l,j} \right) a_{\text{opt},l} = \sum_{i,j=1}^n x_{k,i} (Cov^{-1})_{ij} y_j \quad k = 1, \dots, m \quad (8.27)$$

with *numpy.linalg.solve*.

We briefly give some examples on how to define the functions $(g_k)_{k=1,\dots,l}$ in dependence of the shape of the model function. For a fit to a function $f_a(X)$ with parameters a_1, \dots, a_l , which is multilinear in the arguments X_1, \dots, X_l , we choose $g_k(X) = X_k$ for $k = 1, \dots, l$. To fit an affine linear function with the parameters a_1 and a_2 , which depends on a single random variable $X = (X_1)$, we use $g_1(X) = 1$ and $g_2(X) = X_1$. This can be generalised to a polynomial model function with degree $l-1$ based on fit parameters a_1, \dots, a_l , which is obtained by setting $g_k(X) = (X_k)^{k-1}$ for $k = 1, \dots, l$.

8.4.4. Linearisation of non-linear fit models by variable substitution

As we have seen, the fit problem associated with multilinear fit models can be solved analytically. This is in general not the case for non-linear fit models, for which iterative solvers have to be used. More computing time has to be spent and initial guesses have to be made for the fit parameters. In some cases, it is, however, possible to perform a variable substitution such that the transformed fit problem is linear. A typical example is a single-exponential fit to a correlation function. It is of the form

$$C(t) = c \exp(-mt), \quad (8.28)$$

where a and m are fit parameters. We can easily linearise this model by applying the logarithm, assuming that the correlation function is positive:

$$\log(C(t)) = \log(c) - mt. \quad (8.29)$$

For a negative correlation function one simply multiplies the equation with -1 before applying the logarithm. Measurements (t, C) are translated into measurements of the linearised model $(x, y) = (t, \log(C))$. The model function of the linearised model, given by $f_a(X) = a_1 - a_2X$ with $a_1 = \log(c)$ and $a_2 = m$, is linear in the parameters a and describes an affine linear function in X .

Part III.

Hadronic renormalisation scheme, scale setting and hadron masses

9. Hadronic renormalisation scheme and scale setting

As in the case of QCD_{iso} , discussed for CLS ensembles in chapter 5, the bare parameters of combined lattice QCD and QED have to be fixed by the application of a renormalisation scheme and a scale setting prescription. In this chapter, we describe the settings currently applied in this work, the formulation of the scheme in the context of the perturbative expansion and potential alternatives.

9.1. Hadronic renormalisation scheme and scale setting

We suggest to fix the bare parameters for combined QCD and QED by a hadronic renormalisation consisting of the value of the average pion mass $\frac{1}{2}(m_{\pi^+} + m_{\pi^0})$, of the average kaon mass $\frac{1}{2}(m_{K^+} + m_{K^0})$ and of the kaon mass splitting $m_{K^+} - m_{K^0}$. There is no need to refer to the scheme utilised for the CLS QCD_{iso} simulations, which is based on the isosymmetric pion and kaon masses $m_{\pi} = 134.8(3)$ MeV and $m_K = 494.2(4)$ MeV [45] as discussed in chapter 5, because the bare parameters of QCD+QED and QCD_{iso} are in principle unrelated. Only the imposition of an intermediate scheme introduces relations among them. Although pseudo-scalar decay constants are used for the scale setting in QCD_{iso} , this is a inconvenient choice for QCD+QED. The determination of isospin breaking corrections to decay constants is demanding, as infrared divergences appear in intermediate stages of the computation. They only cancel taking virtual photons exchanged between quarks and charged decay products as well as emitted real final state photons into account [224–227]. Instead, the scale should be set by an additional hadron mass, e.g. the mass of a baryon. As a first simplification, we neglect the influence of isospin breaking effects to the scale, such that the latter is still determined via $\frac{2}{3}(f_K + \frac{1}{2}f_{\pi})$ in the isosymmetric limit. This will be changed in a more comprehensive future effort. Only taking into account leading order QED effects, the electromagnetic coupling can be defined via the electromagnetic fine-structure constant in the Thomson limit [46]. Otherwise, the bare electromagnetic coupling may be fixed by the inclusion of e.g. the pion mass difference into the hadronic scheme or by determining the corresponding renormalised coupling from the QED Wilson flow [41, 184].

In addition to the definition of the physical point after a continuum extrapolation, we also utilise the latter renormalisation scheme as an intermediate scheme, which relates QCD_{iso} and QCD+QED at finite lattice spacing and unphysical quark masses on each ensemble. This is necessary, as we cannot perform an extrapolation to the physical point due to the limit number of gauge ensembles that we consider in this thesis. We suggest to deter-

9. Hadronic renormalisation scheme and scale setting

mine the shifts of the bare dimensionless parameters $\Delta\varepsilon = (a\Delta m_u, a\Delta m_d, a\Delta m_s, \Delta\beta, e^2)$ by demanding

$$\begin{aligned} am_{\pi^+} + am_{\pi^0} &= (am_{\pi^+})^{(0)} + (am_{\pi^0})^{(0)}, \\ am_{K^+} + am_{K^0} &= (am_{K^+})^{(0)} + (am_{K^0})^{(0)}, \\ am_{K^+} - am_{K^0} &= a(m_{K^+}^{\text{phys}} - m_{K^0}^{\text{phys}}). \end{aligned} \quad (9.1)$$

The scale a should then be determined at a later stage by the mass m_B of an additional baryon, i.e. $a = \frac{am_B}{m_B^{\text{phys}}}$. The $\Delta\beta$ coefficient can be used to correct for a renormalisation of the strong coupling due to the electromagnetic interaction, i.e. for a shift in the scale due to isospin corrections. A tuning allows for a determination of isospin breaking effects at a fixed lattice spacing. As we neglect the latter effects, we set $\Delta\beta = 0$. The electromagnetic coupling does not renormalise at this order and can be fixed to $\Delta\varepsilon_{e^2} = e^2 = 4\pi\alpha_{\text{em}}$. In order to rewrite eq. (9.1) in terms of a perturbative expansion, we expand the hadron masses in terms of $\Delta\varepsilon$:

$$am = (am)^{(0)} + \sum_l \Delta\varepsilon_l (am)_l^{(1)} + O(\Delta\varepsilon^2). \quad (9.2)$$

In total, we obtain a system of linear equations that determines the full set of expansion parameters $\Delta\varepsilon$:

$$\begin{aligned} \sum_l \Delta\varepsilon_l ((am_{\pi^+})_l^{(1)} + (am_{\pi^0})_l^{(1)}) &= 0, \\ \sum_l \Delta\varepsilon_l ((am_{K^+})_l^{(1)} + (am_{K^0})_l^{(1)}) &= 0, \\ \sum_l \Delta\varepsilon_l ((am_{K^+})_l^{(1)} - (am_{K^0})_l^{(1)}) &= a(m_{K^+}^{\text{phys}} - m_{K^0}^{\text{phys}}), \\ \Delta\varepsilon_{\Delta\beta} &= \Delta\beta = 0, \\ \Delta\varepsilon_{e^2} &= e^2 = 4\pi\alpha_{\text{em}}. \end{aligned} \quad (9.3)$$

In this scheme, a summation of zeroth- and first-order contributions is avoided. This is advantageous, as first-order contributions can be smaller in magnitude than the statistical errors of the respective zeroth-order contributions. We discuss the required computational steps to determine hadron masses in chapter 10 and apply them to mesons and baryons in chapter 11 and chapter 12, respectively. The relevant quantities to solve the system of linear equations eq. (9.3) can be found in eqs. (11.55), (11.58), (11.67) and (11.70). The determined expansion parameters for the ensemble N200 read:

$$\begin{aligned} a\Delta m_u &= -0.0090866(23)_{\text{st}}(18)_{\text{a}}[29]_{\text{tot}}, \\ a\Delta m_d &= -0.0020158(25)_{\text{st}}(18)_{\text{a}}[31]_{\text{tot}}, \\ a\Delta m_s &= -0.002280(9)_{\text{st}}[9]_{\text{tot}}, \\ \Delta\beta &= 0.0, \\ e^2 &= 0.091701237. \end{aligned} \quad (9.4)$$

The error with respect to the scale appears, as the dimensionful number $m_{K^+}^{\text{phys}} - m_{K^0}^{\text{phys}}$ from eq. (9.3) has to be translated into a dimensionless quantity. Considering leading order contributions, the expansion parameter $a\Delta m_s$ does not depend on the kaon mass splitting.

9.2. Discussion and Outlook

The results for the expansion parameters for the ensembles N200, D450 and H102 are listed in table 9.1. We observe that all mass detunings are negative. This can be understood considering the fact that the latter also serve as counterterms. They absorb the electromagnetic self-energy contribution to the quark masses. For ensembles with smaller lattice spacings we find smaller, negative quark mass detunings. This is consistent with the fact that self-energy contribution to the quark mass diverges, when the lattice cutoff is removed. It is clear that the values of these expansion parameters are scheme dependent and therefore possess very limited physical meaning. E.g. a distinction of electromagnetic effects from strong isospin breaking effects is non-trivial. Nevertheless, different schemes offer different technical advantages. In [228] it is discussed that in a certain class of schemes one can separate mass isospin corrections from electromagnetic corrections. Those schemes are constructed in a way, such that scheme-ambiguities are higher order effects within this class. They are based on the evaluation and matching of renormalised quark masses determined by means of the axial Ward identity. In particular, a determination of Z_A and Z_S in QCD+QED is required. The latter renormalisation factors have not been determined in this work such that we cannot follow this suggestion.

Another possible matching and renormalisation scheme may rely on an unaltered π^0 mass. In section 3.4.6, we discussed that in chiral QCD+QED in the presence of a massive strange quark the π^0 forms a Goldstone boson. In chiral QCD with a massive strange quark, which is the corresponding isosymmetric theory, covered in section 3.4.4, π^0 , π^+ and π^- form the enlarged set of Goldstone bosons. The π^0 mass vanishes in both chiral theories. This equality can be imposed even for non-vanishing renormalised quark masses such that one obtains a matching condition that is compatible with a chiral extrapolation. The remaining parameters can be determined by matching the masses of K^0 and K^+ . This scheme could be of particular relevance for the renormalisation of composite operators, e.g. the local vector current, which is commonly defined with respect to the chiral limit [72, 111, 229], as discussed in section 13.5.

Instead of setting the electromagnetic coupling by the Thomson limit, one may also think about using a hadronic scheme for the latter. A suitable quantity is the pion mass splitting, which, at leading order, only depends on the electromagnetic coupling and not on any further expansion parameter [46]. Such a scheme would at least to some degree take QED finite size corrections automatically into account, as the value of the bare electromagnetic coupling becomes volume dependent.

9. Hadronic renormalisation scheme and scale setting

$a\Delta m_{\text{u}}$	$-0.0090866(23)_{\text{st}}(18)_{\text{a}}[29]_{\text{tot}}$
$a\Delta m_{\text{d}}$	$-0.0020158(25)_{\text{st}}(18)_{\text{a}}[31]_{\text{tot}}$
$a\Delta m_{\text{s}}$	$-0.002280(9)_{\text{st}}[9]_{\text{tot}}$
$\Delta\beta$	0.0
e^2	0.091701237

(a) N200 ($a = 0.064$ fm, $m_{\pi} = 282$ MeV)

$a\Delta m_{\text{u}}$	$-0.0088818(24)_{\text{st}}(26)_{\text{a}}[35]_{\text{tot}}$
$a\Delta m_{\text{d}}$	$-0.0018500(21)_{\text{st}}(26)_{\text{a}}[33]_{\text{tot}}$
$a\Delta m_{\text{s}}$	$-0.002255(6)_{\text{st}}[6]_{\text{tot}}$
$\Delta\beta$	0.0
e^2	0.091701237

(b) D450 ($a = 0.076$ fm, $m_{\pi} = 216$ MeV)

$a\Delta m_{\text{u}}$	$-0.0087214(86)_{\text{st}}(27)_{\text{a}}[91]_{\text{tot}}$
$a\Delta m_{\text{d}}$	$-0.0018148(76)_{\text{st}}(27)_{\text{a}}[81]_{\text{tot}}$
$a\Delta m_{\text{s}}$	$-0.0021630(84)_{\text{st}}[84]_{\text{tot}}$
$\Delta\beta$	0.0
e^2	0.091701237

(c) H102 ($a = 0.086$ fm, $m_{\pi} = 354$ MeV)

Table 9.1.: Expansion parameters.

10. Hadron spectroscopy

The spectrum of hadronic states can be determined by investigating two-point correlation functions of the form

$$C(t_2, t_1) = \langle \mathcal{O}_2(t_2) \mathcal{O}_1(t_1) \rangle, \quad (10.1)$$

where the operators \mathcal{O}_1 and \mathcal{O}_2 are referred to as creation and annihilation operators, respectively. These interpolation operators have to be chosen such that the quantum numbers of the operators coincide with the quantum numbers of the hadronic state to be studied. In this chapter we classify interpolation operators, perform a spectral decomposition of two-point correlation functions distinguishing between fixed and (anti-)periodic temporal boundary conditions and discuss methods for mass extraction.

10.1. Interpolation operators

Interpolation operators are functionals of lattice field operators and serve to manipulate a quantum mechanical state such that a superposition of states with corresponding symmetry properties are added or removed. A general operator creating or removing a state centred at the position x can be written as

$$\mathcal{O}^x = \frac{1}{\bar{n}!} \frac{1}{n!} O[U, A]^{x \mathbf{a}_{\bar{n}} \dots \mathbf{a}_1 \mathbf{b}_n \dots \mathbf{b}_1} \bar{\Psi}_{\mathbf{a}_{\bar{n}}} \dots \bar{\Psi}_{\mathbf{a}_1} \Psi^{\mathbf{b}_n} \dots \Psi^{\mathbf{b}_1}. \quad (10.2)$$

The tensor O may depend on the gauge fields U and A , if gauge invariant or gauge covariant interpolation operators shall be constructed. Due to the anticommutative nature of the fermion fields $\bar{\Psi}$ and Ψ , only the part of the tensor O that is fully antisymmetric in the indices $\mathbf{a}_{\bar{n}} \dots \mathbf{a}_1$ and fully antisymmetric in the indices $\mathbf{b}_n \dots \mathbf{b}_1$ contributes to the interpolation operator, while all remaining parts are projected to zero. In order to exploit the Feynman diagram technique efficiently, it is convenient to demand the tensor to have the above mentioned symmetry properties, and to introduce a corresponding normalisation factor of $\frac{1}{\bar{n}!} \frac{1}{n!}$. Interpolation operators can be classified depending on how they change the baryon number of the state. One distinguishes between mesonic operators, where the baryon number stays unchanged, and single- and multi-baryonic operators, which increase or diminish the baryon number by an integer. From the fact that each operator Ψ decreases the baryon number by $\frac{1}{3}$ and each operator $\bar{\Psi}$ increases the baryon number by $\frac{1}{3}$ we can deduce, that the baryon number is changed by $\Delta B = \frac{1}{3}(\bar{n} - n)$. Interpolation operators are further classified with respect to their transformational behaviour under field transformations and with respect to quantum numbers associated to the symmetries of the theory. This classification is relevant in order to assign operators to experimentally

10. Hadron spectroscopy

observed particles. We will discuss this in more detail for mesonic interpolation operators in section 11.1.

10.2. Euclidean two-point correlation functions in the continuum

For the following discussion, we consider a complete orthonormal set of eigenstates $(|n\rangle)_{n \in \mathbb{N}_0}$ of a Hamilton operator H with energies $E_0 < E_1 \leq \dots$ and $|0\rangle$ is the unique ground state of the theory. For this setup, we find the relations

$$H|n\rangle = E_n|n\rangle, \quad \mathbb{1} = \sum_n |n\rangle\langle n|, \quad \langle n_2|n_1\rangle = \delta_{n_2, n_1}. \quad (10.3)$$

We match the Schrödinger and Heisenberg picture at $t = 0$ such that the time evolution of an operator is given by

$$O(t) = \exp(tH)O\exp(-tH). \quad (10.4)$$

10.2.1. Fixed boundary conditions

Making use of eq. (2.4), a two-point function with fixed boundary conditions $|i\rangle$ at time $t = 0$ and $|f\rangle$ at time $t = T$ can be expressed as

$$C(t_2, t_1) = \frac{\langle f | \exp(-TH) O_2(t_2) O_1(t_1) | i \rangle}{\langle f | \exp(-TH) | i \rangle}. \quad (10.5)$$

Inserting complete sets of eigenstates of the Hamilton operator

$$C(t_2, t_1) = \frac{\sum_{n_1, n_2, n_3} \langle f | n_3 \rangle \langle n_3 | O_2 | n_2 \rangle \langle n_2 | O_1 | n_1 \rangle \langle n_1 | i \rangle \cdot \exp(-(T - t_2)E_{n_3} - t_1 E_{n_1}) \exp(-(t_2 - t_1)E_{n_2})}{\sum_n \langle f | n \rangle \langle n | i \rangle \exp(-TE_n)}. \quad (10.6)$$

The correlation function is obviously not invariant under translations in the time direction. For large time extents T and large time distances $T - t_2$ and $t_1 - T$, we find the asymptotic behaviour

$$\begin{aligned} C(t_2, t_1) &\rightarrow \frac{\sum_n \langle f | 0 \rangle \langle 0 | O_2 | n \rangle \langle n | O_1 | 0 \rangle \langle 0 | i \rangle \cdot \exp(-(T - (t_2 - t_1))E_0 - (t_2 - t_1)E_n)}{\langle f | 0 \rangle \langle 0 | i \rangle \exp(-TE_0)} \\ &= \sum_n \langle 0 | O_2 | n \rangle \langle n | O_1 | 0 \rangle \exp(-(t_2 - t_1)(E_n - E_0)), \end{aligned} \quad (10.7)$$

where we have assumed that the vacuum state has non-vanishing overlap with the boundary states. In this asymptotic regime, translational invariance in the time coordinate is restored. In principle, it is also possible to consider not only consider the overlap between the boundary state and the vacuum but also between the boundary state and higher excitations. This results in an improved asymptotic description of the correlation function, i.e. the time interval for which the asymptotic behaviour is a good description is longer.

10.2.2. Periodic boundary conditions

For periodic boundary conditions we start from eq. (2.4):

$$C(t_2, t_1) = \frac{\sum_n \langle n | \exp(-TH) O_2(t_2) O_1(t_1) | n \rangle}{\sum_n \langle n | \exp(-TH) | n \rangle}. \quad (10.8)$$

The spectral decomposition in this setup becomes [42]

$$C(t_2, t_1) = \frac{\sum_{n_1, n_2} \langle n_1 | O_2 | n_2 \rangle \langle n_2 | O_1 | n_1 \rangle \exp(-\frac{T}{2}(E_{n_2} + E_{n_1})) \cdot \exp((\frac{T}{2} - (t_2 - t_1))(E_{n_2} - E_{n_1}))}{\sum_n \exp(-TE_n)}. \quad (10.9)$$

The correlation function only depends on the time difference $t_2 - t_1$. Thus, it is manifestly invariant under time translations, i.e. it becomes a one-argument function $C(t_2, t_1) = C(t_2 - t_1, 0)$. As the asymptotic behaviour is independent of the boundary states, we find the same relation for periodic boundary conditions as for fixed boundary conditions:

$$C(t_2, t_1) \rightarrow \sum_n \langle 0 | O_2 | n \rangle \langle n | O_1 | 0 \rangle \exp(-(t_2 - t_1)(E_n - E_0)). \quad (10.7)$$

Assuming that the operators O_2 and O_1 fulfil the condition

$$\langle n_1 | O_2 | n_2 \rangle \langle n_2 | O_1 | n_1 \rangle = \langle n_2 | O_2 | n_1 \rangle \langle n_1 | O_1 | n_2 \rangle, \quad (10.10)$$

which is for example the case for $O_2 = \pm O_1$, the spectral decomposition of the correlation function can be further simplified to

$$C(t_2, t_1) = \frac{\sum_{n_1, n_2} \langle n_1 | O_2 | n_2 \rangle \langle n_2 | O_1 | n_1 \rangle \exp(-\frac{T}{2}(E_{n_2} + E_{n_1})) \cdot \cosh(((t_2 - t_1) - \frac{T}{2})(E_{n_2} - E_{n_1}))}{\sum_n \exp(-TE_n)}, \quad (10.11)$$

i.e. the correlation function is symmetric under a reflection at $t = \frac{T}{2}$.

10.3. Mass determination by fitting the correlation function

For interpolation operators that create and annihilate states of zero momentum the energy differences $E_n - E_0$ can be interpreted as the masses of excitations of the vacuum.

10.3.1. Asymptotic behaviour for large time extents

Assuming $0 \ll t_1 \ll t_2 \ll T$ the asymptotic behaviour eq. (10.7) translates further into

$$C(t_2, t_1) \rightarrow c \exp(-m(t_2 - t_1)). \quad (10.12)$$

In this regime, only the lowest eigenstate compatible with the operators and boundary conditions is accessible, i.e. the relevant overlaps do not vanish. As we treat isospin

10. Hadron spectroscopy

breaking effects perturbatively, the respective expansion also has to be applied to the asymptotic behaviour. We expand the parameters

$$c = c^{(0)} + \sum_l \Delta\varepsilon_l c_l^{(1)} + O(\Delta\varepsilon^2), \quad m = m^{(0)} + \sum_l \Delta\varepsilon_l m_l^{(1)} + O(\Delta\varepsilon^2) \quad (10.13)$$

as well as the correlation function

$$C(t_2, t_1) = C^{(0)}(t_2, t_1) + \sum_l \Delta\varepsilon_l C_l^{(1)}(t_2, t_1) + O(\Delta\varepsilon^2). \quad (6.85)$$

For the zeroth-order contribution we find

$$C^{(0)}(t_2, t_1) \rightarrow c^{(0)} \exp(-m^{(0)}(t_2 - t_1)) \quad (10.14)$$

and for the first-order contribution

$$C_l^{(1)}(t_2, t_1) \rightarrow (c_l^{(1)} - c^{(0)} m_l^{(1)}(t_2 - t_1)) \exp(-m^{(0)}(t_2 - t_1)). \quad (10.15)$$

10.3.2. Periodic temporal boundary conditions and symmetric correlation functions

For periodic temporal boundary conditions and a symmetric correlation function, we find in the asymptotic regime $0 \ll t_1 \ll t_2 \ll T$, starting from eq. (10.11), that

$$C(t_2, t_1) \rightarrow c \cosh\left(m\left((t_2 - t_1) - \frac{T}{2}\right)\right). \quad (10.16)$$

Similarly, as in the previous section, we perform the perturbative expansion which, yields the zeroth-order contribution

$$C^{(0)}(t_2, t_1) \rightarrow c^{(0)} \cosh\left(m^{(0)}\left((t_2 - t_1) - \frac{T}{2}\right)\right) \quad (10.17)$$

and the first-order contribution

$$\begin{aligned} C_l^{(1)}(t_2, t_1) &\rightarrow c_l^{(1)} \cosh\left(m^{(0)}\left((t_2 - t_1) - \frac{T}{2}\right)\right) \\ &+ c^{(0)} m_l^{(1)}\left((t_2 - t_1) - \frac{T}{2}\right) \sinh\left(m^{(0)}\left((t_2 - t_1) - \frac{T}{2}\right)\right), \end{aligned} \quad (10.18)$$

respectively.

10.4. Mass determination by fitting the effective mass

Another way to extract the lowest accessible mass, which we have implemented as a cross check, is to consider the so called effective mass of the correlation function [42, 98]. It is defined as

$$m_{\text{eff}}(t_2, t_1) = \frac{1}{a} \log\left(\frac{C(t_2, t_1)}{C(t_2 + a, t_1)}\right), \quad (10.19)$$

10.4. Mass determination by fitting the effective mass

where a denotes the minimal distance between two time slices. The prefactor $\frac{1}{a}$ has to be introduced for dimensional reasons. In the limit $a \rightarrow 0$, the effective mass becomes $m_{\text{eff}}(t_2, t_1) \rightarrow -\frac{d}{dt_2} \log(C(t_2, t_1))$. In principle it is also possible to define effective masses for time differences that are integer multiples of a . This is of particular relevance for staggered fermions. Making use of eq. (10.12), it is straightforward to show, that the effective mass has in the regime $0 \ll t_1 \ll t_2 \ll T$ the asymptotic behaviour

$$m_{\text{eff}}(t_2, t_1) \rightarrow \frac{1}{a} \log \left(\frac{c \exp(-m(t_2 - t_1))}{c \exp(-m(t_2 + a - t_1))} \right) = \frac{1}{a} \log \left(\frac{1}{\exp(-am)} \right) = m. \quad (10.20)$$

In order to derive the perturbative expansion of the effective mass

$$m_{\text{eff}}(t_2, t_1) = (m_{\text{eff}}(t_2, t_1))^{(0)} + \sum_l \Delta \varepsilon_l (m_{\text{eff}}(t_2, t_1))_l^{(1)} + O(\Delta \varepsilon^2), \quad (10.21)$$

we utilise eq. (10.19) and eq. (6.85). The zeroth-order contribution is then given by [194]

$$(m_{\text{eff}}(t_2, t_1))^{(0)} = \log \left(\frac{(C(t_2, t_1))^{(0)}}{(C(t_2 + a, t_1))^{(0)}} \right) \rightarrow m^{(0)} \quad (10.22)$$

and the first-order contribution [194]

$$(m_{\text{eff}}(t_2, t_1))_l^{(1)} = \frac{(C(t_2, t_1))_l^{(1)}}{(C(t_2, t_1))^{(0)}} - \frac{(C(t_2 + a, t_1))_l^{(1)}}{(C(t_2 + a, t_1))^{(0)}} \rightarrow m_l^{(1)}. \quad (10.23)$$

11. Meson masses

In chapter 9, we stated that we want to utilise pseudo-scalar meson masses as a hadronic renormalisation scheme to fix the bare parameters of QCD+QED. In this chapter, we describe how to construct interpolation operators and two-point functions that can be used to determine the mesonic spectrum. We give the diagrammatic expansion of mesonic two-point functions and describe how we evaluate the quark-connected contributions. We discuss our findings for pseudo-scalar meson masses on the basis on one ensemble in more detail.

11.1. Mesonic interpolation operators

In order to extract masses of mesonic states from the QCD+QED spectrum, we consider two-point correlation functions with mesonic interpolation operators. According to the discussion in section 10.1, the simplest form of a zero-momentum projected operator interpolating a mesonic state is constructed with one quark and one antiquark operator:

$$\mathcal{M}^{x^0} = \frac{1}{\sqrt{|\Lambda_{123}|}} \sum_{\vec{x}} \bar{\Psi}_{\mathbf{a}} M[U, A]^{x\mathbf{a}}_{\mathbf{b}} \Psi^{\mathbf{b}}. \quad (11.1)$$

11.1.1. Point-like mesonic interpolation operators

A particular simple subset of interpolation operators is formed by point-like interpolation operators. The interpolation operator defined at a site x only depends on the fields at this particular site. It is further convenient to express the spin and flavour structure of the interpolation operator in terms of matrices Λ , which acts on the flavour indices of the field operators, and Γ , which acts on the spin indices. Λ determines the flavour quantum numbers of the annihilated meson and Γ its spin and parity. In its most general form, the point-like zero-momentum projected interpolation operator is given by [42]

$$\mathcal{M}^{x^0} = \frac{1}{\sqrt{|\Lambda_{123}|}} \sum_{\vec{x}} \bar{\Psi}^x \Gamma \Lambda \Psi^x, \quad (11.2)$$

where we have omitted spin and flavour indices. In order to create a state that is annihilated by the operator \mathcal{M}^{x^0} we apply the charge conjugation transformation. Using

11. Meson masses

J	P	Γ	\mathcal{O}
0	+	$\mathbb{1}, \gamma^0$	$\mathcal{S}, \mathcal{V}^0$
0	-	$\gamma^5, \gamma^5 \gamma^0$	$\mathcal{P}, \mathcal{A}^0$
1	-	$\gamma^1, \gamma^2, \gamma^3, \sigma^{01}, \sigma^{02}, \sigma^{03}$	$\mathcal{V}^1, \mathcal{V}^2, \mathcal{V}^3, \mathcal{T}^{01}, \mathcal{T}^{02}, \mathcal{T}^{03}$
1	+	$\gamma^5 \gamma^1, \gamma^5 \gamma^2, \gamma^5 \gamma^3$	$\mathcal{A}^1, \mathcal{A}^2, \mathcal{A}^3$
2	+	$\sigma^{12}, \sigma^{23}, \sigma^{31}$	$\mathcal{T}^{12}, \mathcal{T}^{23}, \mathcal{T}^{31}$

Table 11.1.: Classification of the Γ matrices and the corresponding operators \mathcal{O} according to the transformation properties under Euclidean transformations.

(p, q)	I	I_3	Y	U	D	S	Q	Λ
(0, 0)	0	0	0	0	0	0	0	$\Lambda^0 = \frac{1}{\sqrt{6}} \mathbb{1}$
(1, 1)	1	1	0	1	1	0	1	$\Lambda^{\bar{u}d} = \frac{1}{2}(\lambda^1 + i\lambda^2)$
(1, 1)	1	0	0	0	0	0	0	$\Lambda^3 = \frac{1}{2}\lambda^3$
(1, 1)	1	-1	0	-1	-1	0	-1	$\Lambda^{\bar{d}u} = \frac{1}{2}(\lambda^1 - i\lambda^2)$
(1, 1)	0	0	0	0	0	0	0	$\Lambda^8 = \frac{1}{2}\lambda^8$
(1, 1)	$\frac{1}{2}$	$\frac{1}{2}$	1	1	0	1	1	$\Lambda^{\bar{u}s} = \frac{1}{2}(\lambda^4 + i\lambda^5)$
(1, 1)	$\frac{1}{2}$	$-\frac{1}{2}$	1	0	-1	-1	-1	$\Lambda^{\bar{s}u} = \frac{1}{2}(\lambda^4 - i\lambda^5)$
(1, 1)	$\frac{1}{2}$	$-\frac{1}{2}$	-1	0	1	1	0	$\Lambda^{\bar{d}s} = \frac{1}{2}(\lambda^6 + i\lambda^7)$
(1, 1)	$\frac{1}{2}$	$\frac{1}{2}$	-1	-1	0	-1	0	$\Lambda^{\bar{s}d} = \frac{1}{2}(\lambda^6 - i\lambda^7)$

Table 11.2.: Classification of Λ matrices according to the approximate $SU(3)$ flavour symmetry in the representation (p, q) with eigenvalues of the operators I , I_3 , Y with $Q = \frac{2}{3}U + \frac{1}{3}D + \frac{1}{3}S$, $I_3 = \frac{1}{2}(U + D)$, $Y = \frac{1}{3}(U + D - 2S)$. In QCD+QED only U , D , S and Q are good quantum numbers.

eq. (6.32) we find that \mathcal{M}^{x^0} transforms via

$$\begin{aligned}
\mathfrak{e}[\mathcal{M}^{x^0}] &= -\frac{1}{\sqrt{|\Lambda_{123}|}} \sum_{\vec{x}} (\Psi^x)^T C \Gamma C^{-1} \Lambda (\bar{\Psi}^x)^T \\
&= \frac{1}{\sqrt{|\Lambda_{123}|}} \sum_{\vec{x}} \bar{\Psi}^x (C \Gamma C^{-1})^T \Lambda^T \Psi^x,
\end{aligned} \tag{11.3}$$

where we have utilised the anti-commutation property of fermion fields. Accordingly, the creation operator is obtained from the annihilation operator by replacing Λ with Λ^T and Γ with $(C \Gamma C^{-1})^T$ with $C = i\gamma^0 \gamma^2$.

11.1.2. Classification of interpolation operators

In order to find suitable interpolation operators for physical states, we classify the interpolation operators according to their behaviour under spacetime and charge conjugation

transformations and with respect to their quark content. We distinguish scalar \mathcal{S} , pseudo-scalar \mathcal{P} , vector \mathcal{V} , axial-vector \mathcal{A} and tensor operators \mathcal{T} :

$$\mathcal{S}^x = \bar{\Psi}^x \Lambda \Psi^x, \quad (11.4)$$

$$\mathcal{P}^x = \bar{\Psi}^x \gamma^5 \Lambda \Psi^x, \quad (11.5)$$

$$\mathcal{V}^{x\mu} = \bar{\Psi}^x \gamma^\mu \Lambda \Psi^x, \quad (11.6)$$

$$\mathcal{A}^{x\mu} = \bar{\Psi}^x \gamma^5 \gamma^\mu \Lambda \Psi^x, \quad (11.7)$$

$$\mathcal{T}^{x\mu_2\mu_1} = \bar{\Psi}^x \sigma^{\mu_2\mu_1} \Lambda \Psi^x. \quad (11.8)$$

Making use of eqs. (6.35) and (6.36) we can determine the transformational behaviour of \mathcal{M}^{x^0} under the spatial parity transformation:

$$\mathfrak{P}[\mathcal{M}^{x^0}] = \frac{1}{\sqrt{|\Lambda_{123}|}} \sum_{\vec{x}} \bar{\Psi}^x \gamma^0 \Gamma \gamma^0 \Lambda \Psi^x. \quad (11.9)$$

For the operators defined in eqs. (11.4) to (11.8) this means

$$\mathfrak{P}[\mathcal{S}^x] = \mathcal{S}^{\mathfrak{P}(x)}, \quad (11.10)$$

$$\mathfrak{P}[\mathcal{P}^x] = -\mathcal{P}^{\mathfrak{P}(x)}, \quad (11.11)$$

$$\mathfrak{P}[\mathcal{V}^{x\mu}] = (-1)^{\mu_0} \mathcal{V}^{\mathfrak{P}(x)\mu}, \quad (11.12)$$

$$\mathfrak{P}[\mathcal{A}^{x\mu}] = -(-1)^{\mu_0} \mathcal{A}^{\mathfrak{P}(x)\mu}, \quad (11.13)$$

$$\mathfrak{P}[\mathcal{T}^{x\mu_2\mu_1}] = (-1)^{\mu_2 0} (-1)^{\mu_1 0} \mathcal{T}^{\mathfrak{P}(x)}, \quad (11.14)$$

where the symbol $(-1)^{\mu_2\mu_1}$ is defined as

$$(-1)^{\mu_2\mu_1} = \begin{cases} 1 & \text{for } \mu_2 = \mu_1 \\ -1 & \text{for } \mu_2 \neq \mu_1 \end{cases}. \quad (6.33)$$

In addition, we classify the operators according to their behaviour under $SU(3)_V$ transformations. The transformation characteristics are determined by the flavour matrices Λ^i . We distinguish the nine matrices Λ^i for $i = 0, 3, 8, \bar{u}d, \bar{d}u, \bar{d}s, \bar{s}d, \bar{u}s, \bar{s}u$, which are classified according to the flavour quantum numbers U , D and S . In table 11.2 the relevant properties are described.

11.2. Mesonic two-point functions

In the following, we consider correlation functions of the form

$$C_{\mathcal{M}_2\mathcal{M}_1}(x_2^0, x_1^0) = \langle \mathcal{M}_2^{x_2^0} \mathcal{M}_1^{x_1^0} \rangle \quad (11.15)$$

with point-like zero-momentum projected interpolation operators defined in eq. (11.2), which have support on the time slices x_2^0 and x_1^0 respectively.

11. Meson masses

Γ_2, Γ_1	$\mathbb{1}$	γ^0	$\gamma^5 \gamma^1$	$\gamma^5 \gamma^2$	$\gamma^5 \gamma^3$	σ^{12}	σ^{23}	σ^{31}
$\mathbb{1}$	•	•						
γ^0	•	•						
$\gamma^5 \gamma^1$			•					
$\gamma^5 \gamma^2$				•				
$\gamma^5 \gamma^3$					•			
σ^{12}						•		
σ^{23}							•	
σ^{31}								•

Table 11.3.: Spin matrix combinations (Γ_2, Γ_1) with potentially non-vanishing mesonic two-point functions $C_{\mathcal{M}_2 \mathcal{M}_1}(x_2^0, x_1^0) = \langle \mathcal{M}_2^{x_2^0} \mathcal{M}_1^{x_1^0} \rangle$ with parity-even operators $\mathcal{M}_i^{x_0} = \frac{1}{\sqrt{|\Lambda_{123}|}} \sum_{\vec{x}} \bar{\Psi}^x \Lambda_i \Gamma_i \Psi^x$ for $i = 1, 2$ are marked with a dot •.

Γ_2, Γ_1	γ^5	$\gamma^5 \gamma^0$	γ^1	γ^2	γ^3	σ^{01}	σ^{02}	σ^{03}
γ^5	•	•						
$\gamma^5 \gamma^0$	•	•						
γ^1			•			•		
γ^2				•			•	
γ^3					•			•
σ^{01}			•			•		
σ^{02}				•			•	
σ^{03}					•			•

Table 11.4.: Spin matrix combinations (Γ_2, Γ_1) with potentially non-vanishing mesonic two-point functions $C_{\mathcal{M}_2 \mathcal{M}_1}(x_2^0, x_1^0) = \langle \mathcal{M}_2^{x_2^0} \mathcal{M}_1^{x_1^0} \rangle$ with parity-odd operators $\mathcal{M}_i^{x_0} = \frac{1}{\sqrt{|\Lambda_{123}|}} \sum_{\vec{x}} \bar{\Psi}^x \Lambda_i \Gamma_i \Psi^x$ for $i = 1, 2$ are marked with a dot •.

Λ_2, Λ_1	Λ^0	Λ^3	Λ^8	$\Lambda^{\bar{u}d}$	$\Lambda^{\bar{d}u}$	$\Lambda^{\bar{d}s}$	$\Lambda^{\bar{s}d}$	$\Lambda^{\bar{u}s}$	$\Lambda^{\bar{s}u}$
Λ^0	•	•	•						
Λ^3	•	•	•						
Λ^8	•	•	•						
$\Lambda^{\bar{u}d}$					•				
$\Lambda^{\bar{d}u}$				•					
$\Lambda^{\bar{d}s}$							•		
$\Lambda^{\bar{s}d}$						•			
$\Lambda^{\bar{u}s}$									•
$\Lambda^{\bar{s}u}$								•	

Table 11.5.: Flavour matrix combinations (Λ_2, Λ_1) with potentially non-vanishing mesonic two-point functions $C_{\mathcal{M}_2 \mathcal{M}_1}(x_2^0, x_1^0) = \langle \mathcal{M}_2^{x_2^0} \mathcal{M}_1^{x_1^0} \rangle$ with operators $\mathcal{M}_i^{x_i^0} = \frac{1}{\sqrt{|\Lambda_{123}|}} \sum_{\vec{x}} \bar{\Psi}^x \Lambda_i \Gamma_i \Psi^x$ for $i = 1, 2$ are marked with a dot •.

11.2.1. Operator combinations

In order to utilise computing time efficiently, we determine which combinations of Γ and Λ matrices lead to non-vanishing expectation values applying symmetry arguments based on section 2.3.2. Considering the global QCD+QED symmetry transformations

$$\mathfrak{T}_{U(1)_{V,f}}(\pi)[(A_s, A_e, \Psi, \bar{\Psi})] = (A_s, A_e, \exp(i\pi T_{U(1)_{V,f}})\Psi, \bar{\Psi} \exp(-i\pi T_{U(1)_{V,f}})) \quad (11.16)$$

for $f = u, d, s$ with the generators defined in eq. (3.63), which generate -1 factors for flavour charged operators, one can argue that all combinations but 15 have vanishing expectation values. The combinations are listed in table 11.5. In contrast to QCD_{iso} , all combinations of flavour-neutral operators based on Λ^0 , Λ^3 and Λ^8 potentially lead to non-vanishing expectation values. In the isosymmetric limit, an overlap between Λ^3 and Λ^0 or Λ^8 is excluded due to the conservation of isospin. Similarly, we construct Euclidean spacetime lattice transformations that generate factors of -1 based on the parity transformation $\mathfrak{P} = \mathfrak{P}^0$ and reflections \mathfrak{R}^μ along the spatial μ -axis

$$\mathfrak{R}^\mu = \prod_{\substack{\nu=0 \\ \nu \neq \mu}}^3 \mathfrak{P}^\nu. \quad (11.17)$$

\mathfrak{P}^ν denote the Euclidean reflections defined in eq. (6.35). We find 10 potentially non-vanishing combinations of parity-even operators, listed in table 11.3, and 16 potentially non-vanishing combinations of parity-odd operators, given in table 11.4. The combination of a parity-even and a parity-odd operator vanishes in QCD+QED as parity is a symmetry, i.e. only 26 out of the 256 combinations have to be considered in the computation.

11.2.2. Diagrammatic expansion

The generic expansion of the correlation function up to first order reads

$$C = C^{(0)} + \sum_l \Delta \varepsilon_l C_l^{(1)} + O(\Delta \varepsilon^2). \quad (6.85)$$

In order to determine the perturbative expansion of the correlation function, we expand the interpolation operators according to

$$\mathcal{O} = \mathcal{O}^{(0)} + e \mathcal{O}_{e^2}^{(\frac{1}{2})} + \frac{1}{2} e^2 \mathcal{O}_{e^2}^{(1)} + O(e^3). \quad (6.86)$$

As the point-like operators do not depend on eA , we have $\mathcal{M}_1 = (\mathcal{M}_1)^{(0)}$ and $\mathcal{M}_2 = (\mathcal{M}_2)^{(0)}$. We represent the vertex $M^{(0)x^0}$ associated with the operator $(\mathcal{M}^{x^0})^{(0)}$ by the diagram

$$M^{(0)x^0} \mathbf{a}_\mathbf{b} = \begin{array}{c} \mathbf{a} \quad \bullet \quad \bullet \quad \mathbf{b} \\ \hline M^{(0)x^0} \end{array}. \quad (11.18)$$

The zeroth-order contribution is calculated via eq. (6.87) and reads in terms of Feynman diagrams

$$(C_{\mathcal{M}_2 \mathcal{M}_1})^{(0)} = \left\langle \begin{array}{c} M_2^{(0)} \bullet \quad \bullet \quad M_1^{(0)} \\ \text{diagram} \end{array} + \begin{array}{c} M_2^{(0)} \bullet \quad \bullet \quad M_1^{(0)} \\ \text{diagram} \end{array} \right\rangle_{\text{eff}}^{(0)} \quad (11.19)$$

The first-order contribution is calculated according to eq. (6.88). In terms of Feynman diagrams, the first-order contribution due to a shift in the quark mass Δm_f reads

$$\begin{aligned} (C_{\mathcal{M}_2 \mathcal{M}_1})_{\Delta m_f}^{(1)} = & \left\langle \begin{array}{c} M_2^{(0)} \bullet \quad \bullet \quad M_1^{(0)} \\ \text{diagram} \end{array} + \begin{array}{c} M_2^{(0)} \bullet \quad \bullet \quad M_1^{(0)} \\ \text{diagram} \end{array} \right. \\ & + \begin{array}{c} M_2^{(0)} \bullet \quad \bullet \quad M_1^{(0)} \\ \text{diagram} \end{array} + \begin{array}{c} M_2^{(0)} \bullet \quad \bullet \quad M_1^{(0)} \\ \text{diagram} \end{array} \\ & + \left(\begin{array}{c} M_2^{(0)} \bullet \quad \bullet \quad M_1^{(0)} \\ \text{diagram} \end{array} + \begin{array}{c} M_2^{(0)} \bullet \quad \bullet \quad M_1^{(0)} \\ \text{diagram} \end{array} \right) \begin{array}{c} \bullet \quad \bullet \\ \text{diagram} \end{array} \Big\rangle_{\text{eff}}^{(0)} \\ & - \left\langle \begin{array}{c} M_2^{(0)} \bullet \quad \bullet \quad M_1^{(0)} \\ \text{diagram} \end{array} + \begin{array}{c} M_2^{(0)} \bullet \quad \bullet \quad M_1^{(0)} \\ \text{diagram} \end{array} \right\rangle_{\text{eff}}^{(0)} \left\langle \begin{array}{c} \bullet \quad \bullet \\ \text{diagram} \end{array} \right\rangle_{\text{eff}}^{(0)}. \end{aligned} \quad (11.20)$$

A detuning in the strong inverse coupling $\Delta\beta$ results in a first-order contribution

$$\begin{aligned}
 (C_{\mathcal{M}_2\mathcal{M}_1})_{\Delta\beta}^{(1)} = & \left\langle \left(M_2^{(0)} \text{---} \text{---} M_1^{(0)} + M_2^{(0)} \text{---} \text{---} M_1^{(0)} \right) \right\rangle_{\text{eff}}^{(0)} \\
 & - \left\langle M_2^{(0)} \text{---} \text{---} M_1^{(0)} + M_2^{(0)} \text{---} \text{---} M_1^{(0)} \right\rangle_{\text{eff}}^{(0)} \left\langle \text{---} \right\rangle_{\text{eff}}^{(0)} .
 \end{aligned} \tag{11.21}$$

The first-order contribution due to a non-vanishing electromagnetic coupling e^2 reads

$$\begin{aligned}
 (C_{\mathcal{M}_2\mathcal{M}_1})_{e^2}^{(1)} = & \left\langle \begin{array}{l} M_2^{(0)} \text{---} \text{---} M_1^{(0)} \\ + M_2^{(0)} \text{---} \text{---} M_1^{(0)} + M_2^{(0)} \text{---} \text{---} M_1^{(0)} \\ + M_2^{(0)} \text{---} \text{---} M_1^{(0)} + M_2^{(0)} \text{---} \text{---} M_1^{(0)} \\ + M_2^{(0)} \text{---} \text{---} M_1^{(0)} + M_2^{(0)} \text{---} \text{---} M_1^{(0)} \\ + M_2^{(0)} \text{---} \text{---} M_1^{(0)} + M_2^{(0)} \text{---} \text{---} M_1^{(0)} \\ + M_2^{(0)} \text{---} \text{---} M_1^{(0)} + M_2^{(0)} \text{---} \text{---} M_1^{(0)} \\ + M_2^{(0)} \text{---} \text{---} M_1^{(0)} + M_2^{(0)} \text{---} \text{---} M_1^{(0)} \end{array} \right\rangle
 \end{aligned} \tag{11.22}$$

11. Meson masses

$$\begin{aligned}
& + \left(\text{Diagram 1} + \text{Diagram 2} \right) \\
& + \left(\text{Diagram 3} + \text{Diagram 4} \right) \\
& \cdot \left(\text{Diagram 5} + \text{Diagram 6} + \text{Diagram 7} \right) \Bigg\rangle_{\text{eff}}^{(0)} \\
& - \left\langle \text{Diagram 3} + \text{Diagram 4} \right\rangle_{\text{eff}}^{(0)} \\
& \cdot \left\langle \text{Diagram 5} + \text{Diagram 6} + \text{Diagram 7} \right\rangle_{\text{eff}}^{(0)}.
\end{aligned}$$

In this thesis, we only consider quark-connected contributions in our calculation. We translate the corresponding Feynman diagrams into contracted tensor-structures of interpolation operators, quark and photon propagators and vertices. This is relevant to ensure the correct application of minus signs and symmetry factors. For the zeroth-order diagram we have

$$\text{Diagram 3} = - \left(S^{\mathbf{b}_1}_{\mathbf{a}_3} M_2^{(0)\mathbf{a}_2}_{\mathbf{b}_2} S^{\mathbf{b}_2}_{\mathbf{a}_1} M_1^{(0)\mathbf{a}_1}_{\mathbf{b}_1} \right). \quad (11.23)$$

Diagrams with first-order contributions due to the quark mass detuning read

$$\text{Diagram 5} = - \left(S^{\mathbf{b}_1}_{\mathbf{a}_3} M_2^{(0)\mathbf{a}_3}_{\mathbf{b}_3} S^{\mathbf{b}_3}_{\mathbf{a}_2} V_{\bar{q}qf}^{\mathbf{a}_2}_{\mathbf{b}_2} S^{\mathbf{b}_2}_{\mathbf{a}_1} M_1^{(0)\mathbf{a}_1}_{\mathbf{b}_1} \right), \quad (11.24)$$

$$\text{Diagram 6} = - \left(S^{\mathbf{b}_1}_{\mathbf{a}_3} V_{\bar{q}qf}^{\mathbf{a}_3}_{\mathbf{b}_3} S^{\mathbf{b}_3}_{\mathbf{a}_2} M_2^{(0)\mathbf{a}_2}_{\mathbf{b}_2} S^{\mathbf{b}_2}_{\mathbf{a}_1} M_1^{(0)\mathbf{a}_1}_{\mathbf{b}_1} \right). \quad (11.25)$$

11.3. Computation of quark-connected Feynman diagrams

Diagrams with first-order contributions due to the electromagnetic interaction read

$$M_2^{(0)} \text{---} M_1^{(0)} = -\Sigma^{c_2 c_1} \left(S^{b_1}_{a_4} V_{\bar{q}q\gamma}^{a_4 b_4 c_2} S^{b_4}_{a_3} M_2^{(0) a_3 b_3} \cdot S^{b_3}_{a_2} V_{\bar{q}q\gamma}^{a_2 b_2 c_1} S^{b_2}_{a_1} M_1^{(0) a_1 b_1} \right), \quad (11.26)$$

$$M_2^{(0)} \text{---} M_1^{(0)} = -\frac{1}{2} \Sigma^{c_2 c_1} \left(S^{b_1}_{a_3} M_2^{(0) a_3 b_3} \cdot S^{b_3}_{a_2} V_{\bar{q}q\gamma\gamma}^{a_2 b_2 c_2 c_1} S^{b_2}_{a_1} M_1^{(0) a_1 b_1} \right), \quad (11.27)$$

$$M_2^{(0)} \text{---} M_1^{(0)} = -\Sigma^{c_2 c_1} \left(S^{b_1}_{a_4} M_2^{(0) a_4 b_4} S^{b_4}_{a_3} V_{\bar{q}q\gamma}^{a_3 b_3 c_2} \cdot S^{b_3}_{a_2} V_{\bar{q}q\gamma}^{a_2 b_2 c_1} S^{b_2}_{a_1} M_1^{(0) a_1 b_1} \right), \quad (11.28)$$

$$M_2^{(0)} \text{---} M_1^{(0)} = -\frac{1}{2} \Sigma^{c_2 c_1} \left(S^{b_1}_{a_3} V_{\bar{q}q\gamma\gamma}^{a_3 b_3 c_2 c_1} S^{b_3}_{a_2} M_2^{(0) a_2 b_2} \cdot S^{b_2}_{a_1} M_1^{(0) a_1 b_1} \right), \quad (11.29)$$

$$M_2^{(0)} \text{---} M_1^{(0)} = -\Sigma^{c_2 c_1} \left(S^{b_1}_{a_4} V_{\bar{q}q\gamma}^{a_4 b_4 c_2} S^{b_4}_{a_3} V_{\bar{q}q\gamma}^{a_3 b_3 c_1} \cdot S^{b_3}_{a_2} M_2^{(0) a_2 b_2} S^{b_2}_{a_1} M_1^{(0) a_1 b_1} \right). \quad (11.30)$$

The only contribution from the reweighting factor that we consider is

$$\Delta\beta = V_g. \quad (11.31)$$

11.3. Computation of quark-connected Feynman diagrams

We introduce two methods to evaluate quark-connected Feynman diagrams with different types of quark sources, continuing the discussion of section 7.1. A first implementation of quark-connected Feynman diagrams was based on point sources. We later changed to stochastic sources, which allow for a more efficient evaluation of quark-connected contributions to mesonic two-point functions on large lattices compared to point sources. We discuss both setups for the zeroth-order quark-connected Feynman diagram defined eq. (11.23) in more detail and later generalise to the remaining quark-connected Feynman diagrams. The implementation of the simulation code is based on data structures provided by the QDP++ library [206].

11.3.1. Point sources

A flavour-colour-spin linked point source η_{x_0} , located at the lattice site x_0 , is a matrix in flavour, colour and spin space and a vector in spacetime. The location x_0 is written as an

11. Meson masses

additional index, but the value of x_0 is fixed and characterises the source. The source is given by [42]

$$\eta_{x_0, (fcs)_1}^{(x fcs)_2} = \delta_{x_0}^{x_2} \delta_{f_1}^{f_2} \delta_{c_1}^{c_2} \delta_{s_1}^{s_2}. \quad (11.32)$$

We define the corresponding propagated source $\Psi[\eta]_{x_0}$, which depends on the point source η_{x_0} , by solving the Dirac equation

$$D^{\mathbf{a}}_{\mathbf{b}} \Psi[\eta]_{x_0 fcs}^{\mathbf{b}} = \eta_{x_0, fcs}^{\mathbf{a}}. \quad (11.33)$$

$\Psi[\eta]_{x_0}$ again is a matrix in flavour, colour and spin space and a vector in spacetime. Point sources can be used, whenever a correlation function can be expressed in terms of a set of point-to-all propagators $S^x_{x_0} = \Psi[\eta]_{x_0}^x$, which start at a small number of fixed source locations x^0 . The diagram in eq. (11.23) with two point-like zero-momentum projected mesonic operators \mathcal{M}_2 and \mathcal{M}_1 , which have support on the time slices x_2^0 and x_1^0 , can be evaluated by means of $\Psi[\eta]_{x_0}$:

$$\begin{aligned} & \left\langle M_2^{(0)} \begin{array}{c} \curvearrowright \\ \curvearrowleft \end{array} M_1^{(0)} \right\rangle_{\text{eff}}^{(0)} \\ &= \left\langle -\frac{1}{|\Lambda_{123}|} \sum_{\vec{x}_2, \vec{x}_1} \text{tr} \left(S^{x_1}_{x_2} \Lambda_2 \Gamma_2 S^{x_2}_{x_1} \Lambda_1 \Gamma_1 \right) \right\rangle_{\text{eff}}^{(0)} \\ &= \left\langle -\frac{1}{|\Lambda_{123}|} \sum_{\vec{x}_2, \vec{x}_1} \text{tr} \left(S^{(x_1^0, \vec{x}_0)}_{(x_2^0, \vec{x}_2 - \vec{x}_1 + \vec{x}_0)} \Lambda_2 \Gamma_2 S^{(x_2^0, \vec{x}_2 - \vec{x}_1 + \vec{x}_0)}_{(x_1^0, \vec{x}_0)} \Lambda_1 \Gamma_1 \right) \right\rangle_{\text{eff}}^{(0)} \\ &= \left\langle -\sum_{\vec{x}} \text{tr} \left(S^{(x_1^0, \vec{x}_0)}_{(x_2^0, \vec{x})} \Lambda_2 \Gamma_2 S^{(x_2^0, \vec{x})}_{(x_1^0, \vec{x}_0)} \Lambda_1 \Gamma_1 \right) \right\rangle_{\text{eff}}^{(0)} \\ &= \left\langle -\sum_{\vec{x}} \text{tr} \left(\gamma^5 (S^{(x_2^0, \vec{x})}_{(x_1^0, \vec{x}_0)})^\dagger \gamma^5 \Lambda_2 \Gamma_2 S^{(x_2^0, \vec{x})}_{(x_1^0, \vec{x}_0)} \Lambda_1 \Gamma_1 \right) \right\rangle_{\text{eff}}^{(0)} \\ &= \left\langle -\sum_{\vec{x}} \text{tr} \left(\gamma^5 (\Psi[\eta]_{x_0}^{(x_2^0, \vec{x})})^\dagger \gamma^5 \Lambda_2 \Gamma_2 \Psi[\eta]_{x_0}^{(x_2^0, \vec{x})} \Lambda_1 \Gamma_1 \right) \right\rangle_{\text{eff}}^{(0)}. \end{aligned} \quad (11.34)$$

We omitted flavour, colour and spin indices. In the calculation, we made use of translational invariance in the spatial directions, which only holds after the gauge expectation value is taken, and of the γ^5 -hermiticity of the quark propagator. We are able to evaluate all combinations of Γ and Σ matrices at the same time for a single propagated point source $\Psi[\eta]_{x_0}$. Per point source, the single-flavour Dirac equation has to be solved $N_f \cdot N_c \cdot N_s$ times. In fact, it is also possible to project the two-point function to a set of momenta with the same quark source [42]. As we are only interested in zero-momentum two-point functions, we do not draw any advantage from this feature. For a better decorrelation it is common to use different quark source positions x_0 at different gauge configurations. In addition, one uses several quark source positions on the same gauge configuration and averages over those to better exploit the gauge configuration and reduce the overall statistical uncertainty.

11.3.2. Stochastic sources

As already anticipated, only early versions of the simulation program were based on the point source setup. We later changed to stochastic sources [230–233], which we will discuss in this section. For an efficient evaluation of quark-connected two-point functions with various interpolation operators, which differ in their spin and flavour structure, we make use of the *generalised one-end trick*, also known as *linked source method* [234–236]. In this setup flavour-spin-linked stochastic quark sources, which have support on a single time slice, are combined with the γ^5 -hermiticity of the quark propagator. The usage of this type of stochastic sources allows to evaluate mesonic two-point functions for all combinations of Λ - and Γ -matrices at the same time, minimising the number of required inversions of the Dirac operator. In addition, our sources are also colour-linked, which is, however, not required, as all considered interpolation operators possess the same colour structure. A flavour-colour-spin-linked stochastic quark source with support on the time slice x^0 is defined as

$$\eta_{x^0, (fcs)_1}^{(xfcs)_2} = \delta_{x^0}^{x_2^0} \xi^{\vec{x}_2} \delta_{f_1}^{f_2} \delta_{c_1}^{c_2} \delta_{s_1}^{s_2}, \quad (11.35)$$

where ξ is a three-dimensional stochastic field satisfying

$$\langle \xi^{\vec{x}_2} (\xi^\dagger)_{\vec{x}_1} \rangle_\xi = \delta_{\vec{x}_1}^{\vec{x}_2}. \quad (11.36)$$

Computing the expectation value of the stochastic source η and its adjoint η^\dagger we find

$$\langle \eta_{x^0, (fcs)_3}^{(xfcs)_4} (\eta^\dagger)_{(xfcs)_2}^{x^0, (fcs)_1} \rangle_\eta = \delta_{x^0}^{x_4^0} \delta_{x_1^0}^{x_0^0} \langle \xi^{\vec{x}_2} (\xi^\dagger)_{\vec{x}_1} \rangle_\xi \delta_{f_1}^{f_4} \delta_{c_1}^{c_4} \delta_{s_1}^{s_4} = \delta_{x^0}^{x_4^0} \delta_{x_1^0}^{x_0^0} \delta_{\vec{x}_1}^{\vec{x}_4} \delta_{f_1}^{f_4} \delta_{c_1}^{c_4} \delta_{s_1}^{s_4}. \quad (11.37)$$

Only the identity with respect to the spatial indices \vec{x}_4 and \vec{x}_1 is only fulfilled in the stochastic limit. With respect to all other indices, the identity is explicit. Various choices for the stochastic field ξ can be made. It was common to make use of Gaussian random fields. In [231] it is argued, that the stochastic variance introduced by the stochastic sources can be minimised, when \mathbb{Z}_n noises are used. The presented argument also holds for $U(1)$ noise, which we use in our setup, i.e. we draw random numbers from the complex unit circle

$$\xi^{x_2} \in U(1) \forall \vec{x}_2 \in \Lambda_{123}. \quad (11.38)$$

The propagated source $\Psi[\eta]_{x^0}^{x_2} = S^{x_2}_{x_1} \eta_{x^0}^{x_1}$ is computed via eq. (11.33). We again illustrate the method with the diagram in eq. (11.23), assuming that the operators have support on

11. Meson masses

the time slices x_2^0 and x_1^0 :

$$\begin{aligned}
& \text{Diagram: A loop with two vertices labeled } M_2^{(0)} \text{ and } M_1^{(0)} \text{ connected by two curved lines with arrows.} \\
& = -\frac{1}{|\Lambda_{123}|} \sum_{\vec{x}_2, \vec{x}_1} \text{tr} \left(S^{x_1}_{x_2} \Lambda_2 \Gamma_2 S^{x_2}_{x_1} \Lambda_1 \Gamma_1 \right) \\
& = \left\langle -\frac{1}{|\Lambda_{123}|} \sum_{\vec{x}_2, \vec{x}_1} \sum_{x_4, x_3} \text{tr} \left(\gamma^5 (S^{x_2}_{x_4})^\dagger \gamma^5 \Lambda_2 \Gamma_2 S^{x_2}_{x_3} \eta_{x_1^0}^{x_3} (\eta^\dagger)_{x_4^0}^{x_1} \Lambda_1 \Gamma_1 \right) \right\rangle_\eta \\
& = \left\langle -\frac{1}{|\Lambda_{123}|} \sum_{\vec{x}_2} \sum_{x_4, x_3} \text{tr} \left(\gamma^5 (S^{x_2}_{x_4} \eta_{x_1^0}^{x_4})^\dagger \gamma^5 \Lambda_2 \Gamma_2 S^{x_2}_{x_3} \eta_{x_1^0}^{x_3} \Lambda_1 \Gamma_1 \right) \right\rangle_\eta \\
& = \left\langle -\frac{1}{|\Lambda_{123}|} \sum_{\vec{x}_2} \text{tr} \left(\gamma^5 (\Psi[\eta]_{x_1^0}^{x_2})^\dagger \gamma^5 \Lambda_2 \Gamma_2 \Psi[\eta]_{x_1^0}^{x_2} \Lambda_1 \Gamma_1 \right) \right\rangle_\eta. \tag{11.39}
\end{aligned}$$

We have commuted the adjoint source η^\dagger through the product of matrices $\Lambda_1 \Sigma_1 \gamma^5$, which is possible because η^\dagger is proportional to the identity matrix in flavour and spin space. The correlation function is entirely expressed in terms of the propagator $\Psi[\eta]_{x_1^0}^{x_2}$, which is the key property of the *generalised one-end trick*. The application of stochastic sources has several advantages over the usage of point sources. The stochastic source has support on a complete time slice and not only on a single lattice site. As a consequence, the propagated source becomes a superposition of several columns of the full quark propagator matrix, such that the final estimate is less dependent on local fluctuations in the gauge field [236]. In comparison, a propagated point source is just a single column of the full quark propagator matrix. In order to achieve a volume average a larger number of sources have to be distributed within a time slice, which results in larger computational costs due to the larger number of solves of the Dirac equation. In addition, it can be shown, that the usage of stochastic sources for the evaluation of a pion two-point function leads to a reduced statistical error in the large volume limit [104]. A drawback of stochastic sources is, however, that the computed two-point function cannot be projected on several momenta for one stochastic source without additional solves of the Dirac equation. For each momentum a separate calculation is required [236], as the desired momentum has to be considered in the Fourier transform at both operators. In addition, stochastic sources turn out to be an inferior choice for baryonic two-point functions [237].

11.3.3. Computation of quark-connected Feynman diagrams with stochastic sources

In this section, we generalise the setup based on stochastic volume $U(1)$ -quark η sources to the remaining quark-connected Feynman diagrams. The photon propagator is evaluated stochastically, as discussed in section 7.2, using stochastic real \mathbb{Z}_2 -photon sources J . In table 11.6, we give more details on the number of evaluated gauge configurations, the number of quark and photon sources, as well as the timeslices, where the quark sources

11.3. Computation of quark-connected Feynman diagrams

ensemble	N_{cnfg}	N_{qsrc}	N_{psrc}	x_{qsrc}^0
N200	1712	16	2	37,39,41,43,45,47,49,51, 76,78,80,82,84,86,88,90
D450	500	16	1	random
H102	2004	32	2	28,29,30,31,32,33,34,35, 60,61,62,63,64,65,66,67

Table 11.6.: Number of gauge configurations N_{cnfg} , quark sources per configuration N_{qsrc} , photon sources per quark source N_{psrc} and timeslices x_{qsrc}^0 the quark sources have support on. Ensemble D450 possesses temporal periodic boundary conditions. The quark sources can therefore be spread randomly.

are located. Making use of this computational setup, we may express the quark-connected Feynman diagrams in eqs. (11.23) to (11.30) in terms of the propagator $\Psi^{(0)}[\eta]$ and the sequential propagators $\Psi_{V_{\bar{q}qf}}^{(0)}[\eta]$, $\Psi_{V_{\bar{q}q\gamma\Sigma}}^{(0)}[\eta]$, $\Psi_{V_{\bar{q}q\gamma\sqrt{\Sigma}}}^{(0)}[\eta, J]$ and $\Psi_{V_{\bar{q}q\gamma\sqrt{\Sigma}V_{\bar{q}q\gamma\sqrt{\Sigma}}}}^{(0)}[\eta, J, J]$, which are constructed from the quark and photon sources η and J according to the discussion in section 7.3. Considering sequential quark propagators we now make use of the γ^5 -hermiticity of both the quark propagator and the vertices. The obtained expressions can be considerably simplified by the definition of a contraction stencil:

$$H_{M_2^{(0)}M_1^{(0)}}^{x_2^0x_1^0}[\Psi_2, \Psi_1] = -\frac{1}{|\Lambda_{123}|} \sum_{\vec{x}_2 \in \Lambda_{123}} \text{tr} \left(\gamma^5 (\Psi_2^{x_2^0})^\dagger \gamma^5 \Lambda_2 \Gamma_2 \Psi_1^{x_1^0} \Lambda_1 \Gamma_1 \right). \quad (11.40)$$

The overall minus sign reflects the closed fermion loop as in eqs. (11.23) to (11.30). All considered diagrams are now evaluated in terms of this contraction stencil:

$$M_2^{(0)} \begin{array}{c} \curvearrowright \\ \curvearrowleft \end{array} M_1^{(0)} = \left\langle H_{M_2^{(0)}M_1^{(0)}}^{x_2^0x_1^0} [\Psi^{(0)}[\eta], \Psi^{(0)}[\eta]] \right\rangle_\eta, \quad (11.41)$$

$$M_2^{(0)} \begin{array}{c} \curvearrowright \\ \curvearrowleft \end{array} M_1^{(0)} = \left\langle H_{M_2^{(0)}M_1^{(0)}}^{x_2^0x_1^0} [\Psi^{(0)}[\eta], \Psi_{V_{\bar{q}qf}}^{(0)}[\eta]] \right\rangle_\eta, \quad (11.42)$$

$$M_2^{(0)} \begin{array}{c} \curvearrowright \\ \curvearrowleft \end{array} M_1^{(0)} = \left\langle H_{M_2^{(0)}M_1^{(0)}}^{x_2^0x_1^0} [\Psi_{V_{\bar{q}qf}}^{(0)}[\eta], \Psi^{(0)}[\eta]] \right\rangle_\eta, \quad (11.43)$$

11. Meson masses

	U	D	S	Q	m^{phys} [MeV]
η'	0	0	0	0	957.78(6)
π^+	1	1	0	1	139.57039(18)
π^0	0	0	0	0	134.9768(5)
π^-	-1	-1	0	-1	139.57039(18)
η	0	0	0	0	547.862(17)
K^+	1	0	1	1	493.677(16)
K^0	0	-1	1	0	497.611(13)
\bar{K}^0	0	1	-1	0	497.611(13)
K^-	-1	0	-1	-1	493.677(16)

Table 11.7.: Quantum numbers and experimentally determined masses of pseudo-scalar singlet and octet mesons [35].

$$M_2^{(0)} \text{---} M_1^{(0)} = \left\langle \left\langle H_{M_2^{(0)} M_1^{(0)}}^{x_2^0 x_1^0} [\Psi_{V_{\bar{q}q\gamma}\sqrt{\Sigma}}^{(0)}[\eta, J], \Psi_{V_{\bar{q}q\gamma}\sqrt{\Sigma}}^{(0)}[\eta, J]] \right\rangle_{\eta} \right\rangle_J \quad (11.44)$$

$$M_2^{(0)} \text{---} M_1^{(0)} = \left\langle H_{M_2^{(0)} M_1^{(0)}}^{x_2^0 x_1^0} [\Psi^{(0)}[\eta], \Psi_{V_{\bar{q}q\gamma\gamma}\Sigma}^{(0)}[\eta]] \right\rangle_{\eta}, \quad (11.45)$$

$$M_2^{(0)} \text{---} M_1^{(0)} = \left\langle \left\langle H_{M_2^{(0)} M_1^{(0)}}^{x_2^0 x_1^0} [\Psi^{(0)}[\eta], \Psi_{V_{\bar{q}q\gamma}\sqrt{\Sigma} V_{\bar{q}q\gamma}\sqrt{\Sigma}}^{(0)}[\eta, J, J]] \right\rangle_{\eta} \right\rangle_J, \quad (11.46)$$

$$M_2^{(0)} \text{---} M_1^{(0)} = \left\langle H_{M_2^{(0)} M_1^{(0)}}^{x_2^0 x_1^0} [\Psi_{V_{\bar{q}q\gamma\gamma}\Sigma}^{(0)}[\eta], \Psi^{(0)}[\eta]] \right\rangle_{\eta}, \quad (11.47)$$

$$M_2^{(0)} \text{---} M_1^{(0)} = \left\langle \left\langle H_{M_2^{(0)} M_1^{(0)}}^{x_2^0 x_1^0} [\Psi_{V_{\bar{q}q\gamma}\sqrt{\Sigma} V_{\bar{q}q\gamma}\sqrt{\Sigma}}^{(0)}[\eta, J, J], \Psi^{(0)}[\eta]] \right\rangle_{\eta} \right\rangle_J. \quad (11.48)$$

The symmetry factors in eqs. (11.27) and (11.29) were absorbed in the definition of the sequential propagator $\Psi_{V_{\bar{q}q\gamma\gamma}\Sigma}^{(0)}[\eta]$ and sequential source $\eta_{V_{\bar{q}q\gamma\gamma}\Sigma}^{(0)}[\eta]$ from eqs. (7.27) and (7.29).

11.4. Pseudo-scalar singlet and octet mesons

As discussed in chapter 9, we use pseudo-scalar meson masses to construct a renormalisation scheme for combined QCD and QED. We therefore determine the masses of π^+ , π^- , π^0 , K^+ , K^- , K^0 and \bar{K}^0 as well as the mass averages and mass differences within the corresponding isospin multiplets. In table 11.7, we display the quantum numbers and

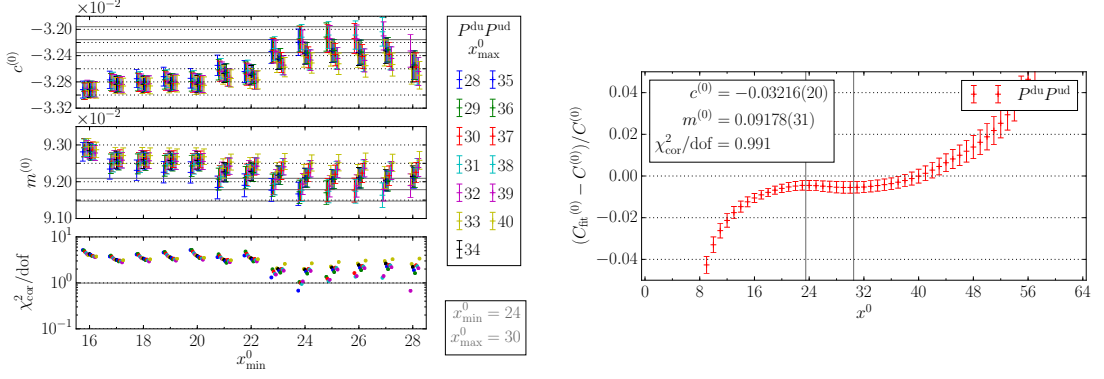


Figure 11.1.: Parameters of the fit to the correlation function $(C_{P^{\text{du}}P^{\text{ud}}})^{(0)}$ and relative deviation between the correlation function and the corresponding fit on N200. The selected fit is marked in grey. The grey lines enclose the fit interval.

experimentally determined masses of the considered mesons. The interpolation operators are chosen such that the flavour quantum numbers of the operators are suitable to interpolate the desired physical state taking tables 11.2 and 11.5 into account. In order to extract the ground state masses, we perform correlated fits to the correlation function based on its asymptotic behaviour as introduced in chapter 8. We only take a single state into account, i.e. we fit

$$C^{(0)}(t_2, t_1) \rightarrow c^{(0)} \exp(-m^{(0)}(t_2 - t_1)) \quad (10.14)$$

to the zeroth-order contribution, based on a linearised fit model as introduced in section 8.4.4. The results for $c^{(0)}$ and $m^{(0)}$ are then used to fit

$$C_l^{(1)}(t_2, t_1) \rightarrow (c_l^{(1)} - c^{(0)}m_l^{(1)}(t_2 - t_1)) \exp(-m^{(0)}(t_2 - t_1)) \quad (10.15)$$

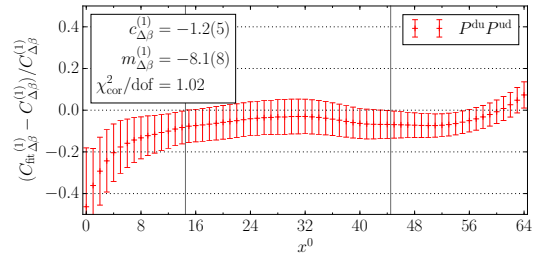
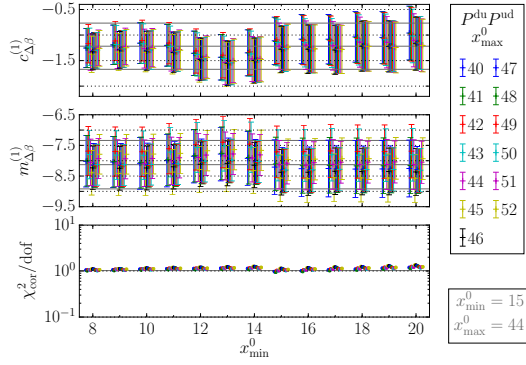
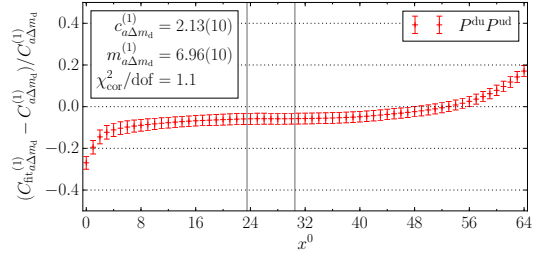
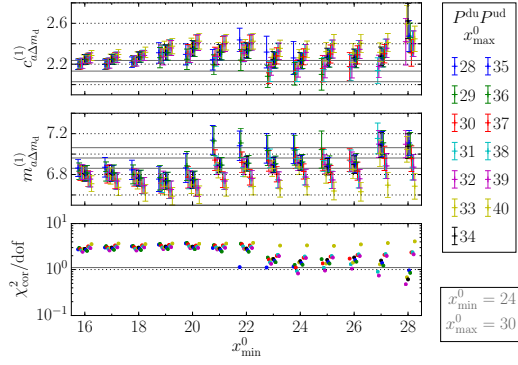
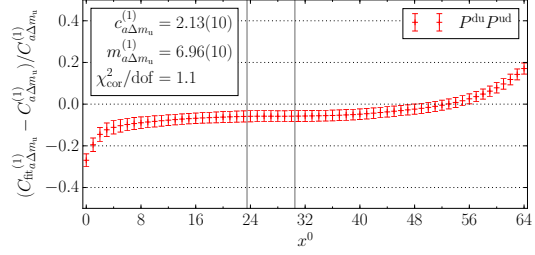
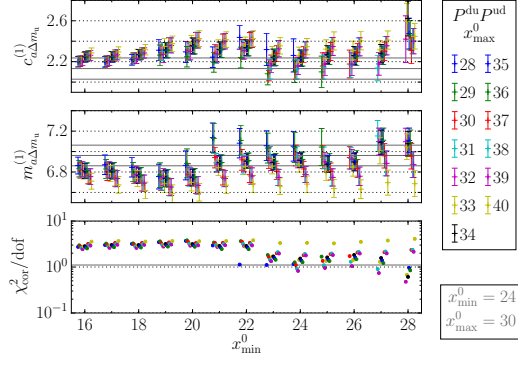
to the first-order contributions. The fit intervals are chosen, so that $\chi_{\text{cor}}^2/\text{dof}$ is closest to 1 and the fit parameters are stable under the variation of both fit interval boundaries. This minimises excited state and boundary effects. In the following, we discuss the results obtained on the ensemble N200 in more detail.

11.4.1. π^+ , π^- , π^0

Mass $m_{\pi^+} = m_{\pi^-}$

The mass m_{π^+} is extracted from the ground state of the correlation function $C_{P^{\text{du}}P^{\text{ud}}}$. Figures 11.1 and 11.2 show the fit to the zeroth- and first-order contribution, respectively.

11. Meson masses



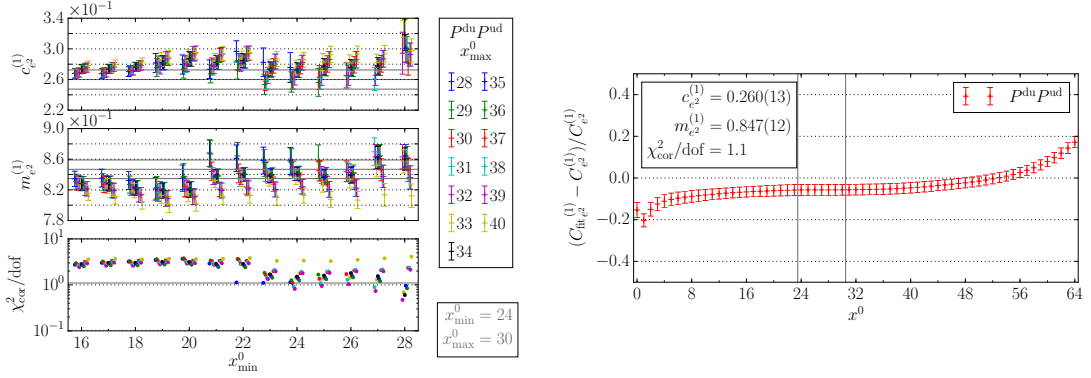


Figure 11.2.: Parameters of the fit to the correlation function $(C_{P^{\text{du}}P^{\text{ud}}})_l^{(1)}$ and relative deviation between the correlation function and the corresponding fit on N200. The selected fit is marked in grey. The grey lines enclose the fit interval.

As a result of the fits we obtain am_{π^+} in dimensionless units:

$$am_{\pi^+} = 0.09178(31) + 6.96(10) a\Delta m_{\text{u}} + 6.96(10) a\Delta m_{\text{d}} - 8.1(8) \Delta\beta + 0.847(12) e^2. \quad (11.49)$$

As we expand around the isosymmetric limit, the coefficients in front of $a\Delta m_{\text{u}}$ and $a\Delta m_{\text{d}}$ are equal. The signs of the coefficients are consistent with the fact that an increase of the bare quark mass should lead to an increase of the mass of the particle. Inserting the values for the expansion parameters in eq. (9.4), we find:

$$am_{\pi^+} = (0.09178(31)_{\text{st}}[31]_{\text{tot}})^{(0)} + (0.000363(17)_{\text{st}}(0)_{\text{a}}[17]_{\text{tot}})^{(1)} = 0.09215(31)_{\text{st}}(0)_{\text{a}}[31]_{\text{tot}}. \quad (11.50)$$

Converting to dimensionful units, m_{π^+} is given by:

$$m_{\pi^+} = (281.8(9)_{\text{st}}(3.3)_{\text{a}}[3.4]_{\text{tot}})^{(0)} + (1.116(54)_{\text{st}}(13)_{\text{a}}[55]_{\text{tot}})^{(1)} = 283.0(9)_{\text{st}}(3.3)_{\text{a}}[3.4]_{\text{tot}}. \quad (11.51)$$

Mass m_{π^0}

The mass m_{π^0} is extracted from the ground state of the correlation function $C_{P^3P^3}$. Figures 11.3 and 11.4 show the fit to the zeroth- and first-order contribution, respectively. As a result of the fits we obtain am_{π^0} in dimensionless units:

$$am_{\pi^0} = 0.09178(31) + 6.96(10) a\Delta m_{\text{u}} + 6.96(10) a\Delta m_{\text{d}} - 8.1(8) \Delta\beta + 0.839(12) e^2. \quad (11.52)$$

11. Meson masses

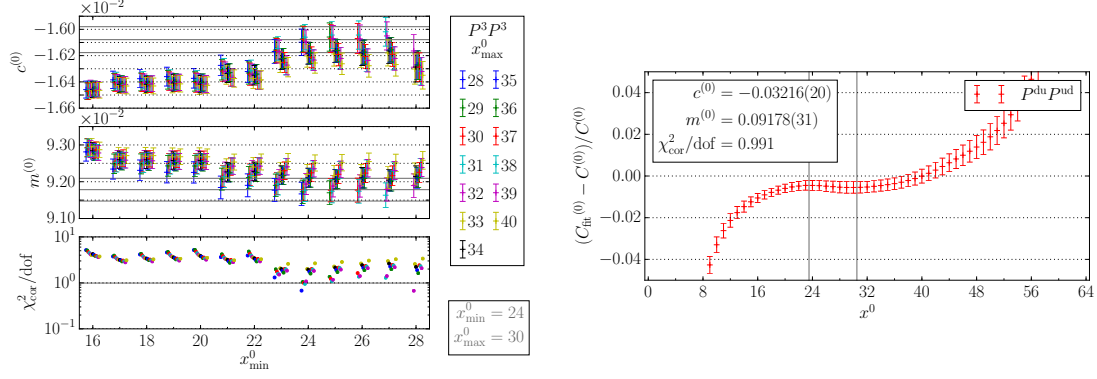


Figure 11.3.: Parameters of the fit to the correlation function $(C_{P^3P^3})^{(0)}$ and relative deviation between the correlation function and the corresponding fit on N200. The selected fit is marked in grey. The grey lines enclose the fit interval.

Again, we find consistent coefficients in front of $a\Delta m_u$ and $a\Delta m_d$. Inserting the values for the expansion parameters in eq. (9.4), we find:

$$\begin{aligned} am_{\pi^0} &= (0.09178(31)_{\text{st}}[31]_{\text{tot}})^{(0)} + (-0.000363(17)_{\text{st}}(0)_{\text{a}}[17]_{\text{tot}})^{(1)} \\ &= 0.09142(31)_{\text{st}}(0)_{\text{a}}[31]_{\text{tot}}. \end{aligned} \quad (11.53)$$

Converting to dimensionful units, m_{π^0} is given by:

$$\begin{aligned} m_{\pi^0} &= (281.8(9)_{\text{st}}(3.3)_{\text{a}}[3.4]_{\text{tot}})^{(0)} + (-1.116(54)_{\text{st}}(13)_{\text{a}}[55]_{\text{tot}})^{(1)} \\ &= 280.7(1.0)_{\text{st}}(3.2)_{\text{a}}[3.4]_{\text{tot}}. \end{aligned} \quad (11.54)$$

Mass difference $m_{\pi^+} - m_{\pi^0}$

The pion mass difference in dimensionless units reads:

$$am_{\pi^+} - am_{\pi^0} = 0.0079(4) e^2. \quad (11.55)$$

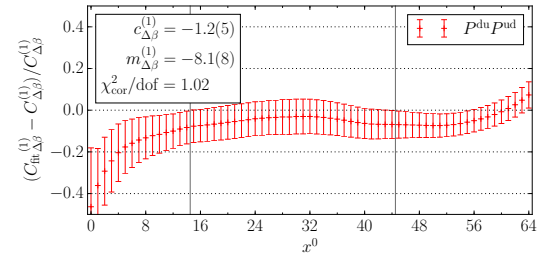
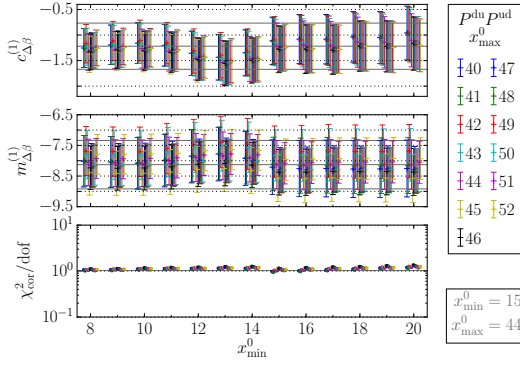
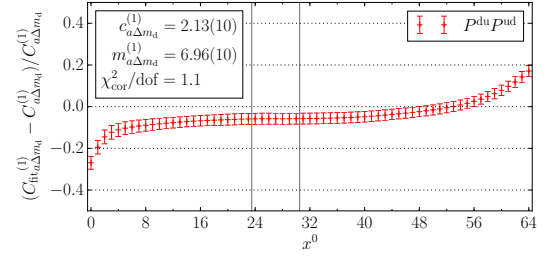
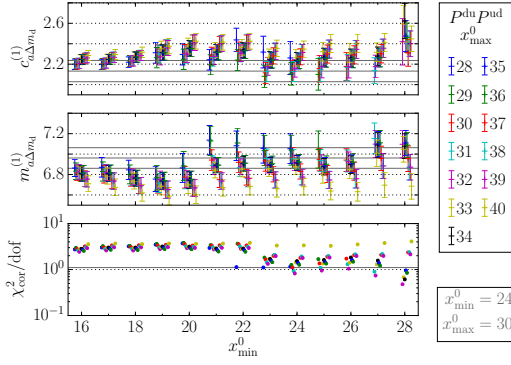
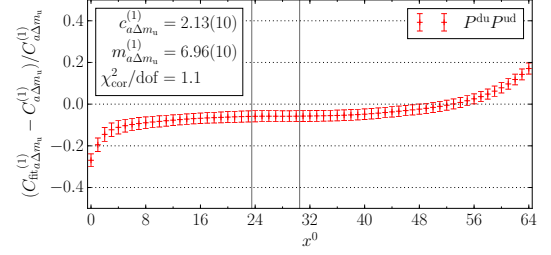
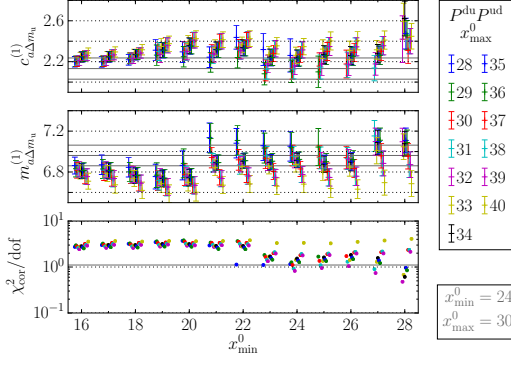
At leading order it is a purely electromagnetic effect [46]. Consequently, the charged π^+ must be heavier than the neutral π^0 due to the self-energy associated with the charge. Inserting the values for the expansion parameters in eq. (9.4), we find:

$$\begin{aligned} am_{\pi^+} - am_{\pi^0} &= (0.000727(35)_{\text{st}}[35]_{\text{tot}})^{(1)} \\ &= 0.000727(35)_{\text{st}}[35]_{\text{tot}}. \end{aligned} \quad (11.56)$$

Converting to dimensionful units, the pion mass difference is given by:

$$\begin{aligned} m_{\pi^+} - m_{\pi^0} &= (2.232(107)_{\text{st}}(26)_{\text{a}}[109]_{\text{tot}})^{(1)} \\ &= 2.232(107)_{\text{st}}(26)_{\text{a}}[109]_{\text{tot}}. \end{aligned} \quad (11.57)$$

11.4. Pseudo-scalar singlet and octet mesons



11. Meson masses

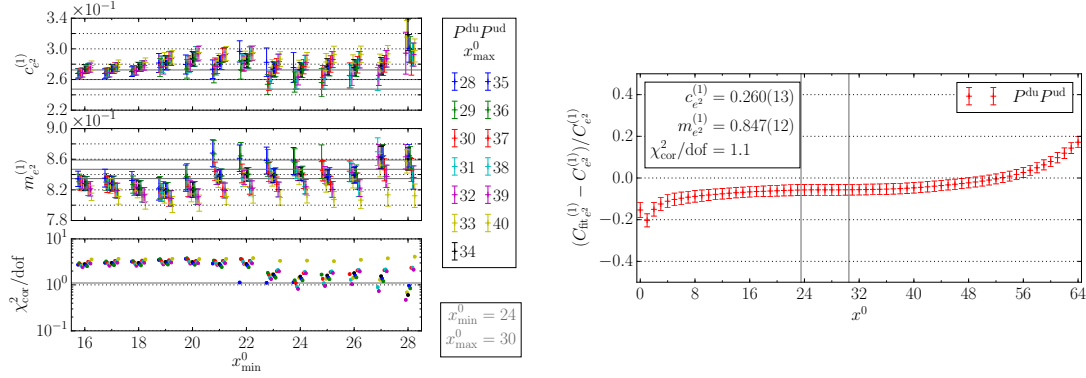


Figure 11.4.: Parameters of the fit to the correlation function $(C_{P^3 P^3})_l^{(1)}$ and relative deviation between the correlation function and the corresponding fit on N200. The selected fit is marked in grey. The grey lines enclose the fit interval.

Mass average $\frac{1}{2}(m_{\pi^+} + m_{\pi^0})$

The pion mass average in dimensionless units reads:

$$\begin{aligned} \frac{1}{2}(am_{\pi^+} + am_{\pi^0}) &= 0.09178(31) \\ &+ 6.96(10) a\Delta m_u + 6.96(10) a\Delta m_d \\ &- 8.1(8) \Delta\beta + 0.843(12) e^2. \end{aligned} \quad (11.58)$$

Inserting the values for the expansion parameters in eq. (9.4), we find:

$$\begin{aligned} \frac{1}{2}(am_{\pi^+} + am_{\pi^0}) &= (0.09178(31)_{\text{st}}[31]_{\text{tot}})^{(0)} \\ &= 0.09178(31)_{\text{st}}[31]_{\text{tot}}. \end{aligned} \quad (11.59)$$

Converting to dimensionful units, the pion mass average is given by:

$$\begin{aligned} \frac{1}{2}(m_{\pi^+} + m_{\pi^0}) &= (281.8(9)_{\text{st}}(3.3)_{\text{a}}[3.4]_{\text{tot}})^{(0)} \\ &= 281.8(9)_{\text{st}}(3.3)_{\text{a}}[3.4]_{\text{tot}} \end{aligned} \quad (11.60)$$

11.4.2. K^+ , K^- , K^0 , \bar{K}^0

Mass $m_{K^+} = m_{K^-}$

The mass m_{K^+} is extracted from the ground state of the correlation function $C_{P^{\text{su}} P^{\text{us}}}$. Figures 11.5 and 11.6 show the fit to the zeroth- and first-order contribution, respectively.

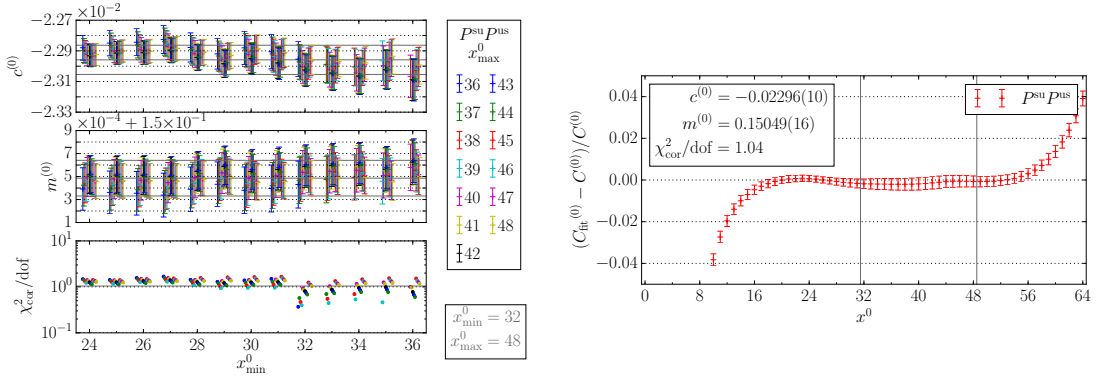


Figure 11.5.: Parameters of the fit to the correlation function $(C_{P^{\text{su}}P^{\text{us}}})^{(0)}$ and relative deviation between the correlation function and the corresponding fit on N200. The selected fit is marked in grey. The grey lines enclose the fit interval.

As a result of the fits we obtain am_{K^+} in dimensionless units:

$$\begin{aligned} am_{K^+} &= 0.15049(16) \\ &+ 4.20(4) a\Delta m_{\text{u}} + 4.204(28) a\Delta m_{\text{s}} \\ &- 5.2(6) \Delta\beta + 0.514(4) e^2. \end{aligned} \quad (11.61)$$

The coefficients in front of $a\Delta m_{\text{u}}$ and $a\Delta m_{\text{s}}$ are positive as expected. There are, however, not of equal magnitude, as the expansion is not performed around a $SU(3)$ flavour symmetric theory. Inserting the values for the expansion parameters in eq. (9.4), we find:

$$\begin{aligned} am_{K^+} &= (0.15049(16)_{\text{st}}[16]_{\text{tot}})^{(0)} + (-0.000641(0)_{\text{st}}(7)_{\text{a}}[7]_{\text{tot}})^{(1)} \\ &= 0.149845(155)_{\text{st}}(7)_{\text{a}}[156]_{\text{tot}}. \end{aligned} \quad (11.62)$$

Converting to dimensionful units, m_{K^+} is given by:

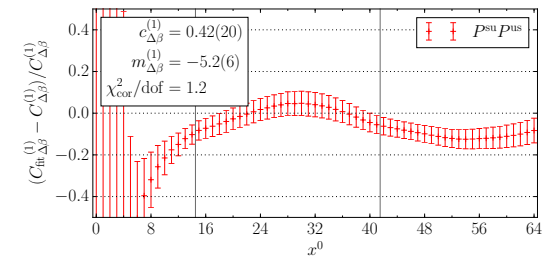
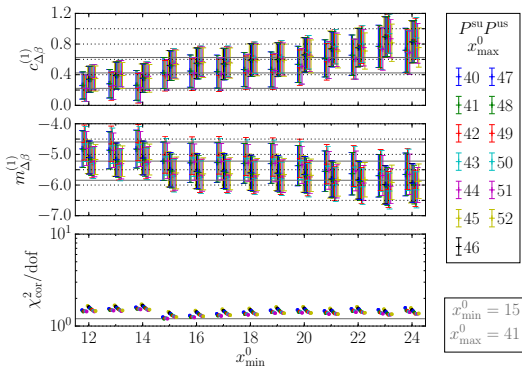
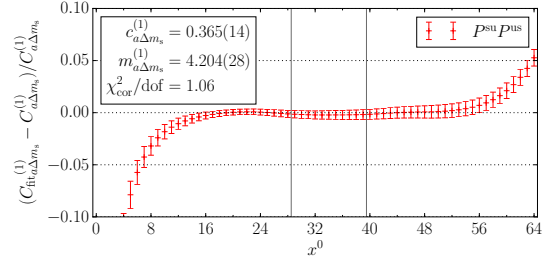
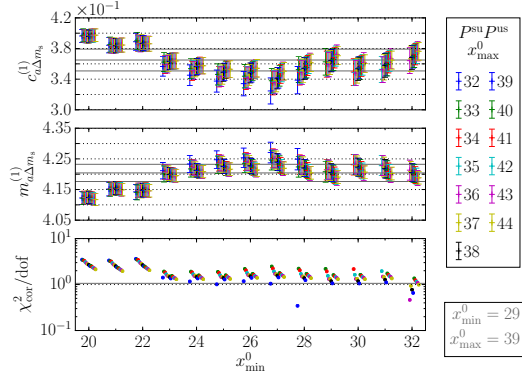
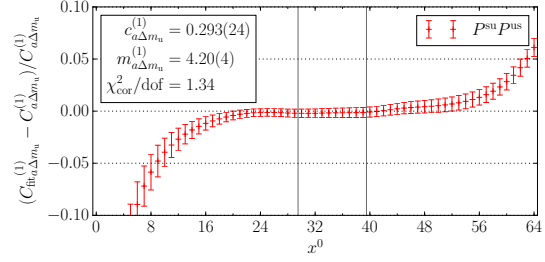
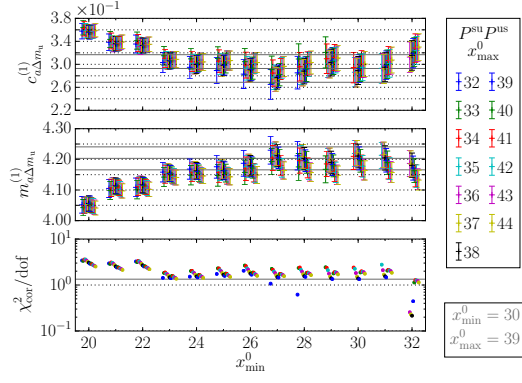
$$\begin{aligned} m_{K^+} &= (462.1(5)_{\text{st}}(5.3)_{\text{a}}[5.4]_{\text{tot}})^{(0)} + (-1.9685)^{(1)} \\ &= 460.1(5)_{\text{st}}(5.3)_{\text{a}}[5.4]_{\text{tot}}. \end{aligned} \quad (11.63)$$

Mass $m_{K^0} = m_{\bar{K}^0}$

The mass m_{K^0} is extracted from the ground state of the correlation function $C_{P^{\text{sd}}P^{\text{ds}}}$. Figures 11.7 and 11.8 show the fit to the zeroth- and first-order contribution, respectively. As a result of the fits we obtain am_{K^0} in dimensionless units:

$$\begin{aligned} am_{K^0} &= 0.15049(16) \\ &+ 4.20(4) a\Delta m_{\text{d}} + 4.204(28) a\Delta m_{\text{s}} \\ &- 5.2(6) \Delta\beta + 0.2039(15) e^2. \end{aligned} \quad (11.64)$$

11. Meson masses



11.4. Pseudo-scalar singlet and octet mesons

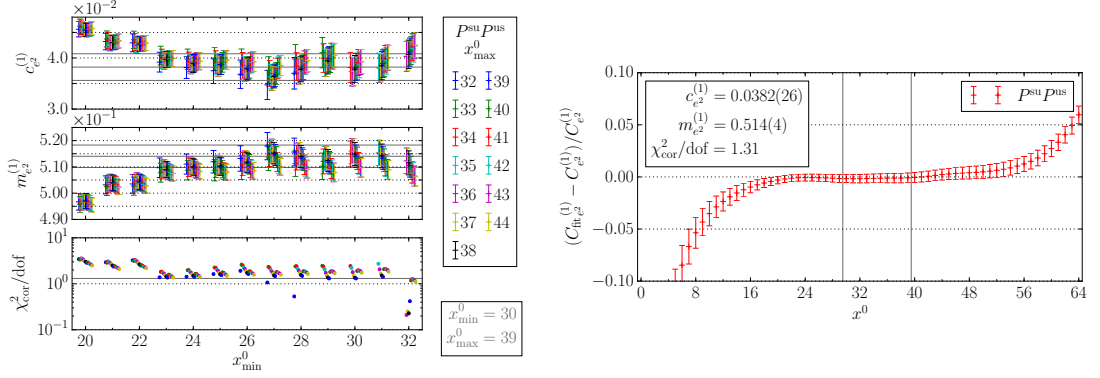


Figure 11.6.: Parameters of the fit to the correlation function $(C_{P^{su}P^{us}})^{(1)}$ and relative deviation between the correlation function and the corresponding fit on N200. The selected fit is marked in grey. The grey lines enclose the fit interval.

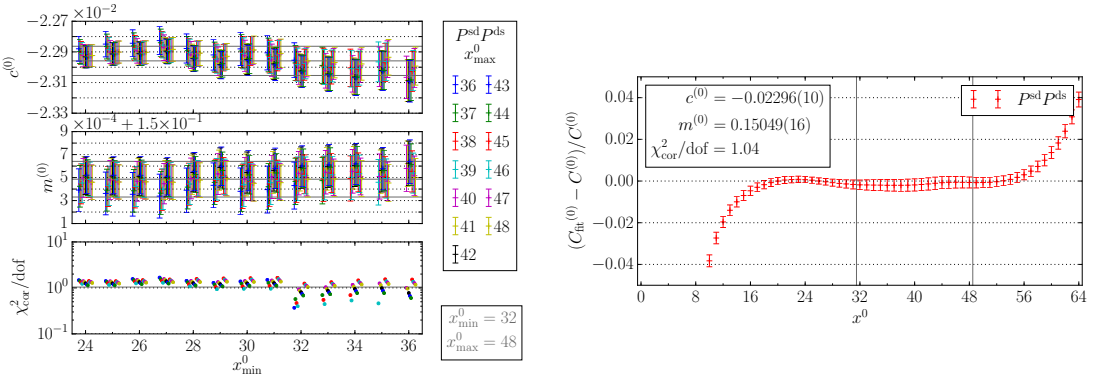
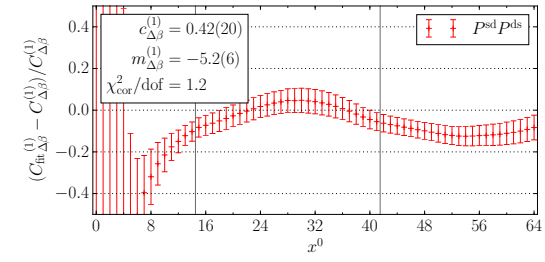
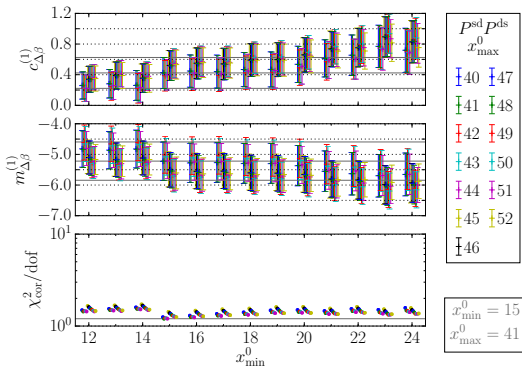
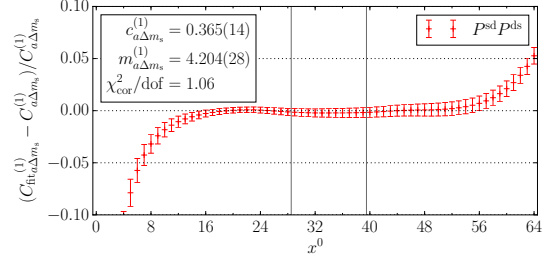
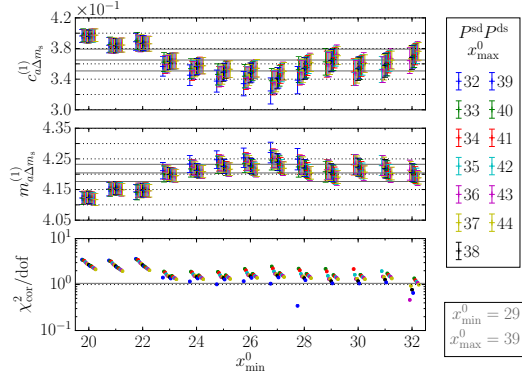
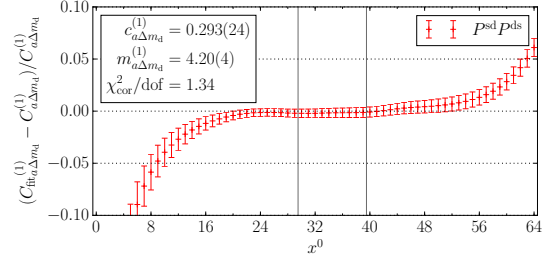
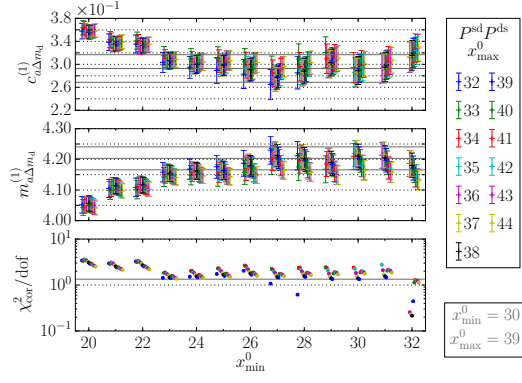


Figure 11.7.: Parameters of the fit to the correlation function $(C_{P^{sd}P^{ds}})^{(0)}$ and relative deviation between the correlation function and the corresponding fit on N200. The selected fit is marked in grey. The grey lines enclose the fit interval.

11. Meson masses



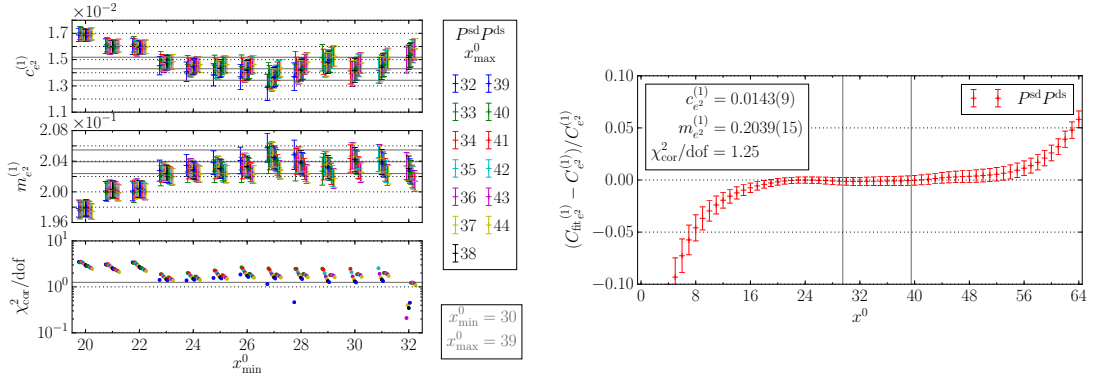


Figure 11.8.: Parameters of the fit to the correlation function $(C_{P^{\text{sd}}P^{\text{ds}}})_l^{(1)}$ and relative deviation between the correlation function and the corresponding fit on N200. The selected fit $P^{\text{sd}}P^{\text{ds}}$ is marked in grey. The grey lines enclose the fit interval.

Inserting the values for the expansion parameters in eq. (9.4), we find:

$$\begin{aligned} am_{K^0} &= (0.15049(16)_{\text{st}}[16]_{\text{tot}})^{(0)} + (0.000641(0)_{\text{st}}(7)_{\text{a}}[7]_{\text{tot}})^{(1)} \\ &= 0.151127(155)_{\text{st}}(7)_{\text{a}}[155]_{\text{tot}}. \end{aligned} \quad (11.65)$$

Converting to dimensionful units, m_{K^0} is given by:

$$\begin{aligned} m_{K^0} &= (462.1(5)_{\text{st}}(5.3)_{\text{a}}[5.4]_{\text{tot}})^{(0)} + (1.9685)^{(1)} \\ &= 464.1(5)_{\text{st}}(5.4)_{\text{a}}[5.4]_{\text{tot}}. \end{aligned} \quad (11.66)$$

Mass difference $m_{K^+} - m_{K^0}$

The kaon mass difference in dimensionless units reads:

$$\begin{aligned} am_{K^+} - am_{K^0} &= 4.20(4) a\Delta m_{\text{u}} - 4.20(4) a\Delta m_{\text{d}} \\ &\quad + 0.3101(28) e^2. \end{aligned} \quad (11.67)$$

As the kaon mass difference depends also on $a\Delta m_{\text{u}}$ and $a\Delta m_{\text{d}}$, the charged kaon K^+ is not necessarily heavier than the neutral kaon K^0 . The coefficient of e^2 is, however, positive as expected. Inserting the values for the expansion parameters in eq. (9.4), we find:

$$\begin{aligned} am_{K^+} - am_{K^0} &= (-0.001282(0)_{\text{st}}(15)_{\text{a}}[15]_{\text{tot}})^{(1)} \\ &= -0.001282(0)_{\text{st}}(15)_{\text{a}}[15]_{\text{tot}}. \end{aligned} \quad (11.68)$$

Converting to dimensionful units, the kaon mass difference is given by:

$$\begin{aligned} m_{K^+} - m_{K^0} &= (-3.9370)^{(1)} \text{ MeV} \\ &= -3.9370 \text{ MeV}. \end{aligned} \quad (11.69)$$

11. Meson masses

Mass average $\frac{1}{2}(m_{K^+} + m_{K^0})$

The kaon mass average in dimensionless units reads:

$$\begin{aligned} \frac{1}{2}(am_{K^+} + am_{K^0}) &= 0.15049(16) \\ &+ 2.102(19) a\Delta m_u + 2.102(19) a\Delta m_d + 4.204(28) a\Delta m_s \\ &- 5.2(6) \Delta\beta + 0.3590(29) e^2. \end{aligned} \quad (11.70)$$

Inserting the values for the expansion parameters in eq. (9.4), we find:

$$\begin{aligned} \frac{1}{2}(am_{K^+} + am_{K^0}) &= (0.15049(16)_{\text{st}}[16]_{\text{tot}})^{(0)} \\ &= 0.15049(16)_{\text{st}}(0)_{\text{a}}[16]_{\text{tot}}. \end{aligned} \quad (11.71)$$

Converting to dimensionful units, the kaon mass average is given by:

$$\begin{aligned} \frac{1}{2}(m_{K^+} + m_{K^0}) &= (462.1(5)_{\text{st}}(5.3)_{\text{a}}[5.4]_{\text{tot}})^{(0)} \text{ MeV} \\ &= 462.1(5)_{\text{st}}(5.3)_{\text{a}}[5.4]_{\text{tot}} \text{ MeV} \end{aligned} \quad (11.72)$$

11.4.3. π^0 , η , η'

A reliable determination of the masses of the three flavour-neutral pseudo-scalar mesons π^0 , η and η' is more difficult than for the electrically and flavour charged pseudo-scalar mesons. In QCD+QED these three mesons cannot be strictly classified according to isospin symmetry or even $SU(3)$ flavour symmetry. As a consequence, there is no strict correspondence between the operators \mathcal{P}_0 , \mathcal{P}_3 and \mathcal{P}_8 and the above states. In fact, all correlation functions included in the matrix

$$C_{i_2, i_1}(x_2^0, x_1^0) = \langle \mathcal{P}_{i_2}^{x_2^0} \mathcal{P}_{i_1}^{x_1^0} \rangle \quad (11.73)$$

for $i = 0, 3, 8$ have overlap with the states mentioned, i.e. the masses of π^0 , η and η' appear in the respective tower of exponentials. The reason why we were able to extract m_{π^0} reliably from $\langle \mathcal{P}_3 \mathcal{P}_3 \rangle$ is that π^0 is the lightest state of the three and the overlap factor with respect to \mathcal{P}_3 is large compared to other states, i.e. π^0 is almost an isospin eigenstate with $I = 1$ and $I_3 = 0$. Consequently, its contribution can be extracted safely at late times. The situation is different for η and η' , as they are not the lightest states. To reliably extract the three lowest accessible states from the matrix of correlation functions, we may perform a combined fit or use the generalised eigenvalue problem (GEVP) for the extraction of masses [238, 239]. The latter method is a generalised construction of an effective mass for matrices of correlation functions. It can also be combined with a perturbative expansion as discussed in [240], which is required in this work.

We do not present the results of this analysis in detail, as we have only dealt with quark-connected contributions. Our GEVP analysis leads to two degenerate mass states with a mass of the π^0 and a heavier state, which contradicts empirical findings. This is consistent

with the discussion in [167], which states that, considering only quark-connected contributions, π^0 and η have the same mass and η' possesses a mass of about $\sqrt{2M_K^2 - M_\pi^2}$. However, it is known from experiments that both the η and η' mesons are much heavier than the π^0 . This effect dominantly originates from zeroth-order quark-disconnected contributions [105, 167, 241, 242]. For the π^0 the latter contribution vanishes exactly in an isosymmetric theory.

Nevertheless, the application of the GEVP combined with a perturbative expansion on the flavour-neutral pseudo-scalar mesons was a good test case for future calculations. In particular, an analysis based on a matrix of correlations functions will be relevant for the determination of masses in the baryonic sector, which we will give an introduction to in chapter 12.

11.5. Discussion and Outlook

We give an overview of the results for pseudo-scalar masses, mass averages and differences obtained on the ensembles N200, D450 and H102 in table 11.8. For all determined meson masses m_{π^+} , m_{π^0} , m_{K^+} and m_{K^0} , we find that the first-order correction is smaller than the error of the zeroth-order contribution, which is dominated by the scale uncertainty. The first-order correction is, however, larger than the statistical error of the zeroth-order contribution. Hence, in order to have a significant correction caused by isospin breaking effects, one needs to reduce the dominant scale uncertainty. In conclusion, the systematic error of neglecting isospin breaking corrections in meson masses is smaller than the error introduced by the scale setting. For the pion mass splitting, which is not used as an input parameter in the calculation, we find the correct behaviour, i.e. it increases for diminished average pion masses. For the estimation of the photon all-to-all propagator, we also varied the type of sources. We tested μ -linked photon sources, where the Euclidean index μ is diluted, but we did not find any gain in statistical precision keeping the computation time fixed. This is compatible with the findings of [194].

In this thesis, we only consider quark-connected contributions. In fact, we have extended the calculation in a trial computation also considering zeroth-order isosymmetric quark-disconnected contributions and first-order quark-disconnected QED-connected contributions to the mesonic two-point correlation function, i.e. we have included the zeroth-order diagram

$$M_2^{(0)} \quad \text{---} \quad M_1^{(0)} \quad (11.74)$$

11. Meson masses

m_{π^+} [MeV]	$(281.8(9)_{\text{st}}(3.3)_{\text{a}}[3.4]_{\text{tot}})^{(0)} + (1.116(54)_{\text{st}}(13)_{\text{a}}[55]_{\text{tot}})^{(1)}$
m_{π^0} [MeV]	$(281.8(9)_{\text{st}}(3.3)_{\text{a}}[3.4]_{\text{tot}})^{(0)} + (-1.116(54)_{\text{st}}(13)_{\text{a}}[55]_{\text{tot}})^{(1)}$
$m_{\pi^+} - m_{\pi^0}$ [MeV]	$(2.232(107)_{\text{st}}(26)_{\text{a}}[109]_{\text{tot}})^{(1)}$
$\frac{1}{2}(m_{\pi^+} + m_{\pi^0})$ [MeV]	$(281.8(9)_{\text{st}}(3.3)_{\text{a}}[3.4]_{\text{tot}})^{(0)}$
m_{K^+} [MeV]	$(462.1(5)_{\text{st}}(5.3)_{\text{a}}[5.4]_{\text{tot}})^{(0)} + (-1.9685)^{(1)}$
m_{K^0} [MeV]	$(462.1(5)_{\text{st}}(5.3)_{\text{a}}[5.4]_{\text{tot}})^{(0)} + (1.9685)^{(1)}$
$m_{K^+} - m_{K^0}$ [MeV]	$(-3.9370)^{(1)}$
$\frac{1}{2}(m_{K^+} + m_{K^0})$ [MeV]	$(462.1(5)_{\text{st}}(5.3)_{\text{a}}[5.4]_{\text{tot}})^{(0)}$

(a) N200 ($a = 0.064$ fm, $m_\pi = 282$ MeV)

m_{π^+} [MeV]	$(216.7(6)_{\text{st}}(2.7)_{\text{a}}[2.8]_{\text{tot}})^{(0)} + (1.657(39)_{\text{st}}(21)_{\text{a}}[43]_{\text{tot}})^{(1)}$
m_{π^0} [MeV]	$(216.7(6)_{\text{st}}(2.7)_{\text{a}}[2.8]_{\text{tot}})^{(0)} + (-1.657(39)_{\text{st}}(21)_{\text{a}}[43]_{\text{tot}})^{(1)}$
$m_{\pi^+} - m_{\pi^0}$ [MeV]	$(3.31(8)_{\text{st}}(4)_{\text{a}}[9]_{\text{tot}})^{(1)}$
$\frac{1}{2}(m_{\pi^+} + m_{\pi^0})$ [MeV]	$(216.7(6)_{\text{st}}(2.7)_{\text{a}}[2.8]_{\text{tot}})^{(0)}$
m_{K^+} [MeV]	$(475.55(24)_{\text{st}}(5.92)_{\text{a}}[5.91]_{\text{tot}})^{(0)} + (-1.9685)^{(1)}$
m_{K^0} [MeV]	$(475.55(24)_{\text{st}}(5.92)_{\text{a}}[5.91]_{\text{tot}})^{(0)} + (1.9685)^{(1)}$
$m_{K^+} - m_{K^0}$ [MeV]	$(-3.9370)^{(1)}$
$\frac{1}{2}(m_{K^+} + m_{K^0})$ [MeV]	$(475.55(24)_{\text{st}}(5.92)_{\text{a}}[5.91]_{\text{tot}})^{(0)}$

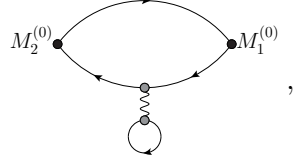
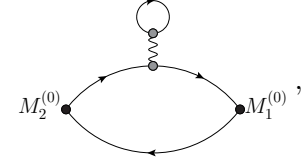
(b) D450 ($a = 0.076$ fm, $m_\pi = 216$ MeV)

m_{π^+} [MeV]	$(353.8(9)_{\text{st}}(4.3)_{\text{a}}[4.3]_{\text{tot}})^{(0)} + (0.984(35)_{\text{st}}(12)_{\text{a}}[37]_{\text{tot}})^{(1)}$
m_{π^0} [MeV]	$(353.8(9)_{\text{st}}(4.3)_{\text{a}}[4.3]_{\text{tot}})^{(0)} + (-0.984(35)_{\text{st}}(12)_{\text{a}}[37]_{\text{tot}})^{(1)}$
$m_{\pi^+} - m_{\pi^0}$ [MeV]	$(1.968(70)_{\text{st}}(24)_{\text{a}}[74]_{\text{tot}})^{(1)}$
$\frac{1}{2}(m_{\pi^+} + m_{\pi^0})$ [MeV]	$(353.8(9)_{\text{st}}(4.3)_{\text{a}}[4.3]_{\text{tot}})^{(0)}$
m_{K^+} [MeV]	$(438.3(7)_{\text{st}}(5.3)_{\text{a}}[5.3]_{\text{tot}})^{(0)} + (-1.9685)^{(1)}$
m_{K^0} [MeV]	$(438.3(7)_{\text{st}}(5.3)_{\text{a}}[5.3]_{\text{tot}})^{(0)} + (1.9685)^{(1)}$
$m_{K^+} - m_{K^0}$ [MeV]	$(-3.9370)^{(1)}$
$\frac{1}{2}(m_{K^+} + m_{K^0})$ [MeV]	$(438.3(7)_{\text{st}}(5.3)_{\text{a}}[5.3]_{\text{tot}})^{(0)}$

(c) H102 ($a = 0.086$ fm, $m_\pi = 354$ MeV)

Table 11.8.: Masses, mass averages and mass differences of pseudo-scalar mesons.

and the first-order electromagnetic diagrams

$$(11.75)$$



$$(11.76)$$

The quark-disconnected correlation functions were computed using $U(1)$ -stochastic quark sources with support on the entire spacetime lattice. We performed simulations in this setup for the ensembles H102 and H105 for the pseudo-scalar channel and discussed the results in [243]. As a main result we found that the diagram in eq. (11.76) contributes to the pion mass splitting and leads to a decrease of the latter by about $O(10\%)$ on these two ensembles. The diagrams in eq. (11.75) contribute to the pion and kaon masses but have no significant influence at our level of precision. The quark-disconnected diagram in eq. (11.74) only contributes to flavour neutral states. It vanishes in the isosymmetric limit, such that it does not contribute to the π^0 state.

At this stage, we have not applied any finite volume corrections to account for the long range of the electromagnetic interaction due to the absence of a mass gap. For periodic temporal boundary conditions a QED_L finite volume correction for both elementary and composite spin-0 particles is known [41]:

$$m_0^2(T, L) \underset{T, L \rightarrow +\infty}{\sim} m^2 \left(1 - q^2 \alpha \left(\frac{\kappa}{mL} \left(1 + \frac{2}{mL} \right) \right) \right) \quad \kappa = 2.837297(1). \quad (11.77)$$

This correction formula should be applied to the determined masses to correct for leading QED finite volume effects.

Not only the pseudo-scalar operator \mathcal{S} , but also the temporal component of the axial operator \mathcal{A}^0 , feature an overlap with pseudo-scalar states. It is therefore interesting to investigate whether a combined GEVP analysis could result in a reduction of excited state effects, such that the fit interval for the extraction of the pseudo-scalar ground state can be further prolonged.

12. Baryon masses

As discussed in chapter 9, baryon masses can be used to set the scale in lattice simulations. E.g., lattice spacing determinations have been performed using the Ω baryon [244, 245]. Other candidates are the Λ and Σ baryons, where mixing has to be considered [246] in a similar way to describe the system formed by π^0 , η and η' discussed in section 11.4.3. In this chapter, we briefly describe the application of the approach used in this thesis to determine leading isospin breaking effects as introduced in chapter 6 to the calculation of baryon masses and discuss a first setup for a first feasibility test. A calculation for the prediction of the proton-neutron mass difference based on the twisted-mass fermion lattice regularisation was performed for pure QCD [191, 192], where a perturbative expansion around QCD_{iso} was applied. This work was later extended in the thesis [247] also taking leading electromagnetic effects into account. The determined mass splitting therein is compatible with zero, which may be a result of a suboptimal computational setup.

12.1. Baryonic interpolation operators

From the discussion in section 10.1, we deduce that the zero-momentum projected operator

$$\mathcal{B}^{x^0} = \frac{1}{\sqrt{|\Lambda_{123}|}} \sum_{\vec{x}} \frac{1}{6} B[U, A]^x_{\mathbf{b}_3 \mathbf{b}_2 \mathbf{b}_1} \Psi^{\mathbf{b}_3} \Psi^{\mathbf{b}_2} \Psi^{\mathbf{b}_1} \quad (12.1)$$

diminishes the baryon number by one and the operator

$$\bar{\mathcal{B}}^{x^0} = \frac{1}{\sqrt{|\Lambda_{123}|}} \sum_{\vec{x}} \frac{1}{6} \bar{B}[U, A]^{x \mathbf{a}_3 \mathbf{a}_2 \mathbf{a}_1} \bar{\Psi}_{\mathbf{a}_3} \bar{\Psi}_{\mathbf{a}_2} \bar{\Psi}_{\mathbf{a}_1} \quad (12.2)$$

increases the baryon number by one, i.e. this pair of operators is suitable for the construction of a two-point function used for single baryon spectroscopy.

12.2. Baryon two-point functions

In the following, we consider correlation functions of the form

$$C_{\mathcal{B}\bar{\mathcal{B}}}(x_2^0, x_1^0) = \langle \mathcal{B}^{x_2^0} \bar{\mathcal{B}}^{x_1^0} \rangle. \quad (12.3)$$

In order to determine the perturbative expansion of the correlation function, we expand the interpolation operators according to

$$\mathcal{O} = \mathcal{O}^{(0)} + e \mathcal{O}_{e^2}^{(\frac{1}{2})} + \frac{1}{2} e^2 \mathcal{O}_{e^2}^{(1)} + \mathcal{O}(e^3). \quad (6.86)$$

12. Baryon masses

For now, we do not further specify the actual shape of the operators, but assume that they are independent of eA , i.e. $\mathcal{B} = (\mathcal{B})^{(0)}$ and $\bar{\mathcal{B}} = (\bar{\mathcal{B}})^{(0)}$, which is the case for point-like interpolation operators.

12.2.1. Diagrammatic expansion

The generic expansion of the correlation function up to first order reads

$$C = C^{(0)} + \sum_l \Delta \varepsilon_l C_l^{(1)} + O(\Delta \varepsilon^2). \quad (6.85)$$

The zeroth-order contribution is calculated via eq. (6.87) and reads in terms of Feynman diagrams

$$(C_{\mathcal{B}\bar{\mathcal{B}}})^{(0)} = \left\langle B^{(0)} \begin{array}{c} \curvearrowright \\ \text{---} \\ \curvearrowleft \end{array} \bar{B}^{(0)} \right\rangle_{\text{eff}}^{(0)}. \quad (12.4)$$

The first-order contribution is calculated according to eq. (6.88). In terms of Feynman diagrams, the first-order contribution due to a shift in the quark mass Δm_f reads

$$\begin{aligned} (C_{\mathcal{B}\bar{\mathcal{B}}})_{\Delta m_f}^{(1)} = & \left\langle B^{(0)} \begin{array}{c} \curvearrowright \\ \text{---} \\ \text{---} \\ \text{---} \\ \curvearrowleft \end{array} \bar{B}^{(0)} \right\rangle_{\text{eff}}^{(0)} \\ & + \left\langle B^{(0)} \begin{array}{c} \curvearrowright \\ \text{---} \\ \curvearrowleft \end{array} \bar{B}^{(0)} \right\rangle_{\text{eff}}^{(0)} \left\langle \text{---} \right\rangle_{\text{eff}}^{(0)} \\ & - \left\langle B^{(0)} \begin{array}{c} \curvearrowright \\ \text{---} \\ \curvearrowleft \end{array} \bar{B}^{(0)} \right\rangle_{\text{eff}}^{(0)} \left\langle \text{---} \right\rangle_{\text{eff}}^{(0)}. \end{aligned} \quad (12.5)$$

A detuning in the strong inverse coupling $\Delta\beta$ results in a first-order contribution

$$\begin{aligned} (C_{\mathcal{B}\bar{\mathcal{B}}})_{\Delta\beta}^{(1)} = & \left\langle B^{(0)} \begin{array}{c} \curvearrowright \\ \text{---} \\ \curvearrowleft \end{array} \bar{B}^{(0)} \right\rangle_{\text{eff}}^{(0)} \\ & - \left\langle B^{(0)} \begin{array}{c} \curvearrowright \\ \text{---} \\ \curvearrowleft \end{array} \bar{B}^{(0)} \right\rangle_{\text{eff}}^{(0)} \left\langle \text{---} \right\rangle_{\text{eff}}^{(0)}. \end{aligned} \quad (12.6)$$

The first-order contribution due to a non-vanishing electromagnetic coupling e^2 reads

$$\begin{aligned}
 (C_{B\bar{B}})_{e^2}^{(1)} = & \left\langle \begin{array}{c} \text{Diagram 1: } B^{(0)} \text{ and } \bar{B}^{(0)} \text{ connected by a quark line with a gluon loop} \\ \text{Diagram 2: } B^{(0)} \text{ and } \bar{B}^{(0)} \text{ connected by a quark line with a photon loop} \\ \text{Diagram 3: } B^{(0)} \text{ and } \bar{B}^{(0)} \text{ connected by a quark line with a gluon loop and a photon loop} \\ \text{Diagram 4: } B^{(0)} \text{ and } \bar{B}^{(0)} \text{ connected by a quark line with a photon loop and a gluon loop} \end{array} \right. \\
 & + B^{(0)} \text{ and } \bar{B}^{(0)} \text{ connected by a quark line with a gluon loop} + B^{(0)} \text{ and } \bar{B}^{(0)} \text{ connected by a quark line with a photon loop} \\
 & + B^{(0)} \text{ and } \bar{B}^{(0)} \text{ connected by a quark line with a gluon loop and a photon loop} \left(\begin{array}{c} \text{Diagram 5: } \text{gluon loop} \\ \text{Diagram 6: } \text{photon loop} \\ \text{Diagram 7: } \text{gluon loop and photon loop} \end{array} \right) \Bigg\rangle_{\text{eff}}^{(0)} \\
 & - \left\langle \begin{array}{c} \text{Diagram 8: } B^{(0)} \text{ and } \bar{B}^{(0)} \text{ connected by a quark line} \end{array} \right\rangle_{\text{eff}}^{(0)} \\
 & \cdot \left\langle \begin{array}{c} \text{Diagram 9: } \text{gluon loop} \\ \text{Diagram 10: } \text{photon loop} \\ \text{Diagram 11: } \text{gluon loop and photon loop} \end{array} \right\rangle_{\text{eff}}^{(0)}.
 \end{aligned} \tag{12.7}$$

Making use of interpolation operators with antisymmetric tensors reduces the number of Feynman diagrams considerably. For general interpolation operators, there are in total 6 zeroth-order diagrams, 24 first-order diagrams for the detuning of quark masses, 6 first-order diagrams for the detuning of the strong coupling and 90 first-order diagrams for electromagnetic effects.

In this thesis, we only consider quark-connected contributions in our calculation. We translate the corresponding Feynman diagrams into contracted tensor-structures of interpolation operators, quark and photon propagators and vertices. This is relevant to ensure the correct application of minus signs and symmetry factors. For the zeroth-order diagram we have

$$\begin{array}{c} \text{Diagram 1: } B^{(0)} \text{ and } \bar{B}^{(0)} \text{ connected by a quark line} \end{array} = \frac{1}{6} B^{(0)}{}_{b_1 b_2 b_3} S^{b_3}{}_{a_3} S^{b_2}{}_{a_2} S^{b_1}{}_{a_1} \bar{B}^{(0)}{}_{a_3 a_2 a_1}. \tag{12.8}$$

The first-order contribution to the quark mass detuning reads

$$\begin{array}{c} \text{Diagram 2: } B^{(0)} \text{ and } \bar{B}^{(0)} \text{ connected by a quark line with a gluon loop} \end{array} = \frac{1}{2} B^{(0)}{}_{b_1 b_2 b_3} S^{b_3}{}_{a_3} S^{b_2}{}_{a_2} \cdot \left(S^{b_1}{}_{a_4} V_{\bar{q}qf}{}^{a_4}{}_{b_4} S^{b_4}{}_{a_1} \right) \bar{B}^{(0)}{}_{a_3 a_2 a_1}. \tag{12.9}$$

12. Baryon masses

Diagrams with first-order contributions due to the electromagnetic interaction read

$$\begin{aligned}
 \text{Diagram 1: } B^{(0)} \text{ and } \bar{B}^{(0)} \text{ connected by a horizontal line with a wavy loop in the middle.} \\
 B^{(0)} \text{ and } \bar{B}^{(0)} = \frac{1}{2} \sum c_2 c_1 B^{(0)}_{b_1 b_2 b_3} S^{b_3}_{a_3} \left(S^{b_2}_{a_5} V_{\bar{q}q\gamma}^{a_5}_{b_5 c_1} S^{b_5}_{a_2} \right) \quad (12.10) \\
 \cdot \left(S^{b_1}_{a_4} V_{\bar{q}q\gamma}^{a_4}_{b_4 c_1} S^{b_4}_{a_1} \right) \bar{B}^{(0) a_3 a_2 a_1},
 \end{aligned}$$

$$\begin{aligned}
 \text{Diagram 2: } B^{(0)} \text{ and } \bar{B}^{(0)} \text{ connected by a horizontal line with a wavy loop in the middle.} \\
 B^{(0)} \text{ and } \bar{B}^{(0)} = \frac{1}{2} \sum c_2 c_1 B^{(0)}_{b_1 b_2 b_3} S^{b_3}_{a_3} S^{b_2}_{a_2} \quad (12.11) \\
 \cdot \left(S^{b_1}_{a_5} V_{\bar{q}q\gamma}^{a_5}_{b_5 c_1} S^{b_5}_{a_4} V_{\bar{q}q\gamma}^{a_4}_{b_4 c_1} S^{b_4}_{a_1} \right) \\
 \cdot \bar{B}^{(0) a_3 a_2 a_1},
 \end{aligned}$$

$$\begin{aligned}
 \text{Diagram 3: } B^{(0)} \text{ and } \bar{B}^{(0)} \text{ connected by a horizontal line with a wavy loop in the middle.} \\
 B^{(0)} \text{ and } \bar{B}^{(0)} = \frac{1}{4} \sum c_2 c_1 B^{(0)}_{b_1 b_2 b_3} S^{b_3}_{a_3} S^{b_2}_{a_2} \quad (12.12) \\
 \cdot \left(S^{b_1}_{a_4} V_{\bar{q}q\gamma}^{a_4}_{b_4 c_2 c_1} S^{b_4}_{a_1} \right) \bar{B}^{(0) a_3 a_2 a_1}.
 \end{aligned}$$

The only contribution from the reweighting factor that we consider is

$$\text{Diagram: A circle with } \Delta\beta \text{ inside.} \quad \Delta\beta = V_g. \quad (12.13)$$

12.3. Discussion and Outlook

Although we do not present any results in this chapter, we have performed a first feasibility test for the determination of baryon masses including leading isospin breaking effects. We investigated a two-point function based on point-like, non-smeared interpolation operators for the proton $\mathcal{B}^x = \frac{1}{2}(1 + \gamma^0) \varepsilon_{c_3 c_2 c_1} \Psi^{xuc_3} ((\Psi^{xuc_2})^T C \gamma^5 \Psi^{xdc_1})$ and $\bar{\mathcal{B}}^x = \varepsilon_{c_3 c_2 c_1} (\bar{\Psi}^{xuc_2} C \gamma^5 (\bar{\Psi}^{xdc_1})^T) \bar{\Psi}^{xuc_3} \frac{1}{2}(1 + \gamma^0)$ [42, 248], evaluated by means of point sources, which we discussed in section 11.3.1, similar to the setup in [247], which we mentioned in the introduction of this chapter. The resulting two-point function was evaluated by means of point sources. We performed simulations on the ensemble H102 ($a = 0.086$ fm, $m_\pi = 354$ MeV), considering only a limited number of gauge configurations. We were able to observe the correct asymptotic behaviour of the zeroth- and first-order contribution to the correlation function. For periodic temporal boundary conditions a QED_L finite volume correction for both elementary and composite spin- $\frac{1}{2}$ particles is known [41] and should be applied to future results:

$$m_{\frac{1}{2}}(T, L) \underset{T, L \rightarrow +\infty}{\sim} m \left(1 - q^2 \alpha \left(\frac{\kappa}{2mL} \left(1 + \frac{2}{mL} \right) - \frac{3\pi}{(mL)^3} \right) \right) \quad \kappa = 2.837297(1). \quad (12.14)$$

It is desirable to extent this first test to a full calculation of octet and decuplet baryon masses. Instead of point-like interpolation operators, smeared operators [249] should be used, as they possess a larger overlap with the baryon ground state. This results in an

earlier onset of the asymptotic behaviour of the correlation function, which is particularly relevant for baryon two-point functions due to the signal-to-noise problem present at larger time distances [42]. The fitting range can be chosen with a longer extension, such that local fluctuations in the time direction are smoothed out in the fitting procedure. A promising setup used in nucleon form factor and nucleon charge calculations [250, 251] is a combination of Wuppertal smearing for the quark fields [252] and APE smearing for the gauge links [253]. This smearing formulation is completely gauge covariant and can in principle be also applied to QCD+QED simulations in terms of the combined gauge links in eq. (6.8). However, the expansion of the smeared interpolation operators in terms of eA is non-trivial due to its iterative nature. It is not clear whether a simple and computationally efficient iterative expression for $\mathcal{O}_{e^2}^{(\frac{1}{2})}$ and $\mathcal{O}_{e^2}^{(1)}$ can be derived. Another possibility is to use a smearing setup that is QCD-covariant but QED-non-covariant, i.e. one uses only the QCD gauge links in the smearing procedure. As the gauge of the photon field is fixed, expectation values of QED-non-covariant combinations of operators do not necessarily vanish. A clear disadvantage of the latter strategy is that correlation functions are gauge dependent even for electromagnetically neutral interpolation operators, such that one cannot use a change in the gauge fixing condition as a cross check of the correctness of the computational implementation. Making use of fully covariant interpolation operators, a different approach is to calculate the contributions $\mathcal{O}_{e^2}^{(\frac{1}{2})}$ and $\mathcal{O}_{e^2}^{(1)}$ via a numerical differentiation in e . The modified computational setup based on smeared interpolation operators is also beneficial for the determination of meson masses, where a point-like shape of the interpolation operators is not required. This is different in the context of the hadronic vacuum polarisation function, which we will discuss in chapter 14.

A considerable increase in computational efficiency can be obtained applying all-mode-averaging [254–256], where the Dirac equation is solved with a reduced number of iterations for a large number of quark sources. A potential bias caused by this reduced numerical precision can be estimated by calculating the difference of the correlation function evaluated with reduced and full precision for a small number of quark sources. This strategy is particularly fruitful for correlation functions for which a signal-to-noise problem is present. In addition, it is desirable to apply a set of interpolation operators that is constructed in more rigorous manner under aspects of spacetime and flavour symmetries. Candidates are the Clebsch-Gordan based construction in [257] and a group theoretical construction in [258].

Part IV.

The hadronic vacuum polarisation function and hadronic contributions to the anomalous magnetic moment of the muon

13. Vector current renormalisation

In quantum field theories bare operators have to be renormalised in order to become physically meaningful quantities. The renormalisation pattern of an operator does not necessarily have to be purely multiplicative, but can also exhibit mixing with other operators. It is commonly assumed that two operators can only mix renormalisation if they show the same behaviour under symmetry transformations, i.e the renormalised theory possesses the same symmetries as the bare theory [58]. In addition, in a theory with dimensionful couplings such as masses, an operator will only mix with operators of the same or smaller mass dimension [58]. In theories in which all couplings are dimensionless the mixing is further restricted to operators of equal mass dimension [58].

In textbooks, it is commonly argued that conserved currents are protected from non-trivial renormalisation by Ward-Takahashi identities, such that they do not mix under renormalisation with other operators and the renormalisation factor is one [51, 56, 98]. In fact, for the electromagnetic current operator in the presence of the photon field, it is shown in [259] that the latter mixes with the four-divergence of the photon field-strength tensor under renormalisation. In the most recent publications of the lattice QCD+QED community this mixing is neither mentioned nor discussed [194, 200, 245]. We also assume a simplified renormalisation structure not taking the mixing with the four-divergence of the photon field-strength tensor into account.

In this chapter, we describe a method to determine the mixing pattern and the relevant renormalisation factors for point-like flavour neutral vector currents, which are the most straightforward discretisation of continuum flavour neutral currents. In section 6.4.1 we have derived another discretisation of the flavour neutral vector currents, namely the conserved vector currents, which satisfy a Ward-Takahashi identity and renormalise trivially under the assumption described in the previous section. The renormalisation procedure is based on the comparison of correlation functions and matrix elements under the replacement of local and conserved vector currents [98, 260]. A related effort was performed in [194] for domain wall fermions. However, a different basis for the flavour neutral currents was chosen and operator mixing was not considered.

13.1. Lattice discretisations of the electromagnetic and flavour diagonal vector currents

The construction of lattice discretisations of continuum operators is ambiguous, as one only has to reobtain the correct operator in the continuum limit. There are two commonly used discretisations of the electromagnetic vector current. The most simple and straightforward discretisation is the local vector current \mathcal{V}_1^γ , which only depends on the fields at

13. Vector current renormalisation

the same site,

$$\mathcal{V}_1^{\gamma x\mu} = \bar{\Psi}^x Q \gamma^\mu \Psi^x, \quad (13.1)$$

with the matrix of fractional quark charges $Q = \text{diag}(\frac{2}{3}, -\frac{1}{3}, -\frac{1}{3})$. Despite its simple structure, which allows for a more efficient computation of correlation functions, one major disadvantage of this particular discretisation is its nontrivial renormalisation. As we will see later, this operator mixes under renormalisation with other flavour neutral local vector currents. In order not having to determine non-trivial renormalisation factors, it is favourable to make use of the conserved forward point-split vector current $\mathcal{V}_c^\gamma = \mathcal{V}_F^\gamma$ from eq. (6.45) as a lattice discretisation of the continuum electromagnetic vector current. It is given by

$$\mathcal{V}_c^{\gamma x\mu} = \frac{1}{2} (\bar{\Psi}^{x+a\hat{\mu}} (W^{x\mu})^\dagger Q (\gamma^\mu + \mathbb{1}) \Psi^x + \bar{\Psi}^x Q (\gamma^\mu - \mathbb{1}) W^{x\mu} \Psi^{x+a\hat{\mu}}), \quad (13.2)$$

where we make use of the combined QCD+QED gauge links

$$W^{x\mu} = U^{x\mu} \exp(iaeQA^{x\mu}). \quad (6.8)$$

As we will see later in the context of renormalisation, it is convenient to decompose the electromagnetic current into a linear combination of flavour diagonal vector currents [261]

$$\mathcal{V}^\gamma = \mathcal{V}^3 + \frac{1}{\sqrt{3}} \mathcal{V}^8, \quad (13.3)$$

where we make use of the local vector currents \mathcal{V}_1^i

$$\mathcal{V}_1^{x\mu i} = \bar{\Psi}^x \Lambda^i \gamma^\mu \Psi^x \quad (13.4)$$

and the conserved vector currents \mathcal{V}_c^i from eq. (6.45)

$$\mathcal{V}_c^{x\mu i} = \frac{1}{2} (\bar{\Psi}^{x+a\hat{\mu}} (W^{x\mu})^\dagger \Lambda^i (\gamma^\mu + \mathbb{1}) \Psi^x + \bar{\Psi}^x \Lambda^i (\gamma^\mu - \mathbb{1}) W^{x\mu} \Psi^{x+a\hat{\mu}}). \quad (13.5)$$

The flavour diagonal matrices $\Lambda^0 = \frac{1}{\sqrt{6}} \mathbb{1}$ and $\Lambda^i = \frac{1}{2} \lambda^i$ for $i = 3, 8$ read

$$\Lambda^0 = \begin{pmatrix} \frac{1}{\sqrt{6}} & 0 & 0 \\ 0 & \frac{1}{\sqrt{6}} & 0 \\ 0 & 0 & \frac{1}{\sqrt{6}} \end{pmatrix}, \quad \Lambda^3 = \begin{pmatrix} \frac{1}{2} & 0 & 0 \\ 0 & -\frac{1}{2} & 0 \\ 0 & 0 & 0 \end{pmatrix}, \quad \Lambda^8 = \begin{pmatrix} \frac{1}{2\sqrt{3}} & 0 & 0 \\ 0 & \frac{1}{2\sqrt{3}} & 0 \\ 0 & 0 & -\frac{1}{\sqrt{3}} \end{pmatrix}. \quad (13.6)$$

For flavour non-diagonal matrices Λ , the definition of the vector current eq. (13.5) is not unique, as the gauge links $W^{x\mu}$ and a general Λ do not commute in a theory which is not fully flavour symmetric. In fact, the current defined above is conserved if and only if $W^{x\mu}$ and Λ commute.

13.2. The bare vector-vector correlation function

In the following section, we discuss the evaluation of the bare vector-vector correlation function on the lattice, taking leading isospin breaking effects into account. We consider the correlation function of two zero-momentum projected vector currents

$$\mathcal{V}_d^{x^0\mu i} = \frac{1}{\sqrt{|\Lambda_{123}|}} \sum_{\vec{x}} \mathcal{V}_d^{x\mu i} \quad (13.7)$$

averaged over the spatial components reading

$$C_{\mathcal{V}_{d_2}^{i_2} \mathcal{V}_{d_1}^{i_1}}(x_2^0, x_1^0) = \frac{1}{3} \sum_{\mu=1}^3 \langle \mathcal{V}_{d_2}^{x_2^0\mu i_2} \mathcal{V}_{d_1}^{x_1^0\mu i_1} \rangle \quad d_2 = 1, c \quad i_2, i_1 = 0, 3, 8. \quad (13.8)$$

One vector current operator is fixed to the local discretisation. For the second operator, both the local and the conserved discretisation are used. We allow for combinations of flavour diagonal vector currents \mathcal{V}^0 , \mathcal{V}^3 and \mathcal{V}^8 . We will see later that two currents are only prone to mixing if the corresponding overlap does not vanish. Rotations by multiples of $\pi/2$ along a spatial axis are symmetries of the action. Thus, we average over the spatial components of the vector currents for noise reduction.

13.2.1. Diagrammatic expansion of the bare vector-vector correlation function

We will now discuss how to derive the diagrammatic expansion of the correlation function eq. (13.8) according to

$$C = C^{(0)} + \sum_l \Delta \varepsilon_l C_l^{(1)} + O(\Delta \varepsilon^2). \quad (6.85)$$

As the vector current operators may be functions of the combined QCD+QED gauge links and consequently of e depending on the particular lattice discretisation, we have to expand the latter in order to derive the diagrammatic expansion. We find

$$\mathcal{V} = \mathcal{V}^{(0)} + e \mathcal{V}_{e^2}^{(\frac{1}{2})} + \frac{1}{2} e^2 \mathcal{V}_{e^2}^{(1)} + \mathcal{V}(e^3). \quad (13.9)$$

The expansion of the gauge links given in eq. (6.8) and their adjoints is

$$W^{x\mu} = U^{x\mu} \left(\mathbb{1} + i a e Q A^{x\mu} - \frac{1}{2} a^2 e^2 Q^2 (A^{x\mu})^2 \right) + O(e^3), \quad (13.10)$$

$$(W^{x\mu})^\dagger = (U^{x\mu})^\dagger \left(\mathbb{1} - i a e Q A^{x\mu} - \frac{1}{2} a^2 e^2 Q^2 (A^{x\mu})^2 \right) + O(e^3), \quad (13.11)$$

where the photon field A and the charge matrices Q are real. As the local vector current does not depend on these gauge links, the expansion is trivial:

$$(\mathcal{V}_1^{x^0\mu i})^{(0)} = \bar{\Psi}_{\mathbf{a}} V_1^{(0)x^0\mu i \mathbf{a}}_{\mathbf{b}} \Psi^{\mathbf{b}} = \mathcal{V}_1^{x^0\mu i}, \quad (13.12)$$

$$(\mathcal{V}_1^{x^0\mu i})_{e^2}^{(\frac{1}{2})} = \bar{\Psi}_{\mathbf{a}} V_1^{(\frac{1}{2})x^0\mu i \mathbf{a}}_{\mathbf{bc}} \Psi^{\mathbf{b}} A^{\mathbf{c}} = 0, \quad (13.13)$$

$$(\mathcal{V}_1^{x^0\mu i})_{e^2}^{(1)} = \bar{\Psi}_{\mathbf{a}} V_c^{(1)x^0\mu i \mathbf{a}}_{\mathbf{bc}_2 \mathbf{c}_1} \Psi^{\mathbf{b}} A^{\mathbf{c}_2} A^{\mathbf{c}_1} = 0. \quad (13.14)$$

13. Vector current renormalisation

We represent the vertex $V_1^{(0)x^0\mu i}$ associated with the operator $(\mathcal{V}_1^{x^0\mu i})^{(0)}$ by the diagram

$$V_1^{(0)x^0\mu i} \mathbf{a} \mathbf{b} = \begin{array}{c} \mathbf{a} \text{---} \bullet \text{---} \mathbf{b} \\ \text{\scriptsize $V_1^{(0)x^0\mu i}$} \end{array} . \quad (13.15)$$

For the conserved vector current we, however, obtain the non-trivial expansion

$$\begin{aligned} (\mathcal{V}_c^{x^0\mu i})^{(0)} &= \bar{\Psi}_{\mathbf{a}} V_c^{(0)x^0\mu i} \mathbf{a} \mathbf{b} \Psi^{\mathbf{b}} \\ &= \frac{1}{\sqrt{|\Lambda_{123}|}} \sum_{\vec{x}} \frac{1}{2} (\bar{\Psi}^{x+a\hat{\mu}} (U^{x\mu})^\dagger \Lambda^i (\gamma^\mu + \mathbb{1}) \Psi^x \\ &\quad + \bar{\Psi}^x \Lambda^i (\gamma^\mu - \mathbb{1}) U^{x\mu} \Psi^{x+a\hat{\mu}}), \end{aligned} \quad (13.16)$$

$$\begin{aligned} (\mathcal{V}_c^{x^0\mu i})_{e^2}^{(\frac{1}{2})} &= \bar{\Psi}_{\mathbf{a}} V_c^{(\frac{1}{2})x^0\mu i} \mathbf{a}_{\mathbf{bc}} \Psi^{\mathbf{b}} A^{\mathbf{c}} \\ &= \frac{1}{\sqrt{|\Lambda_{123}|}} \sum_{\vec{x}} \frac{i}{2} a (-\bar{\Psi}^{x+a\hat{\mu}} (U^{x\mu})^\dagger Q \Lambda^i (\gamma^\mu + \mathbb{1}) \Psi^x \\ &\quad + \bar{\Psi}^x \Lambda^i Q (\gamma^\mu - \mathbb{1}) U^{x\mu} \Psi^{x+a\hat{\mu}}) A^{x\mu}, \end{aligned} \quad (13.17)$$

$$\begin{aligned} (\mathcal{V}_c^{x^0\mu i})_{e^2}^{(1)} &= \bar{\Psi}_{\mathbf{a}} V_c^{(1)x^0\mu i} \mathbf{a}_{\mathbf{bc}_2\mathbf{c}_1} \Psi^{\mathbf{b}} A^{\mathbf{c}_2} A^{\mathbf{c}_1} \\ &= \frac{1}{\sqrt{|\Lambda_{123}|}} \sum_{\vec{x}} -\frac{1}{2} a^2 (\bar{\Psi}^{x+a\hat{\mu}} (U^{x\mu})^\dagger Q^2 \Lambda^i (\gamma^\mu + \mathbb{1}) \Psi^x \\ &\quad + \bar{\Psi}^x \Lambda^i Q^2 (\gamma^\mu - \mathbb{1}) U^{x\mu} \Psi^{x+a\hat{\mu}}) (A^{x\mu})^2. \end{aligned} \quad (13.18)$$

We also introduce diagrammatic representations for the vertices $V_c^{(0)x^0\mu i}$, $V_c^{(\frac{1}{2})x^0\mu i}$ and $V_c^{(1)x^0\mu i}$, which are related to the operators $(\mathcal{V}_c^{x^0\mu i})^{(0)}$, $(\mathcal{V}_c^{x^0\mu i})_{e^2}^{(\frac{1}{2})}$ and $(\mathcal{V}_c^{x^0\mu i})_{e^2}^{(1)}$:

$$V_c^{(0)x^0\mu i} \mathbf{a} \mathbf{b} = \begin{array}{c} \mathbf{a} \text{---} \bullet \text{---} \mathbf{b} \\ \text{\scriptsize $V_c^{(0)x^0\mu i}$} \end{array} , \quad (13.19)$$

$$V_c^{(\frac{1}{2})x^0\mu i} \mathbf{a}_{\mathbf{bc}} = \begin{array}{c} \mathbf{a} \text{---} \bullet \text{---} \mathbf{b} \\ \text{\scriptsize $V_c^{(\frac{1}{2})x^0\mu i}$} \end{array} \begin{array}{c} \text{\scriptsize \hat{c}} \\ \text{\scriptsize \uparrow} \\ \text{\scriptsize \downarrow} \end{array} , \quad (13.20)$$

$$V_c^{(1)x^0\mu i} \mathbf{a}_{\mathbf{bc}_2\mathbf{c}_1} = \begin{array}{c} \mathbf{a} \text{---} \bullet \text{---} \mathbf{b} \\ \text{\scriptsize $V_c^{(1)x^0\mu i}$} \end{array} \begin{array}{c} \text{\scriptsize \hat{c}_2} \\ \text{\scriptsize \uparrow} \\ \text{\scriptsize \downarrow} \\ \text{\scriptsize \hat{c}_1} \end{array} . \quad (13.21)$$

The operators $(\mathcal{V}_c^{x^0\mu i})_{e^2}^{(\frac{1}{2})}$ and $(\mathcal{V}_c^{x^0\mu i})_{e^2}^{(1)}$ lead to additional Feynman diagrams in the diagrammatic expansion of a mesonic two-point function, which we have not considered so far. In detail, the first-order electromagnetic contribution $(C_{\mathcal{M}_2\mathcal{M}_1})_{e^2}^{(1)}$ in eq. (11.22)

13.3. Computation of quark-connected Feynman diagrams

receives additional contributions from the diagrams

$$\begin{aligned}
 & \left\langle M_2^{(\frac{1}{2})} \text{---} M_1^{(0)} + M_2^{(\frac{1}{2})} \text{---} M_1^{(0)} \right. \\
 & + M_2^{(\frac{1}{2})} \text{---} M_1^{(0)} + M_2^{(1)} \text{---} M_1^{(0)} \\
 & + M_2^{(\frac{1}{2})} \text{---} M_1^{(0)} + M_2^{(\frac{1}{2})} \text{---} M_1^{(0)} \\
 & \left. + M_2^{(\frac{1}{2})} \text{---} M_1^{(0)} + M_2^{(1)} \text{---} M_1^{(0)} \right\rangle.
 \end{aligned} \tag{13.22}$$

As in section 11.2.2, we translate the additional quark-connected diagrams into contracted tensor-structures of the interpolation operators, quark and photon propagators and vertices. They read

$$\begin{aligned}
 M_2^{(\frac{1}{2})} \text{---} M_1^{(0)} &= -\Sigma c_2 c_1 \left(S^{b_1}_{a_3} M_2^{(\frac{1}{2})a_3}_{b_3 c_2} \right. \\
 &\quad \left. \cdot S^{b_3}_{a_2} V_{\bar{q}q\gamma}^{a_2}_{b_2 c_1} S^{b_2}_{a_1} M_1^{(0)a_1}_{b_1} \right),
 \end{aligned} \tag{13.23}$$

$$\begin{aligned}
 M_2^{(\frac{1}{2})} \text{---} M_1^{(0)} &= -\Sigma c_2 c_1 \left(S^{b_1}_{a_3} V_{\bar{q}q\gamma}^{a_3}_{b_3 c_2} S^{b_3}_{a_2} M_2^{(\frac{1}{2})a_2}_{b_2} \right. \\
 &\quad \left. \cdot S^{b_2}_{a_1} M_1^{(0)a_1}_{b_1} \right),
 \end{aligned} \tag{13.24}$$

$$M_2^{(1)} \text{---} M_1^{(0)} = -\frac{1}{2} \Sigma c_2 c_1 \left(S^{b_1}_{a_2} M_2^{(1)a_2}_{b_2 c_1 c_2} S^{b_2}_{a_1} M_1^{(0)a_1}_{b_1} \right). \tag{13.25}$$

13.3. Computation of quark-connected Feynman diagrams

For the computation of quark-connected contributions to the vector-vector two-point function, we use the same setup as for mesonic two-point functions described in section 11.3. In fact, the same quark and photon sources, as well as quark propagators in eq. (7.22) and sequential quark propagators in eqs. (7.26), (7.29), (7.34) and (7.37) are used, such that no additional solutions of the Dirac equation have to be computed. Only the contraction

13. Vector current renormalisation

stencils have to be adapted, which we discuss in the following. It is, however, important to point out that we cannot place a conserved vector current at the mesonic source, i.e. for the operator \mathcal{M}_1 . To include a point-split interpolation operator at the mesonic source, the computational setup has to be changed considerably.

13.3.1. Local vector current

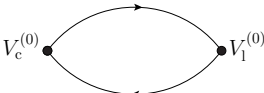
For the quark-connected diagrams, required for the evaluation of the correlation function of two local vector currents, we utilise the contraction stencil derived for mesonic two-point functions with point-like operators defined in eq. (11.40) setting, $M_1^{(0)} = V_1^{(0)(x^0\mu i)_1}$ and $M_2^{(0)} = V_1^{(0)(x^0\mu i)_2}$. The quark-connected diagrams are then evaluated according to eqs. (11.41) to (11.48).

13.3.2. Conserved vector current

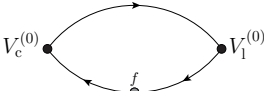
For the quark-connected diagrams, required for the evaluation of the correlation function of one conserved and one local vector current, we define three additional contraction stencils. The first stencil describes quark-connected diagrams originating from correlation functions of the operators $(\mathcal{V}_c)^{(0)}$ and $(\mathcal{V}_1)^{(0)}$:

$$\begin{aligned} & H_{V_c^{(0)}V_1^{(0)}}^{(x^0\mu i)_2(x^0\mu i)_1}[\Psi_2, \Psi_1] \\ &= -\frac{1}{|\Lambda_{123}|} \sum_{\vec{x}_2 \in \Lambda_{123}} \left(\frac{1}{2} \text{tr} \left(\gamma^5 (\Psi_{2_{x_1^0}}^{x_2+a\hat{\mu}_2})^\dagger \gamma^5 (U^{x\mu_2})^\dagger \Lambda^{i_2} (\gamma^{\mu_2} + \mathbf{1}) \Psi_{1_{x_1^0}}^{x_2} \Lambda^{i_1} \gamma^{\mu_1} \right) \right. \\ & \quad \left. + \frac{1}{2} \text{tr} \left(\gamma^5 (\Psi_{2_{x_1^0}}^{x_2})^\dagger \gamma^5 \Lambda^{i_2} (\gamma^{\mu_2} - \mathbf{1}) U^{x\mu_2} \Psi_{1_{x_1^0}}^{x_2+a\hat{\mu}_2} \Lambda^{i_1} \gamma^{\mu_1} \right) \right). \end{aligned} \quad (13.26)$$

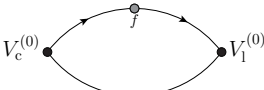
The overall minus sign reflects the closed fermion loop as in eqs. (11.23) to (11.30). This stencil is utilised to evaluate a large number of diagrams, both of zeroth and first-order:



$$V_c^{(0)} \text{---} V_1^{(0)} = \left\langle H_{V_c^{(0)}V_1^{(0)}}[\Psi^{(0)}[\eta], \Psi^{(0)}[\eta]] \right\rangle_\eta, \quad (13.27)$$



$$V_c^{(0)} \text{---} V_1^{(0)} = \left\langle H_{V_c^{(0)}V_1^{(0)}}[\Psi^{(0)}[\eta], \Psi_{V_{\bar{q}qf}}^{(0)}[\eta]] \right\rangle_\eta, \quad (13.28)$$



$$V_c^{(0)} \text{---} V_1^{(0)} = \left\langle H_{V_c^{(0)}V_1^{(0)}}[\Psi_{V_{\bar{q}qf}}^{(0)}[\eta], \Psi^{(0)}[\eta]] \right\rangle_\eta, \quad (13.29)$$

13.3. Computation of quark-connected Feynman diagrams

$$\begin{array}{c} \text{Diagram: } V_c^{(0)} \text{ and } V_1^{(0)} \text{ connected by a loop with a gluon exchange (curly line).} \end{array} = \left\langle H_{V_c^{(0)} V_1^{(0)}} [\Psi^{(0)}[\eta], \Psi_{V_{\bar{q}q\gamma\Sigma}}^{(0)}[\eta]] \right\rangle_\eta, \quad (13.30)$$

$$\begin{array}{c} \text{Diagram: } V_c^{(0)} \text{ and } V_1^{(0)} \text{ connected by a loop with a photon exchange (wavy line).} \end{array} = \left\langle \left\langle H_{V_c^{(0)} V_1^{(0)}} [\Psi^{(0)}[\eta], \Psi_{V_{\bar{q}q\gamma\sqrt{\Sigma}V_{\bar{q}q\gamma\sqrt{\Sigma}}}}^{(0)}[\eta, J, J]] \right\rangle_\eta \right\rangle_J, \quad (13.31)$$

$$\begin{array}{c} \text{Diagram: } V_c^{(0)} \text{ and } V_1^{(0)} \text{ connected by a loop with a gluon exchange (curly line).} \end{array} = \left\langle H_{V_c^{(0)} V_1^{(0)}} [\Psi_{V_{\bar{q}q\gamma\Sigma}}^{(0)}[\eta], \Psi^{(0)}[\eta]] \right\rangle_\eta, \quad (13.32)$$

$$\begin{array}{c} \text{Diagram: } V_c^{(0)} \text{ and } V_1^{(0)} \text{ connected by a loop with a photon exchange (wavy line).} \end{array} = \left\langle \left\langle H_{V_c^{(0)} V_1^{(0)}} [\Psi_{V_{\bar{q}q\gamma\sqrt{\Sigma}V_{\bar{q}q\gamma\sqrt{\Sigma}}}}^{(0)}[\eta, J, J], \Psi^{(0)}[\eta]] \right\rangle_\eta \right\rangle_J, \quad (13.33)$$

$$\begin{array}{c} \text{Diagram: } V_c^{(0)} \text{ and } V_1^{(0)} \text{ connected by a loop with a photon exchange (wavy line).} \end{array} = \left\langle \left\langle H_{V_c^{(0)} V_1^{(0)}} [\Psi_{V_{\bar{q}q\gamma\sqrt{\Sigma}}}^{(0)}[\eta, J], \Psi_{V_{\bar{q}q\gamma\sqrt{\Sigma}}}^{(0)}[\eta, J]] \right\rangle_\eta \right\rangle_J. \quad (13.34)$$

The second stencil is used to compute diagrams with one photon line attached to the conserved vector current:

$$\begin{aligned}
 & H_{V_c^{(\frac{1}{2})} V_1^{(0)}}^{(x^0 \mu i)_2 (x^0 \mu i)_1} [\Psi_2, \Psi_1, A] \\
 &= -\frac{1}{|\Lambda_{123}|} \sum_{\vec{x}_2 \in \Lambda_{123}} \\
 & \cdot \left(-\frac{i}{2} a \operatorname{tr} \left(\gamma^5 (\Psi_{2x_1^0}^{x_2+a\hat{\mu}_2})^\dagger \gamma^5 (U^{x\mu_2})^\dagger Q \Lambda^{i_2} (\gamma^{\mu_2} + \mathbb{1}) \Psi_{1x_1^0}^{x_2} \Lambda^{i_1} \gamma^{\mu_1} \right) A^{x\mu_2} \right. \\
 & \quad \left. + \frac{i}{2} a \operatorname{tr} \left(\gamma^5 (\Psi_{2x_1^0}^{x_2})^\dagger \gamma^5 \Lambda^{i_2} Q (\gamma^{\mu_2} - \mathbb{1}) U^{x\mu_2} \Psi_{1x_1^0}^{x_2+a\hat{\mu}_2} \Lambda^{i_1} \gamma^{\mu_1} \right) A^{x\mu_2} \right). \quad (13.35)
 \end{aligned}$$

In particular, it is used to evaluate the two diagrams

$$\begin{array}{c} \text{Diagram: } V_c^{(\frac{1}{2})} \text{ and } V_1^{(0)} \text{ connected by a loop with a photon exchange (wavy line).} \end{array} = \left\langle \left\langle H_{V_c^{(\frac{1}{2})} V_1^{(0)}} [\Psi^{(0)}[\eta, J], \Psi_{V_{\bar{q}q\gamma\sqrt{\Sigma}}}^{(0)}[\eta, J], A[J]] \right\rangle_\eta \right\rangle_J, \quad (13.36)$$

$$\begin{array}{c} \text{Diagram: } V_c^{(\frac{1}{2})} \text{ and } V_1^{(0)} \text{ connected by a loop with a photon exchange (wavy line).} \end{array} = \left\langle \left\langle H_{V_c^{(\frac{1}{2})} V_1^{(0)}} [\Psi_{V_{\bar{q}q\gamma\sqrt{\Sigma}}}^{(0)}[\eta, J], \Psi^{(0)}[\eta, J], A[J]] \right\rangle_\eta \right\rangle_J. \quad (13.37)$$

13. Vector current renormalisation

The third stencil describes the class of quark-connected diagrams with a photon loop attached to the conserved vector current:

$$\begin{aligned}
& H_{(\mathcal{V}_c)_e^{(1)} \Sigma(\mathcal{V}_1)^{(0)}}^{(x^0 \mu i)_2 (x^0 \mu i)_1} [\Psi_2, \Psi_1] \\
&= -\frac{1}{2} \frac{1}{|\Lambda_{123}|} \sum_{\vec{x}_2 \in \Lambda_{123}} \\
&\quad \cdot \left(-\frac{1}{2} a^2 \text{tr} \left(\gamma^5 (\Psi_{2_{x_1^0}}^{x_2+a\hat{\mu}_2})^\dagger \gamma^5 (U^{x\mu_2})^\dagger Q^2 \Lambda^{i_2} (\gamma^{\mu_2} + \mathbb{1}) \Psi_{1_{x_1^0}}^{x_2} \Lambda^{i_1} \gamma^{\mu_1} \right) \Sigma^{x\mu_2 x\mu_2} \right. \\
&\quad \left. - \frac{1}{2} a^2 \text{tr} \left(\gamma^5 (\Psi_{2_{x_1^0}}^{x_2})^\dagger \gamma^5 \Lambda^{i_2} Q^2 (\gamma^{\mu_2} - \mathbb{1}) U^{x_2\mu} \Psi_{1_{x_1^0}}^{x_2+a\hat{\mu}_2} \Lambda^{i_1} \gamma^{\mu_1} \right) \Sigma^{x\mu_2 x\mu_2} \right). \tag{13.38}
\end{aligned}$$

The factor $-\frac{1}{2}$ appears due to the closed fermion loop and the symmetry factor associated to the photon loop attached to the same vertex as in eq. (13.25). There is only one diagram for which this stencil is used:

$$V_c^{(1)} \text{ (with photon loop) } V_1^{(0)} = \left\langle H_{(\mathcal{V}_c)_e^{(1)} \Sigma(\mathcal{V}_1)^{(0)}} [\Psi^{(0)}[\eta], \Psi^{(0)}[\eta]] \right\rangle_\eta. \tag{13.39}$$

13.4. Renormalisation of the local electromagnetic current

In order to calculate the HVP using local electromagnetic current operators, we have to determine the renormalisation pattern of \mathcal{V}_1^γ . In QCD+QED, local flavour-neutral vector currents are not protected from mixing under renormalisation. Treating isospin-breaking effects perturbatively, it is reasonable to consider an operator basis with definite transformation behaviour under isospin rotations. It is convenient to consider the operator basis introduced in eq. (13.4). \mathcal{V}_1^0 and \mathcal{V}_1^8 are isosinglet vector currents, whereas \mathcal{V}_1^3 belongs to the isotriplet vector currents. For a given μ , the flavour-neutral vector currents $\mathcal{V}_1^{i\mu}$ with $i = 0, 3, 8$ are prone to mixing under renormalisation, such that we have to introduce a matrix of renormalisation factors with entries $Z_{\mathcal{V}_{1,R}^{i_2} \mathcal{V}_1^{i_1}}$ and $i_2, i_1 = 0, 3, 8$ to ensure the correct multiplicative renormalisation. In vector-matrix notation, the bare and renormalised vector currents are related by

$$\mathcal{V}_R = Z_{\mathcal{V}_R} \mathcal{V}. \tag{13.40}$$

The latter choice for the operator basis is convenient, because it leads to vanishing entries in the zeroth-order mixing matrix. Due to lattice symmetries, the renormalisation factors of the spatial components of the vector current are identical. This is not necessarily the case for the temporal component, as the temporal extent of the lattice differs from the spatial one. Equality should, however, be found in the large volume limit. In the following discussion, we only consider the spatial components, as only those are required for the computation of the hadronic vacuum polarisation (HVP) function via the *time-momentum representation* [33]. In the case of open boundary conditions, the translational

13.4. Renormalisation of the local electromagnetic current

invariance in the temporal direction is broken. Considering vector currents located far away from the boundaries, we expect the renormalisation factors to have negligible time dependency. As the conserved vector current \mathcal{V}_c is assumed to renormalise trivially, the corresponding renormalisation matrix is unity:

$$Z_{\mathcal{V}_{c,R}\mathcal{V}_c} = \mathbb{1}. \quad (13.41)$$

Combining eqs. (13.3) and (13.40), we can relate the renormalised electromagnetic current to the bare flavour diagonal vector currents, defined in eqs. (13.4) and (13.5):

$$\mathcal{V}_R^\gamma = \mathcal{V}_R^3 + \frac{1}{\sqrt{3}}\mathcal{V}_R^8 = \sum_{i=0,3,8} \left(Z_{\mathcal{V}_R^3\mathcal{V}^i} + \frac{1}{\sqrt{3}}Z_{\mathcal{V}_R^8\mathcal{V}^i} \right) \mathcal{V}^i. \quad (13.42)$$

Making use of eq. (13.41), we check consistency, if the renormalised conserved electromagnetic current is in fact identical to the bare conserved electromagnetic current:

$$\begin{aligned} \mathcal{V}_{c,R}^\gamma &= \mathcal{V}_{c,R}^3 + \frac{1}{\sqrt{3}}\mathcal{V}_{c,R}^8 = \sum_{i=0,3,8} \left(Z_{\mathcal{V}_{c,R}^3\mathcal{V}_c^i} + \frac{1}{\sqrt{3}}Z_{\mathcal{V}_{c,R}^8\mathcal{V}_c^i} \right) \mathcal{V}_c^i \\ &= \mathcal{V}_c^3 + \frac{1}{\sqrt{3}}\mathcal{V}_c^8 = \mathcal{V}_c^\gamma. \end{aligned} \quad (13.43)$$

13.4.1. Renormalisation condition

In order to fix the renormalisation factors in eq. (13.40), we have to introduce a renormalisation condition. This renormalisation condition is by no means unique. We demand that the matrix element $\langle 0|\mathcal{V}_R|V \rangle$ of the renormalised operators is the same for both discretisations [98, 260],

$$\langle 0|\mathcal{V}_{c,R}|V \rangle = \langle 0|\mathcal{V}_{l,R}|V \rangle, \quad (13.44)$$

where $|V \rangle$ denotes the lowest accessible excitation of the vacuum created by the operators \mathcal{V}_c and \mathcal{V}_l . This matrix element can be extracted from the correlation function $\langle \mathcal{V}_R^{x_2^0}\mathcal{V}_R^{x_1^0} \rangle$ for large time distances $x_1^0 \ll x_2^0$, i.e. the renormalisation condition becomes

$$\langle \mathcal{V}_{c,R}^{x_2^0}\mathcal{V}_{l,R}^{x_1^0} \rangle - \langle \mathcal{V}_{l,R}^{x_2^0}\mathcal{V}_{l,R}^{x_1^0} \rangle \rightarrow 0. \quad (13.45)$$

The renormalised correlation functions are related with their bare counterparts via the renormalisation factors matrices defined in eq. (13.40). Therefore, we find

$$Z_{\mathcal{V}_{c,R}\mathcal{V}_c} \langle \mathcal{V}_c^{x_2^0}\mathcal{V}_l^{x_1^0} \rangle Z_{\mathcal{V}_{l,R}\mathcal{V}_l}^T - Z_{\mathcal{V}_{l,R}\mathcal{V}_l} \langle \mathcal{V}_l^{x_2^0}\mathcal{V}_l^{x_1^0} \rangle Z_{\mathcal{V}_{l,R}\mathcal{V}_l}^T \rightarrow 0. \quad (13.46)$$

Multiplying by the inverse of $Z_{\mathcal{V}_{l,R}\mathcal{V}_l}^T$ from the right, we obtain the asymptotic condition

$$\langle \mathcal{V}_c^{x_2^0}\mathcal{V}_l^{x_1^0} \rangle - Z_{\mathcal{V}_{l,R}\mathcal{V}_l} \langle \mathcal{V}_l^{x_2^0}\mathcal{V}_l^{x_1^0} \rangle \rightarrow 0. \quad (13.47)$$

13. Vector current renormalisation

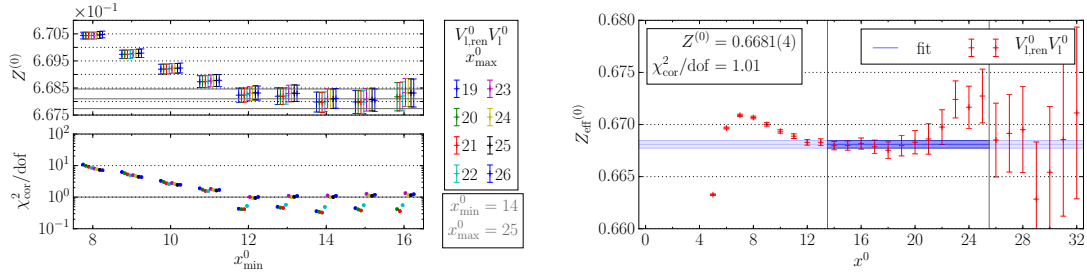


Figure 13.1.: Parameters of the fits to the effective renormalisation factor $(Z_{\text{eff}, \nu_{1,R}^0 \nu_1^0})^{(0)}$ on N200. The selected fits are marked in grey.

After averaging eq. (13.47) over the spatial components of the vector currents, we can express the latter in terms of the correlation functions defined in eq. (13.8), reading

$$C_{\text{cl}}(t_2, t_1) - Z_{\nu_{1,R} \nu_1} C_{\text{ll}}(t_2, t_1) \rightarrow 0. \quad (13.48)$$

In order to extract the renormalisation constants from the correlation functions C_{ll} and C_{cl} , first we define, similar to the effective mass in section 10.4, a matrix of effective time-dependent renormalisation factors

$$Z_{\text{eff}, \nu_{1,R} \nu_1}(t_2, t_1) = C_{\text{cl}}(t_2, t_1) (C_{\text{ll}}(t_2, t_1))^{-1} \rightarrow Z_{\nu_{1,R} \nu_1}. \quad (13.49)$$

As we treat isospin breaking effects perturbatively, we have to expand this definition order by order, finding for the zeroth-order contribution

$$(Z_{\text{eff}, \nu_{1,R} \nu_1})^{(0)}(t_2, t_1) = (C_{\text{cl}}(t_2, t_1))^{(0)} ((C_{\text{ll}}(t_2, t_1))^{(0)})^{-1} \rightarrow (Z_{\nu_{1,R} \nu_1})^{(0)}. \quad (13.50)$$

and for the first-order contribution

$$\begin{aligned} (Z_{\text{eff}, \nu_{1,R} \nu_1})^{(1)}_l(t_2, t_1) &= (C_{\text{cl}}(t_2, t_1))^{(1)}_l \\ &\quad - (C_{\text{cl}}(t_2, t_1))^{(0)} ((C_{\text{ll}}(t_2, t_1))^{(0)})^{-1} (C_{\text{ll}}(t_2, t_1))^{(1)}_l ((C_{\text{ll}}(t_2, t_1))^{(0)})^{-1} \\ &\rightarrow (Z_{\nu_{1,R} \nu_1})^{(1)}_l. \end{aligned} \quad (13.51)$$

Second, we fit the effective renormalisation factor to a constant. The fit intervals are chosen so that $\chi^2_{\text{cor}}/\text{dof}$ is closest to 1 and the fit parameters $(Z_{\nu_{1,R} \nu_1})^{(0)}$ and $(Z_{\nu_{1,R} \nu_1})^{(1)}$ are stable under the variation of both fit interval boundaries. This minimises existed state and boundary effects.

In the following, we discuss the results in more detail on the basis of computations on the ensemble N200. Figures 13.1 to 13.9 and figs. 13.10 to 13.18 show the fit to the zeroth- and first-order contributions, respectively. The zeroth-order contribution to the matrix of renormalisation factors reads

$$(Z_{\nu_{1,R} \nu_1})^{(0)} = \begin{pmatrix} 0.6681(4) & 0.0 & 0.00311(23) \\ 0.0 & 0.6703(5) & 0.0 \\ 0.00311(23) & 0.0 & 0.66598(22) \end{pmatrix}. \quad (13.52)$$

13.4. Renormalisation of the local electromagnetic current

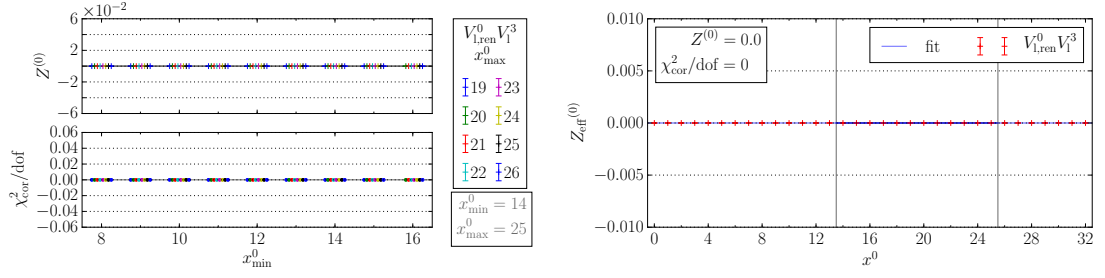


Figure 13.2.: Parameters of the fits to the effective renormalisation factor $(Z_{\text{eff}, \nu_{1,R}^0 \nu_1^3})^{(0)}$ on N200. The selected fits are marked in grey.

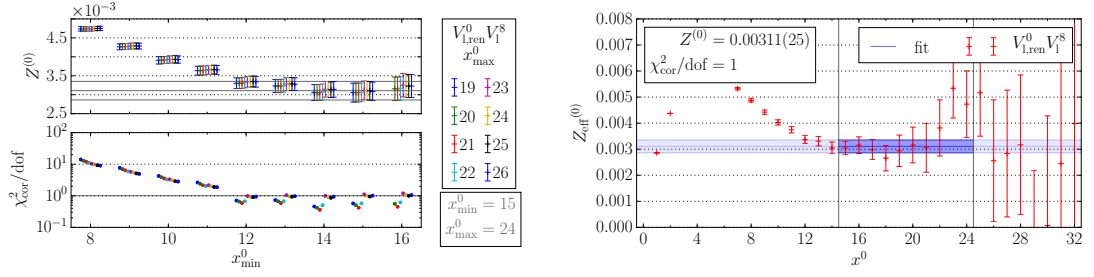


Figure 13.3.: Parameters of the fits to the effective renormalisation factor $(Z_{\text{eff}, \nu_{1,R}^0 \nu_1^8})^{(0)}$ on N200. The selected fits are marked in grey.

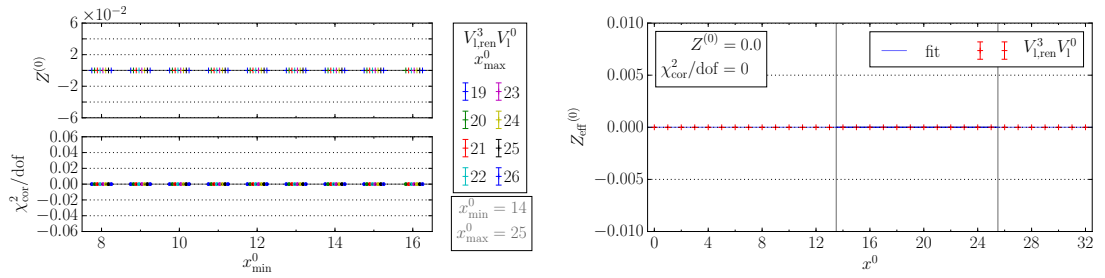


Figure 13.4.: Parameters of the fits to the effective renormalisation factor $(Z_{\text{eff}, \nu_{1,R}^3 \nu_1^0})^{(0)}$ on N200. The selected fits are marked in grey.

13. Vector current renormalisation

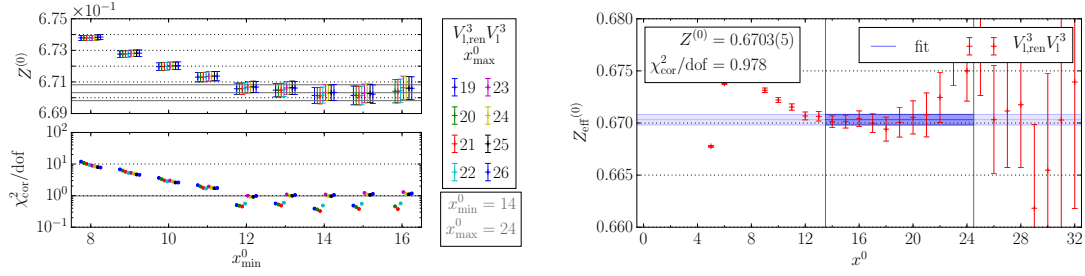


Figure 13.5.: Parameters of the fits to the effective renormalisation factor $(Z_{\text{eff}, \nu_{1,R}^3 \nu_1^3})^{(0)}$ on N200. The selected fits are marked in grey.

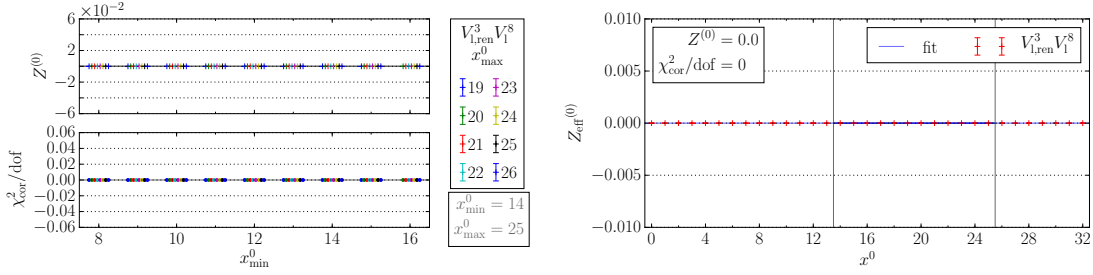


Figure 13.6.: Parameters of the fits to the effective renormalisation factor $(Z_{\text{eff}, \nu_{1,R}^3 \nu_1^8})^{(0)}$ on N200. The selected fits are marked in grey.

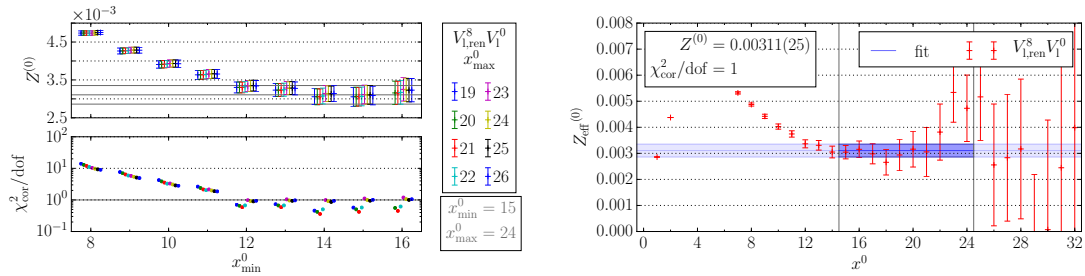


Figure 13.7.: Parameters of the fits to the effective renormalisation factor $(Z_{\text{eff}, \nu_{1,R}^8 \nu_1^0})^{(0)}$ on N200. The selected fits are marked in grey.

13.4. Renormalisation of the local electromagnetic current

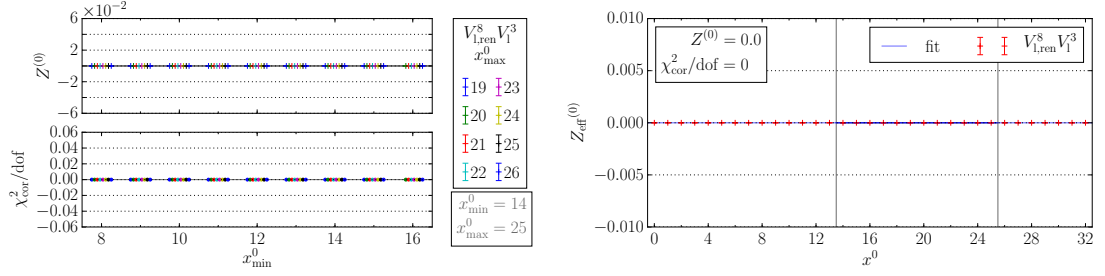


Figure 13.8.: Parameters of the fits to the effective renormalisation factor $(Z_{\text{eff}, \nu_{1,R}^8 \nu_1^3})^{(0)}$ on N200. The selected fits are marked in grey.

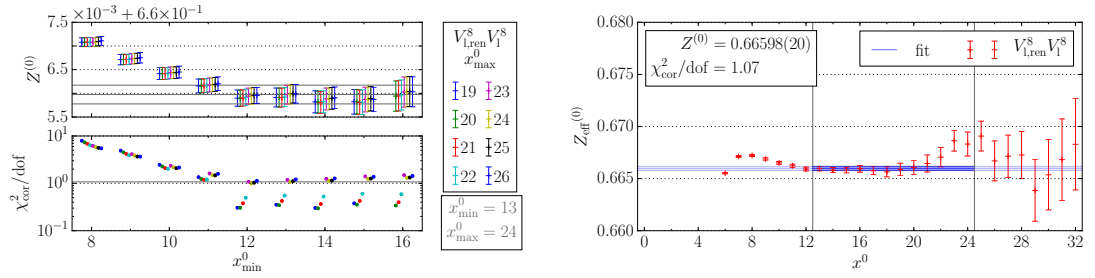


Figure 13.9.: Parameters of the fits to the effective renormalisation factor $(Z_{\text{eff}, \nu_{1,R}^8 \nu_1^8})^{(0)}$ on N200. The selected fits are marked in grey.

13. Vector current renormalisation

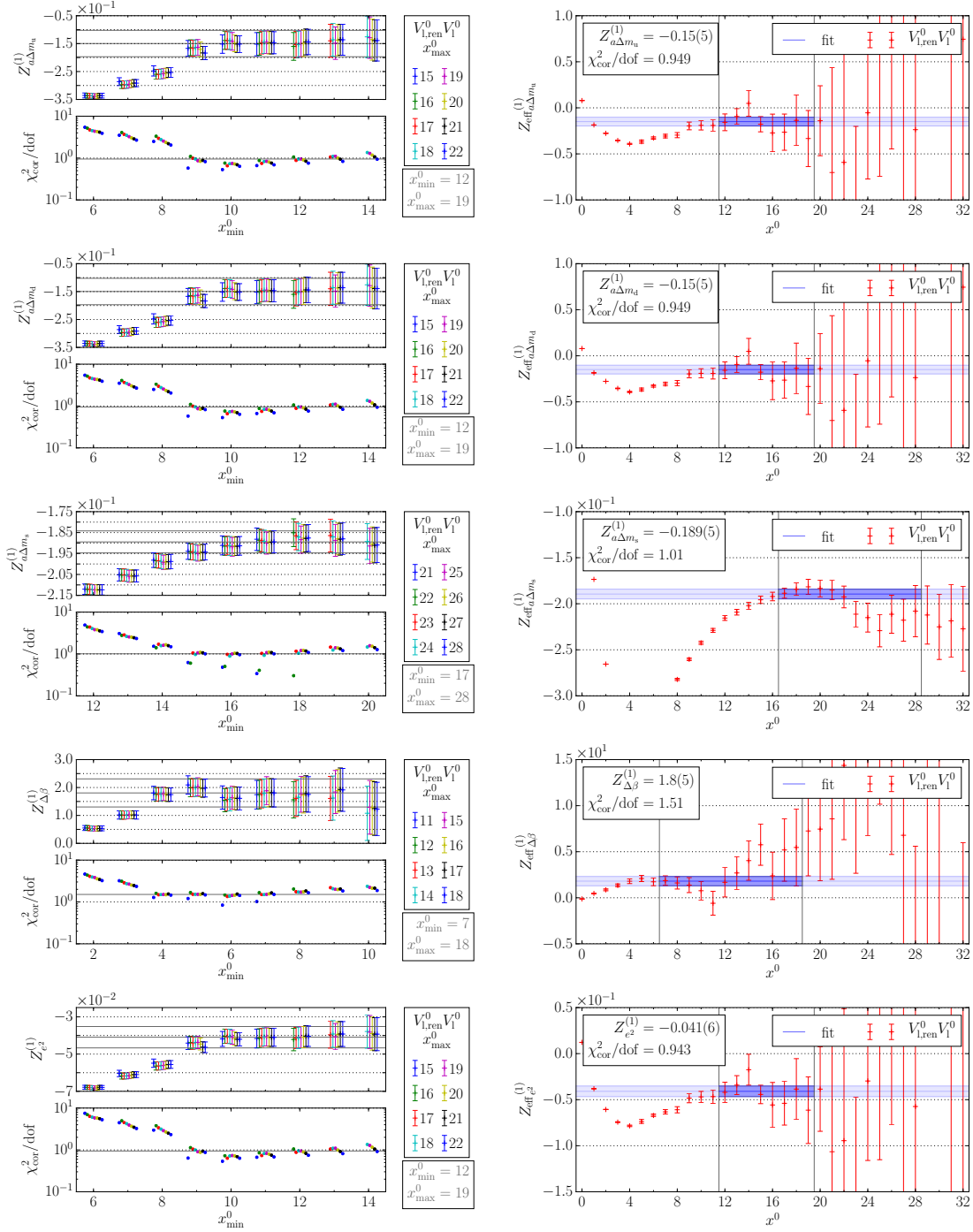


Figure 13.10.: Fit to the effective renormalisation factor $(Z_{\text{eff}, V_l^0 V_l^0}^{(1)})$ on N200. The selected fit intervals are marked in grey.

13.4. Renormalisation of the local electromagnetic current

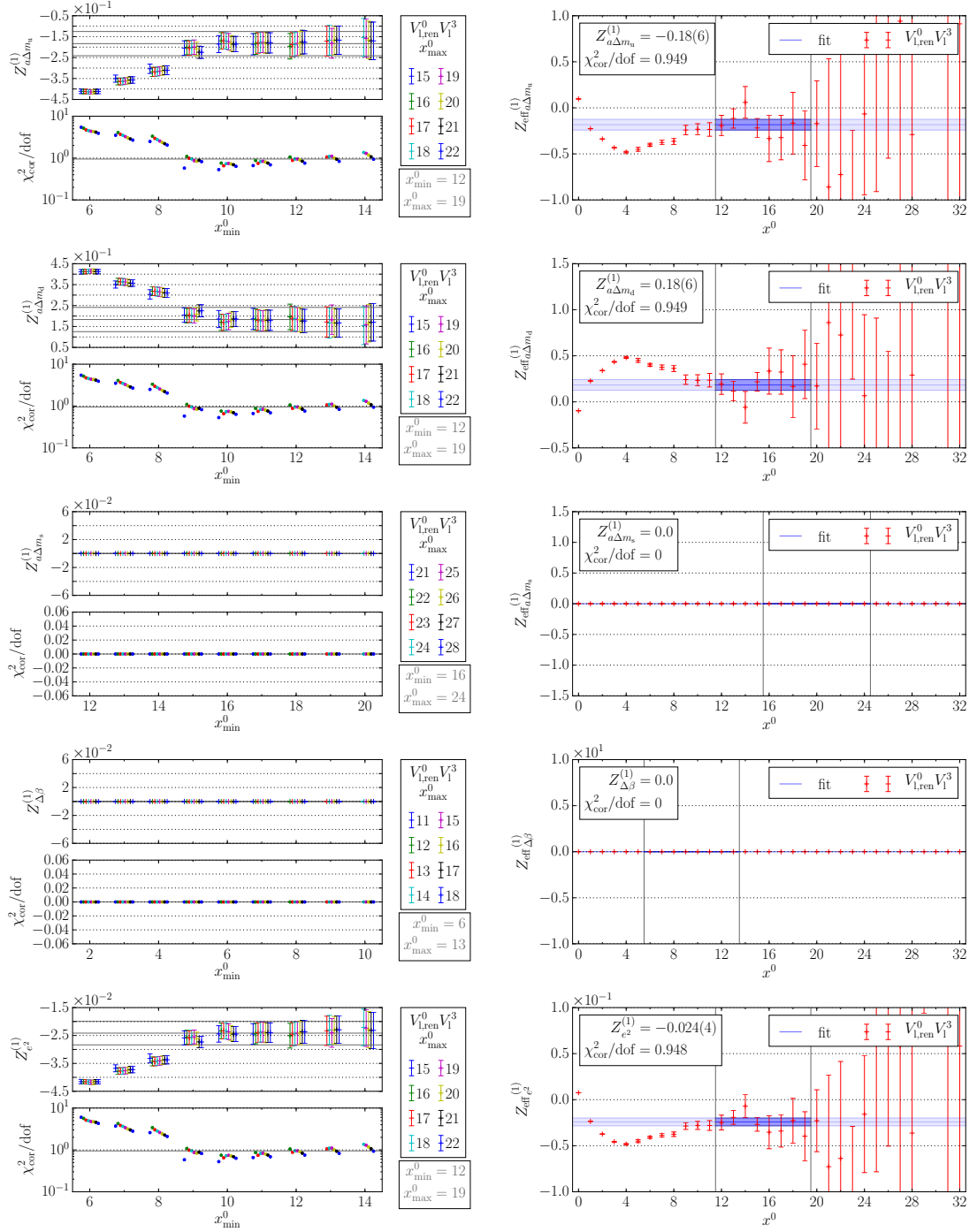


Figure 13.11.: Parameters of the fits to the effective renormalisation factor $(Z_{\text{eff}, \nu_{1,R}^0 \nu_1^3})^{(1)}$ on N200. The selected fits are marked in grey.

13. Vector current renormalisation

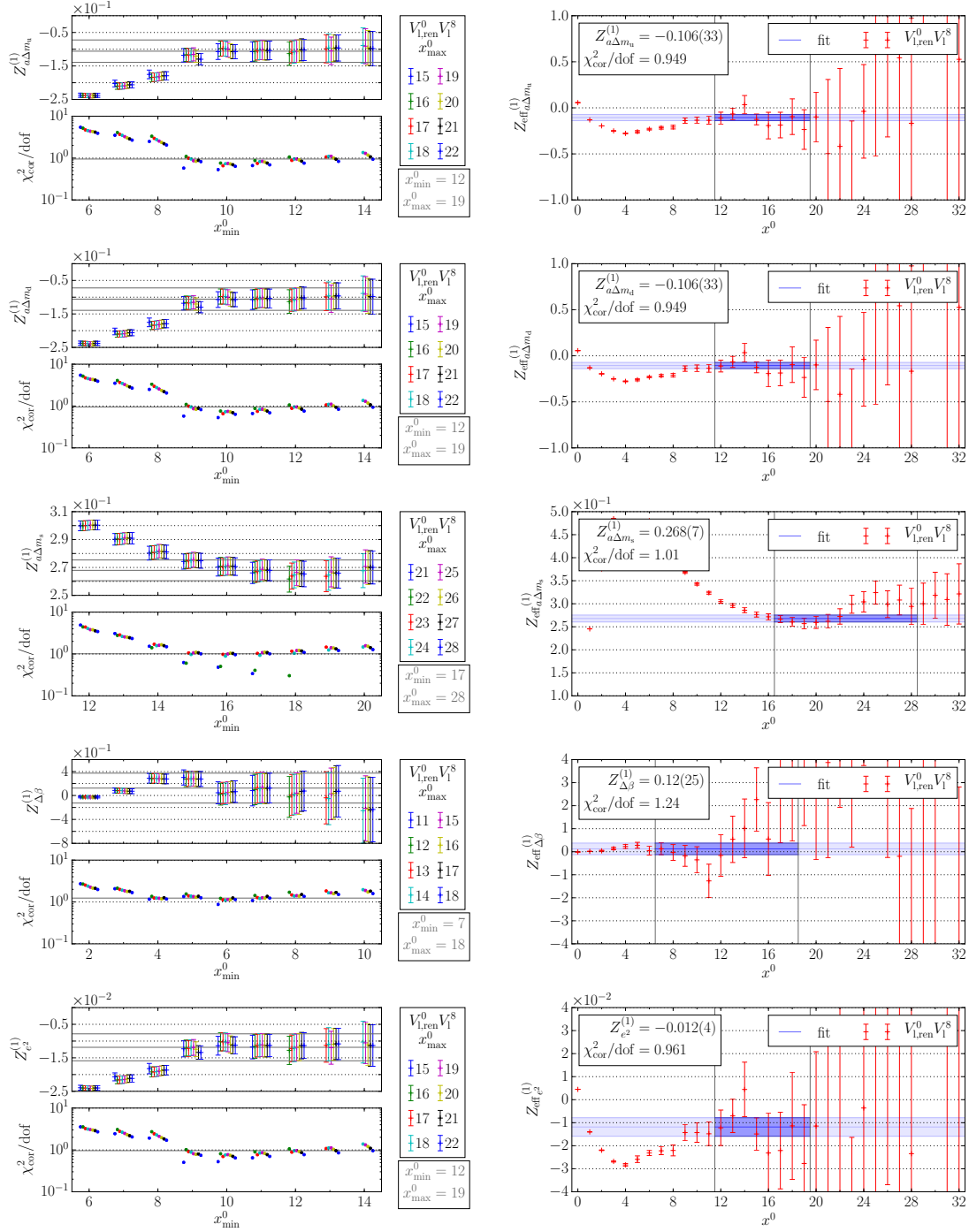


Figure 13.12.: Parameters of the fits to the effective renormalisation factor $(Z_{\text{eff}, \nu_{1,\text{R}}^0 \nu_1^8})^{(1)}$ on N200. The selected fits are marked in grey.

13.4. Renormalisation of the local electromagnetic current

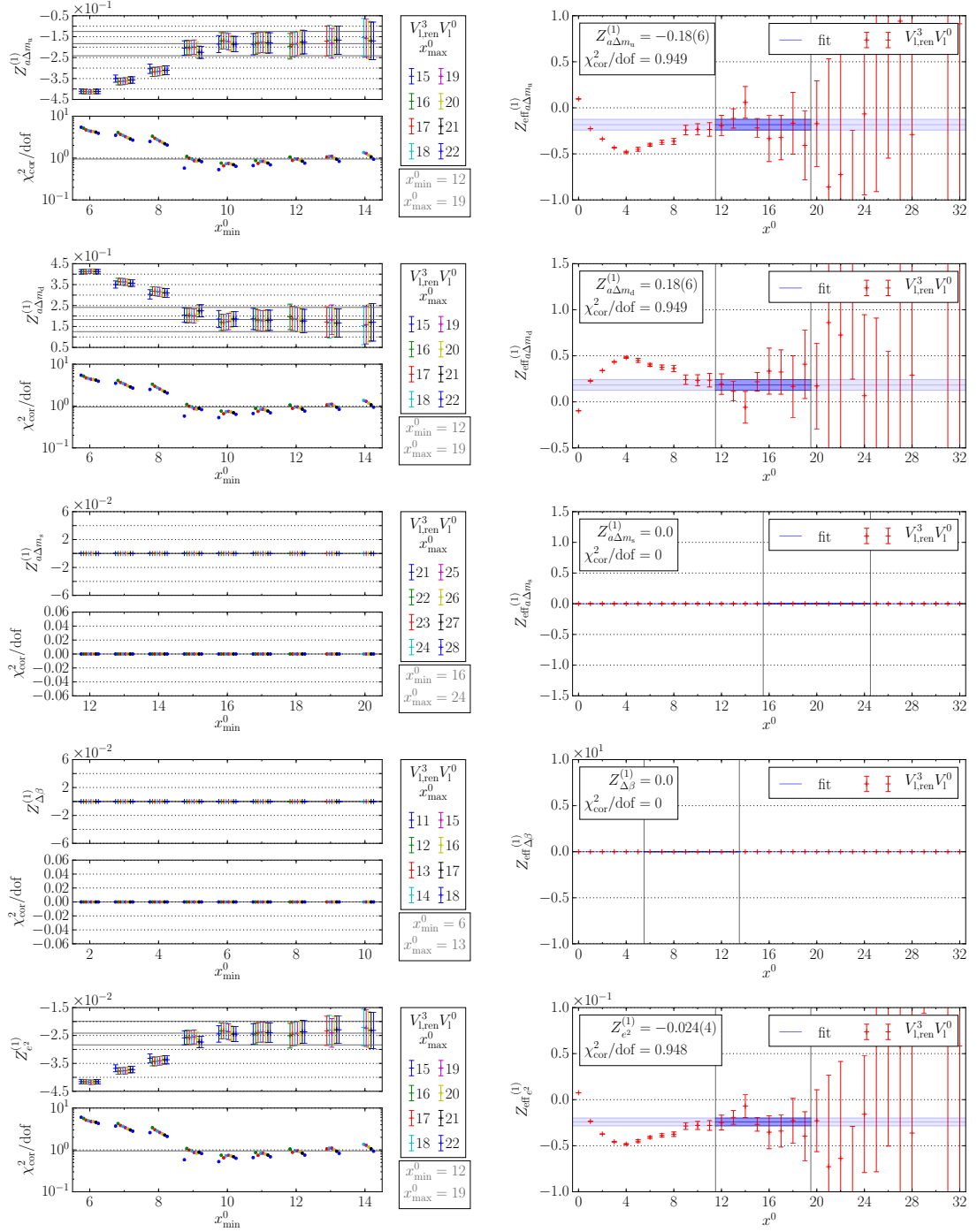


Figure 13.13.: Parameters of the fits to the effective renormalisation factor $(Z_{\text{eff}, V_{1,R}^3 \nu_1^0})^{(1)}$ on N200. The selected fits are marked in grey.

13. Vector current renormalisation

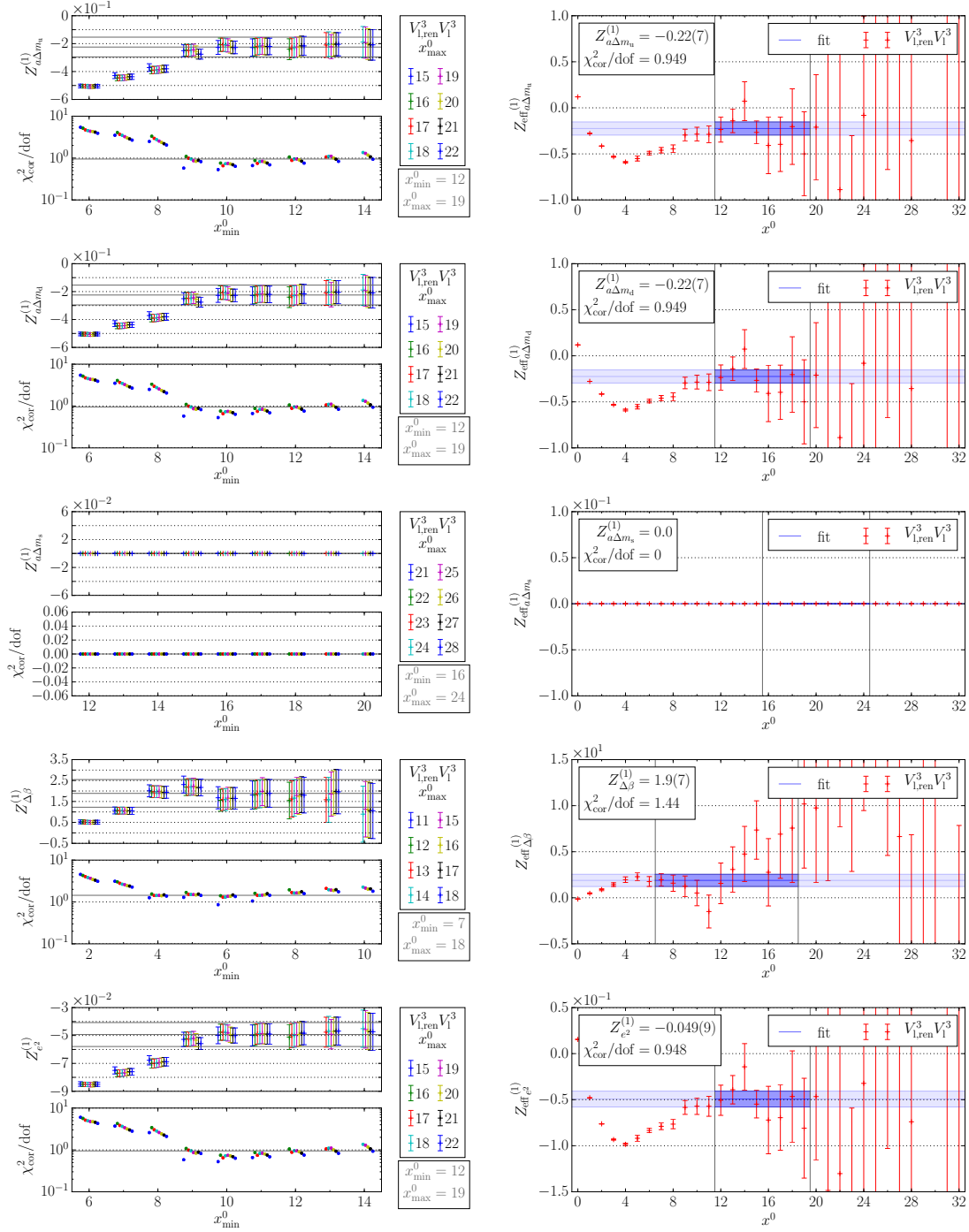


Figure 13.14.: Parameters of the fits to the effective renormalisation factor $(Z_{\text{eff},V_{1,\text{R}}^3 V_1^3})^{(1)}$ on N200. The selected fits are marked in grey.

13.4. Renormalisation of the local electromagnetic current

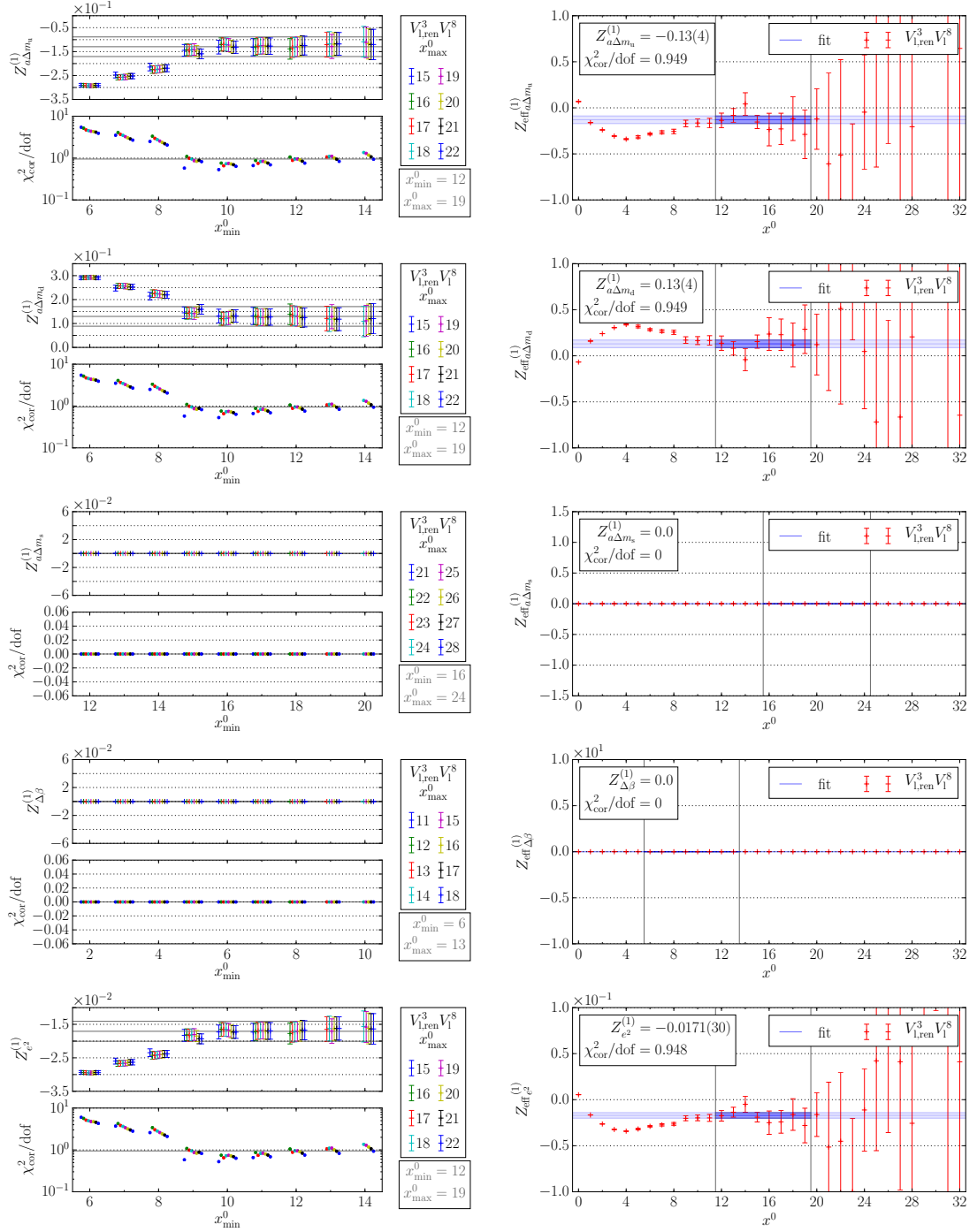


Figure 13.15.: Parameters of the fits to the effective renormalisation factor $(Z_{\text{eff}, \nu_{1,R}^3 \nu_1^8})^{(1)}$ on N200. The selected fits are marked in grey.

13. Vector current renormalisation

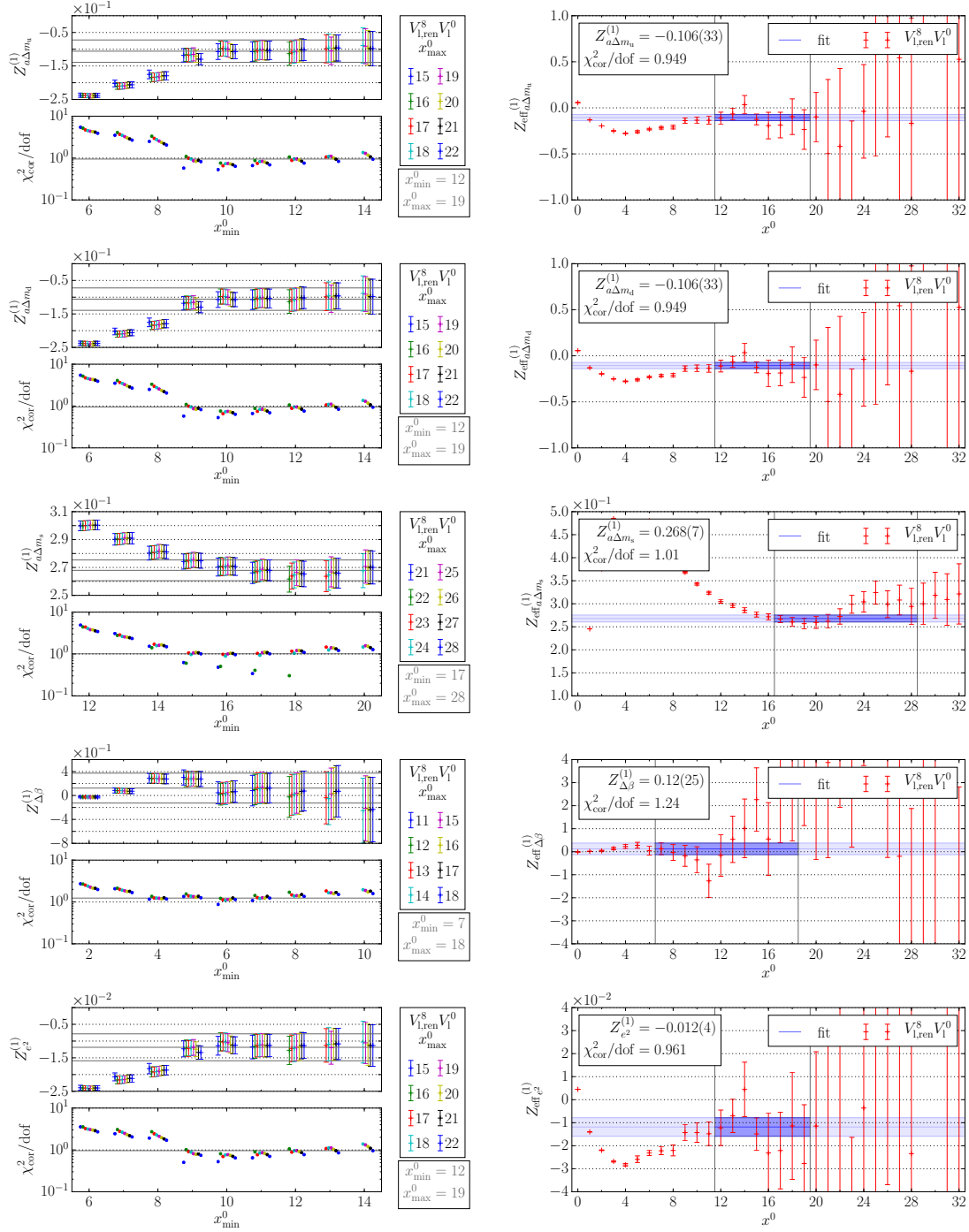


Figure 13.16.: Parameters of the fits to the effective renormalisation factor $(Z_{\text{eff}}, \nu_{1,\text{R}}^8 \nu_1^0)^{(1)}$ on N200. The selected fits are marked in grey.

13.4. Renormalisation of the local electromagnetic current

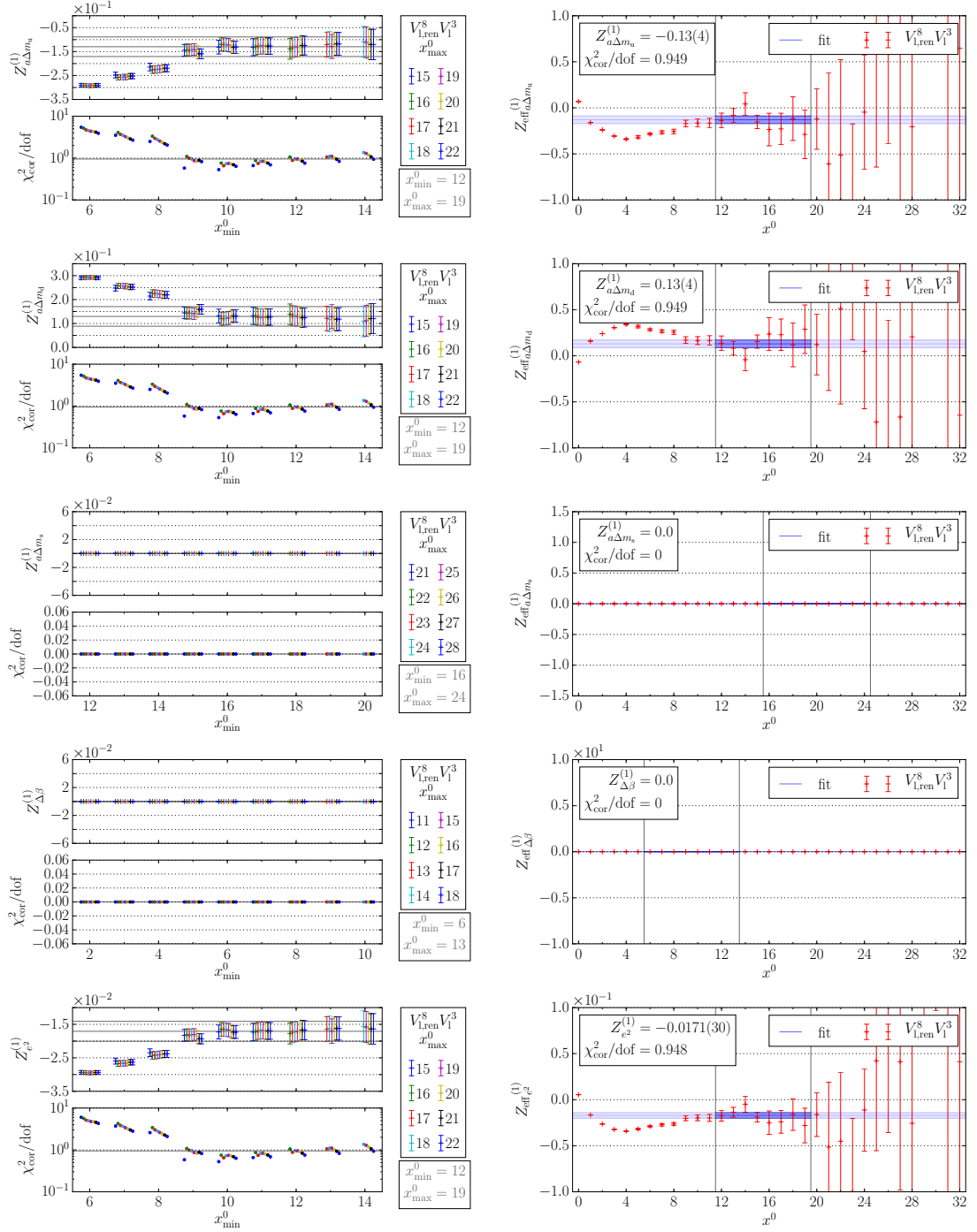


Figure 13.17.: Parameters of the fits to the effective renormalisation factor $(Z_{\text{eff}, \nu_{1,R}^8 \nu_1^3})^{(1)}$ on N200. The selected fits are marked in grey.

13. Vector current renormalisation

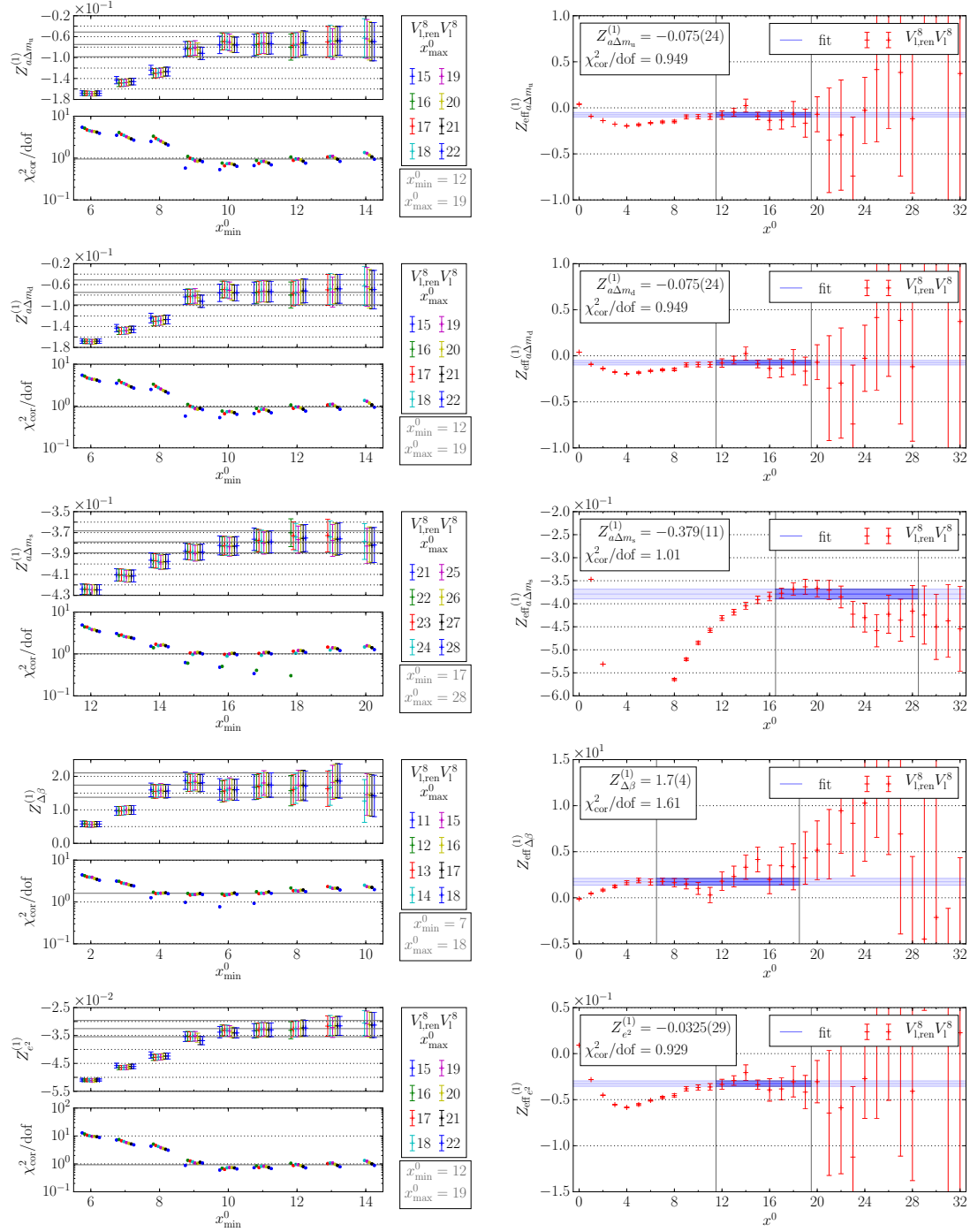


Figure 13.18.: Parameters of the fits to the effective renormalisation factor $(Z_{\text{eff}, \nu_{1,\text{R}}^8 \nu_1^8})^{(1)}$ on N200. The selected fits are marked in grey.

The vanishing entries are consistent with the fact that vector currents with different isospin quantum numbers do not mix in the isosymmetric theory, as already anticipated in section 13.4. Only the isosinglet vector currents \mathcal{V}_1^0 and \mathcal{V}_1^8 have non-vanishing mixing factors. This is still the case when quark-disconnected contributions are considered in addition. The various first-order contributions to the renormalisation matrix read

$$(Z_{\mathcal{V}_{1,R}\mathcal{V}_1})_{\Delta am_u}^{(1)} = \begin{pmatrix} -0.15(7) & -0.18(8) & -0.11(5) \\ -0.18(8) & -0.22(10) & -0.13(6) \\ -0.11(5) & -0.13(6) & -0.075(34) \end{pmatrix}, \quad (13.53)$$

$$(Z_{\mathcal{V}_{1,R}\mathcal{V}_1})_{\Delta am_d}^{(1)} = \begin{pmatrix} -0.15(7) & 0.18(8) & -0.11(5) \\ 0.18(8) & -0.22(10) & 0.13(6) \\ -0.11(5) & 0.13(6) & -0.075(34) \end{pmatrix}, \quad (13.54)$$

$$(Z_{\mathcal{V}_{1,R}\mathcal{V}_1})_{\Delta am_s}^{(1)} = \begin{pmatrix} -0.1895(11) & 0.0 & 0.2679(15) \\ 0.0 & 0.0 & 0.0 \\ 0.2679(15) & 0.0 & -0.3789(21) \end{pmatrix}, \quad (13.55)$$

$$(Z_{\mathcal{V}_{1,R}\mathcal{V}_1})_{\Delta\beta}^{(1)} = \begin{pmatrix} 1.81(21) & 0.0 & 0.12(5) \\ 0.0 & 1.89(17) & 0.0 \\ 0.12(5) & 0.0 & 1.74(26) \end{pmatrix}, \quad (13.56)$$

$$(Z_{\mathcal{V}_{1,R}\mathcal{V}_1})_{e^2}^{(1)} = \begin{pmatrix} -0.041(8) & -0.024(6) & -0.012(6) \\ -0.024(6) & -0.049(12) & -0.017(4) \\ -0.012(6) & -0.017(4) & -0.033(4) \end{pmatrix}. \quad (13.57)$$

Vanishing components in $(Z_{\mathcal{V}_{1,R}\mathcal{V}_1})_{\Delta m_s}^{(1)}$ may receive contributions from quark-disconnected diagrams, which have not been considered. Inserting the values for the expansion parameters in eq. (9.4), we find:

$$\begin{aligned} Z_{\mathcal{V}_{1,R}\mathcal{V}_1} &= \begin{pmatrix} 0.6681(4) & 0.0 & 0.00311(23) \\ 0.0 & 0.6703(5) & 0.0 \\ 0.00311(23) & 0.0 & 0.66598(22) \end{pmatrix}^{(0)} \\ &+ \begin{pmatrix} -0.0016593(16) & -0.000919(34) & -0.0005236(14) \\ -0.000919(34) & -0.0020295(6) & -0.000650(24) \\ -0.0005236(14) & -0.000650(24) & -0.0012894(27) \end{pmatrix}^{(1)} \\ &= \begin{pmatrix} 0.6664(4) & -0.000919(34) & 0.00258(23) \\ -0.000919(34) & 0.6683(5) & -0.000650(24) \\ 0.00258(23) & -0.000650(24) & 0.66469(22) \end{pmatrix}. \end{aligned} \quad (13.58)$$

13.5. Discussion and Outlook

In this chapter, we have computed renormalisation factors for flavour-neutral local vector currents including operator mixing. We give an overview of the results for the ensembles N200, D450 and H102 in table 13.1. We find that the first-order corrections are larger than the error of the zeroth-order contribution, such that isospin breaking effects cannot

13. Vector current renormalisation

$$\begin{aligned}
Z_{\mathcal{V}_{i,R}\mathcal{V}_i} & \left(\begin{array}{ccc} 0.6681(4) & 0.0 & 0.00311(23) \\ 0.0 & 0.6703(5) & 0.0 \\ 0.00311(23) & 0.0 & 0.66598(22) \end{array} \right)^{(0)} \\
& + \left(\begin{array}{ccc} -0.0016593(16) & -0.000919(34) & -0.0005236(14) \\ -0.000919(34) & -0.0020295(6) & -0.000650(24) \\ -0.0005236(14) & -0.000650(24) & -0.0012894(27) \end{array} \right)^{(1)} \\
& = \left(\begin{array}{ccc} 0.6664(4) & -0.000919(34) & 0.00258(23) \\ -0.000919(34) & 0.6683(5) & -0.000650(24) \\ 0.00258(23) & -0.000650(24) & 0.66469(22) \end{array} \right)
\end{aligned}$$

(a) N200 ($a = 0.064$ fm, $m_\pi = 282$ MeV)

$$\begin{aligned}
Z_{\mathcal{V}_{i,R}\mathcal{V}_i} & \left(\begin{array}{ccc} 0.642505(13) & 0.0 & 0.005615(23) \\ 0.0 & 0.646530(14) & 0.0 \\ 0.005615(23) & 0.0 & 0.63922(6) \end{array} \right)^{(0)} \\
& + \left(\begin{array}{ccc} -0.001542(19) & -0.000871(20) & -0.000511(12) \\ -0.000871(20) & -0.0019977(23) & -0.000592(27) \\ -0.000511(12) & -0.000592(27) & -0.001243(5) \end{array} \right)^{(1)} \\
& = \left(\begin{array}{ccc} 0.640963(31) & -0.000871(20) & 0.005103(11) \\ -0.000871(20) & 0.644533(12) & -0.000592(27) \\ 0.005103(11) & -0.000592(27) & 0.63798(5) \end{array} \right)
\end{aligned}$$

(b) D450 ($a = 0.076$ fm, $m_\pi = 216$ MeV)

$$\begin{aligned}
Z_{\mathcal{V}_{i,R}\mathcal{V}_i} & \left(\begin{array}{ccc} 0.61737(35) & 0.0 & 0.001623(6) \\ 0.0 & 0.61856(28) & 0.0 \\ 0.001623(6) & 0.0 & 0.61585(35) \end{array} \right)^{(0)} \\
& + \left(\begin{array}{ccc} -0.001533(5) & -0.0008691(34) & -0.000527(10) \\ -0.0008691(34) & -0.001910(5) & -0.0006145(24) \\ -0.000527(10) & -0.0006145(24) & -0.001167(20) \end{array} \right)^{(1)} \\
& = \left(\begin{array}{ccc} 0.61583(35) & -0.0008691(34) & 0.001097(16) \\ -0.0008691(34) & 0.61665(27) & -0.0006145(24) \\ 0.001097(16) & -0.0006145(24) & 0.61468(33) \end{array} \right)
\end{aligned}$$

(c) H102 ($a = 0.086$ fm, $m_\pi = 354$ MeV)

Table 13.1.: Renormalisation factors for flavour-neutral local vector currents.

be neglected. Comparing the diagonal entries of the matrix of renormalisation factors with respect to the lattice spacing, we find that the smaller the lattice spacing the larger the renormalisation factors. This is consistent with the fact that the renormalisation factors should approach 1 in the continuum limit [229].

The main advantage of the chosen renormalisation condition is that no additional correlation functions had to be computed. The vector-vector correlation function is both used for the determination of the renormalisation factors, as well as for the hadronic vacuum polarisation. The major disadvantage of this condition is the fact, that it relies on a correlation function which suffers from a signal-to-noise problem at long time distances, where the renormalisation factors are extracted. This problem becomes manifest in some of the first-order contributions to the effective renormalisation factor, where it is not completely clear whether the asymptotic plateau has already been reached due to the loss of the signal.

We have tried to extend the analysis of the vector-vector correlation function not only considering quark-connected contributions, but also zeroth-order isosymmetric quark-disconnected and first-order quark-disconnected QED-connected contributions. We have described this effort in section 11.5 and [262]. For the vector-vector correlation function, we applied an additional noise reduction technique based on hierarchical probing [263]. In contrast to the pseudo-scalar channel, we were not able to extract a signal at the considered level of stochastic precision. The vector channel is much noisier compared to the pseudoscalar channel, such that more stochastic quark sources and Hadamard vectors [263] have to be used. Compared to pure QCD_{iso}, QCD+QED calculations based on our computational setup become very expensive due to the additional solves of the Dirac equation, which are required for the computation of sequential propagators. Therefore, we omit the results for this particular calculation. To reduce the computational costs to an acceptable level, we suggest to apply frequency-splitting estimators for the quark-disconnected diagrams [264, 265]. In [262], we gave an outlook on how to apply this concept to calculations including leading isospin breaking effects.

As already mentioned in the beginning of section 13.4.1, the choice of renormalisation conditions is not unique. A condition that avoids the signal-to-noise ratio problem of the vector-vector correlator would let us determine the renormalisation factors more reliably, and thus would be preferable. In pure lattice QCD, the fact that the conserved vector current fulfils the vector Ward identity [202] can be used to define a renormalisation condition for the point-like vector current. This method is based on the evaluation of a three-point correlation function with two pseudo-scalar operators and one vector operator, as well as a two-point correlation function of two pseudo-scalar operators. As the calculation is performed in the pseudo-scalar channel, the signal-to-noise problem for large time separations is absent. This method was used in the $N_f = 2$ CLS determination of the HVP contribution to the anomalous magnetic moment of the muon [266, 267], as well as in the corresponding $N_f = 2 + 1$ calculations [187, 261, 268], where on-shell $O(a)$ -improvement was deployed [229]. As the flavour diagonal conserved vector current in QCD+QED de-

13. Vector current renormalisation

defined in eqs. (13.2) and (13.5) also fulfils a vector Ward identity

$$\left\langle \sum_{\mu=0}^3 (\vec{\partial}_B^\mu \mathcal{V}_F^\mu)^x \mathcal{O}[\Upsilon] \right\rangle = \left\langle i \frac{\delta \mathcal{O}[\mathfrak{T}[\varepsilon]][\Upsilon]}{\delta \varepsilon^x} \Big|_{\varepsilon=0} \right\rangle, \quad (6.46)$$

we propose to apply the method described above for the determination of the renormalisation factors excluding $O(a)$ -improvement. Full $O(a)$ -improvement of QCD+QED is non-trivial due to the large number of additional improvement coefficients. Also, it is questionable whether the Symanzik improvement programme can be applied to QED_L [44] as already mentioned in section 4.5.3. The perturbative expansion of correlation functions with three mesonic operators, which are required for the Ward identity method, leads to an even larger number of diagrams with a more complex structure in comparison to two-point functions, such that the evaluation becomes also expensive with respect to computing resources. Nevertheless, such a determination would result in the precise knowledge of $(Z_{\mathcal{V}_{l,R}\mathcal{V}_l})^{(0)}$ to $O(a^2)$ and $(Z_{\mathcal{V}_{l,R}\mathcal{V}_l})_l^{(1)}$ to $O(a)$, i.e. the overall determination is $O(a^2, a\Delta\varepsilon)$.

14. The hadronic vacuum polarisation function

The vacuum polarisation function, built from two electromagnetic currents, quantifies the polarisability of the vacuum by the passage of a photon, i.e. the magnitude of the creation and annihilation of pairs of virtual particles and anti-particles depending on the photon's momentum. In particular, we are interested in the case in which these virtual particles are quarks. This hadronic contribution to the vacuum polarisation function is a crucial ingredient in various high-precision determinations of physical observables [269, 270], such as the anomalous magnetic moment of the muon [31–33] and the running of the electromagnetic coupling [271, 272]. For large momenta, the hadronic vacuum polarisation (HVP) function can be calculated by perturbation theory, making use of the asymptotic freedom of QCD. For low energies, it can be determined from experimental measurements of cross-sections via a dispersion relation [270]. We aim at a first-principle computation by means of lattice QCD including leading isospin breaking effects, based on the vector-vector correlation functions introduced in chapter 13.

14.1. The hadronic vacuum polarisation function

The hadronic vacuum polarisation tensor in Euclidean continuum spacetime in QCD+QED is defined as the QCD-connected expectation value

$$\Pi_{\mathcal{V}^{\gamma\mu_2}\mathcal{V}^{\gamma\mu_1}}(p) = \int d^4x \exp(ip^\mu x^\mu) \langle \mathcal{V}^{\gamma\mu_2} \mathcal{V}^{\gamma\mu_1} \rangle_{\text{QCD-con}} \quad (14.1)$$

of two electromagnetic currents

$$\mathcal{V}^{\gamma\mu} = \bar{\Psi}^x Q \gamma^\mu \Psi^x. \quad (14.2)$$

The restriction to the QCD-connected part of the expectation value has the following reason: The hadronic vacuum polarisation tensor is a building block for the construction of the dressed photon propagator in a perturbative expansion with respect to QED. QCD-disconnected QED-connected diagrams contribute to dressed photon propagators with multiple insertions of the HVP tensor. Due to the QCD+QED vector Ward identity, we have $p^{\mu_2} \Pi_{\mathcal{V}^{\gamma\mu_2}\mathcal{V}^{\gamma\mu_1}}(p) = 0$, i.e. $\Pi_{\mathcal{V}^{\gamma\mu_2}\mathcal{V}^{\gamma\mu_1}}(p)$ is proportional to the projector $\delta^{\mu_2\mu_1} - p^{\mu_2} p^{\mu_1} / p^2$. Consequently, the vacuum polarisation tensor can be written as a product of the Euclidean structure and the dimensionless vacuum polarisation function $\Pi_{\mathcal{V}\gamma\mathcal{V}}(p^2)$:

$$\Pi_{\mathcal{V}^{\gamma\mu_2}\mathcal{V}^{\gamma\mu_1}}(p) = (p^2 \delta^{\mu_2\mu_1} - p^{\mu_1} p^{\mu_2}) \Pi_{\mathcal{V}\gamma\mathcal{V}}(p^2). \quad (14.3)$$

14. The hadronic vacuum polarisation function

$\Pi_{\gamma\gamma}$ is logarithmically divergent and has to be renormalised [33]. We define the subtracted vacuum polarisation function $\hat{\Pi}_{\gamma\gamma}$

$$\hat{\Pi}_{\gamma\gamma}(p^2) = \Pi_{\gamma\gamma}(p^2) - \Pi_{\gamma\gamma}(0), \quad (14.4)$$

which satisfies the on-shell renormalisation condition $\hat{\Pi}_{\gamma\gamma}(0) = 0$, i.e. the polarisation contribution of the vacuum to the dressed photon propagator vanishes in the infrared limit.

14.2. Time-momentum representation of the hadronic vacuum polarisation function in the continuum

In principle, eq. (14.1) can be evaluated on a spacetime lattice replacing the continuum Fourier transform by its discrete counterpart. In order to calculate the subtracted vacuum polarisation function $\hat{\Pi}_{\gamma\gamma}$, $\Pi_{\gamma\gamma}(0)$ has to be determined in the regulated theory. $\Pi_{\gamma\gamma}(0)$ cannot directly be extracted from $\Pi_{\gamma\mu_2\gamma\mu_1}(p)$ as the factor $(p^2\delta^{\mu_2\mu_1} - p^{\mu_1}p^{\mu_2})$, which relates the two quantities, vanishes at $p = 0$. $\hat{\Pi}_{\gamma\gamma}(0)$ can only be obtained by an extrapolation from small momenta. In this approach one faces two issues: The statistical accuracy deteriorates for smaller p^2 . In addition, on a spacetime lattice only a finite set of momenta is accessible. A possibility to overcome the latter problem is the introduction of twisted boundary conditions [273–275].

In this thesis, we follow a different approach. It is possible to represent the subtracted hadronic vacuum polarisation function in continuum and Euclidean infinite-volume QCD+QED in the *time-momentum representation* [270], reading

$$\hat{\Pi}_{\gamma\gamma}(p^2)\delta^{\mu_2\mu_1} = \int_0^\infty dx^0 K(p^2, x^0) \int dx^3 \langle \mathcal{V}^{\gamma\mu_2}\mathcal{V}^{\gamma\mu_1} \rangle_{\text{QCD-con}} \quad (14.5)$$

with the integration kernel

$$K(p^2, t) = -\frac{1}{p^2} \left(p^2 t^2 - 4 \sin^2 \left(\frac{pt}{2} \right) \right). \quad (14.6)$$

Relying on this representation, one avoids the requirement to determine $\hat{\Pi}_{\gamma\gamma}(0)$, as $\hat{\Pi}_{\gamma\gamma}$ is computed directly. Although the computation of the subtracted hadronic vacuum polarisation function is conceptually simple in this approach, one faces the problem that the vector-vector correlation function suffers from a signal to noise problem at large time distances, i.e. the IR problem, which is also present for small momenta in the computation based on the Fourier transform, persists.

14.3. The renormalised hadronic vacuum polarisation function in lattice QCD+QED

In order to define the renormalised hadronic vacuum polarisation function, we have to express $\hat{\Pi}_{\mathcal{V}_R^\gamma \mathcal{V}_R^\gamma}$ in terms of the bare correlation functions $C_{\mathcal{V}_{d_2}^{i_2} \mathcal{V}_1^{i_1}}$, reading

$$C_{\mathcal{V}_{d_2}^{i_2} \mathcal{V}_1^{i_1}}(x_2^0, x_1^0) = \frac{1}{3} \sum_{\mu=1}^3 \langle \mathcal{V}_{d_2}^{x_2^0 \mu i_2} \mathcal{V}_1^{x_1^0 \mu i_1} \rangle \quad d_2 = 1, c \quad i_2, i_1 = 0, 3, 8. \quad (13.8)$$

The correlation function $C_{\mathcal{V}_{d_2, R}^\gamma \mathcal{V}_{1, R}^\gamma}$ of two renormalised electromagnetic currents is obtained from eq. (13.8) applying the renormalisation factors from eq. (13.42):

$$C_{\mathcal{V}_{d_2, R}^\gamma \mathcal{V}_{1, R}^\gamma} = \sum_{i_2, i_1} \left(Z_{\mathcal{V}_{d_2, R}^3 \mathcal{V}_{d_2}^{i_2}} + \frac{1}{\sqrt{3}} Z_{\mathcal{V}_{d_2, R}^8 \mathcal{V}_{d_2}^{i_2}} \right) \left(Z_{\mathcal{V}_{1, R}^3 \mathcal{V}_1^{i_1}} + \frac{1}{\sqrt{3}} Z_{\mathcal{V}_{1, R}^8 \mathcal{V}_1^{i_1}} \right) C_{\mathcal{V}_{d_2}^{i_2} \mathcal{V}_1^{i_1}}. \quad (14.7)$$

As we can only access the correlation function $C_{\mathcal{V}_R^\gamma \mathcal{V}_R^\gamma}(x_2^0, x_1^0)$ on a discrete set of time separations, we replace the integration in eq. (14.5) by a discrete summation. In principle, it is also possible to approximate the integration by a higher-order quadrature [266], such as the trapezoidal rule or the analytic integration of a spline interpolation, but there is no relevant advantage over performing a simple summation. In chapter 13, we have observed that the vector-vector correlation function shows a noise problem at large time distances. For the determination of the hadronic polarisation function we, however, have to integrate over the entire time range. The naive integral possesses a growing uncertainty, such that no information can be extracted. A possibility to circumvent this problem is the reconstruction of the correlation function at large time distances. As discussed in chapter 10, all Euclidean two-point correlation functions can be decomposed into linear combinations of exponential functions, whose decay rates are characterised by the masses of the corresponding states. At large time distances, only the states with the smallest masses contribute, such that the behaviour of the correlation function can be entirely described in terms of these states. In this thesis, we reconstruct the vector-vector correlation function only considering the ground state contribution, i.e. the correlation function is replaced in the integration by its zeroth-order reconstruction

$$(C_{\mathcal{V}_R^\gamma \mathcal{V}_R^\gamma, \text{rec}}(t_2, t_1))^{(0)} = c^{(0)} \exp(-m^{(0)}(t_2 - t_1)) \quad (14.8)$$

and its first-order reconstruction

$$(C_{\mathcal{V}_R^\gamma \mathcal{V}_R^\gamma, \text{rec}}(t_2, t_1))_l^{(1)} = (c_l^{(1)} - c^{(0)} m_l^{(1)}(t_2 - t_1)) \exp(-m^{(0)}(t_2 - t_1)). \quad (14.9)$$

We denote the time at which we switch from the measured correlation function to its reconstruction as x_{swi}^0 . In addition, as the lattice is finite in the temporal direction, we have to truncate the infinite summation, before boundary effects set in. We call the

14. The hadronic vacuum polarisation function

time separation, at which we truncate the summation, x_{cut}^0 . Eventually, we compute the zeroth-order contribution of the hadronic vacuum polarisation function according to

$$\begin{aligned} (\hat{\Pi}_{\mathcal{V}_R^\gamma \mathcal{V}_R^\gamma}(p^2))^{(0)} &= \sum_{x^0=0}^{x_{\text{swi}}^0} K(p^2, x^0) (C_{\mathcal{V}_R^\gamma \mathcal{V}_R^\gamma}(x^0, 0))^{(0)} \\ &+ \sum_{x^0=x_{\text{swi}}^0+1}^{x_{\text{cut}}^0} K(p^2, x^0) (C_{\mathcal{V}_R^\gamma \mathcal{V}_R^\gamma, \text{rec}}(x^0, 0))^{(0)}. \end{aligned} \quad (14.10)$$

For the expansion parameters $l = \Delta m_u, \Delta m_d, \Delta m_s, \Delta \beta$ the first-order contribution reads

$$\begin{aligned} (\hat{\Pi}_{\mathcal{V}_R^\gamma \mathcal{V}_R^\gamma}(p^2))_l^{(1)} &= \sum_{x^0=0}^{x_{\text{swi}}^0} K(p^2, x^0) (C_{\mathcal{V}_R^\gamma \mathcal{V}_R^\gamma}(x^0, 0))_l^{(1)} \\ &+ \sum_{x^0=x_{\text{swi}}^0+1}^{x_{\text{cut}}^0} K(p^2, x^0) (C_{\mathcal{V}_R^\gamma \mathcal{V}_R^\gamma, \text{rec}}(x^0, 0))_l^{(1)}. \end{aligned} \quad (14.11)$$

In contrast, we have to additionally subtract the QCD-disconnected part [276] for the expansion parameters $l = e^2$:

$$\begin{aligned} (\hat{\Pi}_{\mathcal{V}_R^\gamma \mathcal{V}_R^\gamma}(p^2))_{e^2}^{(1)} &= \sum_{x^0=0}^{x_{\text{swi}}^0} K(p^2, x^0) (C_{\mathcal{V}_R^\gamma \mathcal{V}_R^\gamma}(x^0, 0))_{e^2}^{(1)} \\ &+ \sum_{x^0=x_{\text{swi}}^0+1}^{x_{\text{cut}}^0} K(p^2, x^0) (C_{\mathcal{V}_R^\gamma \mathcal{V}_R^\gamma, \text{rec}}(x^0, 0))_{e^2}^{(1)} \\ &- \left((\hat{\Pi}_{\mathcal{V}_R^\gamma \mathcal{V}_R^\gamma}(p^2))^{(0)} \right)^2. \end{aligned} \quad (14.12)$$

As stated in chapter 13, we only consider quark-connected contributions to the vector-vector correlation function. Hence, we do not have to manually subtract the QCD-disconnected part for the moment, as it is absent in our current analysis.

14.3.1. $\hat{\Pi}_{\mathcal{V}_{c,R}^\gamma \mathcal{V}_{l,R}^\gamma}$ from $C_{\mathcal{V}_{c,R}^\gamma \mathcal{V}_{l,R}^\gamma}$

The subtracted hadronic vacuum polarisation function $\hat{\Pi}_{\mathcal{V}_R^\gamma \mathcal{V}_R^\gamma}$ can be extracted from the correlation function $C_{\mathcal{V}_{c,R}^\gamma \mathcal{V}_{l,R}^\gamma}$, where both the local and conserved vector current have been used. Hence, the renormalisation factors for the local vector current contribute only once in eq. (14.7). As discussed in the previous section, we first determine the mass and the proportionality factor of the lowest accessible state of $C_{\mathcal{V}_{c,R}^\gamma \mathcal{V}_{l,R}^\gamma}$ in order to reconstruct the correlation function at long time differences. The relevant fits are depicted in figs. 14.1 and 14.2 for the zeroth-order and first-order contribution, respectively. We obtain the fit

14.3. The renormalised hadronic vacuum polarisation function in lattice QCD+QED

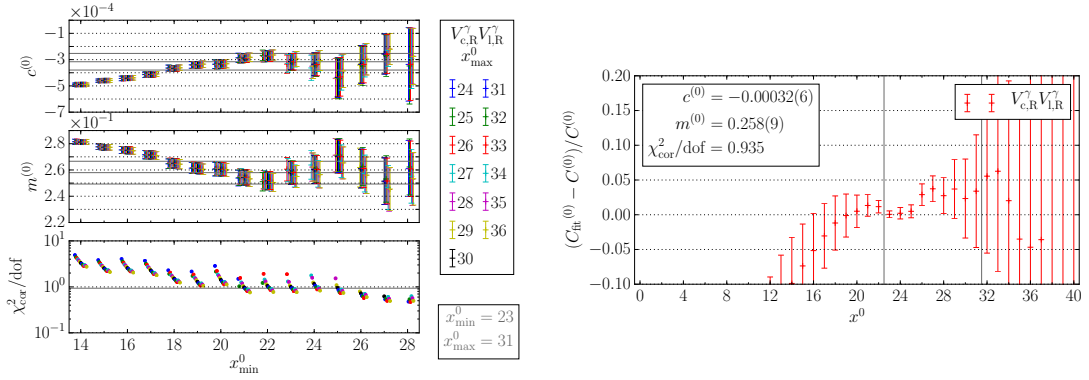


Figure 14.1.: Parameters of the fit to the correlation function $(C_{\mathcal{V}_{c,R}^\gamma \mathcal{V}_{l,R}^\gamma})^{(0)}$ and relative deviation between the correlation function and the corresponding fit on N200. The selected fit is marked in grey. The grey lines enclose the fit interval.

results c and am in dimensionless units:

$$c = -0.00032(6) - 0.0034(16) a\Delta m_u - 0.00024(12) a\Delta m_d + 0.0065(7) a\Delta m_s + 0.044(19) \Delta\beta - 0.00031(17) e^2, \quad (14.13)$$

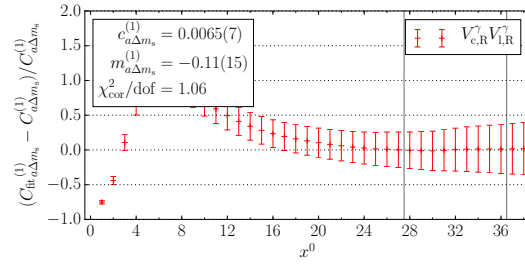
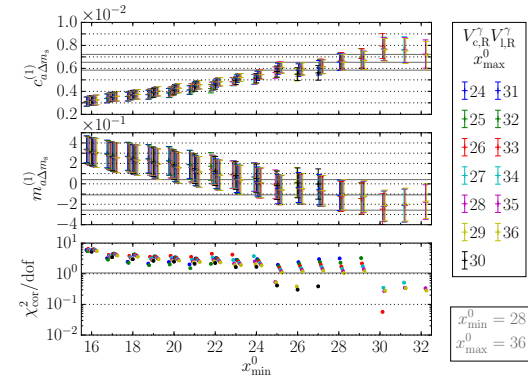
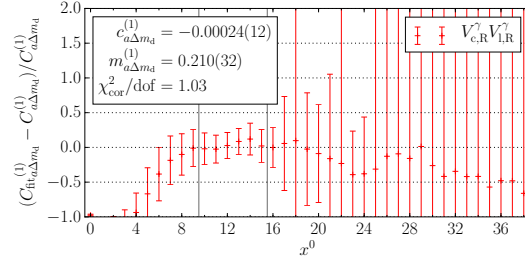
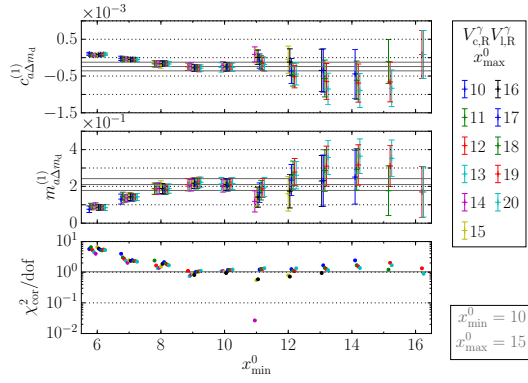
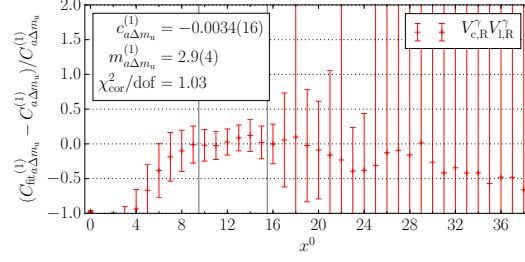
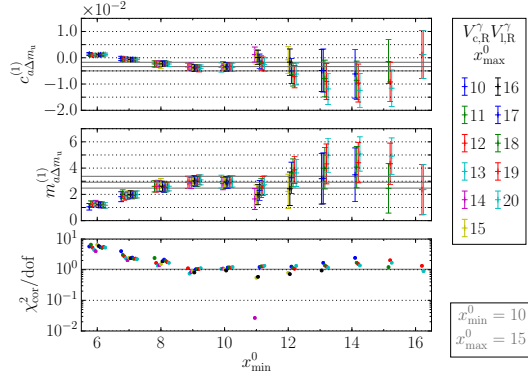
$$am = 0.258(9) + 2.9(4) a\Delta m_u + 0.210(32) a\Delta m_d - 0.11(15) a\Delta m_s - 14(7) \Delta\beta + 0.31(4) e^2. \quad (14.14)$$

We insert the results into eqs. (14.8) and (14.9) and determine the reconstruction of correlation function $C_{\mathcal{V}_{c,R}^\gamma \mathcal{V}_{l,R}^\gamma, \text{rec}}$ according to eqs. (14.10) to (14.12). We determine x_{swi}^0 and x_{cut}^0 observing the dependence of $\hat{\Pi}_{\mathcal{V}_{c,R}^\gamma \mathcal{V}_{l,R}^\gamma}$ evaluated at $p^2 = 1 \text{ GeV}^2$ on the latter quantities. The results are displayed in figs. 14.3 and 14.4. x_{swi}^0 is selected within the interval used to fit the asymptotic behaviour, avoiding the growing noise. x_{cut}^0 has to be chosen large enough, such that the excluded contributions from even larger time separations are negligible compared to the overall statistical precision. The results are depicted in figs. 14.5 and 14.6 for the zeroth- and the individual first-order contributions, respectively. We observe that an increase in the quark masses consistently leads to a decrease in the vacuum polarisation function for all quark flavours. The total first-order contribution, including the expansion parameters $\Delta\varepsilon$, is displayed in fig. 14.6.

14.3.2. $\hat{\Pi}_{\mathcal{V}_R^\gamma \mathcal{V}_R^\gamma}$ from $C_{\mathcal{V}_{l,R}^\gamma \mathcal{V}_{l,R}^\gamma}$

Similarly, $\hat{\Pi}_{\mathcal{V}_R^\gamma \mathcal{V}_R^\gamma}$ can also be extracted from the correlation function $C_{\mathcal{V}_{l,R}^\gamma \mathcal{V}_{l,R}^\gamma}$. In this setup, the matrix of renormalisation factors $Z_{\mathcal{V}_{l,R} \mathcal{V}_l}$ enters twice in eq. (14.7), as both

14. The hadronic vacuum polarisation function



14.3. The renormalised hadronic vacuum polarisation function in lattice QCD+QED

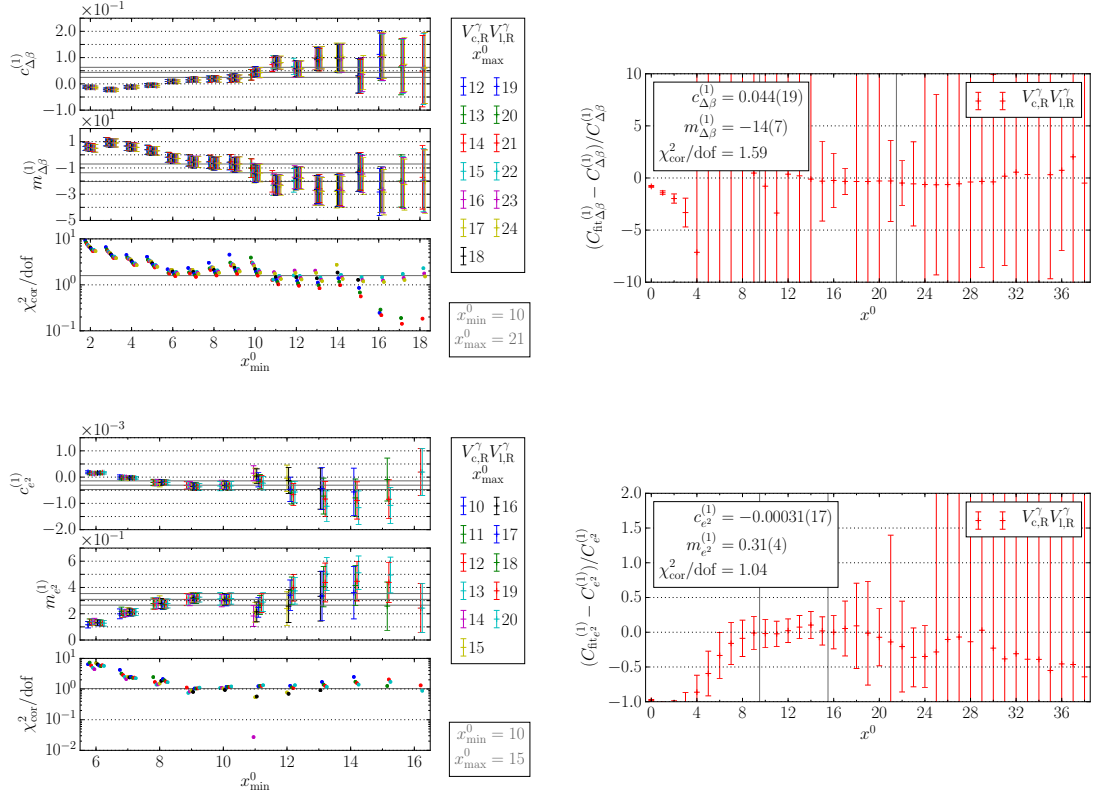


Figure 14.2.: Parameters of the fit to the correlation function $(C_{\mathcal{V}_{c,R}^\gamma \mathcal{V}_{l,R}^\gamma})_l^{(1)}$ and relative deviation between the correlation function and the corresponding fit on N200. The selected fit is marked in grey. The grey lines enclose the fit interval.

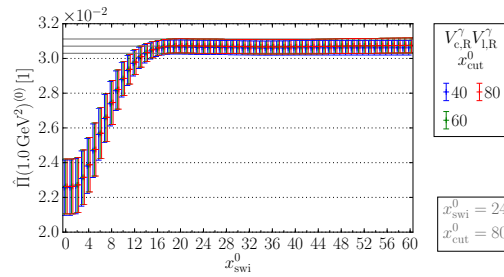


Figure 14.3.: Hadronic vacuum polarisation function $(\hat{\Pi}_{\mathcal{V}_{c,R}^\gamma \mathcal{V}_{l,R}^\gamma})^{(0)}$ evaluated at $p^2 = 1 \text{ GeV}^2$ as a function of x_{swi}^0 and x_{cut}^0 on N200. The selected value is marked in grey.

14. The hadronic vacuum polarisation function

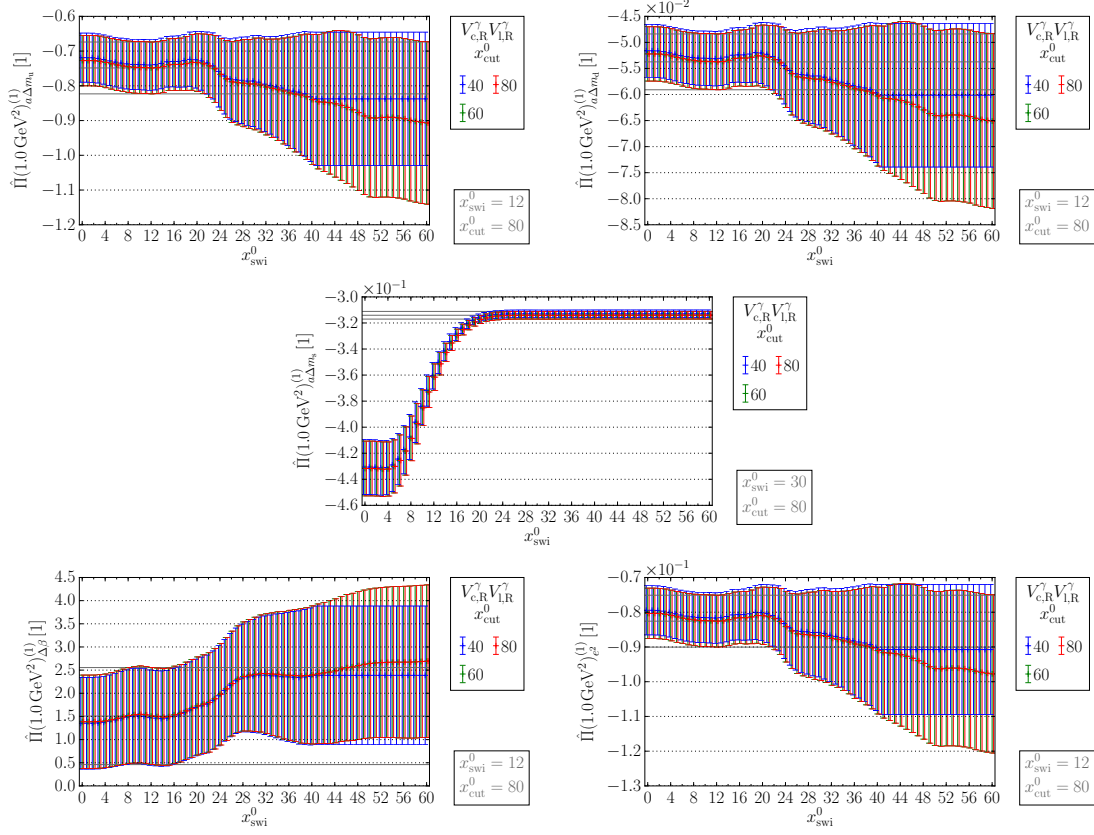


Figure 14.4.: Hadronic vacuum polarisation function $(\hat{\Pi}_{\nu_{c,R}^\gamma \nu_{l,R}^\gamma})_l^{(1)}$ evaluated at $p^2 = 1 \text{ GeV}^2$ as a function of x_{swi}^0 and x_{cut}^0 on N200. The selected value is marked in grey.

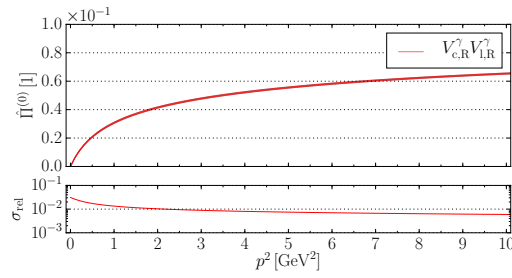


Figure 14.5.: Hadronic vacuum polarisation function $(\hat{\Pi}_{\nu_{c,R}^\gamma \nu_{l,R}^\gamma})^{(0)}$ extracted from the correlation function $(C_{\nu_{c,R}^\gamma \nu_{l,R}^\gamma})^{(0)}$ on N200.

14.3. The renormalised hadronic vacuum polarisation function in lattice QCD+QED

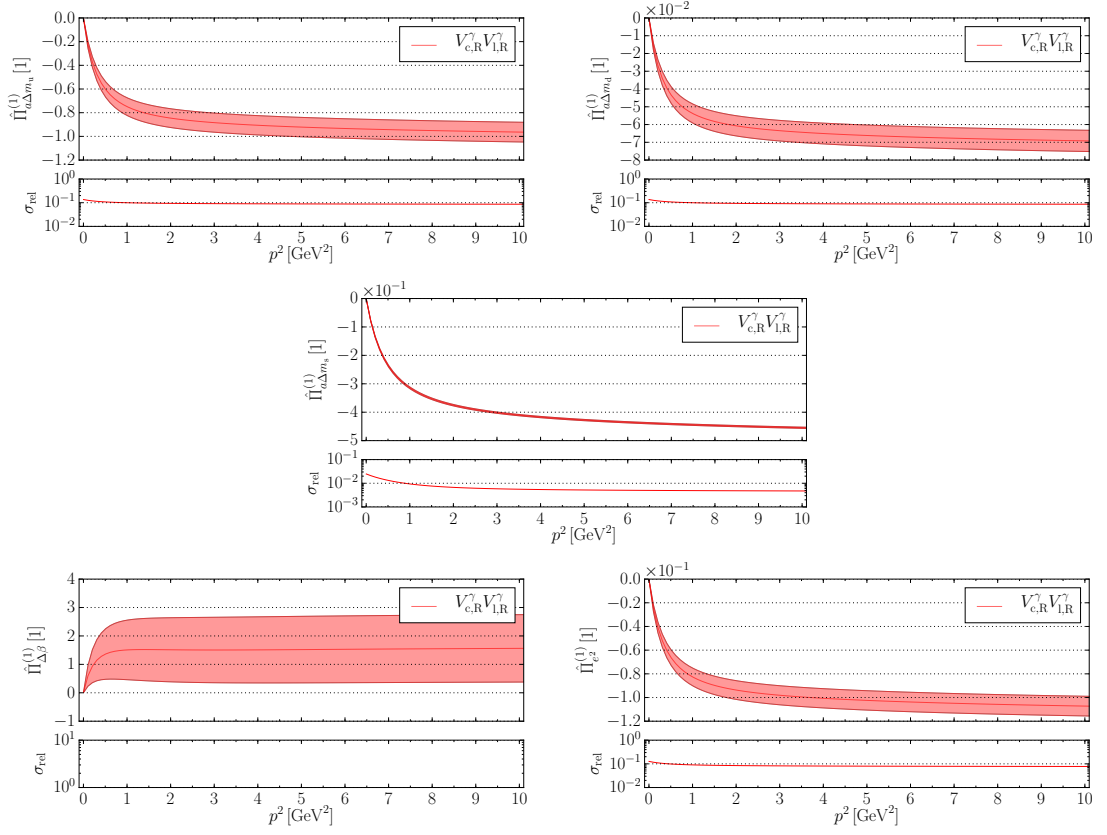


Figure 14.6.: Hadronic vacuum polarisation function $(\hat{\Pi}_{\mathcal{V}_{c,R}^{\gamma} \mathcal{V}_{l,R}^{\gamma}}^{(1)})_l$ extracted from the correlation function $(C_{\mathcal{V}_{c,R}^{\gamma} \mathcal{V}_{l,R}^{\gamma}}^{(1)})_l$ on N200.

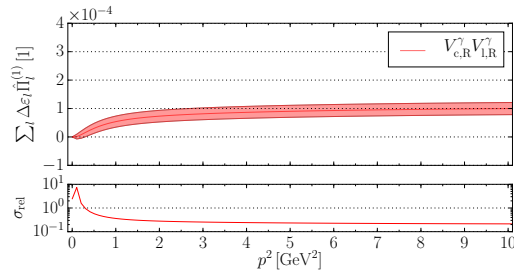


Figure 14.7.: Hadronic vacuum polarisation function $\sum_l \Delta \varepsilon_l (\hat{\Pi}_{\mathcal{V}_{c,R}^{\gamma} \mathcal{V}_{l,R}^{\gamma}}^{(1)})_l$ extracted from the correlation function $\sum_l \Delta \varepsilon_l (C_{\mathcal{V}_{c,R}^{\gamma} \mathcal{V}_{l,R}^{\gamma}}^{(1)})_l$ on N200.

14. The hadronic vacuum polarisation function

vector currents renormalise non-trivially. We omit a detailed discussion, which does not give any new insights, and refer to the next section for the results.

14.4. Discussion and Outlook

In this chapter, we have determined the quark-connected contributions to the hadronic vacuum polarisation function. An overview of the results for the ensembles N200, D450 and H102 is displayed in fig. 14.8 and in table 14.1. For small energies, the results of the two considered discretisations are compatible, whereas they start to differ for larger energies. This is not a sign of an inconsistency, as no extrapolation to the continuum limit was performed, i.e. the two discretisations may differ by lattice artifacts. Nevertheless, the definition of the renormalisation condition of the local vector current, which depends on the lightest state accessible via the vector-vector correlation function, ensures that both discretisations lead to compatible results for the HVP function in the low energy regime. We are able to determine the isosymmetric contribution to the hadronic vacuum polarisation function $(\hat{\Pi}_{\mathcal{V}_R^\gamma \mathcal{V}_{l,R}^\gamma})^{(0)}$ with a relative statistical precision of $O(1\%)$ at 1 GeV^2 . The dominant contribution to the total error comes from the scale setting uncertainty. The first-order corrections $(\hat{\Pi}_{\mathcal{V}_R^\gamma \mathcal{V}_{l,R}^\gamma})^{(1)}$ are $O(1\%)$ of the isosymmetric contribution at 1 GeV^2 , such that they are of the same order of magnitude as the error of the isosymmetric contribution. First-order effects are equipped with an error between $O(10\%)$ and $O(100\%)$, depending on the considered ensemble.

In this thesis, we neglect isosymmetric quark-disconnected contributions, which contribute with a magnitude of $O(5 - 10)\%$ of the quark-connected isosymmetric contribution at 1 GeV^2 [277]. Contributions from the charm quark, which can only be treated in the quenched approximation, as the gauge configurations were generated without a dynamical charm quark, are of similar magnitude [277]. Both contributions should be added for completeness in the future. Further neglected subleading contributions arise from first-order quark-disconnected diagrams, which presumably give corrections smaller than the considered first-order quark-connected diagrams [200].

In this analysis, we have used a very simple model for the reconstruction of the vector-vector correlation function at large time distances, as we only consider a single state to describe the asymptotic behaviour of the correlation function. In principle, it is possible to improve the reconstruction by taking further states into account [261, 268]. For ensembles with light pion masses, the observed asymptotic state is in fact a superposition of multi-pion states with relative angular momentum. These states are associated with the ρ^0 and ω resonances. We cannot entangle these states directly, as the signal deteriorates too fast. Nevertheless, a dedicated GEVP spectroscopy analysis based on an extended set of interpolation operators suited for multi-pion states can be performed at least in the isosymmetric theory [64, 278].

Another approach to deal with the signal-to-noise problem of the vector-vector correlation function at large time distances is the bounding method [245, 279]. Instead of replacing the correlation function by a reconstruction for times larger than x_{swi}^0 , one de-

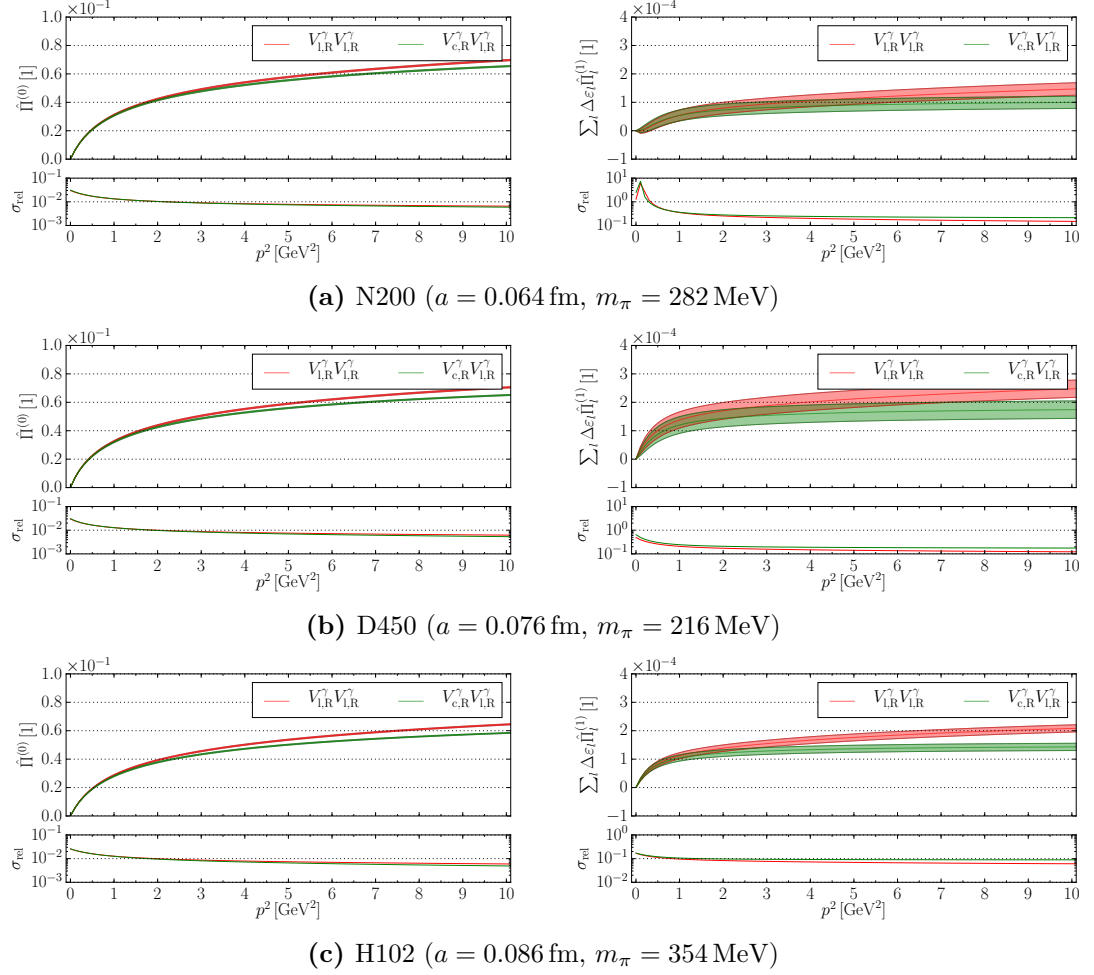


Figure 14.8.: Zeroth- and first-order contribution to the hadronic vacuum polarisation function $(\hat{\Pi}_{\mathcal{V}_R^\gamma \mathcal{V}_R^\gamma})^{(0)}$ and $(\hat{\Pi}_{\mathcal{V}_R^\gamma \mathcal{V}_R^\gamma})^{(1)}$ from the discretisations $\hat{\Pi}_{\mathcal{V}_R^\gamma \mathcal{V}_{l,R}^\gamma}$ and $\hat{\Pi}_{\mathcal{V}_{l,R}^\gamma \mathcal{V}_{l,R}^\gamma}$.

14. The hadronic vacuum polarisation function

p^2 [GeV ²]	$\hat{\Pi}_{V_{l,R}^\gamma V_{l,R}^\gamma} [1]$	$\hat{\Pi}_{V_{c,R}^\gamma V_{l,R}^\gamma} [1]$
1.0	$(0.03117(21)_{\text{st}}(36)_{\text{a}}[41]_{\text{tot}})^{(0)}$ + $(0.000054[19]_{\text{tot}})^{(1)}$	$(0.03071(22)_{\text{st}}(35)_{\text{a}}[41]_{\text{tot}})^{(0)}$ + $(0.000054[20]_{\text{tot}})^{(1)}$
3.0	$(0.04918(23)_{\text{st}}(39)_{\text{a}}[45]_{\text{tot}})^{(0)}$ + $(0.000094[21]_{\text{tot}})^{(1)}$	$(0.04779(23)_{\text{st}}(36)_{\text{a}}[42]_{\text{tot}})^{(0)}$ + $(0.000081[21]_{\text{tot}})^{(1)}$
5.0	$(0.05781(23)_{\text{st}}(39)_{\text{a}}[45]_{\text{tot}})^{(0)}$ + $(0.000114[21]_{\text{tot}})^{(1)}$	$(0.05555(24)_{\text{st}}(34)_{\text{a}}[41]_{\text{tot}})^{(0)}$ + $(0.000090[21]_{\text{tot}})^{(1)}$
7.0	$(0.06352(24)_{\text{st}}(39)_{\text{a}}[46]_{\text{tot}})^{(0)}$ + $(0.000129[22]_{\text{tot}})^{(1)}$	$(0.06044(24)_{\text{st}}(33)_{\text{a}}[40]_{\text{tot}})^{(0)}$ + $(0.000095[21]_{\text{tot}})^{(1)}$
9.0	$(0.06779(24)_{\text{st}}(39)_{\text{a}}[46]_{\text{tot}})^{(0)}$ + $(0.000141[22]_{\text{tot}})^{(1)}$	$(0.06394(24)_{\text{st}}(32)_{\text{a}}[39]_{\text{tot}})^{(0)}$ + $(0.000098[21]_{\text{tot}})^{(1)}$

(a) N200 ($a = 0.064$ fm, $m_\pi = 282$ MeV)

p^2 [GeV ²]	$\hat{\Pi}_{V_{l,R}^\gamma V_{l,R}^\gamma} [1]$	$\hat{\Pi}_{V_{c,R}^\gamma V_{l,R}^\gamma} [1]$
1.0	$(0.03266(15)_{\text{st}}(39)_{\text{a}}[42]_{\text{tot}})^{(0)}$ + $(0.000138[29]_{\text{tot}})^{(1)}$	$(0.03200(16)_{\text{st}}(37)_{\text{a}}[41]_{\text{tot}})^{(0)}$ + $(0.000120[29]_{\text{tot}})^{(1)}$
3.0	$(0.05052(16)_{\text{st}}(41)_{\text{a}}[44]_{\text{tot}})^{(0)}$ + $(0.000188[30]_{\text{tot}})^{(1)}$	$(0.04861(17)_{\text{st}}(37)_{\text{a}}[41]_{\text{tot}})^{(0)}$ + $(0.000154[30]_{\text{tot}})^{(1)}$
5.0	$(0.05900(16)_{\text{st}}(41)_{\text{a}}[44]_{\text{tot}})^{(0)}$ + $(0.000212[30]_{\text{tot}})^{(1)}$	$(0.05597(17)_{\text{st}}(35)_{\text{a}}[39]_{\text{tot}})^{(0)}$ + $(0.000164[31]_{\text{tot}})^{(1)}$
7.0	$(0.06458(16)_{\text{st}}(41)_{\text{a}}[44]_{\text{tot}})^{(0)}$ + $(0.000229[30]_{\text{tot}})^{(1)}$	$(0.06053(17)_{\text{st}}(33)_{\text{a}}[37]_{\text{tot}})^{(0)}$ + $(0.000169[31]_{\text{tot}})^{(1)}$
9.0	$(0.06871(16)_{\text{st}}(41)_{\text{a}}[44]_{\text{tot}})^{(0)}$ + $(0.000242[30]_{\text{tot}})^{(1)}$	$(0.06375(17)_{\text{st}}(31)_{\text{a}}[36]_{\text{tot}})^{(0)}$ + $(0.000173[31]_{\text{tot}})^{(1)}$

(b) D450 ($a = 0.076$ fm, $m_\pi = 216$ MeV)

$p^2 [\text{GeV}^2]$	$\hat{\Pi}_{V_{1,R}^\gamma V_{1,R}^\gamma} [1]$	$\hat{\Pi}_{V_{c,R}^\gamma V_{1,R}^\gamma} [1]$
1.0	$(0.02876(10)_{\text{st}}(35)_{\text{a}}[36]_{\text{tot}})^{(0)}$ $+ (0.000112[11]_{\text{tot}})^{(1)}$	$(0.02797(11)_{\text{st}}(33)_{\text{a}}[35]_{\text{tot}})^{(0)}$ $+ (0.000104[11]_{\text{tot}})^{(1)}$
3.0	$(0.04562(11)_{\text{st}}(38)_{\text{a}}[39]_{\text{tot}})^{(0)}$ $+ (0.000155[12]_{\text{tot}})^{(1)}$	$(0.04339(12)_{\text{st}}(33)_{\text{a}}[35]_{\text{tot}})^{(0)}$ $+ (0.000129[12]_{\text{tot}})^{(1)}$
5.0	$(0.05366(11)_{\text{st}}(38)_{\text{a}}[40]_{\text{tot}})^{(0)}$ $+ (0.000176[12]_{\text{tot}})^{(1)}$	$(0.05017(12)_{\text{st}}(31)_{\text{a}}[33]_{\text{tot}})^{(0)}$ $+ (0.000136[12]_{\text{tot}})^{(1)}$
7.0	$(0.05891(12)_{\text{st}}(37)_{\text{a}}[39]_{\text{tot}})^{(0)}$ $+ (0.000192[12]_{\text{tot}})^{(1)}$	$(0.05432(12)_{\text{st}}(29)_{\text{a}}[31]_{\text{tot}})^{(0)}$ $+ (0.000140[13]_{\text{tot}})^{(1)}$
9.0	$(0.06277(12)_{\text{st}}(37)_{\text{a}}[39]_{\text{tot}})^{(0)}$ $+ (0.000203[13]_{\text{tot}})^{(1)}$	$(0.05721(12)_{\text{st}}(27)_{\text{a}}[29]_{\text{tot}})^{(0)}$ $+ (0.000142[13]_{\text{tot}})^{(1)}$

(c) H102 ($a = 0.086 \text{ fm}$, $m_\pi = 354 \text{ MeV}$)

Table 14.1.: Zeroth- and first-order contribution to the hadronic vacuum polarisation function $(\hat{\Pi}_{\mathcal{V}_R^\gamma \mathcal{V}_R^\gamma})^{(0)}$ and $(\hat{\Pi}_{\mathcal{V}_R^\gamma \mathcal{V}_R^\gamma})^{(1)}$ from the discretisations $\hat{\Pi}_{\mathcal{V}_R^\gamma \mathcal{V}_{1,R}^\gamma}$ and $\hat{\Pi}_{\mathcal{V}_{1,R}^\gamma \mathcal{V}_{1,R}^\gamma}$.

rives, based on the spectral decomposition of C , for $x_{\text{swi}}^0 \leq x^0$ the inequalities

$$0 < C(x_{\text{swi}}^0) \exp(-m_{\text{eff}}(x_{\text{swi}}^0)(x^0 - x_{\text{swi}}^0)) \leq C(x^0), \quad (14.15)$$

$$C(x^0) \leq C(x_{\text{swi}}^0) \exp(-m_0(x^0 - x_{\text{swi}}^0)), \quad (14.16)$$

which limit $C(x^0)$ from below and above. m_{eff} denotes the effective mass associated to the correlation function C and m_0 is the smallest mass of the spectral representation of C . It is not obvious that the bounding method can be applied for individual contributions of the perturbative expansion. Nevertheless, it is applicable to the combined zeroth- and first-order contributions, after the expansion parameters $\Delta\varepsilon$ have been fixed. Similar to the reconstruction method, additional states can be considered in the inequality to narrow the bounds.

In the literature, various treatments of finite volume effects with regard to the hadronic vacuum polarisation function are discussed [34, 280]. One possibility is to correct for QCD finite volume effects using chiral perturbation theory [281, 282], assuming that the effect can be mainly described by a two-pion state. This framework can also be extended to QCD+QED. In particular, finite volume effects associated with the electromagnetic interaction can be treated by scalar QED [199], also taking the electromagnetic charge of the pions into account. Other approaches to treat QCD finite volume effects [200, 277] rely on the Lellouch-Lüscher formalism [283–285] in combination with the timelike pion form factor and the Gounaris-Sakurai parametrisation [286].

As already anticipated in the introduction of this chapter, the hadronic vacuum polarisation function $\hat{\Pi}_{\mathcal{V}^\gamma \mathcal{V}^\gamma}$ is relevant for the computation of several high-precision observables. It is directly related to the renormalisation of the electromagnetic charge, and hence to the

14. The hadronic vacuum polarisation function

running of the fine-structure constant α_{em} . In the on-shell scheme, the running coupling is parametrised as [272, 277]

$$\alpha_{\text{em}}(p^2) = \frac{\alpha_{\text{em}}}{1 - \Delta\alpha_{\text{em}}(p^2)}, \quad (14.17)$$

where $\Delta\alpha_{\text{em}}(p^2)$ is the sum of leptonic and hadronic contributions. Leptonic contributions are commonly calculated by means of perturbation theory. As lattice simulations are performed in Euclidean spacetime, only spacelike momenta can be accessed in the hadronic contribution. The latter can be expressed in terms of the hadronic vacuum polarisation function as

$$(\Delta\alpha_{\text{em}})_{\text{had}}(-p^2) = 4\pi\alpha \hat{\Pi}_{\gamma\gamma}(p^2). \quad (14.18)$$

Other quantities, related to the hadronic vacuum polarisation function, are the hadronic contributions to the anomalous magnetic moments of the leptons e , μ and τ . We will discuss the case of the muon in more detail in chapter 15.

The hadronic vacuum polarisation function is derived from the expectation value of two electromagnetic currents, which only couple to quarks. A similar calculation can be performed in order to determine hadronic contributions to the running of the weak mixing angle [271, 272, 277, 287–289]. In the on-shell scheme, its energy dependence is parametrised by

$$\sin^2 \theta_W(p^2) = \sin^2 \theta_W(1 + \Delta \sin^2 \theta_W(p^2)), \quad (14.19)$$

where $\sin^2 \theta_W$ denotes the value in the low energy limit. Hadronic contributions to $\Delta \sin^2 \theta_W(p^2)$ can be related to the vacuum polarisation function $\hat{\Pi}_{\gamma Z}(p^2)$, which describes the kinetic mixing between the photon and the Z -boson. The vector part of the current associated to the Z -boson can be decomposed into [288]

$$\mathcal{V}^Z = \mathcal{V}^3 - \sin^2 \theta_W \mathcal{V}^\gamma. \quad (14.20)$$

Having computed the correlation functions $C_{\mathcal{V}^{i_2}\mathcal{V}^{i_1}}$ for all $i_2, i_1 = 0, 3, 8$, we can easily construct the correlation function $C_{\mathcal{V}^3\mathcal{V}^\gamma}$, which is required for the evaluation of $\hat{\Pi}_{\gamma Z}(p^2)$ in addition to $C_{\mathcal{V}^\gamma\mathcal{V}^\gamma}$. The hadronic contribution to the running of the weak mixing angle is then obtained by

$$(\Delta \sin^2 \theta_W)_{\text{had}}(-p^2) = -\frac{e^2}{\sin^2 \theta_W} \hat{\Pi}_{\gamma Z}(p^2). \quad (14.21)$$

15. The HVP contribution to the muon anomalous magnetic moment

The anomalous magnetic moment of the muon a_μ , which is currently known with a precision of 0.5 ppm [26], serves as a probe for physics beyond the Standard Model. Comparing the most accurate theoretical and experimental determinations, one finds a discrepancy of about $3\text{--}4\sigma$ [29]. In this chapter, we compute leading isospin breaking effects of the hadronic vacuum polarisation contribution to a_μ , which is the leading order contribution from QCD and dominates the overall uncertainty. The introductory part of this chapter is based on the recent review articles [33, 34, 280], the summary article of the Muon g-2 Theory Initiative [29] and the textbook by *Jegerlehner* [22].

15.1. The anomalous magnetic moment of the muon

The magnetic moment of the muon \vec{M} is related to its spin angular momentum \vec{S} by

$$\vec{M} = g_\mu \frac{e}{2m_\mu} \vec{S}, \quad (15.1)$$

where g_μ denotes the gyromagnetic ratio. The Dirac equation predicts a value of $g_\mu = 2$. Quantum field theoretical effects lead to an alteration of g_μ . One defines the *anomalous magnetic moment*

$$a_\mu = \frac{g_\mu - 2}{2}, \quad (15.2)$$

which measures the deviation from the Dirac prediction.

15.1.1. Experimental determination

The anomalous magnetic moment of the muon has been measured in three experiments at CERN [290–292], beginning in the 1960s. The most up-to-date experimental determination of a_μ was made by the E821 experiment at Brookhaven National Laboratory in 2006 [26], where a value of

$$a_\mu^{(\text{exp})} = 11659208.0(6.3) \cdot 10^{-10} \quad (15.3)$$

was found with an uncertainty of 0.54 ppm. In this experiment, accelerated protons are scattered at a Nickel target. In this process, charged pions are emitted, which decay into muons and antineutrinos in a decay channel. The muons, which are spin-polarised in this

15. The HVP contribution to the muon anomalous magnetic moment

decay, feature a spin parallel to the direction of flight. They are injected into a storage ring in the horizontal plane, which possesses a vertical homogeneous magnetic field \vec{B} . The muons circulate in the storage ring with the cyclotron angular frequency [22, 26, 293]

$$\vec{\omega}_c = -\frac{q\vec{B}}{m_\mu\gamma}. \quad (15.4)$$

As the spin of the muon is not aligned with the magnetic field, it starts a Larmor precession in the horizontal plane with the spin angular frequency [22, 26, 293]

$$\vec{\omega}_s = -\frac{g_\mu q\vec{B}}{2m_\mu} - (1 - \gamma)\frac{q\vec{B}}{\gamma m}. \quad (15.5)$$

The anomalous precession frequency $\vec{\omega}_a$ describes the precession relative to the muon momentum and is given by the difference of the cyclotron and the spin frequency [22, 26, 293]

$$\vec{\omega}_a = \vec{\omega}_s - \vec{\omega}_c = -a_\mu\frac{q\vec{B}}{m_\mu}. \quad (15.6)$$

In the E821 experiment, electric quadrupoles are used to vertically focus the muon beam in the storage ring. In the muon rest frame, this electric field is seen as an additional magnetic field, which affects the spin precession frequency. For a velocity β perpendicular to \vec{E} and \vec{B} , the expression for the anomalous precession frequency is altered to [22, 26, 293]

$$\vec{\omega}_a = -\frac{q}{m}\left(a_\mu\vec{B} - \left(a_\mu - \frac{1}{\gamma^2 - 1}\right)\frac{\vec{\beta} \times \vec{E}}{c}\right). \quad (15.7)$$

If one chooses $\gamma = 29.3$, which is equivalent to a "magic" muon momentum of $3.094 \text{ GeV}/c$, the coefficient $\left(a_\mu - \frac{1}{\gamma^2 - 1}\right)$ vanishes. In this case, the magnetic field \vec{B} of the storage ring determines the precession frequency alone [22, 26, 293]. The muon finally decays into an electron, a neutrino and an anti-neutrino. The direction of the electron trajectory and of the muon spin are correlated due to maximal parity violation of the weak decay. The electrons are finally detected by an electromagnetic calorimeter. The magnetic field \vec{B} is measured using nuclear magnetic resonance. It is proportional to the Larmor frequency of stationary protons $\omega_p = g_p \frac{eB}{2m_p}$ [293]. The average magnetic field seen by the muons is described by $\tilde{\omega}_p$. The anomalous magnetic moment of the muon can now be determined from [22, 26]

$$a_\mu = \frac{\omega_a}{\omega_L - \omega_a} = \frac{\omega_a/\tilde{\omega}_p}{\omega_a/\tilde{\omega}_L - \omega_a/\tilde{\omega}_p}, \quad (15.8)$$

where ω_L denotes the Larmor precession frequency of the muon. In the experiment the ratio $\omega_a/\tilde{\omega}_L$ is determined. $\omega_a/\tilde{\omega}_L$ is extracted from the hyperfine structure of muonium [22, 26, 293].

Currently, there are two new experiments aiming for a reduction of the overall experimental uncertainty by a factor of four: the E989 experiment at Fermilab [294], which started in 2018, and the E34 experiment at J-PARC, which plans to start in 2024 [295].

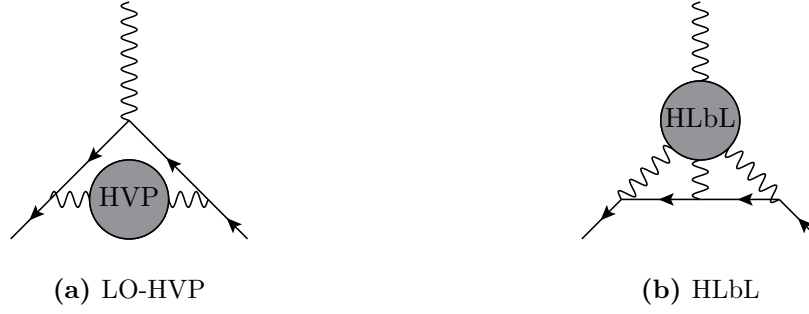


Figure 15.1.: LO-HVP and HLbL contributions to the anomalous magnetic moment of the muon a_μ .

15.1.2. Theoretical prediction

Contribution	$a_\mu \times 10^{11}$	Ref.
QED (order $\mathcal{O}(\alpha^5)$)	$116\,584\,718.93 \pm 0.10$	[296, 297]
Electroweak	153.6 ± 1.0	[298, 299]
QCD		
HVP (LO)	$6\,931 \pm 40$	[300–305]
HVP (NLO)	-98.3 ± 0.7	[305]
HVP (NNLO)	12.4 ± 0.1	[306]
HLbL	94 ± 19	[29, 307]
Total (theory)	$116\,591\,810 \pm 43$	[29]
Experiment	$116\,592\,089 \pm 63$	[26]

Table 15.1.: Standard Model contributions to the anomalous magnetic moment of the muon a_μ in comparison to the experimental value. Table extracted from [280].

The Standard Model prediction of the anomalous magnetic moment of the muon [29]

$$a_\mu^{(\text{theo})} = 116591810(43) \cdot 10^{-11} \quad (15.9)$$

is known with an uncertainty of 0.39 ppm. It can be split up into the three contributions

$$a_\mu = a_\mu^{\text{QED}} + a_\mu^{\text{QCD}} + a_\mu^{\text{EW}} \quad (15.10)$$

from the electromagnetic, the strong and the electro-weak interaction. The magnitudes of the various contributions are presented in table 15.1. The largest contribution is given by QED, which is known up to $\mathcal{O}(\alpha^5)$ and possesses the smallest absolute and relative error. The second largest contribution comes from QCD, which contributes most to the overall error of a_μ . The electro-weak contribution is the smallest. The dominant QCD contribution is given by the LO-HVP contribution, which is proportional to α^2 and depicted in

15. The HVP contribution to the muon anomalous magnetic moment

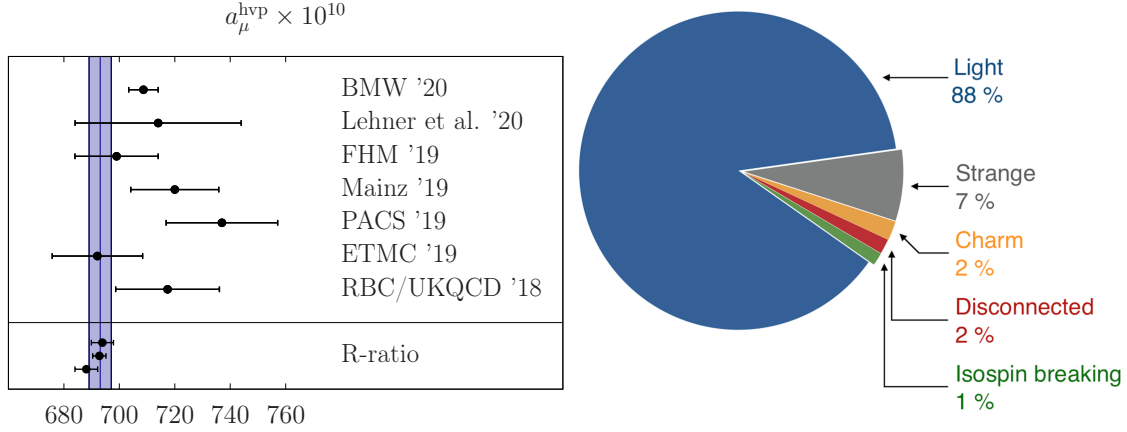


Figure 15.2.: Left: Results from lattice QCD and the R-ratio for the LO-HVP contribution. The blue band represent the value from table 15.1. Right: Components of the LO-HVP contribution to a_μ from lattice QCD. Figures extracted from [280].

fig. 15.1. Higher-order QCD contributions entering at α^3 are the hadronic light-by-light (HLbL), depicted in fig. 15.1, and the NLO-HVP contributions, which are represented by Feynman diagrams with multiple insertions of the HVP function.

Comparing the theoretical prediction and the experimental value in fig. 15.2, one finds a discrepancy of about $3\text{--}4\sigma$ [29], such that a_μ is a candidate to search for physics beyond the SM. To achieve a similar precision of the SM prediction as planned for the upcoming experiments at Fermilab [27] and JPARC [28], the LO-HVP contribution $a_{\mu,\text{HVP}}$ has to be determined with a precision of 0.2% [34]. Figure 15.2 depicts the results for the determinations of $a_{\mu,\text{HVP}}$. The most accurate predictions originate from a data-driven approach based on the optical theorem and the dispersion integral [29]

$$a_{\mu,\text{HVP}} = \frac{\alpha^2}{3\pi^2} \int_{m_\pi^2}^{\infty} ds \frac{K(s)}{s} R(s). \quad (15.11)$$

The kernel function is given by [29]

$$K(s) = \frac{x^2}{2}(2-x^2) + \frac{(1+x^2)(1+x)^2}{x^2} \left(\log(1+x) - x + \frac{x^2}{2} \right) + \frac{1+x}{1-x} x^2 \log(x) \quad (15.12)$$

with $x = \frac{1-\beta_\mu}{1+\beta_\mu}$ and $\beta_\mu = \sqrt{1 - \frac{4m_\mu^2}{s}}$. The R-ratio [29]

$$R(s) = \frac{\sigma(e^+e^- \rightarrow \text{hadrons}(+\gamma))}{\frac{4\pi\alpha^2}{3s}} \quad (15.13)$$

is determined from the cross section $\sigma(e^+e^- \rightarrow \text{hadrons}(+\gamma))$, which is measured experimentally. However, it is preferable to determine $a_{\mu,\text{HVP}}$ from an ab-initio calculation based

15.2. The time-momentum representation of the hadronic vacuum polarisation contribution

on lattice QCD. Only the BMW results from 2020 [200] possess a precision similar to the approach based on the R-ratio, as depicted in fig. 15.2. Commonly, the LO-HVP contribution to a_μ is split into several parts: The connected light, strange and charm quark contributions, the disconnected contributions and the isospin breaking contribution. The relative sizes of the various contributions are depicted in fig. 15.2. In this thesis, we are mainly interested in the isospin breaking contribution, which is of $O(1\%)$, but we also compute the sum of the strange and the light quark contributions, which are defined in the isosymmetric limit. We do not consider charm and quark-disconnected contributions.

15.2. The time-momentum representation of the hadronic vacuum polarisation contribution

Making use of the *time-momentum representation*, the LO-HVP contribution $a_{\mu,\text{HVP}}$ can be represented by [266]

$$a_{\mu,\text{HVP}} = \left(\frac{\alpha}{\pi}\right)^2 \int_0^\infty dx^0 \tilde{K}(x^0, m_\mu) \int dx^3 \langle V^{\gamma x \mu_2} V^{\gamma 0 \mu_1} \rangle_{\text{QCD-con}} \quad (15.14)$$

with the integration kernel [266]

$$\tilde{K}(t, m_\mu) = -8\pi^2 \int_0^\infty \frac{d\omega}{\omega} K(\omega^2, m_\mu) \left(\omega^2 t^2 - 4 \sin^2 \left(\frac{\omega t}{2} \right) \right), \quad (15.15)$$

$$K(\omega^2, m_\mu) = \frac{1}{m_\mu^2} \hat{s} Z(\hat{s})^3 \frac{1 - \hat{s} Z(\hat{s})}{1 + \hat{s} Z(\hat{s})^2}, \quad (15.16)$$

$$Z(\hat{s}) = -\frac{\hat{s} - \sqrt{\hat{s}^2 + 4\hat{s}}}{2\hat{s}}, \quad \hat{s} = \frac{s}{m_\mu^2}. \quad (15.17)$$

We only consider the QCD-connected part of the vector-vector correlation function to retrieve the LO-HVP contribution to a_μ . The full vector-vector correlation function in QCD+QED also includes a contribution to NLO-HVP. $m_\mu^{\text{phys}} = 105.66 \text{ MeV}$ denotes the mass of the muon, which enters as the only scale into the kernel function. In practice, the kernel \tilde{K} is evaluated numerically by an approximation described in [266].

15.3. The hadronic vacuum polarisation contribution from lattice QCD+QED

The kernel function \tilde{K} depends explicitly on the muon mass m_μ . In order to compute $a_{\mu,\text{HVP}}$ on a particular ensemble, using only dimensionless quantities, m_μ has to be expressed in terms of am_μ , i.e. we have to multiply the physical value of the muon mass with the lattice spacing of the particular ensemble. In principle, the scale has to be expanded in terms of $\Delta\varepsilon$, such that the first-order contribution $(a_{\mu,\text{HVP}})_l^{(1)}$ also depends on the partial derivative of \tilde{K} with respect to m_μ and on $(a)_l^{(1)}$. However, as stated in chapter 9, we

15. The HVP contribution to the muon anomalous magnetic moment

neglect isospin breaking effects in the scale setting in this thesis. To evaluate the integral which determines $a_{\mu,\text{HVP}}$ we proceed similar to the HVP function. We replace the time integration by a discrete summation, switch from the renormalised vector-vector correlation function $C_{\mathcal{V}_R^\gamma \mathcal{V}_R^\gamma}$ to its reconstruction $C_{\mathcal{V}_R^\gamma \mathcal{V}_R^\gamma, \text{rec}}$ at time x_{swi}^0 and truncate the infinite summation at x_{cut}^0 . We obtain the expression

$$(a_{\mu,\text{HVP}})^{(0)} = \left(\frac{\alpha}{\pi}\right)^2 \sum_{x^0=0}^{x_{\text{swi}}^0} \tilde{K}(x^0, m_\mu) (C_{\mathcal{V}_R^\gamma \mathcal{V}_R^\gamma}(x^0, 0))^{(0)} \\ + \left(\frac{\alpha}{\pi}\right)^2 \sum_{x^0=x_{\text{swi}}^0+1}^{x_{\text{cut}}^0} \tilde{K}(x^0) (C_{\mathcal{V}_R^\gamma \mathcal{V}_R^\gamma, \text{rec}}(x^0, 0))^{(0)} \quad (15.18)$$

for the zeroth-order contribution. The first-order contributions for $l = \Delta m_u, \Delta m_d, \Delta m_s, \Delta \beta$ read

$$(a_{\mu,\text{HVP}})_l^{(1)} = \left(\frac{\alpha}{\pi}\right)^2 \sum_{x^0=0}^{x_{\text{swi}}^0} \tilde{K}(x^0, m_\mu) (C_{\mathcal{V}_R^\gamma \mathcal{V}_R^\gamma}(x^0, 0))_l^{(1)} \\ + \left(\frac{\alpha}{\pi}\right)^2 \sum_{x^0=x_{\text{swi}}^0+1}^{x_{\text{cut}}^0} \tilde{K}(x^0) (C_{\mathcal{V}_R^\gamma \mathcal{V}_R^\gamma, \text{rec}}(x^0, 0))_l^{(1)}. \quad (15.19)$$

For the expansion parameters $l = e^2$, we have to subtract the QCD-disconnected part similar to the HVP function. As we only deal with quark-connected contributions, we can avoid this step. For further details we refer to [276]. In a second strategy, we rescale the muon mass m_μ , which enters the kernel function [261, 308]. We choose the pion decay constant f_π , neglecting isospin breaking effects on this quantity. f_π increases with the pion mass, such that the m_π -dependence of a_μ becomes weaker and the chiral extrapolation to a physical pion mass flatter, which makes the extrapolation better to control. On each gauge ensemble the muon mass is altered according to [261]

$$am_\mu = \frac{m_\mu^{\text{phys}}}{f_\pi^{\text{phys}}} af_\pi = 1.144 \cdot af_\pi, \quad (15.20)$$

where af_π is determined on the particular ensemble. The rescaling removes the explicit dependency of $a_{\mu,\text{HVP}}$ on the scale a . However, it reenters the results when a continuum extrapolation is performed.

15.3.1. $a_{\mu,\text{HVP}}$ from $C_{\mathcal{V}_{c,R}^\gamma \mathcal{V}_{l,R}^\gamma}$

The leading hadronic contribution to the muon anomalous magnetic moment $a_{\mu,\text{HVP}, \mathcal{V}_{c,R}^\gamma \mathcal{V}_{l,R}^\gamma}$ is extracted from the integral over $C_{\mathcal{V}_{c,R}^\gamma \mathcal{V}_{l,R}^\gamma} \cdot \tilde{K}$. Figures 15.3 and 15.4 show the integrand and the integral for the zeroth-order and first-order contribution, respectively. We observe a significant noise problem in the first-order integrands for the expansion parameters Δm_u ,

15.3. The hadronic vacuum polarisation contribution from lattice QCD+QED

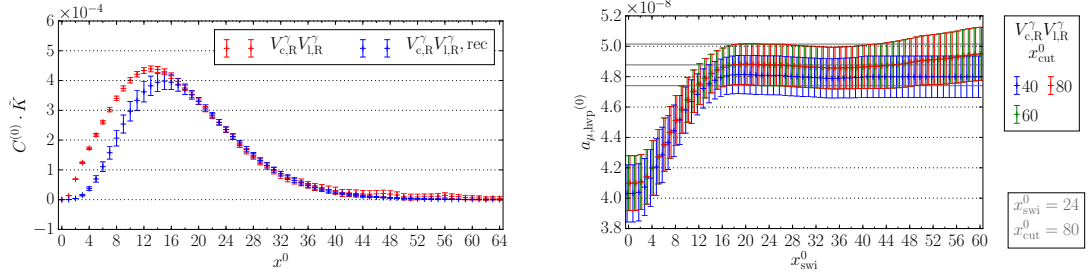


Figure 15.3.: Integrand $(C_{V_{c,R}^\gamma V_{l,R}^\gamma})^{(0)} \cdot \tilde{K}$ and reconstruction on N200. $(a_{\mu, \text{HVP}, V_{c,R}^\gamma V_{l,R}^\gamma})^{(0)}$ in dependence of x_{swi}^0 and x_{cut}^0 . The selected value is marked in grey.

Δm_d , $\Delta\beta$ and e^2 , which underlines the necessity to reconstruct the correlation function at large time distances. We determine x_{swi}^0 and x_{cut}^0 in the same way as described in chapter 14. On N200, we obtain

$$\begin{aligned}
 a_{\mu, \text{HVP}, V_{c,R}^\gamma V_{l,R}^\gamma} = & \left(488(9)_{\text{st}}(10)_{\text{a}}[14]_{\text{tot}} \right. \\
 & + 49000(29700)_{\text{st}}(1000)_{\text{a}}[29800]_{\text{tot}} \Delta\beta \\
 & - 1312(169)_{\text{st}}(27)_{\text{a}}[171]_{\text{tot}} a\Delta m_d \\
 & - 6190(60)_{\text{st}}(130)_{\text{a}}[140]_{\text{tot}} a\Delta m_s \\
 & - 18300(2400)_{\text{st}}(400)_{\text{a}}[2400]_{\text{tot}} a\Delta m_u \\
 & \left. - 1990(240)_{\text{st}}(40)_{\text{a}}[240]_{\text{tot}} e^2 \right) \cdot 10^{10}.
 \end{aligned} \tag{15.21}$$

Inserting the values for the expansion parameters in eq. (9.4), we find:

$$\begin{aligned}
 a_{\mu, \text{HVP}, V_{c,R}^\gamma V_{l,R}^\gamma} &= \left((488(9)_{\text{st}}(10)_{\text{a}}[14]_{\text{tot}})^{(0)} + (-0.1[7]_{\text{tot}})^{(1)} \right) \cdot 10^{10} \\
 &= \left(488(9)_{\text{st}}(10)_{\text{a}}[13]_{\text{tot}} \right) \cdot 10^{10}.
 \end{aligned} \tag{15.22}$$

For the second approach with the rescaled muon mass, we find on N200

$$\begin{aligned}
 a_{\mu, \text{HVP}, V_{c,R}^\gamma V_{l,R}^\gamma} = & \left(526(10)_{\text{st}}(4)_{\text{f}_\pi}[11]_{\text{tot}} \right. \\
 & + 52600(31900)_{\text{st}}(400)_{\text{f}_\pi}[31900]_{\text{tot}} \Delta\beta \\
 & - 1410(181)_{\text{st}}(10)_{\text{f}_\pi}[182]_{\text{tot}} a\Delta m_d \\
 & - 6660(60)_{\text{st}}(50)_{\text{f}_\pi}[80]_{\text{tot}} a\Delta m_s \\
 & - 19640(2530)_{\text{st}}(140)_{\text{f}_\pi}[2530]_{\text{tot}} a\Delta m_u \\
 & \left. - 2143(256)_{\text{st}}(16)_{\text{f}_\pi}[256]_{\text{tot}} e^2 \right) \cdot 10^{10}.
 \end{aligned} \tag{15.23}$$

15. The HVP contribution to the muon anomalous magnetic moment

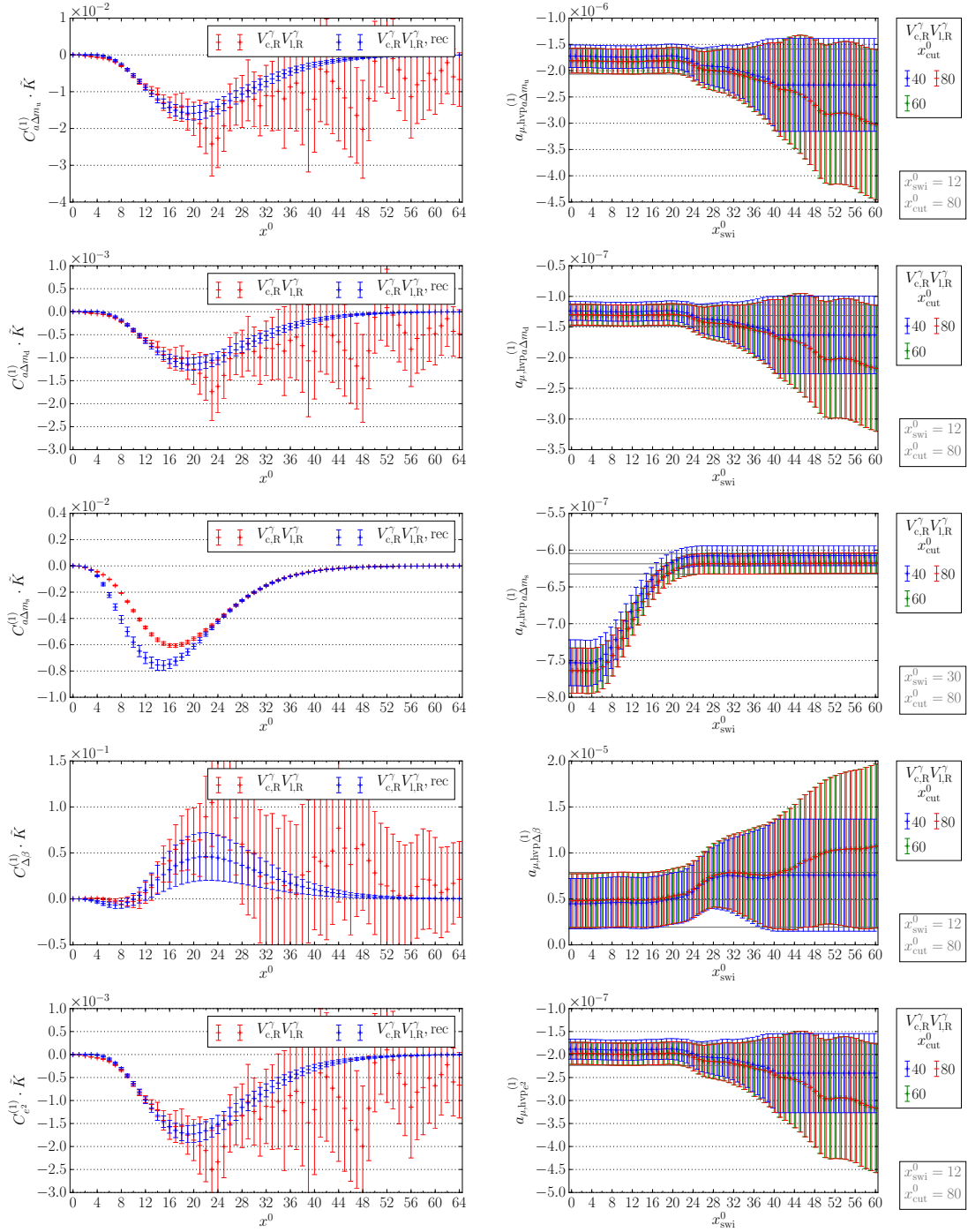


Figure 15.4.: Integrant $(C_{V_{c,R}^\gamma V_{l,R}^\gamma}^{(1)}) \cdot \tilde{K}$ and reconstruction on N200. $(a_{\mu, \text{HVP}, V_{c,R}^\gamma V_{l,R}^\gamma}^{(1)})$ in dependence of x_{swi}^0 and x_{cut}^0 . The selected value is marked in grey.

The scale dependency is now replaced by the dependency on the pion decay constant f_π . Inserting the values for the expansion parameters in eq. (9.4), we find

$$\begin{aligned} a_{\mu, \text{HVP}, V_{c,R}^\gamma V_{l,R}^\gamma} &= \left((526(10)_{\text{st}}(4)_{f_\pi} [11]_{\text{tot}})^{(0)} + (-0.1[8]_{\text{tot}})^{(1)} \right) \cdot 10^{10} \\ &= \left(525(10)_{\text{st}}(4)_{f_\pi} [10]_{\text{tot}} \right) \cdot 10^{10}. \end{aligned} \quad (15.24)$$

15.3.2. $a_{\mu, \text{HVP}}$ from $C_{\mathcal{V}_{l,R}^\gamma \mathcal{V}_{l,R}^\gamma}$

Similarly, $a_{\mu, \text{HVP}}$ can also be extracted from the correlation function $C_{\mathcal{V}_{l,R}^\gamma \mathcal{V}_{l,R}^\gamma}$. As in the case of $\hat{\Pi}_{\mathcal{V}_{l,R}^\gamma \mathcal{V}_{l,R}^\gamma}$ we omit a detailed discussion and refer to the next section for the results.

15.4. Discussion and Outlook

We have computed the leading order hadronic vacuum polarisation contribution to the anomalous magnetic moment of the muon including leading order isospin breaking effects. An overview of the results for the ensembles N200, D450 and H102 is given in table 15.2 for the unrescaled muon mass and in table 15.3 for the rescaled muon mass. We find that the results for both discretisations of the vector-vector correlation function $a_{\mu, \text{HVP}, V_{c,R}^\gamma V_{l,R}^\gamma}$ and $a_{\mu, \text{HVP}, \mathcal{V}_{l,R}^\gamma \mathcal{V}_{l,R}^\gamma}$ coincide within errors. Comparing the unrescaled with the rescaled results, we observe that the rescaling procedure reduces the overall error. This is in accordance with the findings in [261]. The leading isospin breaking correction is 0.6%, at most, of the isosymmetric contribution. The error of the zeroth-order contribution is of the same order of magnitude as the first-order contribution, albeit larger.

Other collaborations find isospin breaking corrections of similar relative size [200, 245, 309, 310]. A strict comparison of the total QCD+QED results can only be made after an extrapolation to the continuum and to physical quark masses has been performed. A comparison of the isospin breaking correction further requires that the renormalisation schemes, which are used to separate QCD+QED and QCD_{iso}, are compatible.

Further improvements of the analysis are directly related to the discussion concerning the HVP function in section 14.4, as both $a_{\mu, \text{HVP}}$ and $\hat{\Pi}_{\mathcal{V}_R^\gamma \mathcal{V}_R^\gamma}$ are computed from $C_{\mathcal{V}_R^\gamma \mathcal{V}_R^\gamma}$. In particular, the inclusion of zeroth-order quark-disconnected diagrams as well as charm quark contributions, which account each for 2% of the total value [280], should be added to the analysis. Minor contributions are expected from first-order quark-disconnected diagrams [200]. Improvements with respect to the large time distance reconstruction of $C_{\mathcal{V}_R^\gamma \mathcal{V}_{l,R}^\gamma}$ also affect $a_{\mu, \text{HVP}}$ [261]. Similar to $\hat{\Pi}_{\mathcal{V}_R^\gamma \mathcal{V}_R^\gamma}$, the bounding method [245, 279] can also be applied for $a_{\mu, \text{HVP}}$.

15. The HVP contribution to the muon anomalous magnetic moment

$a_{\mu, \text{HVP}, \mathcal{V}_{c,R}^\gamma \mathcal{V}_{l,R}^\gamma}$	$\left((488(9)_{\text{st}}(10)_{\text{a}}[14]_{\text{tot}})^{(0)} + (-0.1[7]_{\text{tot}})^{(1)} \right) \cdot 10^{10}$
	$= (488(9)_{\text{st}}(10)_{\text{a}}[13]_{\text{tot}}) \cdot 10^{10}$
$a_{\mu, \text{HVP}, \mathcal{V}_{l,R}^\gamma \mathcal{V}_{l,R}^\gamma}$	$\left((491(8)_{\text{st}}(11)_{\text{a}}[13]_{\text{tot}})^{(0)} + (-0.3[7]_{\text{tot}})^{(1)} \right) \cdot 10^{10}$
	$= (491(8)_{\text{st}}(11)_{\text{a}}[13]_{\text{tot}}) \cdot 10^{10}$
(a) N200 ($a = 0.064$ fm, $m_\pi = 282$ MeV)	
$a_{\mu, \text{HVP}, \mathcal{V}_{c,R}^\gamma \mathcal{V}_{l,R}^\gamma}$	$\left((541(8)_{\text{st}}(12)_{\text{a}}[15]_{\text{tot}})^{(0)} + (2[1]_{\text{tot}})^{(1)} \right) \cdot 10^{10}$
	$= (543(9)_{\text{st}}(12)_{\text{a}}[15]_{\text{tot}}) \cdot 10^{10}$
$a_{\mu, \text{HVP}, \mathcal{V}_{l,R}^\gamma \mathcal{V}_{l,R}^\gamma}$	$\left((546(8)_{\text{st}}(12)_{\text{a}}[15]_{\text{tot}})^{(0)} + (2[1]_{\text{tot}})^{(1)} \right) \cdot 10^{10}$
	$= (548(8)_{\text{st}}(13)_{\text{a}}[15]_{\text{tot}}) \cdot 10^{10}$
(b) D450 ($a = 0.076$ fm, $m_\pi = 216$ MeV)	
$a_{\mu, \text{HVP}, \mathcal{V}_{c,R}^\gamma \mathcal{V}_{l,R}^\gamma}$	$\left((440(4)_{\text{st}}(10)_{\text{a}}[10]_{\text{tot}})^{(0)} + (2.3[4]_{\text{tot}})^{(1)} \right) \cdot 10^{10}$
	$= (442(4)_{\text{st}}(10)_{\text{a}}[11]_{\text{tot}}) \cdot 10^{10}$
$a_{\mu, \text{HVP}, \mathcal{V}_{l,R}^\gamma \mathcal{V}_{l,R}^\gamma}$	$\left((445(4)_{\text{st}}(10)_{\text{a}}[10]_{\text{tot}})^{(0)} + (2.2[4]_{\text{tot}})^{(1)} \right) \cdot 10^{10}$
	$= (448(4)_{\text{st}}(10)_{\text{a}}[11]_{\text{tot}}) \cdot 10^{10}$
(c) H102 ($a = 0.086$ fm, $m_\pi = 354$ MeV)	

Table 15.2.: LO-HVP contribution to a_μ .

$a_{\mu, \text{HVP}, \mathcal{V}_{c,R}^\gamma \mathcal{V}_{l,R}^\gamma}$	$\left((526(10)_{\text{st}}(4)_{f_\pi} [11]_{\text{tot}})^{(0)} + (-0.1[8]_{\text{tot}})^{(1)} \right) \cdot 10^{10}$
	$= \left(525(10)_{\text{st}}(4)_{f_\pi} [10]_{\text{tot}} \right) \cdot 10^{10}$
$a_{\mu, \text{HVP}, \mathcal{V}_{l,R}^\gamma \mathcal{V}_{l,R}^\gamma}$	$\left((529(9)_{\text{st}}(4)_{f_\pi} [10]_{\text{tot}})^{(0)} + (-0.3[7]_{\text{tot}})^{(1)} \right) \cdot 10^{10}$
	$= \left(529(9)_{\text{st}}(4)_{f_\pi} [10]_{\text{tot}} \right) \cdot 10^{10}$
(a) N200 ($a = 0.064$ fm, $m_\pi = 282$ MeV)	
$a_{\mu, \text{HVP}, \mathcal{V}_{c,R}^\gamma \mathcal{V}_{l,R}^\gamma}$	$\left((525(8)_{\text{st}}(5)_{f_\pi} [9]_{\text{tot}})^{(0)} + (2[1]_{\text{tot}})^{(1)} \right) \cdot 10^{10}$
	$= \left(527(9)_{\text{st}}(5)_{f_\pi} [10]_{\text{tot}} \right) \cdot 10^{10}$
$a_{\mu, \text{HVP}, \mathcal{V}_{l,R}^\gamma \mathcal{V}_{l,R}^\gamma}$	$\left((530(7)_{\text{st}}(5)_{f_\pi} [9]_{\text{tot}})^{(0)} + (2[1]_{\text{tot}})^{(1)} \right) \cdot 10^{10}$
	$= \left(532(8)_{\text{st}}(5)_{f_\pi} [9]_{\text{tot}} \right) \cdot 10^{10}$
(b) D450 ($a = 0.076$ fm, $m_\pi = 216$ MeV)	
$a_{\mu, \text{HVP}, \mathcal{V}_{c,R}^\gamma \mathcal{V}_{l,R}^\gamma}$	$\left((491(4)_{\text{st}}(5)_{f_\pi} [7]_{\text{tot}})^{(0)} + (2.5[4]_{\text{tot}})^{(1)} \right) \cdot 10^{10}$
	$= \left(493(4)_{\text{st}}(5)_{f_\pi} [7]_{\text{tot}} \right) \cdot 10^{10}$
$a_{\mu, \text{HVP}, \mathcal{V}_{l,R}^\gamma \mathcal{V}_{l,R}^\gamma}$	$\left((497(4)_{\text{st}}(5)_{f_\pi} [6]_{\text{tot}})^{(0)} + (2.4[4]_{\text{tot}})^{(1)} \right) \cdot 10^{10}$
	$= \left(499(4)_{\text{st}}(5)_{f_\pi} [7]_{\text{tot}} \right) \cdot 10^{10}$
(c) H102 ($a = 0.086$ fm, $m_\pi = 354$ MeV)	

Table 15.3.: LO-HVP contribution to a_μ with rescaled muon mass.

16. Conclusion and Outlook

In this thesis, we investigated the consequences of isospin symmetry breaking on hadronic matrix elements. An observable of special interest is the anomalous magnetic moment of the muon a_μ , which is currently known with a precision of 0.5 ppm [26] and serves as a probe for physics beyond the Standard Model (SM). Comparing the experimental determination with the SM prediction, one finds a deviation of about 3-4 σ [29]. Upcoming experiments at Fermilab [27] and JPARC [28] aim for a reduction of the overall uncertainty by a factor of four. To achieve a similar precision of the SM prediction, the hadronic vacuum polarisation (HVP) contribution $a_{\mu,\text{HVP}}$ has to be determined with a precision of 0.2% [34]. This desired precision can only be obtained from lattice QCD simulations, if non-degenerate light quark masses and electromagnetic effects are included.

We described a strategy, which enables us to perform QCD+QED computations based on QCD_{iso} Monte Carlo simulations using CLS $N_f = 2 + 1$ gauge ensembles [45, 168–172]. The latter were generated with an $O(a)$ -improved Wilson fermion action and a tree-level improved Lüscher-Weisz gauge action. We related QCD+QED to QCD_{iso} by Monte Carlo reweighting [160, 161] and introduced a perturbative expansion of QCD+QED correlation functions around QCD_{iso} [46, 143, 191, 192], which we adapted to the applied lattice fermion discretisation. The expansion is formulated in terms of the parameters $\Delta\varepsilon = (\Delta m_u, \Delta m_d, \Delta m_s, \Delta\beta, e^2)$. Δm_f denotes the detuning of the bare quark mass, $\Delta\beta$ the detuning of the bare inverse strong coupling and e^2 the bare electromagnetic coupling. We regulated the manifest infrared divergence of non-compact lattice QED via the QED_L prescription [41, 44, 140], which removes the spatial zero-modes on each timeslice from the theory. We derived Ward identities for continuum QCD+QED as well as for the considered lattice regularisation. We further derived analytic expressions for the lattice photon propagator for open and periodic temporal boundary conditions in Feynman and Coulomb gauge, based on discrete Fourier, sine and cosine transforms. The QCD+QED simulations were performed in Coulomb gauge and the photon boundary conditions were chosen in accordance with the boundary conditions of the gauge ensembles. Feynman gauge served as a cross-check of the implementation applied to gauge invariant correlation functions. As we only investigated leading isospin breaking effects, we truncated the perturbative expansion at first order. We focussed on quark-connected contributions, taking only isospin breaking effects in the valence quark sector into account. We performed computations on the gauge ensembles H102 ($a = 0.086$ fm, $m_\pi = 354$ MeV), D450 ($a = 0.076$ fm, $m_\pi = 216$ MeV) and N200 ($a = 0.064$ fm, $m_\pi = 282$ MeV).

We determined the masses m_{π^+} , m_{π^0} , m_{K^+} and m_{K^0} as well as the corresponding mass differences $m_{\pi^+} - m_{\pi^0}$ and $m_{K^+} - m_{K^0}$ and averages $\frac{1}{2}(m_{\pi^+} + m_{\pi^0})$ and $\frac{1}{2}(m_{K^+} + m_{K^0})$ within the isospin multiplets. We suggested a hadronic renormalisation scheme based on $\frac{1}{2}(m_{\pi^+} + m_{\pi^0})$, $\frac{1}{2}(m_{K^+} + m_{K^0})$ and $m_{K^+} - m_{K^0}$, which served to fix the bare quark

16. Conclusion and Outlook

mass detunings Δm_u , Δm_d and Δm_s . We matched QCD+QED and QCD_{iso} on each gauge ensemble demanding equal pion and kaon mass averages. The kaon mass difference was set to its physical value. Considering a leading order calculation, we discussed the non-renormalisation of the electromagnetic coupling [46, 143] in QCD+QED due to the vector Ward identity. Consequently, we fixed the bare electromagnetic coupling via the fine-structure constant, i.e. $e^2 = 4\pi\alpha$. Isospin breaking effects in the scale setting were neglected. We found that the first-order contributions to the masses m_{π^+} , m_{π^0} , m_{K^+} and m_{K^0} are smaller than the error associated with the zeroth-order contribution. The latter is dominated by the scale setting uncertainty. We determined the pion mass splitting on the three gauge ensembles with a precision of $O(5\%)$. The latter is not an input parameter with respect to the chosen renormalisation scheme.

We discussed the renormalisation procedure of the local and conserved vector current \mathcal{V}_1 and \mathcal{V}_c in QCD+QED. We demanded that the matrix element of the renormalised vector current $\langle 0|\mathcal{V}_R|V\rangle$, where $|V\rangle$ denotes the lowest accessible state created by \mathcal{V}_R from the vacuum $|0\rangle$, is the same for both discretisations [260]. In the computation of the matrix of renormalisation factors $Z_{\mathcal{V}_{1,R}\mathcal{V}_1}$ we took operator mixing into account. The leading isospin breaking correction was significant compared to the statistical uncertainty associated with the isosymmetric contribution. We computed the leading isospin breaking correction for the renormalised HVP function $\hat{\Pi}_{\mathcal{V}_R^*\mathcal{V}_R^*}$. It is proportional to the HVP contribution to the running of the fine-structure constant α . In the considered energy range between 1 GeV^2 and 9 GeV^2 , the leading isospin breaking correction was in the range of 0.7% and 0.3% of the isosymmetric contribution. The error of the isosymmetric contribution, which is dominated by the scale setting uncertainty, was of the same order of magnitude as the leading isospin breaking correction. We further computed the LO-HVP contribution to the anomalous magnetic moment of the muon $a_{\mu,\text{HVP}}$ in QCD+QED. The leading isospin breaking correction was 0.6% and less of the isosymmetric contribution. Again, the error of the isosymmetric contribution, which was dominated by scale setting uncertainty, was of the same order of magnitude as the leading isospin breaking correction. Other collaborations find corrections of similar relative size [200, 245, 309, 310]. However, it has to be pointed out that a strict comparison of the total QCD+QED result can only be made after an extrapolation to the continuum and to physical quark masses has been performed. In addition, the comparison of isospin breaking corrections is only possible if the same renormalisation scheme, which is used to separate QCD+QED and QCD_{iso}, is used.

In this thesis, we have developed a concept for the computation of isospin breaking corrections on the basis of CLS gauge ensembles. We demonstrated that a determination of the latter for phenomenologically relevant observables is, in principle, feasible. However, further computational efforts are required to enable a precise prediction of the HVP contribution to the muon anomalous magnetic moment and to the running of the fine-structure constant at the physical point. A strategy on how this target can be achieved by means of existing methods has been outlined in the above paragraphs.

We were not able to perform a continuum and chiral extrapolation to the physical point, due to the limited number of analysed gauge ensembles. Particularly relevant ensembles

to be considered are J303 ($a = 0.050$ fm, $m_\pi = 257$ MeV), which allows to investigate the effect of even smaller lattice spacings, and E250 ($a = 0.076$ fm, $m_\pi = 130$ MeV), which is an ensemble possessing physical pion and kaon masses. To study finite volume effects of QCD and especially QED, it is reasonable to investigate the two ensembles H105 and N101 ($a = 0.086$ fm, $m_\pi = 282$ MeV), which only differ in the simulated volume.

Compared to the QCD_{iso} computations of the Mainz group [187, 229, 261, 268, 277], we find considerably lower values of $a_{\mu,\text{HVP}}$ on the analysed ensembles. This effect is caused by the different renormalisation condition used to renormalise the local vector current and the absence of $O(a)$ -improvement of the operators. To be able to combine the results, it is important to harmonise the setup of QCD+QED computations of $a_{\mu,\text{HVP}}$ and $\hat{\Pi}_{\mathcal{V}_R^\gamma \mathcal{V}_R^\gamma}$, used in this thesis, with the setup of the corresponding QCD_{iso} computations of the Mainz group [187, 229, 261, 268, 277]. In particular, this means that the renormalisation factors $Z_{\mathcal{V}_{l,R} \mathcal{V}_l}$ have to be determined by a renormalisation condition based on the vector Ward identity in QCD+QED as performed in QCD_{iso} [229]. In addition, all operators should be $O(a)$ -improved with respect to QCD_{iso} . Consequently, the computed observables would converge with $O(a^2, a\Delta\varepsilon)$ to the continuum limit. Due to the perturbative character of the isospin breaking correction, the violation of the $O(a^2)$ convergence can be assumed to be mild and the construction of operators improved with respect to QCD+QED, which is rather tedious, can presumably be avoided.

As the leading isospin breaking corrections of dimensionful quantities, which we computed in this thesis, are of the same order of magnitude as the error of the isosymmetric contribution, which is dominated by the scale uncertainty, a major focus of future efforts has to be put on the reduction of the latter. An improvement of the theoretical prediction can only be achieved if the precision of the scale setting is increased and if isospin breaking effects are included in the scale setting. The computation of hadronic decay constants for leptonic decays including isospin breaking effects is highly non-trivial due to the photon exchange between the quarks of the decaying particle and the charged lepton as well as infrared finale state photons [224–227]. In addition, uncertainties associated with the CKM matrix enter the experimental determinations of mesonic decay constants. By contrast, the measurements of the low-lying baryon masses are unaffected by such additional uncertainties. Therefore, it is advisable to perform the scale setting for QCD+QED based on the mass of a baryon belonging to the baryon octet or decuplet.

In the future, two main types of simulation programs to study leading isospin breaking effects in hadronic observables should be developed. The first program computes quark-connected contributions to mesonic and baryonic two-point functions with interpolation operators based on smeared quark fields. The latter type of operators has a larger overlap with the interpolated ground state and allows for a more reliable extraction of the corresponding mass. This program computes all relevant quantities for the hadronic renormalisation scheme and is used to determine the values of the expansion parameters $\Delta\varepsilon$. The second program is an extension of the currently existing code and is based on point-like interpolation operators. It should compute quark-connected contributions to both mesonic two- and three-point functions. The calculation of leading isospin breaking effects in mesonic three-point functions is expensive due to the large number of diagrams

16. Conclusion and Outlook

and sequential propagators with up to four solves of the Dirac equation. Therefore, an emphasis has to be put on potential code optimisations. The HVP functions $\hat{\Pi}_{\gamma_R \gamma_R}$ and $\hat{\Pi}_{\gamma_R^Z \gamma_R^Z}$, as well as the HVP contribution to the running of the fine-structure constant α , to the weak mixing angle θ_W and to the anomalous magnetic moment of the muon a_μ can be computed from the mesonic two-point functions. In addition, PCAC quark masses can be extracted from the two-point functions, which may serve to define the chiral point in QCD+QED and to determine the additive mass renormalisation of Wilson quarks in the presence of the electromagnetic interaction. The three-point function, in combination with the two-point function, allows for the calculation of the renormalisation factors of the local vector current based on the Ward identity method. Combining the computation of two- and three-point functions is advantageous, as building blocks computed for the two-point functions can be reused for three-point functions. For future runs, a considerable increase in computational efficiency can be obtained by the application of all-mode-averaging [254–256], which can be easily integrated into the analysis framework. Other collaborations, performing combined QCD+QED computations based on the perturbative expansion around the isosymmetric limit, rely on low-mode averaging [198, 200, 311]. A major problem one has to face when calculating the HVP is the signal-to-noise problem for large time distances. First promising results for a noise reduction in the vector channel were obtained in investigations of multi-level integration techniques for fermions [312–317].

The set of Feynman diagrams in this work and also in the two simulation programs suggested above is restricted to quark-connected diagrams for both zeroth- and first-order contributions. To reduce systematic effects, further diagrams have to be included into the analysis. In particular, for the HVP function the zeroth-order quark-disconnected diagram has to be considered. This diagram was recently computed in the Mainz group on a large set of ensembles, based on frequency-splitting estimators of single-propagator traces [264, 265]. The remaining first-order quark-disconnected diagrams, which presumably are of little relevance, can be split into two categories: Diagrams which describe isospin corrections only in the valence sector and diagrams that also consider the effect on sea quarks. In both cases, the frequency-splitting technique can be applied for this class of diagrams [262]. The computation is, however, considerably more expensive compared to other contributions. Other collaborations made use of low-mode averaging [198, 200, 311] to compute disconnected contributions.

For a more complete investigation, it is necessary to remove finite volume effects from meson and baryon masses, as well as the HVP, considering both QCD and the electromagnetic correction. A common method, which can be applied to QCD+QED, is the derivation of analytic corrections based on chiral perturbation theory, which includes the electromagnetic interaction [199, 281, 282].

Compared to pure QCD_{iso} computations, the number of fits performed in QCD+QED, where leading isospin breaking effects are considered, is increased by a factor of six. This amounts to a very large number of fits, which were analysed by hand. The usage of Akaike’s information criterion [318] allows for a considerable reduction of manual effort. Akaike’s information criterion facilitates the combination of the results of several fits weighted according to their Akaike weights [319], which depend on χ^2 and the number of parameters

of the model [41], such that not a single representative fit has to be chosen by hand.

Part V.

Appendix

Acknowledgements

We are grateful to our colleagues in the CLS initiative for sharing ensembles. Calculations for this project were partly performed on the HPC clusters "Clover" and "HIMster II" at the Helmholtz-Institut Mainz and "Mogon II" at JGU Mainz. Parts of this research were conducted using the supercomputer "Mogon II" and/or advisory services offered by Johannes Gutenberg University Mainz (hpc.uni-mainz.de), which is a member of the AHRP (Alliance for High Performance Computing in Rhineland Palatinate, www.ahrp.info) and the Gauss Alliance e.V. . The authors gratefully acknowledge the computing time granted on the supercomputer "Mogon II" at Johannes Gutenberg University Mainz (hpc.uni-mainz.de). Additional computer time has been allocated through the project HMZ21 on the HPC cluster "JUWELS" at NIC, Jülich [320]. The authors gratefully acknowledge the Gauss Centre for Supercomputing e.V. (www.gauss-centre.eu) for funding this project by providing computing time on the GCS Supercomputer JUWELS at Jülich Supercomputing Centre (JSC). Andreas Risch is a recipient of a fellowship through GRK Symmetry Breaking (DFG/GRK1581).

Bibliography

- [1] H. Fritzsch, M. Gell-Mann and H. Leutwyler, *Advantages of the Color Octet Gluon Picture*, *Phys. Lett. B* **47** (1973) 365.
- [2] C.-N. Yang and R. L. Mills, *Conservation of Isotopic Spin and Isotopic Gauge Invariance*, *Phys. Rev.* **96** (1954) 191.
- [3] S. Glashow, *Partial Symmetries of Weak Interactions*, *Nucl. Phys.* **22** (1961) 579.
- [4] S. Weinberg, *A Model of Leptons*, *Phys. Rev. Lett.* **19** (1967) 1264.
- [5] A. Salam, *Weak and Electromagnetic Interactions*, *Conf. Proc. C* **680519** (1968) 367.
- [6] F. Englert and R. Brout, *Broken Symmetry and the Mass of Gauge Vector Mesons*, *Phys. Rev. Lett.* **13** (1964) 321.
- [7] P. W. Higgs, *Broken Symmetries and the Masses of Gauge Bosons*, *Phys. Rev. Lett.* **13** (1964) 508.
- [8] G. Guralnik, C. Hagen and T. Kibble, *Global Conservation Laws and Massless Particles*, *Phys. Rev. Lett.* **13** (1964) 585.
- [9] S. Glashow, J. Iliopoulos and L. Maiani, *Weak Interactions with Lepton-Hadron Symmetry*, *Phys. Rev. D* **2** (1970) 1285.
- [10] G. Abrams et al., *The Discovery of a Second Narrow Resonance in e^+e^- Annihilation*, *Phys. Rev. Lett.* **33** (1974) 1453.
- [11] E598 collaboration, J. Aubert et al., *Experimental Observation of a Heavy Particle J* , *Phys. Rev. Lett.* **33** (1974) 1404.
- [12] UA1 collaboration, G. Arnison et al., *Experimental Observation of Isolated Large Transverse Energy Electrons with Associated Missing Energy at $s^{1/2} = 540\text{-GeV}$* , *Phys. Lett. B* **122** (1983) 103.
- [13] UA2 collaboration, M. Banner et al., *Observation of Single Isolated Electrons of High Transverse Momentum in Events with Missing Transverse Energy at the CERN anti- $p p$ Collider*, *Phys. Lett. B* **122** (1983) 476.
- [14] UA1 collaboration, G. Arnison et al., *Experimental Observation of Lepton Pairs of Invariant Mass Around $95\text{-GeV}/c^{*2}$ at the CERN SPS Collider*, *Phys. Lett. B* **126** (1983) 398.

Bibliography

- [15] UA2 collaboration, P. Bagnaia et al., *Evidence for $Z^0 \rightarrow e^+e^-$ at the CERN $\bar{p}p$ Collider*, *Phys. Lett. B* **129** (1983) 130.
- [16] ATLAS collaboration, G. Aad et al., *Observation of a new particle in the search for the Standard Model Higgs boson with the ATLAS detector at the LHC*, *Phys. Lett. B* **716** (2012) 1 [1207.7214].
- [17] CMS collaboration, S. Chatrchyan et al., *Combined results of searches for the standard model Higgs boson in pp collisions at $\sqrt{s} = 7$ TeV*, *Phys. Lett. B* **710** (2012) 26 [1202.1488].
- [18] S. Deser and P. van Nieuwenhuizen, *Nonrenormalizability of the Quantized Einstein-Maxwell System*, *Phys. Rev. Lett.* **32** (1974) 245.
- [19] G. 't Hooft and M. Veltman, *One loop divergencies in the theory of gravitation*, *Ann. Inst. H. Poincaré Phys. Theor. A* **20** (1974) 69.
- [20] U. Mosel, *Fields, symmetries, and quarks*, 1999.
- [21] T. Blum, A. Denig, I. Logashenko, E. de Rafael, B. Roberts, T. Teubner et al., *The Muon ($g-2$) Theory Value: Present and Future*, 1311.2198.
- [22] F. Jegerlehner, *The anomalous magnetic moment of the muon*, 2017. 10.1007/978-3-319-63577-4.
- [23] P. A. Dirac, *The quantum theory of the electron*, *Proc. Roy. Soc. Lond. A* **117** (1928) 610.
- [24] P. Dirac, *The Quantum theory of electron. 2.*, *Proc. Roy. Soc. Lond. A* **118** (1928) 351.
- [25] J. S. Schwinger, *On Quantum electrodynamics and the magnetic moment of the electron*, *Phys. Rev.* **73** (1948) 416.
- [26] MUON G-2 collaboration, G. Bennett et al., *Final Report of the Muon E821 Anomalous Magnetic Moment Measurement at BNL*, *Phys. Rev. D* **73** (2006) 072003 [hep-ex/0602035].
- [27] FERMILAB E989 collaboration, G. Venanzoni, *The New Muon $g-2$ experiment at Fermilab*, *Nucl. Part. Phys. Proc.* **273-275** (2016) 584 [1411.2555].
- [28] E34 collaboration, M. Otani, *Status of the Muon $g-2$ /EDM Experiment at J-PARC (E34)*, *JPS Conf. Proc.* **8** (2015) 025008.
- [29] T. Aoyama et al., *The anomalous magnetic moment of the muon in the Standard Model*, *Phys. Rept.* **887** (2020) 1 [2006.04822].
- [30] T. Goecke, C. S. Fischer and R. Williams, *Leading-order calculation of hadronic contributions to the muon $g-2$ using the Dyson-Schwinger approach*, *Phys. Lett. B* **704** (2011) 211 [1107.2588].

- [31] T. Blum, *Lattice calculation of the lowest order hadronic contribution to the muon anomalous magnetic moment*, *Phys. Rev. Lett.* **91** (2003) 052001 [hep-lat/0212018].
- [32] C. Aubin and T. Blum, *Calculating the hadronic vacuum polarization and leading hadronic contribution to the muon anomalous magnetic moment with improved staggered quarks*, *Phys. Rev. D* **75** (2007) 114502 [hep-lat/0608011].
- [33] H. B. Meyer and H. Wittig, *Lattice QCD and the anomalous magnetic moment of the muon*, *Prog. Part. Nucl. Phys.* **104** (2019) 46 [1807.09370].
- [34] V. Gülpers, *Recent Developments of Muon $g-2$ from Lattice QCD*, *PoS LATTICE2019* (2020) 224 [2001.11898].
- [35] PARTICLE DATA GROUP collaboration, M. Tanabashi, K. Hagiwara, K. Hikasa, K. Nakamura, Y. Sumino, F. Takahashi et al., *Review of particle physics*, *Phys. Rev. D* **98** (2018) 030001.
- [36] W. Heisenberg, *Über den Bau der Atomkerne*, *Zeitschrift für Physik* **77** (1932) 1.
- [37] N. Cabibbo, *Unitary Symmetry and Leptonic Decays*, *Phys. Rev. Lett.* **10** (1963) 531.
- [38] A. Portelli, *Review on the inclusion of isospin breaking effects in lattice calculations*, *PoS KAON13* (2013) 023 [1307.6056].
- [39] FLAVOUR LATTICE AVERAGING GROUP collaboration, S. Aoki et al., *FLAG Review 2019: Flavour Lattice Averaging Group (FLAG)*, *Eur. Phys. J. C* **80** (2020) 113 [1902.08191].
- [40] R. L. Jaffe, A. Jenkins and I. Kimchi, *Quark Masses: An Environmental Impact Statement*, *Phys. Rev. D* **79** (2009) 065014 [0809.1647].
- [41] S. Borsanyi, S. Durr, Z. Fodor, C. Hoelbling, S. D. Katz, S. Krieg et al., *Ab initio calculation of the neutron-proton mass difference*, *Science* **347** (2015) 1452 [1406.4088].
- [42] C. Gattringer and C. B. Lang, *Quantum chromodynamics on the lattice : an introductory presentation*, 2010.
- [43] A. Portelli, *Inclusion of isospin breaking effects in lattice simulations*, *PoS LATTICE2014* (2015) 013 [1505.07057].
- [44] A. Patella, *QED Corrections to Hadronic Observables*, *PoS LATTICE2016* (2017) 020 [1702.03857].
- [45] M. Bruno, D. Djukanovic, G. P. Engel, A. Francis, G. Herdoiza, H. Horch et al., *Simulation of QCD with $N_f = 2 + 1$ flavors of non-perturbatively improved Wilson fermions*, *JHEP* **02** (2015) 043 [1411.3982].

Bibliography

- [46] RM123 collaboration, G. de Divitiis, R. Frezzotti, V. Lubicz, G. Martinelli, R. Petronzio, G. Rossi et al., *Leading isospin breaking effects on the lattice*, *Phys. Rev. D* **87** (2013) 114505 [1303.4896].
- [47] BUDAPEST-MARSEILLE-WUPPERTAL collaboration, S. Borsanyi, S. Dür, Z. Fodor, J. Frison, C. Hoelbling, S. D. Katz et al., *Isospin splittings in the light baryon octet from lattice QCD and QED*, *Phys. Rev. Lett.* **111** (2013) 252001 [1306.2287].
- [48] Z. Fodor, C. Hoelbling, S. Krieg, L. Lellouch, T. Lippert, A. Portelli et al., *Up and down quark masses and corrections to Dashen's theorem from lattice QCD and quenched QED*, *Phys. Rev. Lett.* **117** (2016) 082001 [1604.07112].
- [49] R. Jackiw and C. Rebbi, *Vacuum Periodicity in a Yang-Mills Quantum Theory*, *Phys. Rev. Lett.* **37** (1976) 172.
- [50] G. 't Hooft, *Symmetry Breaking Through Bell-Jackiw Anomalies*, *Phys. Rev. Lett.* **37** (1976) 8.
- [51] M. E. Peskin and D. V. Schroeder, *An introduction to quantum field theory*, 1997.
- [52] M. A. Srednicki, *Quantum field theory*, 2007.
- [53] F. Mandl and G. Shaw, *Quantum field theory*, 2010.
- [54] S. Weinberg, *The quantum theory of fields : 1. foundations*, 2005.
- [55] S. Weinberg, *The quantum theory of fields : 2. modern applications*, 1996.
- [56] S. Pokorski, *Gauge field theories*, 1989.
- [57] K. Fujikawa and H. Suzuki, *Path integrals and quantum anomalies*, 2004.
- [58] J. C. Collins, *Renormalization : an introduction to renormalization, the renormalization group, and the operator-product expansion*, 1998.
- [59] J. Zinn-Justin, *Quantum field theory and critical phenomena*, 2010.
- [60] A. Wipf, *Statistical approach to quantum field theory : an introduction*, 2013.
- [61] B. B. Brandt, *Chiral properties of two-flavour QCD at zero and non-zero temperature*, Ph.D. thesis, 2012.
- [62] B. Jäger, *Hadronic matrix elements in lattice QCD*, Ph.D. thesis, 2014.
- [63] V. M. Gülpers, *Hadronic correlation functions with quark-disconnected contributions in lattice QCD*, Ph.D. thesis, 2015.
- [64] F. B. Erben, *A Lattice QCD study of the rho resonance and the timelike pion form factor*, Ph.D. thesis, Mainz, 2018.

- [65] J. Wilhelm, *The strangeness form factors of the nucleon from lattice QCD*, Ph.D. thesis, Mainz, 2019.
- [66] J. Schwinger, *On the Euclidean structure of relativistic field theory*, *Proc. Nat. Acad. Sci.* **44** (1958) 956.
- [67] K. Symanzik, *Euclidean quantum field theory. i. equations for a scalar model*, *Journal of Mathematical Physics* **7** (1966) 510 [<https://doi.org/10.1063/1.1704960>].
- [68] G. Wick, *Properties of Bethe-Salpeter Wave Functions*, *Phys. Rev.* **96** (1954) 1124.
- [69] N. Backhouse and A. Fellouris, *On the Superdeterminant function for Supermatrices*, *J. Phys. A* **17** (1984) 1389.
- [70] E. Witten, *Notes On Supermanifolds and Integration*, 1209.2199.
- [71] A. Messiah, *Quantum mechanics : 2.*, 1969.
- [72] M. Lüscher, S. Sint, R. Sommer and P. Weisz, *Chiral symmetry and $O(a)$ improvement in lattice QCD*, *Nucl. Phys. B* **478** (1996) 365 [[hep-lat/9605038](#)].
- [73] <http://cern.ch/luscher/openQCD/> .
- [74] M. Durante et al., *All the fun of the FAIR: fundamental physics at the facility for antiproton and ion research*, *Phys. Scripta* **94** (2019) 033001 [[1903.05693](#)].
- [75] U. W. Heinz and M. Jacob, *Evidence for a new state of matter: An Assessment of the results from the CERN lead beam program*, [nucl-th/0002042](#).
- [76] D. J. Gross and F. Wilczek, *Ultraviolet Behavior of Nonabelian Gauge Theories*, *Phys. Rev. Lett.* **30** (1973) 1343.
- [77] A. Deur, S. J. Brodsky and G. F. de Teramond, *The QCD Running Coupling*, *Nucl. Phys.* **90** (2016) 1 [[1604.08082](#)].
- [78] W. E. Caswell, *Asymptotic Behavior of Nonabelian Gauge Theories to Two Loop Order*, *Phys. Rev. Lett.* **33** (1974) 244.
- [79] W. A. Bardeen, A. Buras, D. Duke and T. Muta, *Deep Inelastic Scattering Beyond the Leading Order in Asymptotically Free Gauge Theories*, *Phys. Rev. D* **18** (1978) 3998.
- [80] J. Komijani, P. Petreczky and J. H. Weber, *Strong coupling constant and quark masses from lattice QCD*, *Prog. Part. Nucl. Phys.* **113** (2020) 103788 [[2003.11703](#)].
- [81] A. Kataev and S. Larin, *Analytical five-loop expressions for the renormalization group QED β -function in different renormalization schemes*, *Pisma Zh. Eksp. Teor. Fiz.* **96** (2012) 64 [[1205.2810](#)].

Bibliography

- [82] M. Gockeler, R. Horsley, P. E. Rakow, G. Schierholz and R. Sommer, *Scaling laws, renormalization group flow and the continuum limit in noncompact lattice QED*, *Nucl. Phys. B* **371** (1992) 713.
- [83] M. Gockeler, R. Horsley, V. Linke, P. E. Rakow, G. Schierholz and H. Stuben, *Is there a Landau pole problem in QED?*, *Phys. Rev. Lett.* **80** (1998) 4119 [[hep-th/9712244](#)].
- [84] M. Gockeler, R. Horsley, V. Linke, P. E. Rakow, G. Schierholz and H. Stuben, *Resolution of the Landau pole problem in QED*, *Nucl. Phys. B Proc. Suppl.* **63** (1998) 694 [[hep-lat/9801004](#)].
- [85] L. Cieri, G. Ferrera and G. F. Sborlini, *Combining QED and QCD transverse-momentum resummation for Z boson production at hadron colliders*, *JHEP* **08** (2018) 165 [[1805.11948](#)].
- [86] A. Bacchetta and M. G. Echevarria, *QCD \times QED evolution of TMDs*, *Phys. Lett. B* **788** (2019) 280 [[1810.02297](#)].
- [87] K. Fujikawa, *Path Integral Measure for Gauge Invariant Fermion Theories*, *Phys. Rev. Lett.* **42** (1979) 1195.
- [88] K. Fujikawa, *Path Integral for Gauge Theories with Fermions*, *Phys. Rev. D* **21** (1980) 2848.
- [89] K. Fukushima and T. Hatsuda, *The phase diagram of dense QCD*, *Rept. Prog. Phys.* **74** (2011) 014001 [[1005.4814](#)].
- [90] J. Goldstone, *Field Theories with Superconductor Solutions*, *Nuovo Cim.* **19** (1961) 154.
- [91] J. Goldstone, A. Salam and S. Weinberg, *Broken Symmetries*, *Phys. Rev.* **127** (1962) 965.
- [92] S. Scherer, *A primer for chiral perturbation theory*, 2011.
- [93] R. F. Dashen, *Chiral SU(3) \times SU(3) as a symmetry of the strong interactions*, *Phys. Rev.* **183** (1969) 1245.
- [94] R. Urech, *Virtual photons in chiral perturbation theory*, *Nucl. Phys. B* **433** (1995) 234 [[hep-ph/9405341](#)].
- [95] L. Varnhorst, S. Durr, Z. Fodor, C. Hoelbling, S. Krieg, L. Lellouch et al., *Up and down quark masses and corrections to Dashen’s theorem from lattice QCD and quenched QED*, *PoS LATTICE2016* (2017) 200 [[1702.00309](#)].
- [96] I. Montvay and G. Münster, *Quantum fields on a lattice*, 1997.
- [97] H. J. Rothe, *Lattice gauge theories : an introduction*, 2005.

- [98] T. DeGrand and C. DeTar, *Lattice methods for quantum chromodynamics*, 2006.
- [99] J. Smit, *Introduction to quantum fields on a lattice : "a robust mate"*, 2002.
- [100] M. Creutz, *Quarks, gluons and lattices*, 1990.
- [101] R. Gupta, *Introduction to lattice QCD: Course*, [hep-lat/9807028](#).
- [102] U.-J. Wiese, *An introduction to lattice field theory*, .
- [103] M. Lüscher, *Advanced lattice QCD*, [hep-lat/9802029](#).
- [104] M. Lüscher, *Computational Strategies in Lattice QCD*, [1002.4232](#).
- [105] A. C. Kalloniatis, D. B. Leinweber and A. G. Williams, *Lattice hadron physics*, 2005.
- [106] H.-W. Lin, *Lattice qcd for nuclear physics*, 2015. [10.1007/978-3-319-08022-2](#).
- [107] K. G. Wilson, *Confinement of Quarks*, *Phys. Rev.* **D10** (1974) 2445.
- [108] K. Symanzik, *Continuum Limit and Improved Action in Lattice Theories. 1. Principles and φ^4 Theory*, *Nucl. Phys. B* **226** (1983) 187.
- [109] K. Symanzik, *Continuum Limit and Improved Action in Lattice Theories. 2. $O(N)$ Nonlinear Sigma Model in Perturbation Theory*, *Nucl. Phys. B* **226** (1983) 205.
- [110] M. Lüscher, S. Sint, R. Sommer, P. Weisz and U. Wolff, *Nonperturbative $O(a)$ improvement of lattice QCD*, *Nucl. Phys. B* **491** (1997) 323 [[hep-lat/9609035](#)].
- [111] T. Bhattacharya, R. Gupta, W. Lee, S. R. Sharpe and J. M. Wu, *Improved bilinears in lattice QCD with non-degenerate quarks*, *Phys. Rev. D* **73** (2006) 034504 [[hep-lat/0511014](#)].
- [112] M. Luscher and P. Weisz, *Computation of the Action for On-Shell Improved Lattice Gauge Theories at Weak Coupling*, *Phys. Lett. B* **158** (1985) 250.
- [113] M. Lüscher and P. Weisz, *On-Shell Improved Lattice Gauge Theories*, *Commun. Math. Phys.* **97** (1985) 59.
- [114] Y. Iwasaki, *Renormalization Group Analysis of Lattice Theories and Improved Lattice Action: Two-Dimensional Nonlinear $O(N)$ Sigma Model*, *Nucl. Phys. B* **258** (1985) 141.
- [115] S. Chandrasekharan and U. Wiese, *An Introduction to chiral symmetry on the lattice*, *Prog. Part. Nucl. Phys.* **53** (2004) 373 [[hep-lat/0405024](#)].
- [116] L. H. Karsten and J. Smit, *Lattice Fermions: Species Doubling, Chiral Invariance, and the Triangle Anomaly*, .

Bibliography

- [117] H. Nielsen and M. Ninomiya, *A no-go theorem for regularizing chiral fermions*, *Physics Letters B* **105** (1981) 219 .
- [118] H. Nielsen and M. Ninomiya, *Absence of neutrinos on a lattice: (i). proof by homotopy theory*, *Nuclear Physics B* **185** (1981) 20 .
- [119] H. Nielsen and M. Ninomiya, *Absence of neutrinos on a lattice: (ii). intuitive topological proof*, *Nuclear Physics B* **193** (1981) 173 .
- [120] L. H. Karsten, *Lattice fermions in euclidean space-time*, *Physics Letters B* **104** (1981) 315 .
- [121] M. Lüscher, *Exact chiral symmetry on the lattice and the Ginsparg-Wilson relation*, *Phys. Lett. B* **428** (1998) 342 [[hep-lat/9802011](#)].
- [122] M. Lüscher, *Construction of a Selfadjoint, Strictly Positive Transfer Matrix for Euclidean Lattice Gauge Theories*, *Commun. Math. Phys.* **54** (1977) 283.
- [123] B. Sheikholeslami and R. Wohlert, *Improved Continuum Limit Lattice Action for QCD with Wilson Fermions*, *Nucl. Phys. B* **259** (1985) 572.
- [124] P. H. Ginsparg and K. G. Wilson, *A remnant of chiral symmetry on the lattice*, *Phys. Rev. D* **25** (1982) 2649.
- [125] S. Chandrasekharan, *Lattice QCD with Ginsparg-Wilson fermions*, *Phys. Rev. D* **60** (1999) 074503 [[hep-lat/9805015](#)].
- [126] D. B. Kaplan, *A Method for simulating chiral fermions on the lattice*, *Phys. Lett. B* **288** (1992) 342 [[hep-lat/9206013](#)].
- [127] Y. Shamir, *Chiral fermions from lattice boundaries*, *Nucl. Phys. B* **406** (1993) 90 [[hep-lat/9303005](#)].
- [128] Y. Shamir, *Constraints on the existence of chiral fermions in interacting lattice theories*, *Phys. Rev. Lett.* **71** (1993) 2691 [[hep-lat/9306023](#)].
- [129] V. Furman and Y. Shamir, *Axial symmetries in lattice QCD with Kaplan fermions*, *Nucl. Phys. B* **439** (1995) 54 [[hep-lat/9405004](#)].
- [130] H. Neuberger, *Exactly massless quarks on the lattice*, *Phys. Lett. B* **417** (1998) 141 [[hep-lat/9707022](#)].
- [131] H. Neuberger, *More about exactly massless quarks on the lattice*, *Phys. Lett. B* **427** (1998) 353 [[hep-lat/9801031](#)].
- [132] R. Frezzotti, P. A. Grassi, S. Sint and P. Weisz, *A Local formulation of lattice QCD without unphysical fermion zero modes*, *Nucl. Phys. B Proc. Suppl.* **83** (2000) 941 [[hep-lat/9909003](#)].

- [133] ALPHA collaboration, R. Frezzotti, P. A. Grassi, S. Sint and P. Weisz, *Lattice QCD with a chirally twisted mass term*, *JHEP* **08** (2001) 058 [[hep-lat/0101001](#)].
- [134] R. Frezzotti and G. Rossi, *Chirally improving Wilson fermions. 1. $O(a)$ improvement*, *JHEP* **08** (2004) 007 [[hep-lat/0306014](#)].
- [135] A. Shindler, *Twisted mass lattice QCD*, *Phys. Rept.* **461** (2008) 37 [[0707.4093](#)].
- [136] L. Susskind, *Lattice fermions*, *Phys. Rev. D* **16** (1977) 3031.
- [137] M. Creutz, *Why rooting fails*, *PoS LATTICE2007* (2007) 007 [[0708.1295](#)].
- [138] A. S. Kronfeld, *Lattice Gauge Theory with Staggered Fermions: How, Where, and Why (Not)*, *PoS LATTICE2007* (2007) 016 [[0711.0699](#)].
- [139] Z. Davoudi, J. Harrison, A. Jüttner, A. Portelli and M. J. Savage, *Theoretical aspects of quantum electrodynamics in a finite volume with periodic boundary conditions*, *Phys. Rev. D* **99** (2019) 034510 [[1810.05923](#)].
- [140] M. Hayakawa and S. Uno, *QED in finite volume and finite size scaling effect on electromagnetic properties of hadrons*, *Prog. Theor. Phys.* **120** (2008) 413 [[0804.2044](#)].
- [141] A. Duncan, E. Eichten and H. Thacker, *Electromagnetic splittings and light quark masses in lattice QCD*, *Phys. Rev. Lett.* **76** (1996) 3894 [[hep-lat/9602005](#)].
- [142] A. Duncan, E. Eichten and H. Thacker, *Electromagnetic splittings and light quark masses*, *Nucl. Phys. B Proc. Suppl.* **53** (1997) 295 [[hep-lat/9609015](#)].
- [143] N. Tantalo, *Isospin Breaking Effects on the Lattice*, *PoS LATTICE2013* (2014) 007 [[1311.2797](#)].
- [144] M. G. Endres, A. Shindler, B. C. Tiburzi and A. Walker-Loud, *Photon mass term as an IR regularization for QCD+QED on the lattice*, *PoS LATTICE2015* (2016) 078 [[1512.08983](#)].
- [145] M. G. Endres, A. Shindler, B. C. Tiburzi and A. Walker-Loud, *Massive photons: an infrared regularization scheme for lattice QCD+QED*, *Phys. Rev. Lett.* **117** (2016) 072002 [[1507.08916](#)].
- [146] B. Lucini, A. Patella, A. Ramos and N. Tantalo, *Charged hadrons in local finite-volume QED+QCD with C^* boundary conditions*, *JHEP* **02** (2016) 076 [[1509.01636](#)].
- [147] M. Hansen, B. Lucini, A. Patella and N. Tantalo, *Simulations of QCD and QED with C^* boundary conditions*, *EPJ Web Conf.* **175** (2018) 09001 [[1710.08838](#)].
- [148] M. Hansen, B. Lucini, A. Patella and N. Tantalo, *Gauge invariant determination of charged hadron masses*, *JHEP* **05** (2018) 146 [[1802.05474](#)].

Bibliography

- [149] I. Campos, P. Fritzsche, M. Hansen, M. K. Marinković, A. Patella, A. Ramos et al., *openQ*D simulation code for QCD+QED*, *EPJ Web Conf.* **175** (2018) 09005 [1710.08839].
- [150] RC* collaboration, I. Campos, P. Fritzsche, M. Hansen, M. K. Marinkovic, A. Patella, A. Ramos et al., *openQ*D code: a versatile tool for QCD+QED simulations*, *Eur. Phys. J. C* **80** (2020) 195 [1908.11673].
- [151] D. Scalapino and R. Sugar, *A Method for Performing Monte Carlo Calculations for Systems with Fermions*, *Phys. Rev. Lett.* **46** (1981) 519.
- [152] H. W. Hamber, *Monte Carlo Simulations of Systems With Fermions*, *Phys. Rev. D* **24** (1981) 951.
- [153] D. Weingarten and D. Petcher, *Monte Carlo Integration for Lattice Gauge Theories with Fermions*, *Phys. Lett. B* **99** (1981) 333.
- [154] M. Lüscher, *A New approach to the problem of dynamical quarks in numerical simulations of lattice QCD*, *Nucl. Phys. B* **418** (1994) 637 [hep-lat/9311007].
- [155] A. D. Kennedy, I. Horvath and S. Sint, *A New exact method for dynamical fermion computations with nonlocal actions*, *Nucl. Phys. Proc. Suppl.* **73** (1999) 834 [hep-lat/9809092].
- [156] M. A. Clark and A. D. Kennedy, *Accelerating dynamical fermion computations using the rational hybrid Monte Carlo (RHMC) algorithm with multiple pseudofermion fields*, *Phys. Rev. Lett.* **98** (2007) 051601 [hep-lat/0608015].
- [157] J. Finkenrath, F. Knechtli and B. Leder, *One flavor mass reweighting in lattice QCD*, *Nucl. Phys. B* **877** (2013) 441 [1306.3962].
- [158] J. Finkenrath, F. Knechtli and B. Leder, *Isospin Effects by Mass Reweighting*, *PoS LATTICE2014* (2015) 297 [1501.06441].
- [159] S. Duane, A. D. Kennedy, B. J. Pendleton and D. Roweth, *Hybrid Monte Carlo*, *Phys. Lett. B* **195** (1987) 216.
- [160] A. Ferrenberg and R. Swendsen, *New Monte Carlo Technique for Studying Phase Transitions*, *Phys. Rev. Lett.* **61** (1988) 2635.
- [161] A. M. Ferrenberg and R. H. Swendsen, *Optimized Monte Carlo analysis*, *Phys. Rev. Lett.* **63** (1989) 1195.
- [162] Z. Fodor and S. Katz, *A New method to study lattice QCD at finite temperature and chemical potential*, *Phys. Lett. B* **534** (2002) 87 [hep-lat/0104001].
- [163] A. Hasenfratz, R. Hoffmann and S. Schaefer, *Reweighting towards the chiral limit*, *Phys. Rev. D* **78** (2008) 014515 [0805.2369].

- [164] B. Leder, J. Finkenrath and F. Knechtli, *One flavor mass reweighting: foundations*, *PoS LATTICE2013* (2014) 035 [1401.1079].
- [165] A. Duncan, E. Eichten and R. Sedgewick, *Computing electromagnetic effects in fully unquenched QCD*, *Phys. Rev. D* **71** (2005) 094509 [hep-lat/0405014].
- [166] R. Johnson, *ANGULAR MOMENTUM ON A LATTICE*, *Phys. Lett. B* **114** (1982) 147.
- [167] ETM collaboration, C. Michael, K. Ottnad and C. Urbach, *η and η' mixing from Lattice QCD*, *Phys. Rev. Lett.* **111** (2013) 181602 [1310.1207].
- [168] M. Lüscher and S. Schaefer, *Lattice QCD with open boundary conditions and twisted-mass reweighting*, *Comput. Phys. Commun.* **184** (2013) 519 [1206.2809].
- [169] S. Schaefer, *Status and challenges of simulations with dynamical fermions*, *PoS LATTICE2012* (2012) 001 [1211.5069].
- [170] M. Bruno, P. Korcyl, T. Korzec, S. Lottini and S. Schaefer, *On the extraction of spectral quantities with open boundary conditions*, *PoS LATTICE2014* (2014) 089 [1411.5207].
- [171] M. Bruno, T. Korzec and S. Schaefer, *Setting the scale for the CLS 2 + 1 flavor ensembles*, *Phys. Rev. D* **95** (2017) 074504 [1608.08900].
- [172] J. Bulava and S. Schaefer, *Improvement of $N_f = 3$ lattice QCD with Wilson fermions and tree-level improved gauge action*, *Nucl. Phys. B* **874** (2013) 188 [1304.7093].
- [173] M. Lüscher and S. Schaefer, *Lattice QCD without topology barriers*, *JHEP* **07** (2011) 036 [1105.4749].
- [174] T. A. DeGrand, *A Conditioning Technique for Matrix Inversion for Wilson Fermions*, *Comput. Phys. Commun.* **52** (1988) 161.
- [175] M. Hasenbusch, *Speeding up the hybrid Monte Carlo algorithm for dynamical fermions*, *Phys. Lett.* **B519** (2001) 177 [hep-lat/0107019].
- [176] M. Hasenbusch and K. Jansen, *Speeding up lattice QCD simulations with clover improved Wilson fermions*, *Nucl. Phys.* **B659** (2003) 299 [hep-lat/0211042].
- [177] D. Mohler and S. Schaefer, *Remarks on strange-quark simulations with Wilson fermions*, 2003.13359.
- [178] J. Sexton and D. Weingarten, *Hamiltonian evolution for the hybrid Monte Carlo algorithm*, *Nucl. Phys. B* **380** (1992) 665.

Bibliography

- [179] I. Omelyan, I. Mryglod and R. Folk, *Symplectic analytically integrable decomposition algorithms: classification, derivation, and application to molecular dynamics, quantum and celestial mechanics simulations*, *Computer Physics Communications* **151** (2003) 272 .
- [180] M. Lüscher, *Deflation acceleration of lattice QCD simulations*, *JHEP* **12** (2007) 011 [0710.5417].
- [181] M. Lüscher, *Solution of the Dirac equation in lattice QCD using a domain decomposition method*, *Comput. Phys. Commun.* **156** (2004) 209 [hep-lat/0310048].
- [182] Y. Saad and M. Schultz, *Gmres: a generalized minimal residual algorithm for solving nonsymmetric linear systems*, *Siam Journal on Scientific and Statistical Computing* **7** (1986) 856.
- [183] M. Lüscher, *Trivializing maps, the Wilson flow and the HMC algorithm*, *Commun. Math. Phys.* **293** (2010) 899 [0907.5491].
- [184] M. Lüscher, *Properties and uses of the Wilson flow in lattice QCD*, *JHEP* **08** (2010) 071 [1006.4518].
- [185] R. Sommer, *A New way to set the energy scale in lattice gauge theories and its applications to the static force and alpha-s in SU(2) Yang-Mills theory*, *Nucl. Phys. B* **411** (1994) 839 [hep-lat/9310022].
- [186] R. Sommer, *Scale setting in lattice QCD*, *PoS LATTICE2013* (2014) 015 [1401.3270].
- [187] A. Gérardin, T. Harris, G. von Hippel, B. Hörz, H. Meyer, D. Mohler et al., *The hadronic vacuum polarization contribution to $(g - 2)_\mu$ from 2 + 1 flavours of $O(a)$ improved Wilson quarks*, *PoS LATTICE2018* (2018) 139 [1812.03553].
- [188] D. Mohler, S. Schaefer and J. Simeth, *CLS 2+1 flavor simulations at physical light- and strange-quark masses*, *EPJ Web Conf.* **175** (2018) 02010 [1712.04884].
- [189] RQCD collaboration, G. S. Bali, E. E. Scholz, J. Simeth and W. Söldner, *Lattice simulations with $N_f = 2 + 1$ improved Wilson fermions at a fixed strange quark mass*, *Phys. Rev. D* **94** (2016) 074501 [1606.09039].
- [190] RQCD collaboration, G. S. Bali, S. Collins, F. Hutzler, M. Göckeler, A. Schäfer, E. E. Scholz et al., *Towards the continuum limit with improved Wilson fermions employing open boundary conditions*, *PoS LATTICE2016* (2017) 106 [1702.01035].
- [191] G. de Divitiis et al., *Isospin breaking effects due to the up-down mass difference in Lattice QCD*, *JHEP* **04** (2012) 124 [1110.6294].

- [192] F. Sanfilippo et al., *Lattice QCD calculation of isospin breaking effects due to the up-down mass difference*, *PoS LATTICE2011* (2011) 290.
- [193] P. Boyle, V. Gülpers, J. Harrison, A. Jüttner, A. Portelli and C. Sachrajda, *Electromagnetic Corrections to Meson Masses and the HVP*, *PoS LATTICE2016* (2016) 172 [1612.05962].
- [194] P. Boyle, V. Gülpers, J. Harrison, A. Jüttner, C. Lehner, A. Portelli et al., *Isospin breaking corrections to meson masses and the hadronic vacuum polarization: a comparative study*, *JHEP* **09** (2017) 153 [1706.05293].
- [195] RBC, UKQCD collaboration, C. Lehner, *A precise determination of the HVP contribution to the muon anomalous magnetic moment from lattice QCD*, *EPJ Web Conf.* **175** (2018) 01024 [1710.06874].
- [196] P. Boyle, V. Gülpers, J. Harrison, A. Jüttner, C. Lehner, A. Portelli et al., *Isospin Breaking Corrections to the HVP with Domain Wall Fermions*, *EPJ Web Conf.* **175** (2018) 06024 [1710.07190].
- [197] V. Gülpers, A. Jüttner, C. Lehner and A. Portelli, *Isospin breaking corrections to the HVP at the physical point*, 1812.09562.
- [198] P. Boyle, V. Gülpers, A. Jüttner, C. Lehner, F. hOgain, A. Portelli et al., *QED corrections to leptonic decay rates*, *PoS LATTICE2018* (2019) 267 [1902.00295].
- [199] N. Hermansson-Truedsson, J. Bijnens, J. Harrison, T. Janowski, A. Jüttner and A. Portelli, *Electromagnetic finite-size effects to the hadronic vacuum polarisation*, *PoS LATTICE2019* (2019) [1910.03250].
- [200] S. Borsanyi et al., *Leading-order hadronic vacuum polarization contribution to the muon magnetic moment from lattice QCD*, 2002.12347.
- [201] M. Lüscher, *The Schrodinger functional in lattice QCD with exact chiral symmetry*, *JHEP* **05** (2006) 042 [hep-lat/0603029].
- [202] M. Bochicchio, L. Maiani, G. Martinelli, G. C. Rossi and M. Testa, *Chiral Symmetry on the Lattice with Wilson Fermions*, *Nucl. Phys. B* **262** (1985) 331.
- [203] T. Blum, R. Zhou, T. Doi, M. Hayakawa, T. Izubuchi, S. Uno et al., *Electromagnetic mass splittings of the low lying hadrons and quark masses from 2+1 flavor lattice QCD+QED*, *Phys. Rev. D* **82** (2010) 094508 [1006.1311].
- [204] A. Portelli et al., *Systematic errors in partially-quenched QCD plus QED lattice simulations*, *PoS LATTICE2011* (2011) 136 [1201.2787].
- [205] <https://http://www.fftw.org/> .

Bibliography

- [206] SciDAC, LHPC, UKQCD collaboration, R. G. Edwards and B. Joo, *The Chroma software system for lattice QCD*, *Nucl. Phys. B Proc. Suppl.* **140** (2005) 832 [[hep-lat/0409003](#)].
- [207] P. Young, *Everything you wanted to know about Data Analysis and Fitting but were afraid to ask*, 1210.3781.
- [208] B. Efron and R. Tibshirani, *An introduction to the bootstrap*, 1993.
- [209] R. Andrae, T. Schulze-Hartung and P. Melchior, *Dos and don'ts of reduced chi-squared*, 1012.3754.
- [210] R. Andrae, *Error estimation in astronomy: A guide*, 1009.2755.
- [211] G. Van Rossum and F. L. Drake, *Python 3 Reference Manual*. CreateSpace, Scotts Valley, CA, 2009.
- [212] <https://www.h5py.org/> .
- [213] <https://numpy.org/> .
- [214] <https://www.scipy.org/> .
- [215] <https://matplotlib.org/> .
- [216] <https://www.json.org/> .
- [217] <https://docs.python.org/3/library/random.html> .
- [218] B. Efron, *Bootstrap methods: Another look at the jackknife*, *Ann. Statist.* **7** (1979) 1.
- [219] ALPHA collaboration, U. Wolff, *Monte Carlo errors with less errors*, *Comput. Phys. Commun.* **156** (2004) 143 [[hep-lat/0306017](#)].
- [220] B. De Palma, M. Erba, L. Mantovani and N. Mosco, *A Python program for the implementation of the Γ -method for Monte Carlo simulations*, *Comput. Phys. Commun.* **234** (2019) 294 [[1703.02766](#)].
- [221] P. Virtanen, R. Gommers, T. E. Oliphant, M. Haberland, T. Reddy, D. Cournapeau et al., *SciPy 1.0: Fundamental Algorithms for Scientific Computing in Python*, *Nature Methods* **17** (2020) 261.
- [222] C. Michael, *Fitting correlated data*, *Phys. Rev. D* **49** (1994) 2616 [[hep-lat/9310026](#)].
- [223] C. Michael and A. McKerrell, *Fitting correlated hadron mass spectrum data*, *Phys. Rev. D* **51** (1995) 3745 [[hep-lat/9412087](#)].

- [224] N. Carrasco, V. Lubicz, G. Martinelli, C. Sachrajda, N. Tantalo, C. Tarantino et al., *QED Corrections to Hadronic Processes in Lattice QCD*, *Phys. Rev. D* **91** (2015) 074506 [1502.00257].
- [225] D. Giusti, V. Lubicz, G. Martinelli, C. Sachrajda, F. Sanfilippo, S. Simula et al., *First lattice calculation of the QED corrections to leptonic decay rates*, *Phys. Rev. Lett.* **120** (2018) 072001 [1711.06537].
- [226] M. Di Carlo, D. Giusti, V. Lubicz, G. Martinelli, C. Sachrajda, F. Sanfilippo et al., *Light-meson leptonic decay rates in lattice QCD+QED*, *Phys. Rev. D* **100** (2019) 034514 [1904.08731].
- [227] A. Desiderio et al., *First lattice calculation of radiative leptonic decay rates of pseudoscalar mesons*, 2006.05358.
- [228] A. Bussone, M. Della Morte, T. Janowski and A. Walker-Loud, *On the definition of schemes for computing leading order isospin breaking corrections*, *PoS LATTICE2018* (2018) 293 [1810.11647].
- [229] A. Gérardin, T. Harris and H. B. Meyer, *Nonperturbative renormalization and $O(a)$ -improvement of the nonsinglet vector current with $N_f = 2 + 1$ Wilson fermions and tree-level Symanzik improved gauge action*, *Phys. Rev. D* **99** (2019) 014519 [1811.08209].
- [230] S. Dong and K. Liu, *Quark loop calculations*, *Nucl. Phys. B Proc. Suppl.* **26** (1992) 353.
- [231] S.-J. Dong and K.-F. Liu, *Stochastic estimation with $Z(2)$ noise*, *Phys. Lett. B* **328** (1994) 130 [hep-lat/9308015].
- [232] S. Bernardson, P. McCarty and C. Thron, *Monte Carlo methods for estimating linear combinations of inverse matrix entries in lattice QCD*, *Comput. Phys. Commun.* **78** (1993) 256.
- [233] S. Bernardson, P. McCarthy and C. Thron, *Efficient methods for Monte Carlo inversion of quark matrices*, *Nucl. Phys. B Proc. Suppl.* **34** (1994) 759.
- [234] ETM collaboration, P. Boucaud, P. Dimopoulos, F. Farchioni, R. Frezzotti, V. Gimenez, G. Herdoiza et al., *Dynamical Twisted Mass Fermions with Light Quarks: Simulation and Analysis Details*, *Comput. Phys. Commun.* **179** (2008) 695 [0803.0224].
- [235] P. Boyle, A. Juttner, C. Kelly and R. Kenway, *Use of stochastic sources for the lattice determination of light quark physics*, *JHEP* **08** (2008) 086 [0804.1501].
- [236] E. Endress, A. Juttner and H. Wittig, *On the efficiency of stochastic volume sources for the determination of light meson masses*, 1111.5988.

Bibliography

- [237] HADRON SPECTRUM collaboration, J. Bulava, R. Edwards and C. Morningstar, *Stochastic All-to-All Propagators for Baryon Correlators*, *PoS LATTICE2008* (2008) 124 [0810.1469].
- [238] C. Michael, *Adjoint Sources in Lattice Gauge Theory*, *Nucl. Phys. B* **259** (1985) 58.
- [239] M. Lüscher and U. Wolff, *How to Calculate the Elastic Scattering Matrix in Two-dimensional Quantum Field Theories by Numerical Simulation*, *Nucl. Phys. B* **339** (1990) 222.
- [240] B. Blossier, G. von Hippel, T. Mendes, R. Sommer and M. Della Morte, *Efficient use of the Generalized Eigenvalue Problem*, *PoS LATTICE2008* (2008) 135 [0808.1017].
- [241] K. Schilling, H. Neff and T. Lippert, *Computing the eta and eta-prime mesons in lattice QCD*, *Lect. Notes Phys.* **663** (2005) 147 [hep-lat/0401005].
- [242] ETM collaboration, K. Ottnad and C. Urbach, *Flavor-singlet meson decay constants from $N_f = 2 + 1 + 1$ twisted mass lattice QCD*, *Phys. Rev. D* **97** (2018) 054508 [1710.07986].
- [243] A. Risch and H. Wittig, *Towards leading isospin breaking effects in mesonic masses with open boundaries*, *PoS LATTICE2018* (2018) 059 [1811.00895].
- [244] S. Capitani, M. Della Morte, G. von Hippel, B. Knippschild and H. Wittig, *Scale setting via the Ω baryon mass*, *PoS LATTICE2011* (2011) 145 [1110.6365].
- [245] RBC, UKQCD collaboration, T. Blum, P. Boyle, V. Gülpers, T. Izubuchi, L. Jin, C. Jung et al., *Calculation of the hadronic vacuum polarization contribution to the muon anomalous magnetic moment*, *Phys. Rev. Lett.* **121** (2018) 022003 [1801.07224].
- [246] CSSM/QCDSF/UKQCD collaboration, Z. Kordov, R. Horsley, Y. Nakamura, H. Perlt, P. Rakow, G. Schierholz et al., *Electromagnetic contribution to Σ - Λ mixing using lattice QCD+QED*, *Phys. Rev. D* **101** (2020) 034517 [1911.02186].
- [247] D. Giusti, *Leading isospin breaking effects on hadronic quantities in lattice QCD: The neutron-proton mass splitting*, .
- [248] RQCD collaboration, W. Söldner, *Lattice QCD with 2+1 Flavors and Open Boundaries: First Results of the Baryon Spectrum*, *PoS LATTICE2014* (2015) 099 [1502.05481].
- [249] S. Gusken, U. Low, K. Mutter, R. Sommer, A. Patel and K. Schilling, *Nonsinglet Axial Vector Couplings of the Baryon Octet in Lattice QCD*, *Phys. Lett. B* **227** (1989) 266.

- [250] T. Harris, G. von Hippel, P. Junnarkar, H. B. Meyer, K. Ottnad, J. Wilhelm et al., *Nucleon isovector charges and twist-2 matrix elements with $N_f = 2 + 1$ dynamical Wilson quarks*, *Phys. Rev. D* **100** (2019) 034513 [1905.01291].
- [251] D. Djukanovic, K. Ottnad, J. Wilhelm and H. Wittig, *Strange electromagnetic form factors of the nucleon with $N_f = 2 + 1$ $\mathcal{O}(a)$ -improved Wilson fermions*, *Phys. Rev. Lett.* **123** (2019) 212001 [1903.12566].
- [252] S. Gusken, *A Study of smearing techniques for hadron correlation functions*, *Nucl. Phys. B Proc. Suppl.* **17** (1990) 361.
- [253] G. S. Bali, S. Collins and A. Schafer, *Effective noise reduction techniques for disconnected loops in Lattice QCD*, *Comput. Phys. Commun.* **181** (2010) 1570 [0910.3970].
- [254] T. Blum, T. Izubuchi and E. Shintani, *New class of variance-reduction techniques using lattice symmetries*, *Phys. Rev. D* **88** (2013) 094503 [1208.4349].
- [255] T. Blum, T. Izubuchi and E. Shintani, *Error reduction technique using covariant approximation and application to nucleon form factor*, *PoS LATTICE2012* (2012) 262 [1212.5542].
- [256] E. Shintani, R. Arthur, T. Blum, T. Izubuchi, C. Jung and C. Lehner, *Covariant approximation averaging*, *Phys. Rev. D* **91** (2015) 114511 [1402.0244].
- [257] LATTICE HADRON PHYSICS (LHPC) collaboration, S. Basak, R. Edwards, G. T. Fleming, U. M. Heller, C. Morningstar, D. Richards et al., *Clebsch-Gordan construction of lattice interpolating fields for excited baryons*, *Phys. Rev. D* **72** (2005) 074501 [hep-lat/0508018].
- [258] S. Basak, R. Edwards, G. Fleming, U. Heller, C. Morningstar, D. Richards et al., *Group-theoretical construction of extended baryon operators in lattice QCD*, *Phys. Rev. D* **72** (2005) 094506 [hep-lat/0506029].
- [259] J. C. Collins, A. V. Manohar and M. B. Wise, *Renormalization of the vector current in QED*, *Phys. Rev. D* **73** (2006) 105019 [hep-th/0512187].
- [260] G. Martinelli, M. Paciello, S. Petrarca, C. Pittori, C. Sachrajda, B. Taglienti et al., *Non-perturbative renormalisation of composite operators*, *Nuclear Physics B - Proceedings Supplements* **34** (1994) 507 .
- [261] A. Gérardin, M. Cè, G. von Hippel, B. Hörz, H. B. Meyer, D. Mohler et al., *The leading hadronic contribution to $(g - 2)_\mu$ from lattice QCD with $N_f = 2 + 1$ flavours of $\mathcal{O}(a)$ improved Wilson quarks*, *Phys. Rev. D* **100** (2019) 014510 [1904.03120].
- [262] A. Risch and H. Wittig, *Leading isospin breaking effects in the hadronic vacuum polarisation with open boundaries*, *PoS LATTICE2019* (2019) 296 [1911.04230].

Bibliography

- [263] A. Stathopoulos, J. Laeuchli and K. Orginos, *Hierarchical probing for estimating the trace of the matrix inverse on toroidal lattices*, 1302.4018.
- [264] L. Giusti, T. Harris, A. Nada and S. Schaefer, *Frequency-splitting estimators of single-propagator traces*, *Eur. Phys. J. C* **79** (2019) 586 [1903.10447].
- [265] L. Giusti, T. Harris, A. Nada and S. Schaefer, *Frequency-splitting estimators of single-propagator traces*, *PoS LATTICE2019* (2020) 157 [2001.08783].
- [266] M. Della Morte, A. Francis, V. Gülpers, G. Herdoíza, G. von Hippel, H. Horch et al., *The hadronic vacuum polarization contribution to the muon $g - 2$ from lattice QCD*, *JHEP* **10** (2017) 020 [1705.01775].
- [267] M. Della Morte, A. Francis, A. Gérardin, V. Gülpers, G. Herdoíza, G. von Hippel et al., *A lattice calculation of the hadronic vacuum polarization contribution to $(g - 2)_\mu$* , *EPJ Web Conf.* **175** (2018) 06031 [1710.10072].
- [268] A. Gérardin, M. Cè, G. von Hippel, B. Hörz, H. Meyer, D. Mohler et al., *The leading hadronic vacuum polarization contribution to the muon anomalous magnetic moment using $N_f = 2 + 1$ $O(a)$ improved Wilson quarks*, 1911.04733.
- [269] F. Jegerlehner, *Hadronic contributions to the photon vacuum polarization and their role in precision physics*, *J. Phys. G* **29** (2003) 101 [hep-ph/0104304].
- [270] D. Bernecker and H. B. Meyer, *Vector Correlators in Lattice QCD: Methods and applications*, *Eur. Phys. J. A* **47** (2011) 148 [1107.4388].
- [271] F. Burger, K. Jansen, M. Petschlies and G. Pientka, *Leading hadronic contributions to the running of the electroweak coupling constants from lattice QCD*, *JHEP* **11** (2015) 215 [1505.03283].
- [272] A. Francis, V. Gülpers, G. Herdoíza, H. Horch, B. Jäger, H. B. Meyer et al., *Study of the hadronic contributions to the running of the QED coupling and the weak mixing angle*, *PoS LATTICE2015* (2015) 110 [1511.04751].
- [273] P. F. Bedaque, *Aharonov-Bohm effect and nucleon nucleon phase shifts on the lattice*, *Phys. Lett. B* **593** (2004) 82 [nucl-th/0402051].
- [274] G. de Divitiis, R. Petronzio and N. Tantalo, *On the discretization of physical momenta in lattice QCD*, *Phys. Lett. B* **595** (2004) 408 [hep-lat/0405002].
- [275] M. Della Morte, B. Jager, A. Juttner and H. Wittig, *Towards a precise lattice determination of the leading hadronic contribution to $(g - 2)_\mu$* , *JHEP* **03** (2012) 055 [1112.2894].
- [276] B. Chakraborty, C. T. Davies, J. Koponen, G. P. Lepage and R. S. Van de Water, *Higher-Order Hadronic-Vacuum-Polarization Contribution to the Muon $G-2$ from Lattice QCD*, *Phys. Rev. D* **98** (2018) 094503 [1806.08190].

- [277] M. Cè, T. S. José, A. Gérardin, H. B. Meyer, K. Miura, K. Ottnad et al., *The hadronic contribution to the running of the electromagnetic coupling and the electroweak mixing angle*, *PoS LATTICE2019* (2019) 010 [1910.09525].
- [278] F. Erben, J. R. Green, D. Mohler and H. Wittig, *Rho resonance, timelike pion form factor, and implications for lattice studies of the hadronic vacuum polarization*, *Phys. Rev. D* **101** (2020) 054504 [1910.01083].
- [279] S. Borsanyi, Z. Fodor, T. Kawanai, S. Krieg, L. Lellouch, R. Malak et al., *Slope and curvature of the hadronic vacuum polarization at vanishing virtuality from lattice QCD*, *Phys. Rev. D* **96** (2017) 074507 [1612.02364].
- [280] A. Gérardin, *The anomalous magnetic moment of the muon: status of Lattice QCD calculations*, in *38th International Symposium on Lattice Field Theory*, 12, 2020, 2012.03931.
- [281] C. Aubin, T. Blum, P. Chau, M. Golterman, S. Peris and C. Tu, *Finite-volume effects in the muon anomalous magnetic moment on the lattice*, *Phys. Rev. D* **93** (2016) 054508 [1512.07555].
- [282] BUDAPEST-MARSEILLE-WUPPERTAL collaboration, S. Borsanyi et al., *Hadronic vacuum polarization contribution to the anomalous magnetic moments of leptons from first principles*, *Phys. Rev. Lett.* **121** (2018) 022002 [1711.04980].
- [283] M. Lüscher, *Signatures of unstable particles in finite volume*, *Nucl. Phys. B* **364** (1991) 237.
- [284] L. Lellouch and M. Lüscher, *Weak transition matrix elements from finite volume correlation functions*, *Commun. Math. Phys.* **219** (2001) 31 [hep-lat/0003023].
- [285] H. B. Meyer, *Lattice QCD and the Timelike Pion Form Factor*, *Phys. Rev. Lett.* **107** (2011) 072002 [1105.1892].
- [286] G. Gounaris and J. Sakurai, *Finite width corrections to the vector meson dominance prediction for $\rho \rightarrow e^+ e^-$* , *Phys. Rev. Lett.* **21** (1968) 244.
- [287] F. Jegerlehner, *Hadronic contributions to electroweak parameter shifts*, *Zeitschrift für Physik C Particles and Fields* **32** (1986) 195.
- [288] V. Gülpers, H. Meyer, G. von Hippel and H. Wittig, *The leading hadronic contribution to γ -Z mixing*, *PoS LATTICE2015* (2016) 263.
- [289] M. Cè, A. Gérardin, K. Ottnad and H. B. Meyer, *The leading hadronic contribution to the running of the Weinberg angle using covariant coordinate-space methods*, *PoS LATTICE2018* (2018) 137 [1811.08669].
- [290] G. Charpak, F. Farley and R. Garwin, *A New Measurement of the Anomalous Magnetic Moment of the Muon*, *Phys. Lett.* **1** (1962) 16.

Bibliography

- [291] J. Bailey, W. Bartl, G. von Bochmann, R. Brown, F. Farley, M. Giesch et al., *Precise Measurement of the Anomalous Magnetic Moment of the Muon*, *Nuovo Cim. A* **9** (1972) 369.
- [292] CERN-MAINZ-DARESBUURY collaboration, J. Bailey et al., *Final Report on the CERN Muon Storage Ring Including the Anomalous Magnetic Moment and the Electric Dipole Moment of the Muon, and a Direct Test of Relativistic Time Dilation*, *Nucl. Phys. B* **150** (1979) 1.
- [293] J. P. Miller, E. de Rafael and B. Roberts, *Muon ($g-2$): Experiment and theory*, *Rept. Prog. Phys.* **70** (2007) 795 [[hep-ph/0703049](#)].
- [294] MUON G-2 collaboration, J. Grange et al., *Muon ($g-2$) Technical Design Report*, 1501.06858.
- [295] M. Abe et al., *A New Approach for Measuring the Muon Anomalous Magnetic Moment and Electric Dipole Moment*, *PTEP* **2019** (2019) 053C02 [[1901.03047](#)].
- [296] T. Aoyama, M. Hayakawa, T. Kinoshita and M. Nio, *Complete Tenth-Order QED Contribution to the Muon $g-2$* , *Phys. Rev. Lett.* **109** (2012) 111808 [[1205.5370](#)].
- [297] T. Aoyama, T. Kinoshita and M. Nio, *Theory of the Anomalous Magnetic Moment of the Electron*, *Atoms* **7** (2019) 28.
- [298] A. Czarnecki, W. J. Marciano and A. Vainshtein, *Refinements in electroweak contributions to the muon anomalous magnetic moment*, *Phys. Rev. D* **67** (2003) 073006 [[hep-ph/0212229](#)].
- [299] C. Gnendiger, D. Stöckinger and H. Stöckinger-Kim, *The electroweak contributions to $(g-2)_\mu$ after the Higgs boson mass measurement*, *Phys. Rev. D* **88** (2013) 053005 [[1306.5546](#)].
- [300] M. Davier, A. Hoecker, B. Malaescu and Z. Zhang, *Reevaluation of the hadronic vacuum polarisation contributions to the Standard Model predictions of the muon $g-2$ and $\alpha(m_Z^2)$ using newest hadronic cross-section data*, *Eur. Phys. J. C* **77** (2017) 827 [[1706.09436](#)].
- [301] A. Keshavarzi, D. Nomura and T. Teubner, *Muon $g-2$ and $\alpha(M_Z^2)$: a new data-based analysis*, *Phys. Rev. D* **97** (2018) 114025 [[1802.02995](#)].
- [302] G. Colangelo, M. Hoferichter and P. Stoffer, *Two-pion contribution to hadronic vacuum polarization*, *JHEP* **02** (2019) 006 [[1810.00007](#)].
- [303] M. Hoferichter, B.-L. Hoid and B. Kubis, *Three-pion contribution to hadronic vacuum polarization*, *JHEP* **08** (2019) 137 [[1907.01556](#)].
- [304] M. Davier, A. Hoecker, B. Malaescu and Z. Zhang, *A new evaluation of the hadronic vacuum polarisation contributions to the muon anomalous magnetic moment and to $\alpha(m_Z^2)$* , *Eur. Phys. J. C* **80** (2020) 241 [[1908.00921](#)].

- [305] A. Keshavarzi, D. Nomura and T. Teubner, $g - 2$ of charged leptons, $\alpha(M_Z^2)$, and the hyperfine splitting of muonium, *Phys. Rev. D* **101** (2020) 014029 [1911.00367].
- [306] A. Kurz, T. Liu, P. Marquard and M. Steinhauser, *Hadronic contribution to the muon anomalous magnetic moment to next-to-next-to-leading order*, *Phys. Lett. B* **734** (2014) 144 [1403.6400].
- [307] G. Colangelo, M. Hoferichter, A. Nyffeler, M. Passera and P. Stoffer, *Remarks on higher-order hadronic corrections to the muon $g-2$* , *Phys. Lett. B* **735** (2014) 90 [1403.7512].
- [308] X. Feng, K. Jansen, M. Petschlies and D. B. Renner, *Two-flavor QCD correction to lepton magnetic moments at leading-order in the electromagnetic coupling*, *Phys. Rev. Lett.* **107** (2011) 081802 [1103.4818].
- [309] D. Giusti, V. Lubicz, G. Martinelli, F. Sanfilippo and S. Simula, *Isospin-breaking corrections to the muon magnetic anomaly in Lattice QCD*, *PoS CD2018* (2019) 063 [1909.01962].
- [310] D. Giusti and S. Simula, *The hadronic vacuum polarization contribution to $(g_\mu - 2)$: Lattice QCD+QED calculations*, *Nuovo Cim. C* **43** (2020) 46 [1910.00611].
- [311] J. Foley, K. Jimmy Juge, A. O’Cais, M. Peardon, S. M. Ryan and J.-I. Skullerud, *Practical all-to-all propagators for lattice QCD*, *Comput. Phys. Commun.* **172** (2005) 145 [hep-lat/0505023].
- [312] M. Cè, L. Giusti and S. Schaefer, *A local factorization of the fermion determinant in lattice QCD*, *Phys. Rev. D* **95** (2017) 034503 [1609.02419].
- [313] M. Cè, L. Giusti and S. Schaefer, *Domain decomposition and multilevel integration for fermions*, *PoS LATTICE2016* (2016) 263 [1612.06424].
- [314] L. Giusti, M. Cè and S. Schaefer, *Multi-boson block factorization of fermions*, *EPJ Web Conf.* **175** (2018) 01003 [1710.09212].
- [315] M. Cè, L. Giusti and S. Schaefer, *Local multiboson factorization of the quark determinant*, *EPJ Web Conf.* **175** (2018) 11005 [1711.01592].
- [316] L. Giusti, T. Harris, A. Nada and S. Schaefer, *Multi-level integration for meson propagators*, *PoS LATTICE2018* (2018) 028 [1812.01875].
- [317] L. Giusti, M. D. Brida, T. Harris and M. Pepe, *A novel computational paradigm for a precise determination of the hadronic contribution to $(g_\mu - 2)$ from lattice QCD*, *PoS ICHEP2020* (2020) 378 [2101.04642].
- [318] H. Akaike, *A new look at the statistical model identification*, *IEEE Transactions on Automatic Control* **19** (1974) 716.

Bibliography

- [319] H. Akaike, *Likelihood of a model and information criteria*, *Journal of Econometrics* **16** (1981) 3 .
- [320] Jülich Supercomputing Centre, *JUWELS: Modular Tier-0/1 Supercomputer at the Jülich Supercomputing Centre*, *Journal of large-scale research facilities* **5** (2019) .